UNIVERSITY OF CALIFORNIA
RIVERSIDE

Understanding Fault Creep from the Macroscopic to the Microscopic Scale

A Dissertation submitted in partial satisfaction
of the requirements for the degree of

Doctor of Philosophy

in

Geological Sciences

by

Jerlyn L. Swiatlowski

March 2020

Dissertation Committee:

Dr. Gareth J. Funning, Chairperson
Dr. Nicolas Barth
Dr. David Oglesby

The Dissertation of Jerlyn L. Swiatlowski is approved:

Committee Chairperson

University of California, Riverside

Acknowledgments

Thank you to Gareth Funning, my advisor, for your guidance and encouragement through my time at UC Riverside. You always supported me in each of my research and outreach interests in and outside of the department which I have truly appreciated. I have grown to appreciate your mentoring style which has challenged me to find solutions to problems on my own and has made me a stronger scientist. You giving me the freedom to explore different avenues has really helped me discover what I am most passionate about — be it research and/or outreach. Your own passion for your research has always been an inspiration and I hope to apply that attitude in my future endeavors.

Thank you to my research collaborators. David Bekaert at JPL, you have been a tremendous help with the processing of my InSAR data since the beginning. Without your help, I wouldnt have gotten as far as quickly as I did and I greatly appreciate the time you invested in me. Diane Moore and David Lockner at USGS, thank you for unexpectedly taking me on as part of the NSF GFRP Graduate Research Internship program. I had a great time at USGS, working in the lab and learning from both of you in a research area that was new to me. It really has been a wonderful experience to work with you.

Thank you to my Dissertation Committee, Nicolas Barth and David Oglesby for reading and providing me with feedback on my dissertation to make my arguments stronger. David, you have always been a great motivator throughout my time at UC Riverside and taking classes has always been a fun experience while learning something new, for the both of us! Nic, you have been a large factor in my Structure from Motion work from the first trip to ASU to learn about SfM to your help in applying and refining the methods to my

offset sidewalks work. Thank you especially for allowing me to come into your lab to use the necessary programs and providing me with feedback all along the way.

I want to also thank Heather Ford, who has been not only an inspirational women scientist and mentor from the beginning but who has become a great friend in the processes. You have been a person I can go to for advice and to talk things through with, whether it is school or personal challenges in my life. I will miss our talks in your office.

Thank you to all the professors and researchers who have taught me and/or have given me support through my time here: Christodoulos Kyriakopoulos, Roby Douilly, Abhijit Ghosh, Peter Sadler, James Dieterich, Katherine Kendrick, and Keith Richards-Dinger.

Thank you to all of the graduate students that I have become close with throughout my time here. Without you being here, I would not be the person I am today.

To the people whom I have become very close with and would call my best friends through my time here. It was a cycle of who I became close with as each graduated from Kayla Kroll to Allie Hutchison to Jozi Pearson to Rachel Terry. I am very proud to have had such a strong group of women scientists during my graduate career and will continue to have after. You have made my life a happy one.

To Matthew Mendoza, Jennifer Humphreys, Xueying Zhao, and Baoning Wu whom I have gotten the pleasure of growing closer with in my last year and who have been cheerleaders for me through all the emotional highs and lows. Thank you for being there.

To all the other geophysics graduate students who have graced me with their presence throughout the years: Nader Shakibay-Senobari, Shankho Niyogui, Kuntal Chaudhuri, Bo Li, Tisha Irwin, Jacqui Gilchrist, John Conrad, and Kenny Ryan.

Lastly, I want to thank my family. Thank you Mom and Dad, you have always encouraged me to go do what I want, push me to finish the things I have started, and to do my best. Jenny, thank you for always listening to my many rants no matter the time of day. Mark, thank you for riding our education-edition roller coaster together through long distance undergrad, to long distance higher education. You are such a passionate person about your work and I am glad to have you as my partner in this life. You have been a large support these past 5.5 years, helping me, teaching me, listening to me, hugging me, supporting me, and growing with me. I cannot wait to see what is next for us.

ABSTRACT OF THE DISSERTATION

Understanding Fault Creep from the Macroscopic to the Microscopic Scale

by

Jerlyn L. Swiatlowski

Doctor of Philosophy, Graduate Program in Geological Sciences
University of California, Riverside, March 2020
Dr. Gareth J. Funning, Chairperson

Fault creep is a behavior of some faults where the two sides of a fault slowly slide past one another in the absence of large earthquakes. This is a form of aseismic slip and can be continuous or episodic. Understanding what drives fault creep is important as it can reduce the amount of strain that accumulates in the crust and can impede future earthquake ruptures. Both of these aspects play an important role in analyzing the seismic hazard of a region, therefore mapping the extent of where fault creep is occurring and identifying common lithology between creeping faults is necessary for accurate hazard assessment.

In this dissertation, we focus on fault creep in northern California using three different methods – satellite imagery, 3D models derived from photographs, and rock mechanics experiments. In the first project, we focus on mapping the extent of fault creep along on two faults in the North Bay (north of the San Francisco Bay Area), the Maacama and Rodgers Creek faults. Both faults have observations of fault creep at specific locations but the extent and variability of fault creep on each fault is not well mapped. We use Interferometric Synthetic Aperture Radar (InSAR) to map the extent of fault creep along

both faults and estimate at least 55% of the Maacama fault and 40% of the Rodgers Creek faults are creeping at the surface.

The second project focuses on offset sidewalk observations along the southern Hayward Fault, known to be creeping at rates up to ∼8 mm/yr and how fault creep is being expressed in an urban setting. We construct 3D models from 2D photos taken from 2015 to 2018 to measure 3D displacements of each offset sidewalk. In this way we can monitor how the fault is being expressed in an urban environment due to the creeping fault. We find that on average, individual offset curbs sample <40% of the overall creep rate measured from nearby alignment arrays (which span a fault-perpendicular distance of 100 m or more). In some locations, multiple adjacent curbs are actively deforming. These findings imply that there is significant off-fault deformation along the southern Hayward fault, and suggests that the 'fault trace' can more correctly be considered a zone of deformation, narrower than an alignment array width but wider than one curb length.

The third and fourth projects center on an exposure of the Bartlett Springs fault core near Lake Pillsbury, which is known to be creeping at 3.4 mm/yr from a nearby alignment array. We collected the fault gouge and ran two sets of experiments to investigate the frictional and mineralogical properties needed for a fault to creep. The first set of experiments investigated which of the minerals that we found in the fault gouge, are promoting or not promoting fault creep. We find that the presence of talc has the strongest influence on creep behavior. The second set of experiments explored the frictional properties of the natural fault gouge and compared their frictional properties to samples collected from the creeping section of the San Andreas fault. We found that both fault gouges have simi-

lar compositions and frictional properties. In order for fault creep to occur on the Bartlett Springs fault, we estimate that there needs to be at least 50% talc in the gouge, concentrated into layers in which the majority of shear is taking place.

Through the various approaches to understanding fault creep used in this dissertation and the compilation of previous studies using various techniques (e.g. GPS-derived models, seismology, additional geodetic observations), we have a better understanding of fault creep mechanisms and distribution in the North Bay. We estimate a larger extent of the Maacama and Rodgers Creek faults to be creeping than previously observed, supplementing previous estimates from repeating earthquake families, GPS-based models, alignment arrays, and prior InSAR studies in the area. The measurement of offset sidewalks along the Hayward fault shows along-strike variations in the rates of movement but also allows us to quantify how much of the total creep occurs in a narrow zone near the mapped surface trace (3–10 meters wide) versus the wider zone measured by alignment arrays ($\sim$100 meters wide). The low frictional strength of talc within the Bartlett Springs fault gouge is the main driving factor of fault creep on the fault, and can promote creep at depths up to 9 km. The mineral assemblage is also similar in its elemental composition to the fault gouge collected within the creeping section of the San Andreas fault, suggesting that the creep in both places is controlled by a similar lithology sampled by each fault. This suggests that the Bartlett Springs fault may also be creeping at deeper depths, up to 9 km, consistent with the depths of repeating earthquakes located on the fault.

Contents

List of Figures

List of Tables

Chapter 1

Introduction

Fault creep is continuous or episodic slow slip on a fault in the absence of large earthquakes. It was first observed in Hollister, CA in the 1960s along the Calaveras fault (Steinbrugge and Zacher, 1960). Since then, creep has been identified on many faults in California, for example the central San Andreas fault (Moore and Rymer, 2007a), the Hayward fault (Bürgmann et al., 2000; Simpson et al., 2001; Schmidt et al., 2005; Stoffer, 2008; Chaussard et al., 2015), the Calaveras fault (Stoffer, 2008; McFarland et al., 2018; Chaussard et al., 2015), the Rodgers Creek fault (Funning et al., 2007; Jin and Funning, 2017), the Maacama fault (McFarland et al., 2018; Lienkaemper et al., 2014), the Bartlett Springs and Green Valley faults (McFarland et al., 2018; Lienkaemper et al., 2014), and also on a few faults worldwide, e.g. the North Anatolian fault in Turkey (Ambraseys, 1970; Cetin et al., 2014), the Haiyuan Fault in Tibet (Jolivet et al., 2012), and the Longitudinal Valley fault in Taiwan (Lee et al., 2003; Thomas et al., 2014). The extent, and ubiquity of

fault creep and the chemical and mineralogical properties associated with it are topics of active investigation.

Here we focus on northern California faults (north of the San Francisco Bay Area) that are observed to be creeping at a few discrete locations and use different, complimentary approaches to studying creep on them through geodetic techniques and rock mechanics experiments.

1.1 Frictional Behaviors of Faults

In order to understand how a fault can slip stably or unstably, a brief summary of the frictional behavior of faults is provided here.

The seismogenic cycle on a stick-slip fault begins with the interseismic period in which the fault is locked and slowly accumulates elastic strain until its frictional strength is exceeded, and the fault slips unstably in an earthquake (coseismic period). If this fault were creeping during the interseismic period instead of being locked, the fault would be slowly sliding, not accumulating as much elastic strain as a locked fault. Depending on the creep rate, compared to the long-term slip rate of the fault, this would result in an earthquake not occurring as often or at all.

Both stable and unstable slip are seen in many experimental studies that are explained by the rate- and state-dependent constitutive law of friction

$$\tau = \bar{\sigma}\mu = \bar{\sigma}[\mu_0 + a\ln(V/V_0) + b\ln(\theta V_0/D_C)]$$

(Dieterich, 1978; Ruina, 1983), where a and b are parameters that describe material, τ is the shear stress, $\bar{\sigma}$ is the effective normal stress, μ_0 is the steady state friction at a reference

velocity V_0, V is the slip speed during sliding, and D_C is the characteristic slip distance over which the state variable Θ evolves. At constant normal stress, after a step change in slip speed, the state will evolve to a constant steady state value, $\Theta_{ss} = D_C/V$ and the equation can be rewritten as:

$$\tau = \bar{\sigma}[\mu_0 + (a - b)\ln(V/V_0)]$$

This shows that μ depends on the material properties (a and b) and on the magnitude of the slip speed change.

There is a characteristic response of the coefficient of friction (μ) of a material to an instantaneous velocity step increase, shown in Figure 1.1. There is an instantaneous change in strength that accompanies the velocity change (with amplitude a) which is followed by a gradual decrease in strength over a slip distance, D_c, to the new steady-state value for μ (with amplitude b). Thus $(a - b)$ is the net change in μ resulting from the velocity change (Figure 1.1). This net change is indicative of whether the material will slip stably (i.e., creep) or unstably (i.e., in stick-slip).

For stable slip, after a velocity step increase, the fault becomes stronger as μ increases, i.e., $(a - b) > 0$, this is called **velocity strengthening friction** (Figure 1.1A).

For unstable slip, the fault becomes weaker, as μ decreases after a velocity step increase, i.e., $(a - b) < 0$, this is called **velocity weakening friction** (Figure 1.1B).

1.2 Seismic Hazard Assessment for Creeping Faults

The presence of creep along a fault can reduce the amount of strain that accumulates in the crust and impede earthquake rupture. Identifying creeping sections of a

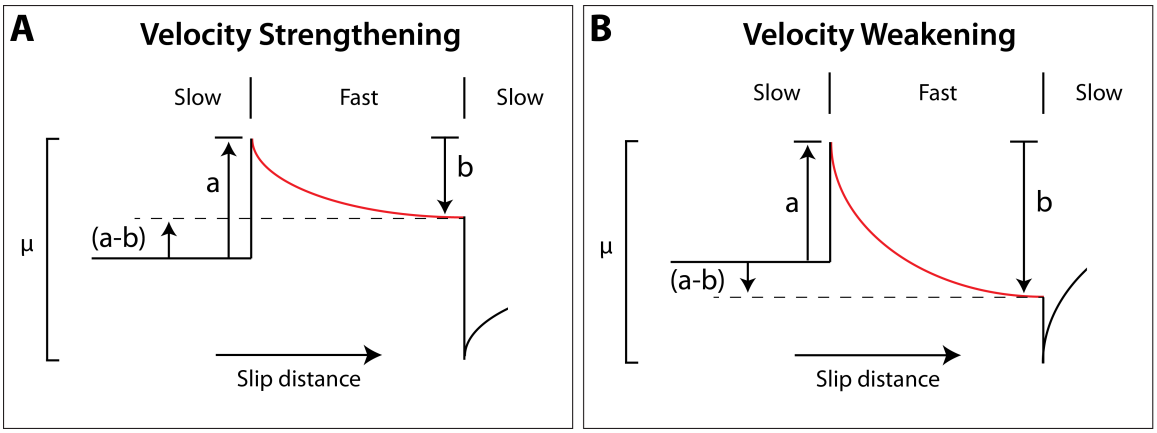

Figure 1.1: Predicted frictional response of a material to an instantaneous velocity step increase. Slow and fast denotes the slip speeds. a is the instantaneous change in strength due to the change in velocity, b is the evolution of a strength over a slip distance, D_c, to the new steady-state value of μ.

fault, we can better constrain the sections that are accumulating strain (i.e., locked) – thus allowing a more accurate seismic hazard assessment. Fault creep can reduce seismic hazard in two ways:

First, the presence of fault creep can reduce the rate of elastic strain accumulation compared to full locking. Therefore, the potential seismic moment of a future earthquake on a creeping fault is lower compared to the case of a fully locked fault. Fault creep is in contrast to stick-slip behavior in which a fault slowly builds up strain over time (i.e., 10s to 100s of years) only to be released in a sudden movement – an earthquake. A fault that is partially or fully creeping is not accumulating as much elastic strain as a locked fault would. This slow movement reduces the total accumulated strain that can be released in a future earthquake. It can also lead to a longer delay time in between earthquakes so the likelihood of a large earthquake occurring is reduced. This is accounted for in the newest publication of the Uniform California Earthquake Rupture Forecast, version 3 (UCERF3; Weldon et al.,

2013) which estimates the potential seismic moment reduction for each section of a fault due to reduced strain accumulation.

The identification of sections of faults that are creeping can lower the probability of a large damaging ($M > 6.7$) earthquake on these faults. The UCERF3 and UCERF2 reports both compiled all known surface creep rates in Northern California at the time of publication (Weldon et al., 2013; Wisely et al., 2008) with the exception of InSAR observations being added to UCERF3. These observations have helped identify additional creeping areas and improved the assessment of the regional seismic hazard. Therefore, mapping what portions of faults are creeping becomes important to highlight sections of faults that are locked which is where a future earthquake could rupture (this is discussed in Chapter 2)

Second, the frictional regime that supports fault creep does not also support earthquake rupture. This is also accounted for in the UCERF3 model. From rate-state friction, there are two distinct frictional regimes; velocity weakening and velocity strengthening behavior (Dieterich, 1978). Velocity weakening friction promotes stick-slip behavior, whereas velocity strengthening friction suppresses fast movement and favors sliding that is slow and stable. Due to this difference in frictional regimes, an earthquake will propagate differently through regions exhibiting velocity strengthening versus velocity weakening behavior. If the creeping area is large enough, the rupture can possibly be impeded, be forced to move around, or ultimately be stopped by the creeping area (Lozos, 2013). A more detailed picture of the distribution of creep and locked areas can allow for better understanding of how an earthquake rupture will propagate along a fault (e.g., Lozos et al., 2015). This will be very important if there are multiple creeping sections along one fault which can affect the

propagation of rupture. This difference in frictional behavior between a locked and creeping fault is related to the lithology which points to specific minerals that have low friction and promote velocity strengthening behaviors (discussed in Chapter 4 and 5).

1.3 Summary of Projects

Each project contained within this dissertation explores complementary approaches to understanding different aspects of fault creep at different scales. The first project is on a regional scale, mapping the extent of fault creep along the Maacama and Rodgers Creek faults. The second project is on a city scale, observing how fault creep manifests in an urban environment. Finally, the third project is at a micro-scale, investigating the possible mineralogical and frictional controls on why fault creep is limited to specific fault segments. Through investigating these topics of fault creep at different levels, we hope to build a more thorough seismic hazard assessment of fault creep in northern California (north of the San Francisco Bay Area) by locating where faults are creeping, identifying potentially creeping segments through geology, and by assessing how damage will occur in the future on creeping faults.

The first project (Chapter 2) focuses on a regional scale using Interferometric Synthetic Aperture Radar (InSAR), a geodetic technique using differenced satellite radar imagery, to map the extent of fault creep along two faults in northern California – the Rodgers Creek and Maacama Faults. There is no written records (since the 1800s) of major earthquakes on the Rodgers Creek fault (Hecker et al., 2005) but there is evidence of large and infrequent earthquakes on the Maacama fault (Prentice et al., 2014).

On these faults, creep has already been identified on a 'city scale', at specific offset sidewalks and through alignment arrays, but its extent outside of cities or if there is variability of creep along the fault is not known. InSAR allows for the mapping of fault creep at a regional scale which extends outside of the cities. The European Space Agency's Sentinel-1A and Sentinel-1B are the two newest SAR satellites, launched in 2014 and 2016, respectively. The repeat times of each satellite is shorter than for previous missions at 12 days, and the combined constellation allows a 6 day repeat time. This has allowed for higher quality InSAR data set along the Maacama and Rodgers Creek faults with higher coherence across the entire area. Our results show that both faults are creeping at the surface with 55% of the 170 km Maacama fault and 40% of the 70 km Rodgers Creek fault slipping aseismically.

The second project (Chapter 3), focuses on city scale observations of fault creep on offset sidewalks along the Hayward Fault to understand how fault creep is being expressed in an urban setting. The Hayward fault is a major fault in the San Francisco Bay Area that is known to be creeping along most of its extent, with the highest amount of creep observed at its southern end, in the city of Fremont, CA. In Fremont, photos of offset sidewalks from 2015 to 2018 were used to construct 3D models from the 2D photographs to measure 3D displacement of the offset sidewalks over time. This method is used to observe and measure movement of the curbs due to the creeping fault and if there are any consistent observations between sites.

The third project (Chapters 4 and 5), investigates the micro-scale frictional and mineralogical properties needed for a fault to creep. We obtained samples of fault gouge from

a site along the Bartlett Springs fault in Northern California that is known to be creeping. We conduct two sets of experiments; the first on synthetic mixtures of the main minerals found within the gouge to understand which minerals are promoting or not promoting fault creep within the fault (discussed in Ch. 4) The second set of experiments investigate the frictional properties of the collected natural fault gouge and compare the mineralogy and frictional properties to samples collected from the creeping section of the San Andreas fault (discussed in Ch. 5).

These three projects approach the understanding of fault creep at three different scales and in three very different, yet complimentary ways. We hope to gain a better knowledge of fault creep on a regional scale of where fault creep is occurring on the Maacama and Rodgers Creek faults, on the city scale by understanding how a creeping fault is deforming an urban city, and on a microscale by learning what type of fault geology is needed to support fault creep. Each of the three projects will help to refine seismic hazard assessments for the region. Mapping the extent of fault creep can help refine the seismic hazard estimates especially in an area where no creep observations were previously made. Measuring offset sidewalks can help estimate the main zone of fault deformation within a city and help define the area which will have the most damage over time. Investigating what minerals promote fault creep will help to identify potential sections of faults that could creep, based on mapped lithology.

Each method has its own place in influencing seismic hazards assessments, from the identification of the amount of fault creep, to identifying the main zone of creep deformation

within a city, and to the identification of specific geological materials that could point towards creep.

Chapter 2

Mapping the spatial extent of fault creep in northern California using InSAR

2.1 Introduction

Fault creep, aseismic slip of a fault, was first observed in the 1960s along the Calaveras Fault in the San Francisco Bay Area from mapping offset sidewalks (Steinbrugge et al., 1970). Since then, it has been identified on at least 9 faults in California and 3 more faults elsewhere in the world (Harris, 2017). There have been many studies that have proposed explanations for the mechanism of fault creep and why specific faults creep (Moore and Rymer, 2007a; Wei et al., 2013; Lindsey and Fialko, 2013). For the San Andreas Fault system, the proposed mechanism for fault creep in northern California is weak friction due to the presence of serpentinite (Moore et al., 2018). The association of serpentinite and fault creep are discussed in greater detail in Chapters 4 and 5.

Experiments suggest that fault creep falls under the frictionally stable regime (i.e., velocity strengthening) where the strength of the fault increases with an increase in velocity of the fault (Dieterich, 1978). In contrast, faults that are able to nucleate earthquakes (stick-slip events) are frictionally unstable (i.e., velocity weakening) where the strength of the fault decreases with an increase in slip on the fault. Faults that exhibit some portion of fault creep along their extent, accumulate less elastic strain energy than if it were fully locked. Thus, if an earthquake were to occur on such a fault, it would have a lower seismic moment release compared to the same fault being fully locked. Additionally, if a creeping section of a fault is large enough, it can act as a barrier to through-going rupture or potentially stop the earthquake from propagating further (Lozos, 2013).

In the North Bay (north of the San Francisco Bay Area), fault creep has been observed through different methods. Small-scale observations can be made from offset man-

made features such as buildings, fences, and sidewalks (discussed in Chapter 3). Another method for observing creep on a local scale (on a length scale of $\sim$ 100 m across the fault) is through alignment arrays (Lienkaemper et al., 2014) which measure the change in angle between three monuments (two monuments on one side of the fault and one on the other) and relate this to fault-parallel slip. These can capture how creep varies along a fault (McFarland et al., 2018). There are also creepmeters which measure the change in length of an invar (nickel-iron alloy metal) rod installed at an oblique angle to the fault trace at shallow depths (spans $\sim$ 10 m across the fault) and attached to a pair of monuments on either side of the fault (Bilham et al., 2004). There are no creepmeters installed north of the San Francisco Bay Area (Bilham et al., 2004). Larger scale observations include GPS in which measurements can be made on either side of a fault (Murray et al., 2014) and InSAR which uses satellite imagery to observe fault movement on the largest scales up to 250 km widths (e.g., Funning et al., 2007; Tong et al., 2013; Jin and Funning, 2017).

Delimiting the extent of fault creep along northern California faults will help provide a more accurate seismic hazard assessment for the region. In this study, we aim to fill in a gap of knowledge along two northern California faults which are known to creep at specific locations. We use small baseline InSAR data from different viewing geometries to measure surface deformation along the Rodgers Creek and Maacama faults.

2.1.1 The Rodgers Creek-Maacama Fault Zone

In the North Bay, the overall plate motion between the Pacific and North American plates is taken up by three sub-parallel fault zones, the San Andreas fault, Maacama-Rodgers Creek faults and the Bartlett Springs-Green Valley faults, with slip rates of 20-

25 mm/yr, 6-10 mm/yr, and 5 mm/yr, respectively (Freymueller et al., 1999; Chéry, 2008; McLaughlin et al., 2012; Prentice et al., 2014). The San Andreas fault is locked here but the Maacama-Rodgers Creek and Bartlett Springs-Green Valley faults are found to be creeping at specific locations (Lienkaemper et al., 2014).

Rodgers Creek Fault

The Rodgers Creek fault is the northern continuation of the Hayward fault that trends northwest-ward for ∼70 km through the eastern San Francisco Bay Area (also known as the East Bay) (Figure 2.1; Watt et al., 2016; Funning et al., 2007; Parsons et al., 2003). The estimated geologic slip rate for the southern section of the fault is 6.4-10.4 mm/yr, (Schwartz et al., 1992) which is in a agreement with geodetic observations (d'Alessio et al., 2005; Funning et al., 2007). Paleoseismic studies have shown there have been at least three **M**∼7 earthquakes in the past with the most recent **M**7 earthquake occurring in the 18th Century (Budding et al., 1991; Wong, 1991; Schwartz et al., 1992; Hecker et al., 2005). Current seismic hazard assessments suggest a 32% probability of a large earthquake (**M**6.7 or greater) occurring within the next 30 years (Field et al., 2015). Now, with evidence of the Rodgers Creek fault being connected to the Hayward fault, there is a possibility of a joint rupture of both faults resulting in a larger earthquake of up to **M**7.4 (Watt et al., 2016). Such an earthquake would be devastating to the densely populated San Francisco Bay Area region and the North Bay region, including Santa Rosa, CA.

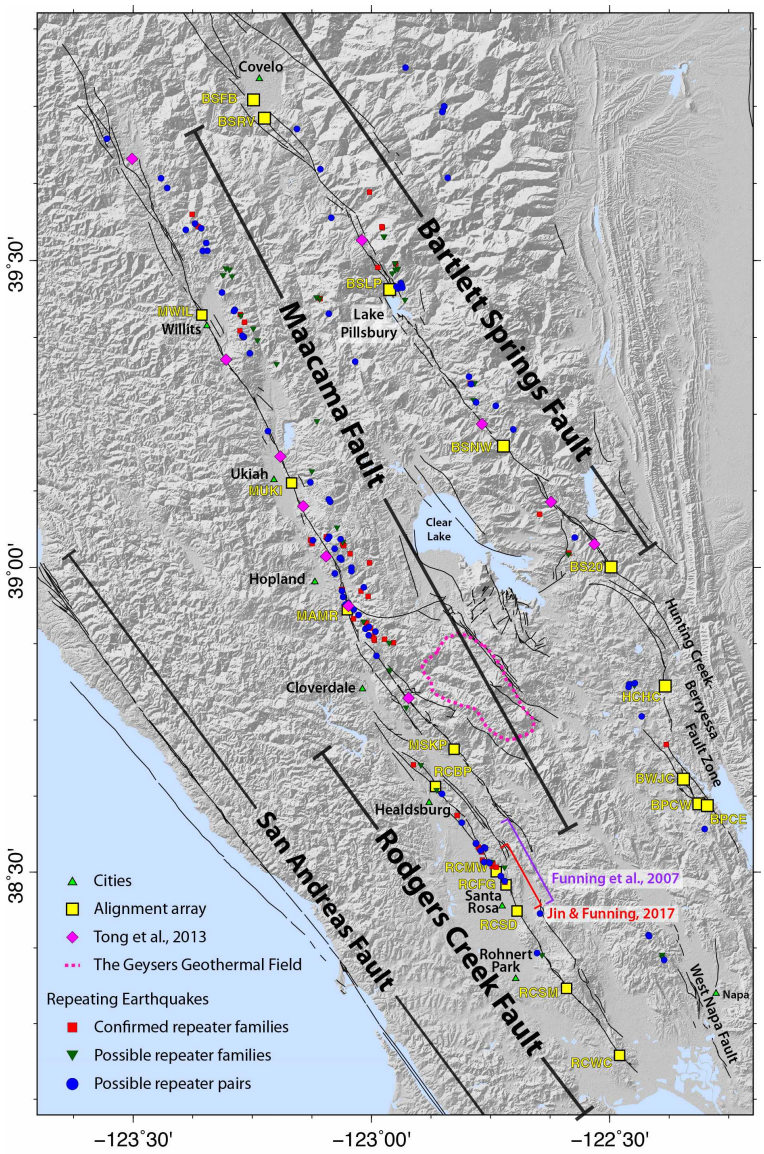

Figure 2.1: Summary of prior fault creep evidence along the Maacama, Rodgers Creek and Bartlett Springs faults (black lines) in northern California. Locations where fault creep is observed include alignment arrays (yellow squares), and InSAR from Tong et al. (2013) (pink diamonds). Funning et al. (2007) (purple bracket) and Jin and Funning (2017) (red bracket), defining a zone of fault creep along a section of the Rodgers Creek fault NW of Santa Rosa. Shakibay Senobari and Funning (2019) identified groups of repeating earthquakes, which are indicators of creep, categorized as either confirmed repeating earthquake families with precise locations validated (red squares), possible repeating earthquake families with highly correlated waveforms (dark green inverted triangles), and possible repeating earthquake pairs with overlapping locations (blue circles). Cities are marked with bright green triangles and The Geysers Geothermal Field is outlined in pink, south of Clear Lake.

Maacama Fault

The Maacama fault is the northernmost continuation of the Hayward-Rodgers Creek fault system that extends 170 km northwestward (Figure 2.1). The estimated geologic slip rate is 5.5–7.9 mm/yr (McLaughlin et al., 2012; Prentice et al., 2014) and paleoseismic evidence shows the fault having large and infrequent earthquakes (at least two) in the past between 770 C.E and 1150 C.E. (Prentice et al., 2014). From GPS modeling, Murray et al. (2014) suggests the Maacama fault is mostly locked below 5 km, in agreement with Prentice et al. (2014).

2.1.2 Prior evidence of fault creep

There is observational evidence of fault creep along both the Rodgers Creek and Maacama faults from offset man-made structures such as curbs, fences, buildings, en echelon cracks in pavement, and theodolite surveys of alignment arrays (Galehouse and Lienkaemper, 2003; Lienkaemper et al., 2014; McFarland et al., 2018). Heavily forested terrain along these faults make alignment array measurements difficult as one needs to have a visual of each monument. There are little observations of offset man-made structures because there are fewer cities / urban development as you travel north. Due to these sparse observations of fault creep, capturing the spatial variability of creep is difficult. InSAR measurements have provided a way to observe and measure surface deformation along each fault over large areas (Tong et al., 2013; Funning et al., 2007; Jin and Funning, 2017).

Rodgers Creek Fault

Initially from 1980 to 1986, there was no evidence of fault creep on the Rodgers Creek fault – no offset cultural features and no movement from two initial alignment arrays installed (Galehouse and Lienkaemper, 2003). It was not until a third alignment array (RCSD) was installed in 2002, in the city of Santa Rosa, that creep was observed at rates of 1.4 mm/yr (McFarland et al., 2018). Five additional alignment arrays were then installed on the northern and southern ends of the fault (Lienkaemper et al., 2014; McFarland et al., 2018). The creep rates estimated from these measurements range from 0.2 to 4.3 mm/yr where the highest creep rate of 4.3 mm/yr is observed in the middle section of the fault, within the city of Santa Rosa, where the creep rates taper off to zero at the northern and southern ends (McFarland et al., 2018).

The first evidence of shallow creep was observed by Funning et al. (2007) with a permanent scatterer InSAR study, which used the European Space Agency (ESA) satellites ERS-1 and ERS-2 between 1992-2001, where they infer shallow creep to the northwest of Santa Rosa at rates up to 6 mm/yr. This was further corroborated by the installment of an alignment array (RCMW) nearby in 2008 that has measured a creep rate of 4.3 mm/yr (McFarland et al., 2018). An additional study, by Jin and Funning (2017), used both the ascending and descending viewing geometries from ESA's Envisat satellite from 2003 to 2010 to distinguish between vertical and horizontal components of surface deformation. This additional viewing geometry helped constrain the variability of fault creep as it showed that some of the inferred creep in the study of Funning et al. (2007) was likely vertical motion. Neither of these previous studies resolves any line-of-sight velocity offset south of Santa

Rosa. Thus, the Rodgers Creek fault zone north of Santa Rosa is creeping and the fault zone south of Santa Rosa is locked (Jin and Funning, 2017). There is an additional InSAR study which used the Advanced Observation Land Satellite (ALOS) to observe line-of-sight velocity changes across the Rodgers Creek fault from 2006 to 2010 (Tong et al., 2013). Tong et al. (2013) estimated creep rates that varied along the fault ranging from -3 to 4 mm/yr with large uncertainties.

There is also evidence of fault creep from repeating earthquakes along the Rodgers Creek fault, starting near the city of Santa Rosa and the northern most mapped extent of the fault (Figure 2.1, Shakibay Senobari and Funning, 2019). These 'repeaters' extend down to ∼7 km depth; the estimated creep rates from confirmed repeaters (i.e., repeating earthquakes with precise relocations) is 2–3 mm/yr.

Maacama Fault

Fault creep was first identified in 1978 in the city of Willits from the observation of offset curbs (Harsh et al., 1978). The first two alignment arrays on the fault, out of four total, were installed on the northern section of the Maacama fault in the cities of Ukiah and Willits, in the early 1990s (Figure 2.1, yellow squares). It was not until 2008 that two additional arrays were installed to measure the southern section of the fault (Galehouse and Lienkaemper, 2003). Since then, these alignment arrays have measured creep rates ranging from 1.4 to 5.3 mm/yr (McFarland et al., 2018). The highest creep rate of 5.4 mm/yr is observed in the city of Willits (alignment array MWIL) where there is also paleoseismic evidence of creep in trench sites nearby (Prentice et al., 2014; McFarland et al., 2018). The

lowest creep rate of 1.4 mm/yr is observed on the southern end of the fault near the city of Geyserville (MSKP) (Figure 2.1).

The InSAR study by Tong et al. (2013) using ALOS also observed velocity changes across the Maacama fault. Tong et al. (2013) estimated creep rates that varied along the fault ranging from 0 to 8 mm/yr although with large uncertainties. These estimates included negative creep rates, mostly at the northern end of the Maacama faukt, which they infer to be either left-lateral faulting or vertical motion. Murray et al. (2014)'s results from Bayesian inversion modeling of GPS data suggests the Maacama fault has surface creep from 1.8 to 9.9 mm/yr along its entire extent with locally high estimates near Ukiah and Willits at 8.1 and 9.9 mm/yr, respectively. They also estimate a deep slip rate of ∼13 mm/yr along its entire extent which exceeds the long term slip rate estimated geologically (McLaughlin et al., 2012; Prentice et al., 2014) but is most likely due to the amalgamation of modeled slip from multiple fault strands.

Additionally, there are repeating earthquakes along most of the fault starting near Cloverdale and northward to Laytonville (Figure 2.1, Shakibay Senobari and Funning, 2019). Shakibay Senobari and Funning (2019) estimates creep rates of 2-3 mm/yr in the Cloverdale-Hopland area and as high as 5 mm/yr, just north of the city of Willits.

In this study, we focus on using ascending and descending InSAR data sets from the current Sentinel-1 mission to map surface deformation along the Rodgers Creek and Maacama faults — where the overall distribution of fault creep is poorly constrained due to the low density of observations. In this way, we can learn about the variability of fault creep along the extent of each fault.

2.2 Interferometric Synthetic Aperture Radar (InSAR)

2.2.1 Synthetic Aperture Radar (SAR) Satellite

InSAR is a geodetic technique that differences the phase of Synthetic Aperture Radar (SAR) satellite imagery to measure surface deformation in the direction of the satellite Line-Of-Sight. The first civilian SAR satellite, SeaSat, was launched into space in 1978 with many following after including ERS-1 (1991), ERS-2 (1995), Envisat (2002), ALOS-1 (2006), ALOS-2 (2014), and the newest additions Sentinel-1A (2014) and Sentinel-1B (2016). Radar is used in remote sensing as it is capable of penetrating through heavy cloud cover and works in darkness, thus providing a 24/7, all weather operational coverage capability. Most SAR satellites have a right-looking configuration (Figure 2.2) where the satellite moves in the azimuth direction (i.e., the flight path direction) and the radar antenna is mounted on the right side of the satellite and points in the range direction (i.e., orthogonal to the azimuth direction). The angle at which the radar ray path meets the ground is called the incidence angle and is defined as the angle from the local vertical. The distance from the satellite to the ground/point target, in the range direction, is called the 'range' measurement. The satellite emits a radar pulse which illuminates a portion of the ground, called a footprint, which moves at the satellite's speed. There are a few different acquisition modes for how this footprint is acquired; the simplest mode is stripmap mode where there is one footprint that traces a swath on the ground from a right, side-looking vantage point (i.e. slant range) in the range direction (Figure 2.3,A). In ScanSAR mode, as the satellite moves, the beam is steered in the range direction, trading azimuthal resolution for wider swath coverage (Figure 2.3).

Within this footprint, the radar scatters off ground objects, and a portion of this back-scattered radar returns to the satellite and is recorded. The back-scattered radar contains amplitude and phase information related to characteristics of the ground surface. The amplitude is the intensity of the returned signal which is influenced by the back-scattered radar pulse (e.g., a smooth surface like a road, lake, or a rough surface like rocks). The phase has information on the total path length of the pulse – the round trip distance from the satellite to the ground and back. This information is contained in a Single Look Complex (SLC) image which is a complex radar image taken in the viewing orientation of the satellite – the slant range-direction by azimuth-direction plane. Each pixel within the image represents a complex value containing the sum of the backscatter amplitudes and phase information on the radar path length and contributions of scatterers for a given area on the ground. Each row and column of the SLC corresponds to a different azimuth and range location, respectively.

The resolution in the range direction is determined by the radar pulse width, thus the narrower the pulse correlates with a finer resolution in range. The azimuth resolution is determined by the physical length of the radar antenna aperture. The longer the antenna, the better it can focus the energy of the transmitted and received radar pulse into a sharp beam, thus the higher the resolution. Since it is not practical to launch a long antenna instead, we make use of the idea that the satellite illuminates the same point multiple times as it passes over, and the radar echoes during this illumination can be combined into a longer, virtual antenna and the distance the satellite moved is the *synthetic aperture* of

the radar. The typical length of a SAR antenna is on the order of meters but using this technique, the synthetic aperture can be on the order of kilometers long.

2.2.2 SAR Interferometry

Once there are at least 2 SLCs over an area of interest, if the ground surface has moved in between the two acquisitions, for example in an earthquake, there will be a difference in the radar path length (Figure 2.4). When the phases of the two SLCs are differenced, this change in path length results in a phase difference due to constructive and destructive interference of the two radar waves. This phase difference is mapped spatially to show surface deformation and is called an interferogram. Any movement – between the two SLC dates – of the ground surface towards or away from the satellite in the direction of the satellite (i.e., line-of-sight) can be measured from this phase difference.

The total phase for each SLC image is

$$\phi = \phi_{path} + \phi_{atmosphere} + \phi_{pixel}$$

where ϕ_{path} is the path length, $\phi_{atmosphere}$ is the atmospheric phase delay, and ϕ_{pixel} is contribution of individual scatterer within a pixel. The path length is itself a sum of three contributions – the viewing position of the satellite during each acquisition ($\phi_{position}$), the different distances to the ground pixel due to topographic parallax effects ($\phi_{topography}$), and surface deformation ($\phi_{deformation}$), if any.

Thus the formation of an interferogram is the sum of the differential phase contributions (Hooper et al., 2007)

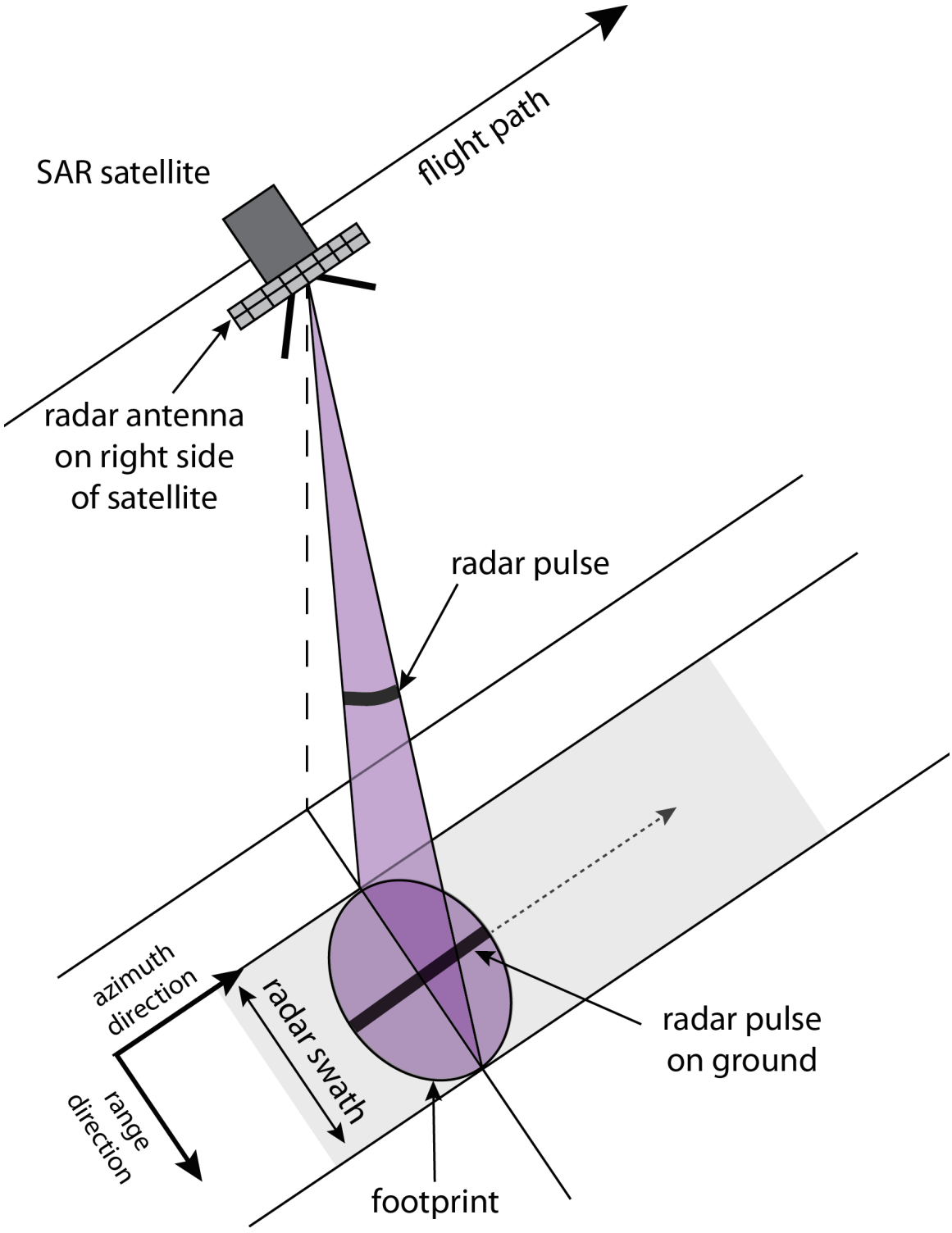

Figure 2.2: Right-looking SAR satellite configuration

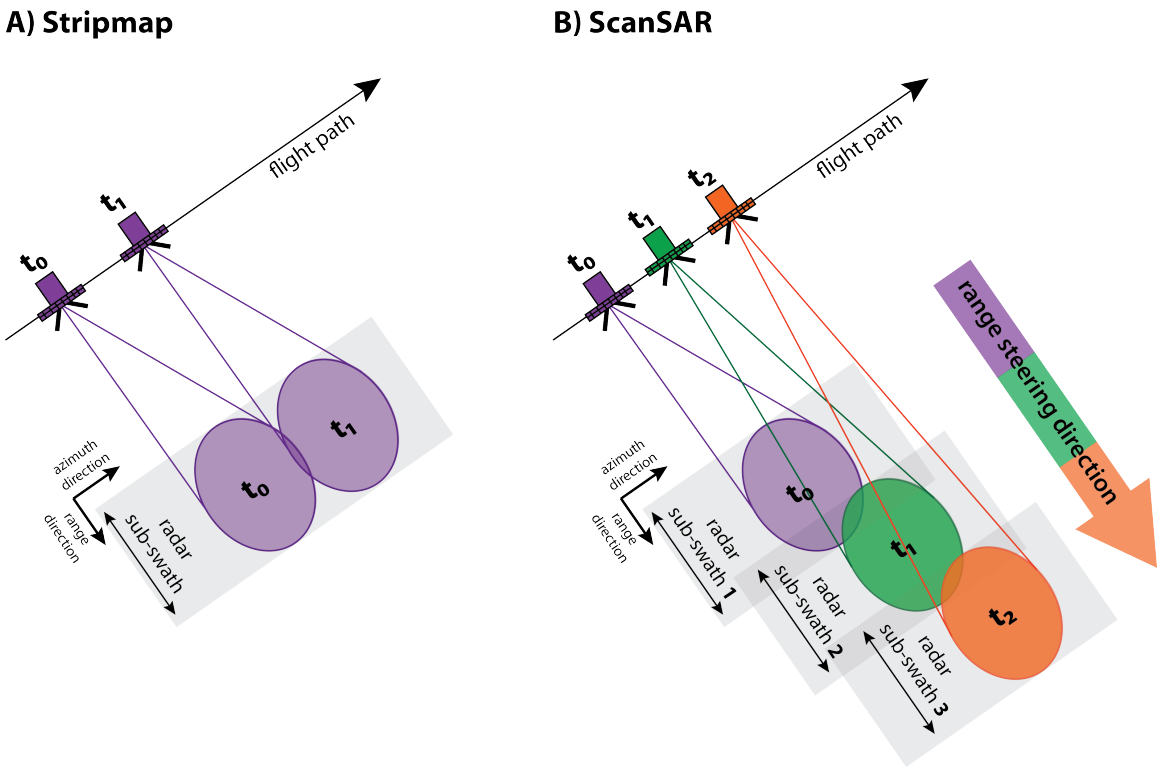

Figure 2.3: SAR satellite acquisition modes showing stripmap mode (A) which acquires images along the flight path and ScanSAR mode (B) which steers the beam in the range direction along the flight path.

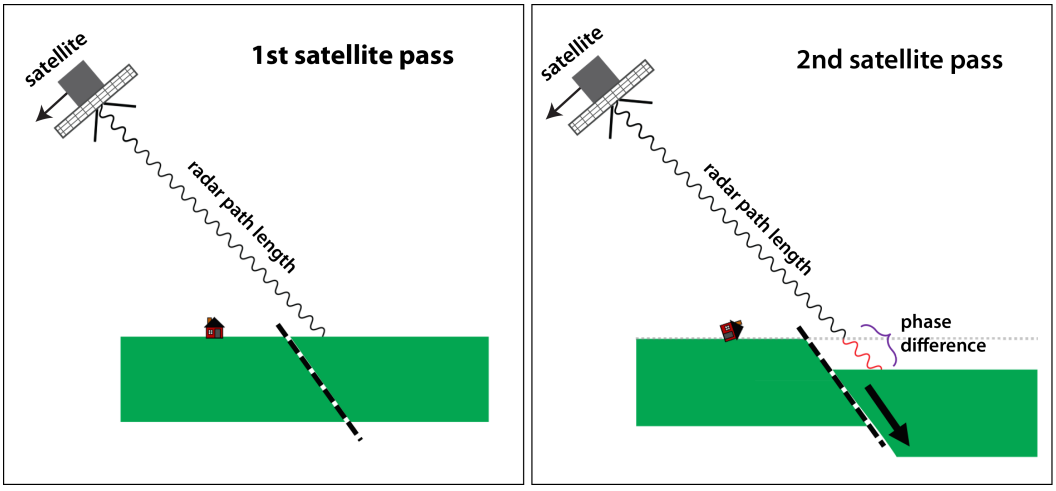

Figure 2.4: InSAR satellite passes showing if the ground moves between the first and second satellite passes, the result is a change in path length which is a difference in phase between the two passes.

$$\Delta\phi = \Delta\phi_{position} + \Delta\phi_{topography} + \Delta\phi_{deformation} + \Delta\phi_{atmosphere} + \Delta\phi_{pixel}$$

Each of these phase contributions can be corrected or accounted for, leaving only the deformation phase, $\Delta\phi_{deformation}$ at the end. For $\Delta\phi_{pixel}$, if there is no change to the scatterers' phases within a pixel, this contribution will be zero (Massonnet and Feigl, 1998).

Satellite position: The ability to have the exact same viewing geometry of the satellite for each acquisition is not likely due to external forces such as solar and thermal radiation pressure that can alter the orbital trajectory. Any difference in satellite position, called baseline, must be accounted for as it modifies the path length between the satellite and ground. The baseline consists of two components, a parallel baseline (i.e., how far ahead or behind in the azimuth direction one acquisition is to another) and perpendicular baseline (i.e., the difference in satellite position perpendicular to the azimuth direction) (Bürgmann et al., 2000). Information of the satellites' precise orbital paths during each acquisition allows us to calculate the satellites precise position during each acquisition and correct for it during processing. This accounts for the $\Delta\phi_{position}$ contribution to the interferogram.

Topography: The distance from the satellite to the ground is not uniform due to the topography. Each pixel will have a different elevation, thus a different path length contribution. With the satellite's position varying from acquisition to acquisition, the satellite views the ground at a slightly different vantage point leading to a phase signal related to the topographic height difference in the interferogram (Massonnet and Feigl, 1998). This topographic change, $\Delta\phi_{topography}$, can be accounted for during processing with high resolution topographic information, such as a digital elevation model.

Atmosphere: Contributions of the atmosphere, $\Delta\phi_{atmosphere}$, in an interferogram greatly vary in space and time. Variations in the temperature, pressure, and relative humidity in the troposphere can cause a change in the phase (e.g., Massonnet and Feigl, 1998; Bekaert et al., 2015) by refracting the radar on its path to the ground. In some cases, these 'phase delays' can become large enough to mask any tectonic signal (e.g., Bekaert et al., 2015). Depending on the location of interest, any difference in the atmospheric state between two SLCs, which is highly likely, will result in a phase difference in the interferogram. There are tropospheric corrections that can help mitigate the phase delays such as weather models (e.g., Liu et al., 2009; Jolivet et al., 2011), GPS observations (e.g., Li et al., 2006; Yu et al., 2017), multi-spectral observations (e.g., Li et al., 2009), or a combination of GPS and spectrometer data (e.g., Li et al., 2005; Bekaert et al., 2015). If there is a large atmosphere contribution, it should be taken into account when estimating deformation.

Deformation: Once all of the other phase contributions are removed or accounted for, the remaining phase is deformation of the ground. The phase of the interferogram is the difference in the radar path length of the two SLCs phases in the line-of-sight (LOS) direction The interferogram resolves 3D deformation of the ground, $\mathbf{u}$, into the line-of-sight (LOS) direction, $\hat{\boldsymbol{p}}$, where the change in phase from deformation is given by

$$\Delta\phi = \frac{4\pi\Delta r}{\lambda} = (\frac{4\pi}{\lambda})\mathbf{u}\cdot\hat{\boldsymbol{p}}$$

Here, Δr is the change in range between the initial satellite position and the target (i.e., LOS) and λ is the wavelength of the satellite (e.g., Simons and Rosen, 2007). In the case of the Sentinel-1 satellites, $\lambda \approx 5.6$ cm, and a change of the ground by $\frac{1}{2}\lambda$, 2.8 cm, in the line-of-sight direction of the satellite corresponds to one interference fringe in the

interferogram. This provides the ability to measure crustal deformation on the sub-cm scale in the LOS direction (Massonnet and Feigl, 1998).

One satellite orbit track does not provide enough information to discern the full 3D displacement field. To do this, we need at least three independent observations of ground displacement from different viewing geometries (Funning et al., 2005), such as the combination of the ascending (northward moving) and descending (southward moving) satellite orbits tracks, sensitive to the east-west and vertical motion, and SAR amplitude azimuth offsets, sensitive to the north-south motion.

2.2.3 InSAR Satellites and Data Used

We use data from the European Space Agency's Sentinel-1A and -1B SAR satellites, between March 2015 and March 2018. The data products used were acquired in the Interferometric Wide (IW) Swath mode which captures three subswaths of SAR imagery using Terrain Observation with Progressive Scans SAR (TOPSAR). It is an evolution of the ScanSAR method (Figure 2.3) which helps solve the problems of scalloping and varying azimuth resolution (De Zan and Guarnieri, 2006). TOPSAR mode involves steering the radar beam in the range and azimuth directions in short bursts (i.e., series of echoes). Figure 2.5 shows the difference in this configuration with strip map mode from Figure 2.2. The total swath width is 250 km with a 5 m (range) by 20 m (azimuth) resolution (De Zan and Guarnieri, 2006). Each satellite has a sun-synchronous, near polar orbit with a 12-day revisit time. Given that the satellites are positioned 6 days apart in orbit, the two satellites combined offer a 6-day revisit in priority areas.

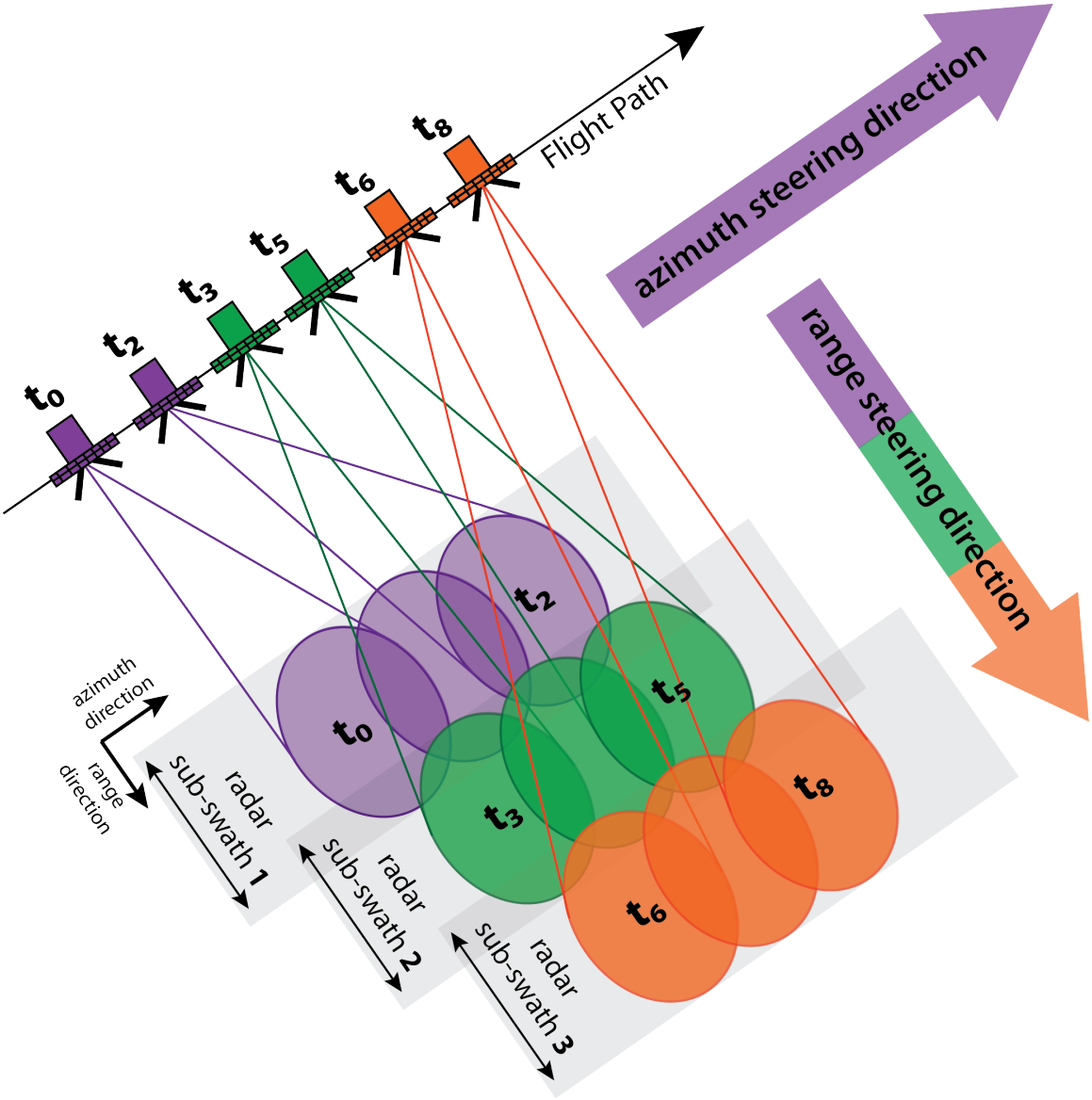

Figure 2.5: Sentinel-1 TOPSAR acquisition geometry showing the satellite steering the beam in range and azimuth directions instead of only one swath for stripmap mode (i.e., purple, sub-swath 1; Figure 2.2), there are now 3 subswaths.

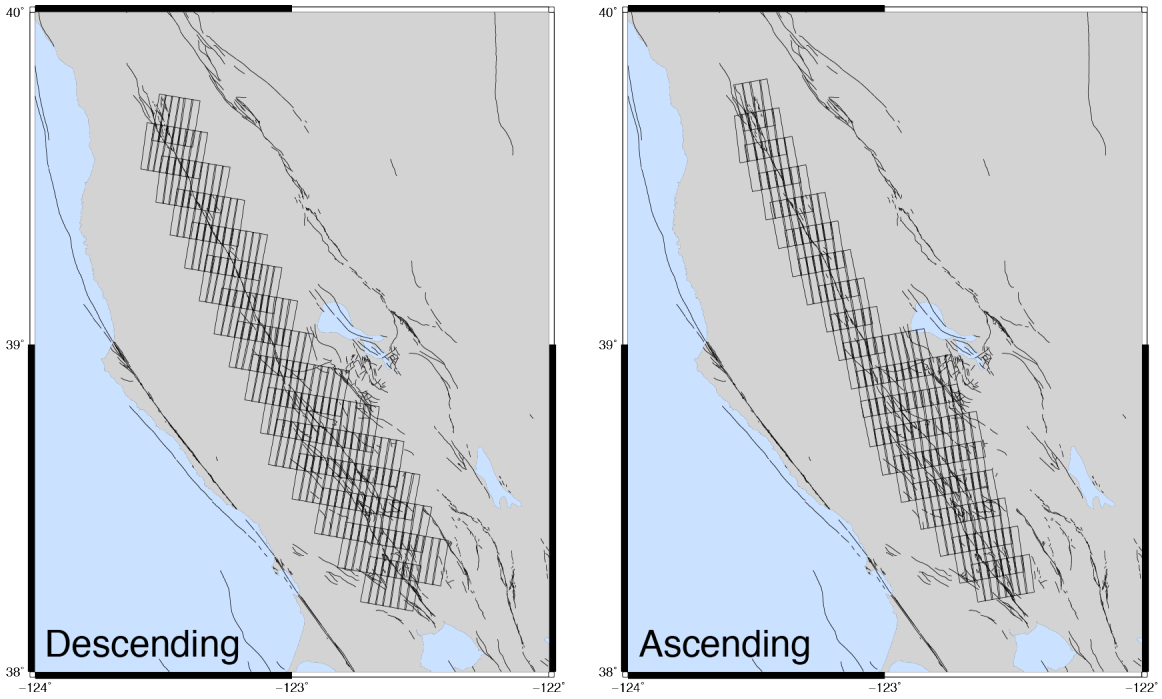

Figure 2.6: Map showing the area covered by the selected patches in the ascending (172 patches) and descending (213 patches) frames.

We processed one ascending track and one descending track data set between March 2015 and March 2018 over the Rodgers Creek and Maacama faults. The descending track (track 115, frame 462) has 68 SAR images during the study period and the ascending track (track 35, frame 122) has 59 SAR images (Figure 2.7; Table 2.1 and 2.2). Since we are interested in fault creep across the faults, we use a subset of the full frame spanning 15 km on either side of the fault to process the data faster (Figure 2.6).

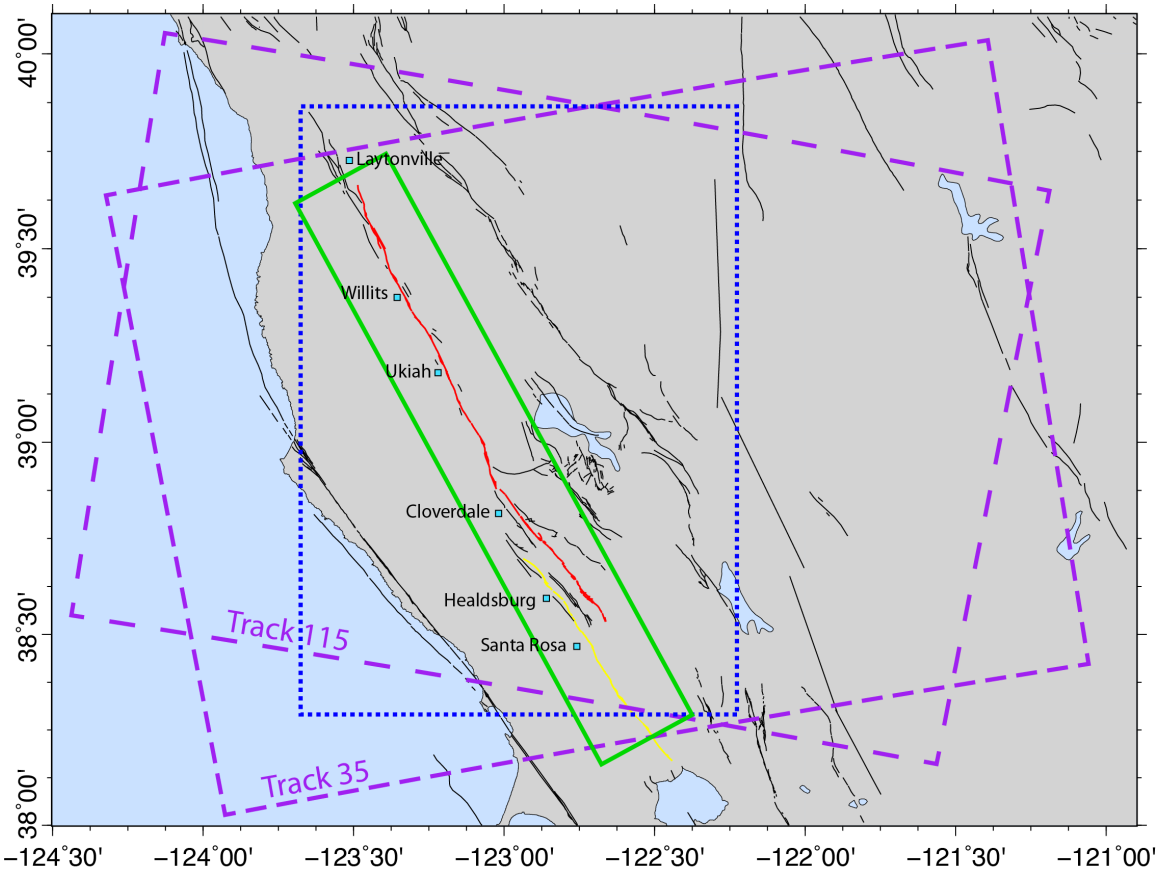

Figure 2.7: Location map showing study area in northern California, along the Maacama (red line) and Rodgers Creek (yellow line) faults. Locations of prominent cities are shown as blue squares. Dashed rectangles show the coverage of the ascending (track 35) and descending (track 115) Sentinel-1 tracks. Blue dashed rectangle shows the area of interest for this study. Green rectangle show the near-fault InSAR coverage.

Table 2.1: Dates and perpendicular baselines for the descending data set. The perpendicular baselines are calculated assuming a reference date of 20170124.

Descending

Date	B_{perp} (m)	Date	B_{perp} (m)
20150306	-64	20170217	27
20150318	-39	20170223	-9
20150330	28	20170307	90
20150411	100	20170319	85
20150423	181	20170331	32
20150610	28	20170412	-16
20150704	-26	20170424	-27
20150728	-8	20170506	-29
20150821	-4	20170518	27
20150914	29	20170530	110
20151008	49	20170611	-23
20151101	-20	20170623	-57
20151125	-40	20170705	68
20151219	39	20170717	91
20160112	-35	20170729	17
20160205	-55	20170810	3
20160229	34	20170822	35
20160417	12	20170903	6
20160511	45	20170915	5
20160604	-46	20170927	45
20160628	23	20171009	6
20160722	14	20171021	-32
20160815	7	20171102	-46
20160908	74	20171114	3
20161002	-65	20171126	26
20161026	-14	20171208	58
20161119	-4	20171220	-56
20161213	-67	20180101	-32
20161219	-39	20180113	-26
20161225	-34	20180125	61
20170106	57	20180206	10
20170118	75	20180218	-41
20170124	0	20180302	-46
20170130	-33	20180314	11

Table 2.2: Dates and perpendicular baselines for the ascending data set. The perpendicular baselines are calculated assuming a reference date of 20170119.

Ascending

Date	B_{perp} (m)	Date	B_{perp} (m)
20150301	-12	20170224	-40
20150313	22	20170308	-45
20150325	-38	20170320	26
20150406	-97	20170401	19
20150418	-39	20170413	-6
20150524	51	20170425	-21
20150711	-28	20170507	72
20150828	-34	20170519	71
20150921	67	20170531	-19
20160119	-9	20170612	5
20160212	-56	20170624	-90
20160319	19	20170706	-96
20160424	-29	20170718	73
20160518	-40	20170730	11
20160611	35	20170811	-26
20160705	-32	20170823	-69
20160729	-12	20170904	-63
20160822	26	20170916	80
20161003	-70	20170928	105
20161027	-27	20171010	41
20161120	3	20171022	-30
20161214	-92	20171103	-59
20161220	30	20171115	-78
20161226	-52	20171127	45
20170107	-11	20171209	2
20170113	-72	20180102	-105
20170119	0	20180207	11
20170131	-16	20180303	-21
20170206	-24	20180315	-48
20170218	-3		

2.3 Data Processing

There are different methods/software available for processing InSAR data (e.g., GMT5SAR, ISCE, StaMPS/MTI, ROI_PAC, SNAP) and they all have their advantages. For the purpose of this study, we use the Stanford Method for Persistent Scatterers (StaMPS) Small Baselines (SBAS) method which requires small perpendicular and temporal baselines to obtain good coherence over a heavily vegetated area, such as the North Bay. Before using StaMPS, we use the JPL InSAR Scientific Computing Environment (ISCE) software to produce a coregistered stack of SLC images (Rosen et al., 2012). Each image pixel is represented by a complex value containing the amplitude and phase information where the different rows and columns correspond to a different azimuth and range location, respectively. The SLCs are coregistered to one common master image using the amplitudes of each SLC as well as a geometric/Digital Elevation Model to further align the stack of SLCs. This coregistered stack is then cropped to the same size as the master image and inputted into the Stanford Method for Persistent Scatterers /Multi-Temporal InSAR (StaMPS/MTI) software package to produce a time series of surface deformation from interferograms using the Small Baselines method (e.g., Hooper, 2008; Hooper et al., 2010, 2012).

2.3.1 StaMPS Processing

StaMPS/MTI is a software package is used to produce a time series InSAR by two different methods – a persistent scatterer (PS) InSAR method and a small baselines (SBAS) method – and optionally combining the PS and SBAS results into a full multi-temporal solution (Hooper, 2008; Hooper et al., 2012). StaMPS/MTI was developed to work in non-

urban settings and in areas experiencing non-steady deformation which makes it a good candidate for measuring surface deformation in a highly vegetated area. The PS and SBAS methods each produce a spatially dense time series of surface displacement while reducing atmospheric noise through the combination and filtering of data. The difference between the two methods is either using the best points that are persistent in each interferogram or trying to identify more points using filtered interferograms. In this study, we focus on the SBAS approach, which is likely to be more effective in a less developed region like the North Bay.

The SBAS method maximizes the available data coverage by only using interferograms with small perpendicular and temporal baselines. In this study, we use a maximum perpendicular baseline of 100 meters and a maximum temporal baseline of 1 year (Figure 2.8, bottom; Berardino et al., 2002; Schmidt and Bürgmann, 2003). Small perpendicular baselines are used because the interferograms are less likely to have topographic errors and are more likely to be coherent over a larger area. Similarly, short temporal baselines are preferred as a means of limiting temporal decorrelation due to changes in scattering of the ground. SBAS is successful in areas that have no dominant scatterers such as in the vegetated areas of the North Bay (Hooper et al., 2012). Modern satellites add to the success of this method as they have shorter repeat times which helps keep the spatial correlation high in these vegetated areas. Slowly decorrelating filtered phase (SDFP) pixels are identified and used for this method which are pixels that have similar phases over short time intervals but that might not be correlated over larger time intervals (Hooper, 2008). The SBAS method uses a network of redundant interferograms with the perpendicular and temporal

baseline maxima mentioned above to limit the amount of decorrelation (Figure 2.8). Since SBAS has a redundant network of interferograms, this also allows us to check for unwrapping errors within individual interferograms, by summing the total unwrapped phase within closed loops in the network.

The StaMPS/MTI software prepares the data for the selection of persistent or distributed scatterers through specific processing steps: estimating the phase noise, selecting candidate pixels, weeding out the selected candidates, and phase correction of all phases. The final steps unwrap the individual interferograms, estimate any errors associated with noise in the data and produces a velocity map of the study area. More detail on each of each step can be found in the StaMPS/MTI manual (Hooper et al., 2010).

2.4 Observations

Here we present new results combining ascending and descending viewing geometries of Sentinel-1, from March 2015 to March 2018. We estimate a relative LOS velocity offset from multiple fault-perpendicular profiles through our data at regular short intervals – every 2.5 km along the fault strike.

2.4.1 Descending track

The JPL ISCE software produced 425 descending interferograms from 68 SLCs (Figure 2.8) and the SBAS code identified 622,563 SFDP velocity points in the Line-of-Sight (LOS) direction (Figure 2.9). The LOS velocities are plotted in Figure 2.9.

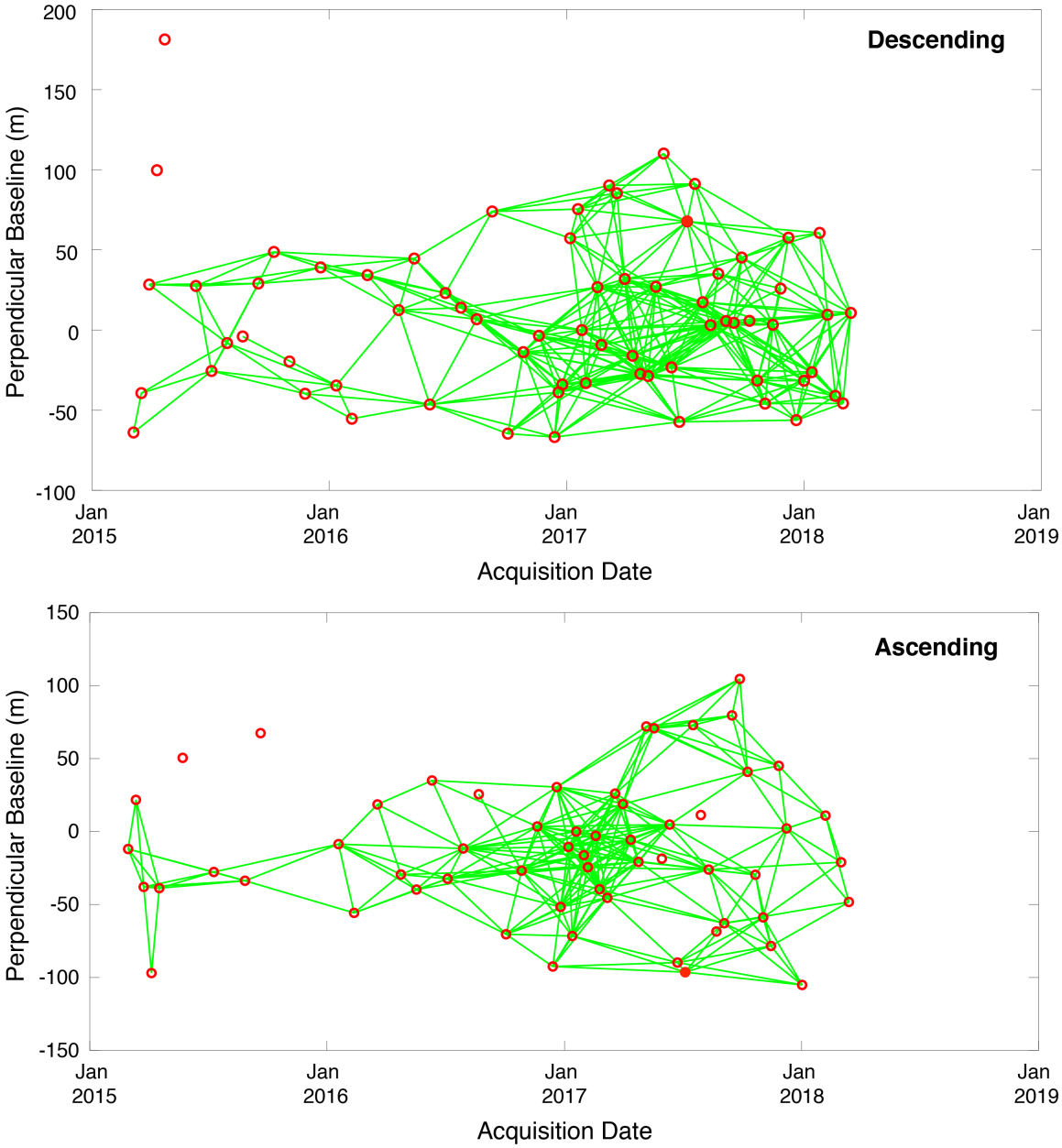

Figure 2.8: Time-perpendicular baseline plot for all acquisition dates (open red circles) for Sentinel-1 descending track 122, frame 35 and ascending track 115, frame 461. Each green line is an interferogram produced between the two corresponding dates with 425 descending and 338 ascending interferograms. The acquisition date used for the master geometry is denoted as the red filled circles.

Positive velocities (red) are movement towards the satellite which is uplift or south-westward movement. Negative velocities (blue) is movement away from the satellite which can be subsidence or northwestward movement. The largest negative velocities in the data set are located within the Geysers Geothermal Field, just south of Clear Lake, showing large subsidence (dashed outline in Figure 2.9). There are varying LOS offset rates along the extent of both faults which we interpret as possible locations of fault creep, if we assume the LOS velocity offsets to be predominantly due to fault-parallel motion. On the Maacama fault near Willits and Ukiah, there is an abrupt change in LOS velocity across the fault going from blue colored to green colored velocities near Willits and green colored to red colored velocities near Ukiah, with estimated LOS velocity offset rates of 3–6 mm/yr. In addition, there is an abrupt red to green colored change in LOS velocities across the fault south of Cloverdale, near the northern boundary of the Geysers Geothermal Field, with LOS velocity offset rates up to 5 mm/yr. The Rodgers Creek fault shows LOS velocity changes across the fault near Healdsburg and Santa Rosa with an offset rate of up to 1.8 mm/yr.

2.4.2 Ascending track

For the ascending track, with a total of 59 SLCs, the ISCE software produced 338 interferograms (Figure 2.8) and the SBAS code identified 379,759 SFDP pixels (Figure 2.10). The sense of motion is the same as the descending data set but with a different sign convention due to the direction the satellite is moving. Movement away from the satellite is subsidence and South-East movement (negative values; colored blue) and movement towards the satellite is uplift or North-West movement (positive values; colored red).

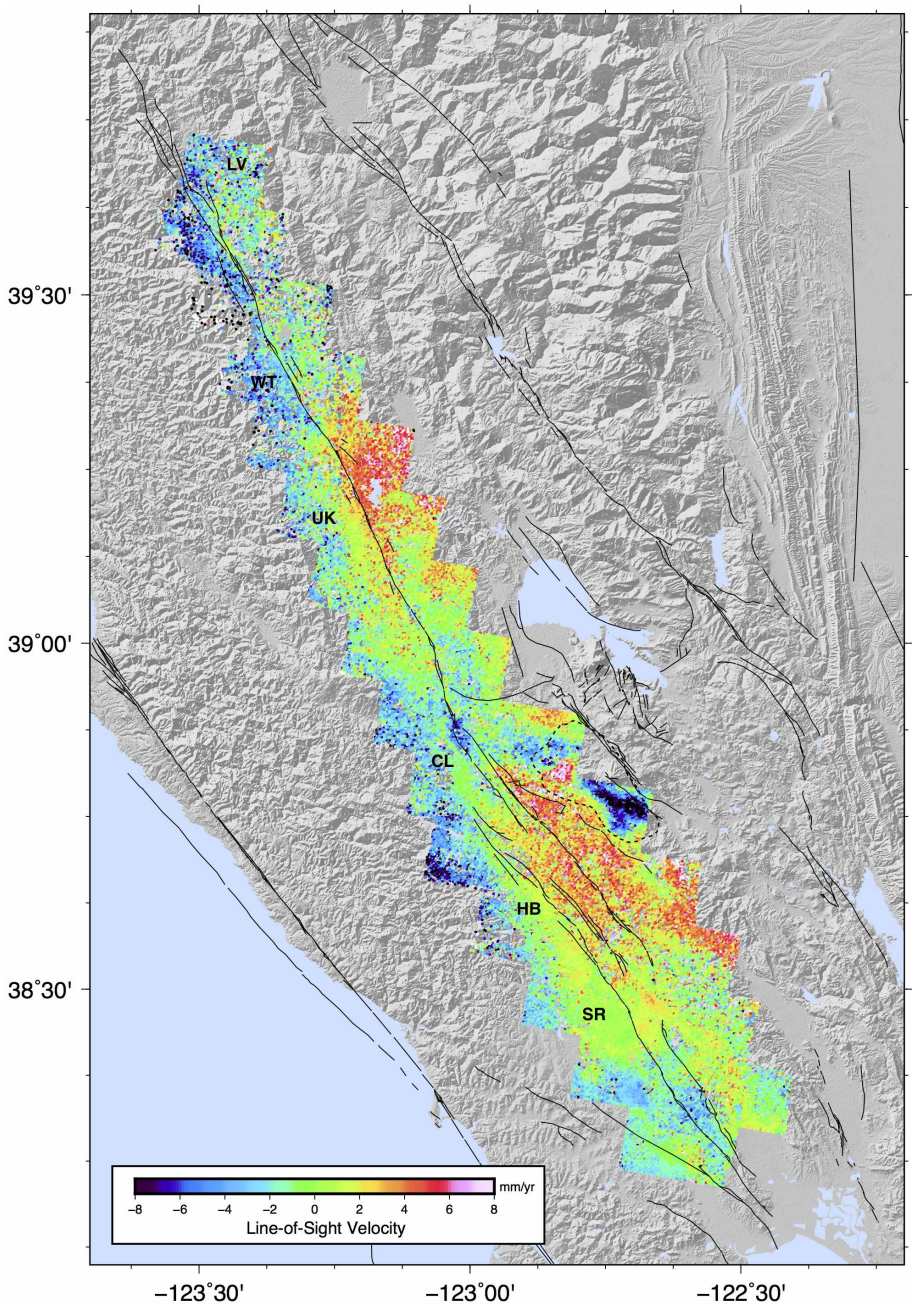

Figure 2.9: Small Baselines Descending (track 115) InSAR data covering the Maacama and Rodgers Creek faults spanning 2015 to 2018. Negative velocities (blue) indicate movement away from the satellite and positive velocities (red) indicate movement towards the satellite. Black lines indicate main faults in Northern California. Black dashed outline indicates the boundaries of the Geysers Geothermal Field. Cities on the map are Santa Rosa (SR), Healdsburg (HB), Cloverdale (CL), Ukiah (UK), Willits (WT), and Laytonville (LV).

There is an orange-red colored area between the latitudes of 39°25' to 38°40' that has a distinctive shape, similar to the shape of the Ukiah Valley which is present in multiple SLCs. We attribute this to a large wavelength atmosphere contribution where there is an area of higher LOS velocities (red colored area). Corrections using GACOS (Generic Atmosphere Correction Online Service), an Iterative Tropospheric Decomposition model that generates high spatial resolution zenith total delay maps, were incorporated into the StaMPS SBAS processing to correct for atmosphere errors (Yu et al., 2017, 2018,?). The GACOS corrections for the long wavelength atmosphere error help to mitigate the long wavelength error but introduced new, shorter wavelength errors in the process. Since our study is focused on measuring short wavelength velocity changes across the fault, we decided to keep the longer wavelength atmosphere error and take it into account when estimating creep rates in the area between Ukiah and Cloverdale. This atmosphere contribution was also noticed in the descending data but was largely mitigated by removing four acquisition dates with large atmosphere contributions. In the ascending data set, we did remove 9 SLC dates that had the largest atmosphere contributions which helped but this did not fully mitigate the atmosphere contributions in the data.

2.5 Analysis

We estimate the LOS velocity offsets in both data sets across the faults of interest by taking fault-perpendicular profiles at regular short intervals of 2.5 km along the fault strike, using data within 5 km on either side of the fault. We then decompose the velocity offsets into the fault-parallel and vertical motion by using both satellite viewing geometries.

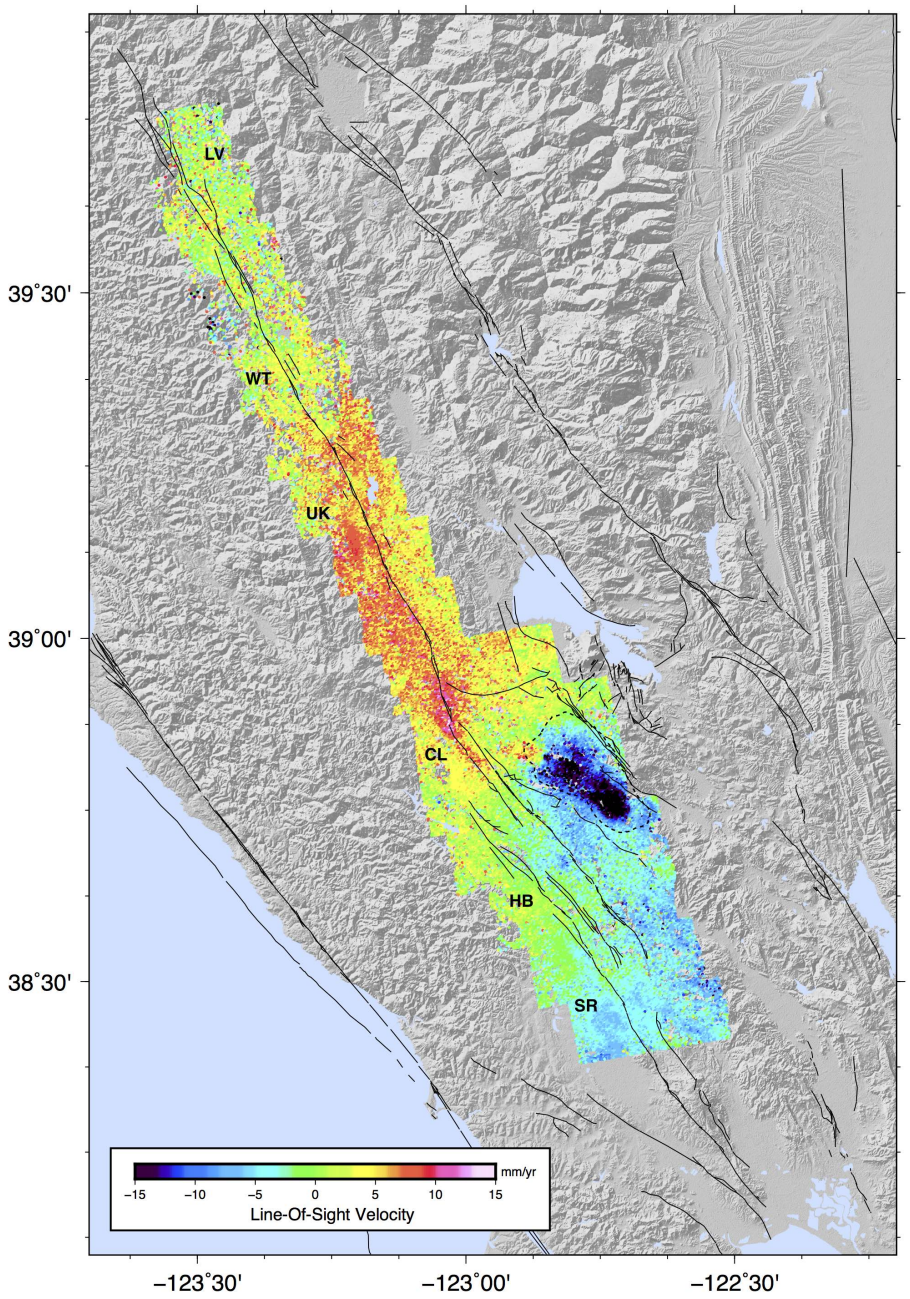

Figure 2.10: Small Baselines Ascending (track 35) InSAR data covering the Maacama and Rodgers Creek faults spanning 2015 to 2018. Negative velocities (blue) indicate movement away from the satellite and positive velocities (red) indicate movement towards the satellite. Black lines indicate main faults in Northern California. Black dashed outline indicates the boundaries of the Geysers Geothermal Field. Major cities on the map are Santa Rosa (SR), Healdsburg (HB), Cloverdale (CL), Ukiah (UK), Willits (WT), and Laytonville (LV).

The decomposition method that we apply has been implemented by Funning et al. (2007) and Jin and Funning (2017) and is described in Section 2.5.2.

2.5.1 Line-of-sight Velocity Estimates from Profiles

We divide the fault into profiles that sample the fault every 2.5 km with a total of 79 profiles that are sampled in both data sets (Figure 2.11). Each profile includes data within a rectangle 2.5 km wide and 10 km in length, assuming an average local fault strike within each rectangle, and centering the profile on the fault. All LOS velocity points located within the profile box are projected onto the profile line and are plotted as a velocity profile shown in Figure 2.12. The velocities within each profile are referenced to a location 1 km west of the fault trace along the profile line, shown as a black rectangle in Figure 2.12. We take the average of the values within the black rectangle, an area of 100 m by 250 m, and subtract them from all values within the profile box to mitigate atmosphere errors assuming that they are correlated over distances of 6 km or less. If there are no LOS velocities within this specified reference area we do not perform analysis on that profile, this occurred for 7 profiles (4, 7, 10, 11, 12, 17, and 57). Profiles 29–31 are also carefully constrained on the west side of the fault where there is an abrupt change that is most likely due to atmosphere contributions of the mountain versus valley area (discussed in 2.5.1).

We estimate the fault offset rates for each profile by first separating the LOS velocities on the east and west sides of the fault. Second, we use the least squares method to fit a best fit line with a common gradient to both sides of the fault. The best fit line for each side of the fault will have a common gradient but different y-intercepts; the difference between these intercepts is the LOS velocity offset between the east and west sides of the

fault. The common gradient we estimate and remove helps to mitigate any regional gradient present in the data that might be due to the strain accumulation across the fault system. To account for variations in fault strike or multiple mapped fault traces within the each profile, data within a $\pm$ 100 meter zone on either side of the fault are not used (Area between the two dashed lines, shown in Figure 2.12). The errors of our offset rate estimates are estimated from the standard deviations of the residuals to this best fitting trend line for each profile. Data that is outside of 3 standard deviations are considered outliers and are not used when fitting the best fit line to either side of the fault.

Due to the viewing geometries of each satellite track (Figure 2.18), vertical LOS motions will be in the same direction for the ascending and descending tracks and east-west motion will be in opposite directions. If the motion is wholly or partially due to fault-parallel creep, the LOS offset will be a positive step in the descending data and a negative step in the ascending data or there will be a larger positive LOS offset in the descending data than in the ascending data.

From the areas observed by both ascending and descending data, we analyze a total of 79 profiles: 60 profiles along the Maacama fault and 19 along the Rodgers Creek fault. Of these 79 profiles, we focus on fault sections where neighboring velocity profile offsets are consistent with fault-parallel creep along sections near the cities of Willits (Figure 2.13), Ukiah (Figure 2.14), Cloverdale (Figure 2.15), Healdsburg (Figure 2.16), and Santa Rosa (Figure 2.17) and the areas are noted in Figure 2.11 as the colored bars.

There are 13 profiles where fault-parallel motion is not resolved because the LOS velocity offsets indicate motion in the opposite sense of fault-parallel creep. In the displace-

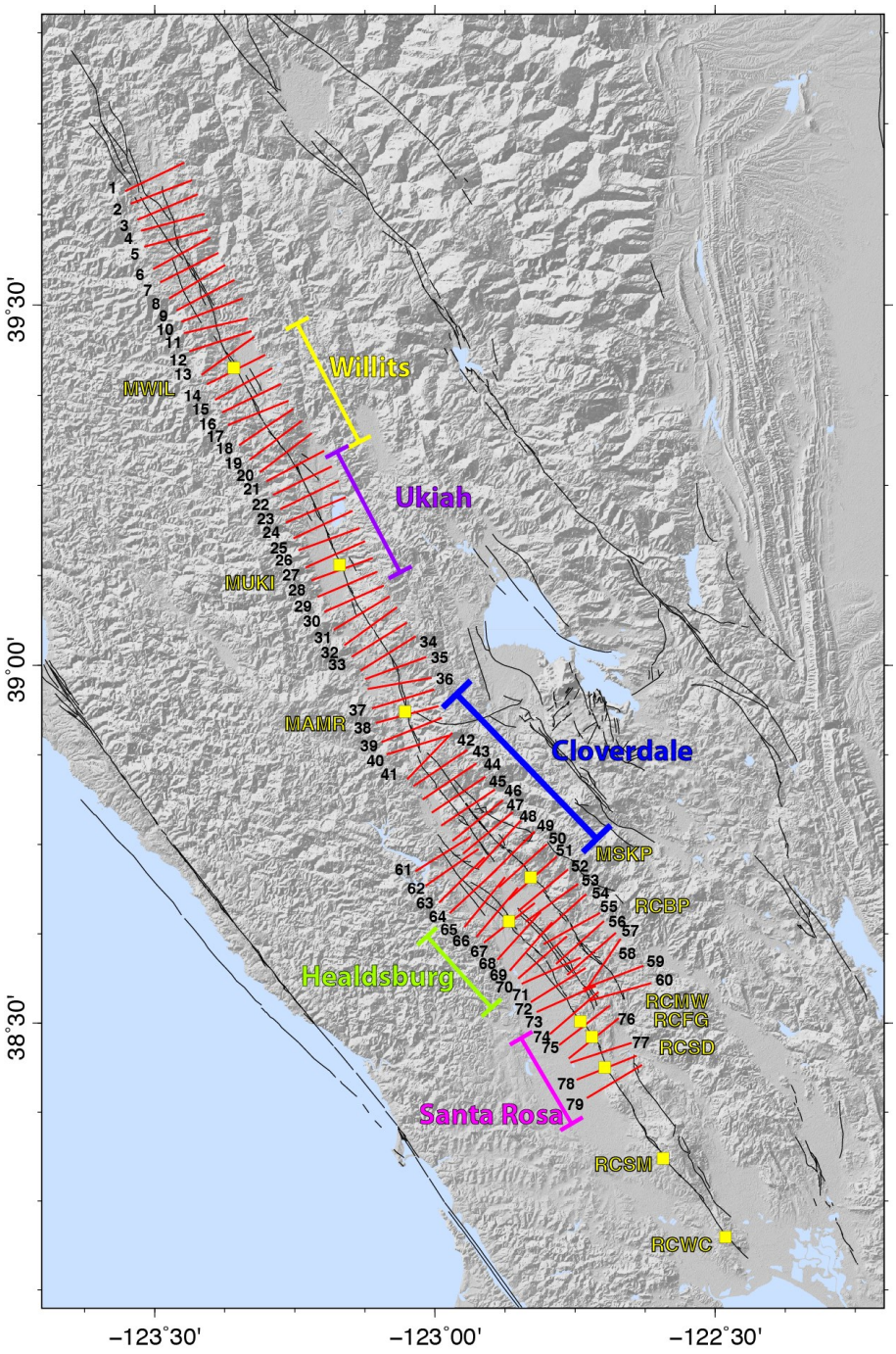

Figure 2.11: The Maacama and Rodgers Creek faults were divided into 2.5 km sections where each red line is a profile, which is the center of each 2.5 km section. Dashed boxes denote main profiles discussed below.

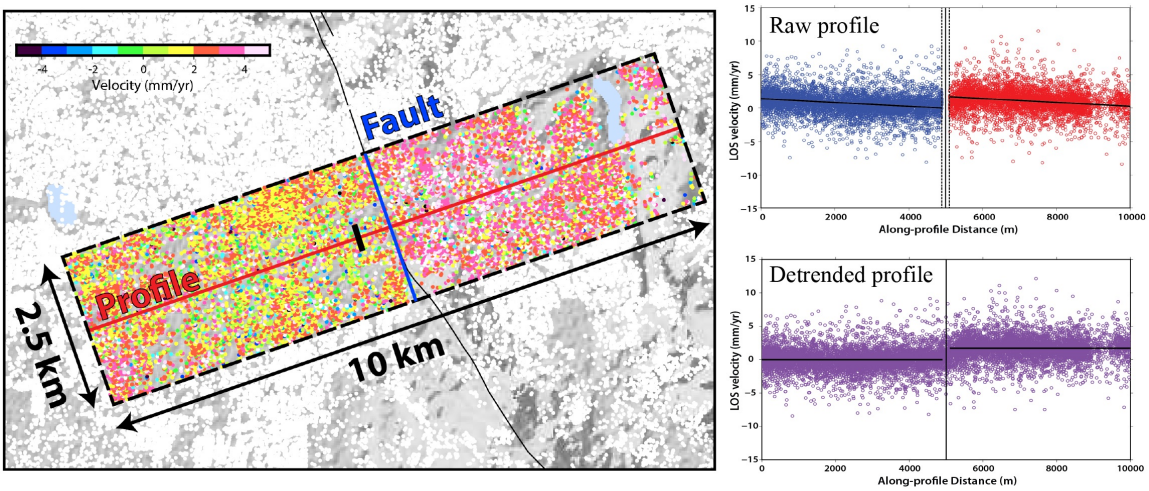

Figure 2.12: Profile definition and profile fitting. The map shows what LOS velocites were chosen for each profile where the red profile line is centered on the blue averaged fault strike (real fault line in black) spanning 10 km across the fault and 2.5 km along the fault. All values within this defined box are projected onto the profile (top, right) where a best fitting line with a common gradient is calculated and used to detrend the profile (bottom, right).

ment time series for these profiles, there is a seasonal variation seen in both the ascending and descending data sets along with an overall decrease in LOS displacement on the west side of the fault, with respect to the east side. These observations could be due to anthropogenic activities and/or variations in water storage in aquifers. Therefore, we do not use these 13 profiles in our analysis. We also note 9 other profiles that show little to no descending LOS velocity offsets and plot them as gray boxes when plotting the LOS velocities along strike (Figure 2.19). All profiles are provided in Appendix 2.10.

Data within the urban areas (i.e., cities) have less scatter than data outside of the cities because there are more stable structures within cities that the radar wave can reflect off of, and thus less phase noise in the data. For example, profile 68 (Figure 2.16) from the along-profile distances of 2500 m to 5000 m, the city of Healdsburg has less scatter due to the higher density of infrastructure with a scatter between ± 2.5 mm/yr and high scatter

outside the city limits varying between ±5 mm/yr. Another example is comparing the 2 standard deviation (2σ) range between profiles spanning smaller cities versus larger cities such as Willits and Ukiah versus Santa Rosa, respectively. Most profiles covering Willits and Ukiah are sampling vegetated areas (Figures 2.13 and 2.14) and have an average 2σ uncertainty of 1.5 mm/yr compared to Santa Rosa, a larger city spanning majority of the profile length, has a 2σ uncertainty of 0.9 mm/yr (Figure 2.17). This difference in 2σ shows that estimated offset rates within larger cities are better constrained, with a smaller uncertainty, than in less urban/more vegetated areas, which have higher scatter in the data, thus high uncertainty.

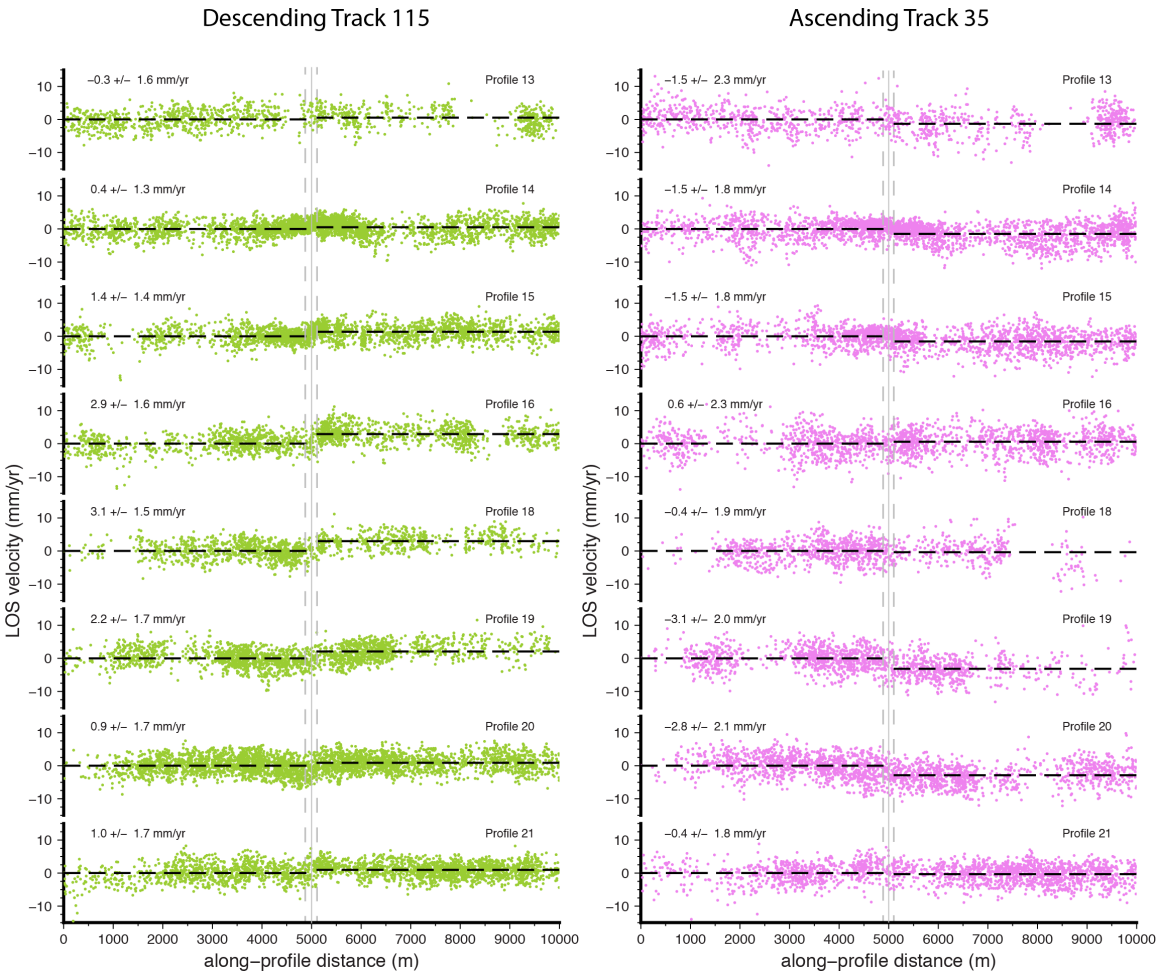

Figure 2.13: Detrended InSAR LOS velocity profiles from Sentinel-1 descending track 115 (left) and ascending track 35 (right) in the Willits, CA area. Procedure for detrending and estimating the offset are described in Figure 2.12 with errors presented as 2 standard deviation uncertainties. Solid gray line is the fault location and the dashed gray lines denotes the area not included in the offset estimation. Location of profiles are given in Figure 2.11.

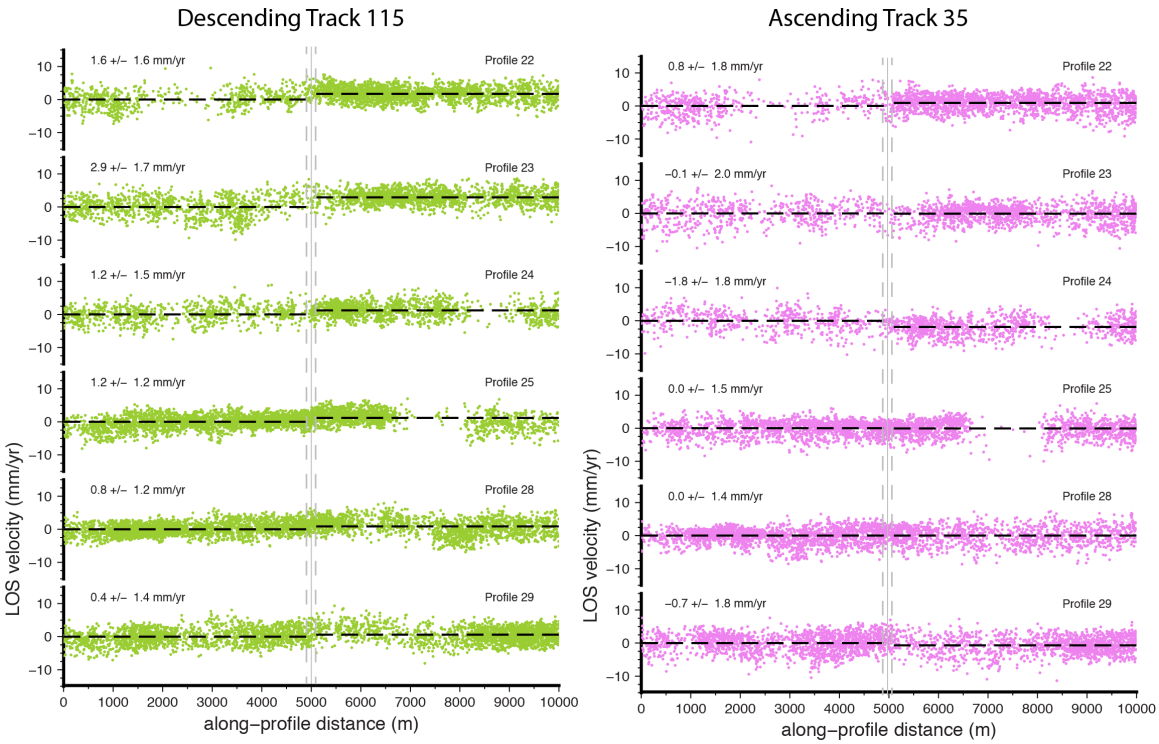

Figure 2.14: Detrended InSAR LOS velocity profiles from Sentinel-1 descending track 115 (left) and ascending track 35 (right) in the Ukiah, CA area. Procedure for detrending and estimating the offset are described in Figure 2.12 with errors presented as 2 standard deviation uncertainties. Solid gray line is the fault location and the dashed gray lines denotes the area not included in the offset estimation. Location of profiles are given in Figure 2.11.

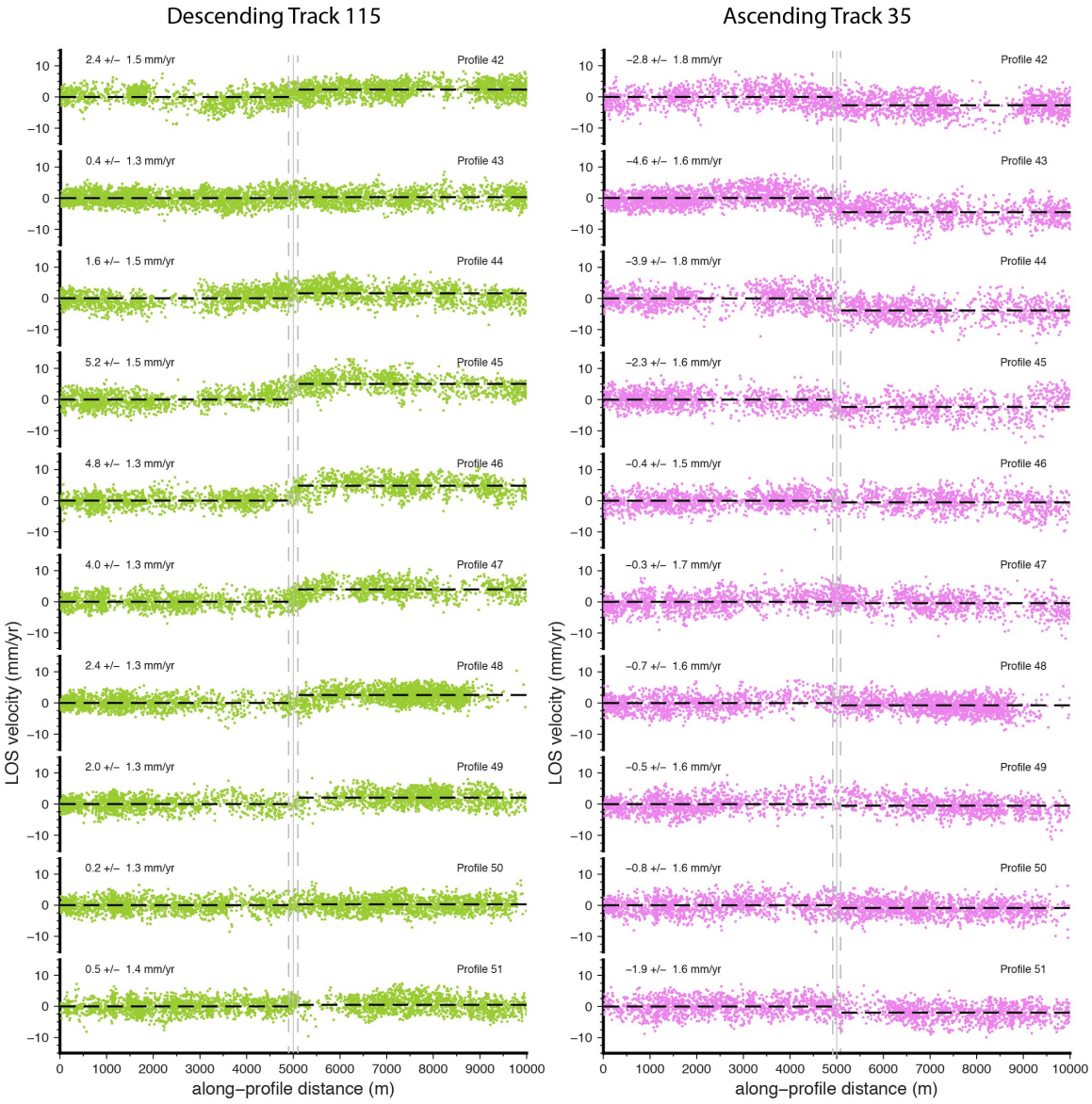

Figure 2.15: Detrended InSAR LOS velocity profiles from Sentinel-1 descending track 115 (left) and ascending track 35 (right) in the Cloverdale, CA area. Procedure for detrending and estimating the offset are described in Figure 2.12 with errors presented as 2 standard deviation uncertainties. Solid gray line is the fault location and the dashed gray lines denotes the area not included in the offset estimation. Location of profiles are given in Figure 2.11.

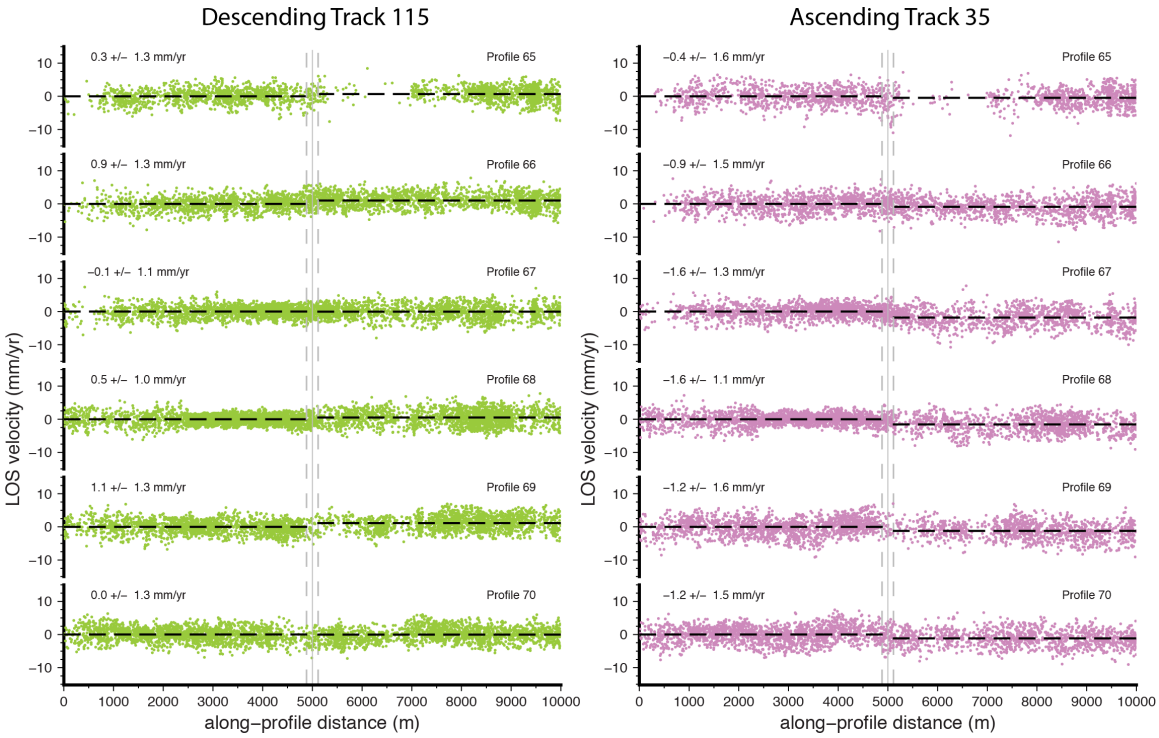

Figure 2.16: Detrended InSAR LOS velocity profiles from Sentinel-1 descending track 115 (left) and ascending track 35 (right) in the Healdsburg, CA area. Procedure for detrending and estimating the offset are described in Figure 2.12 with errors presented as 2 standard deviation uncertainties. Solid gray line is the fault location and the dashed gray lines denotes the area not included in the offset estimation. Location of profiles are given in Figure 2.11.

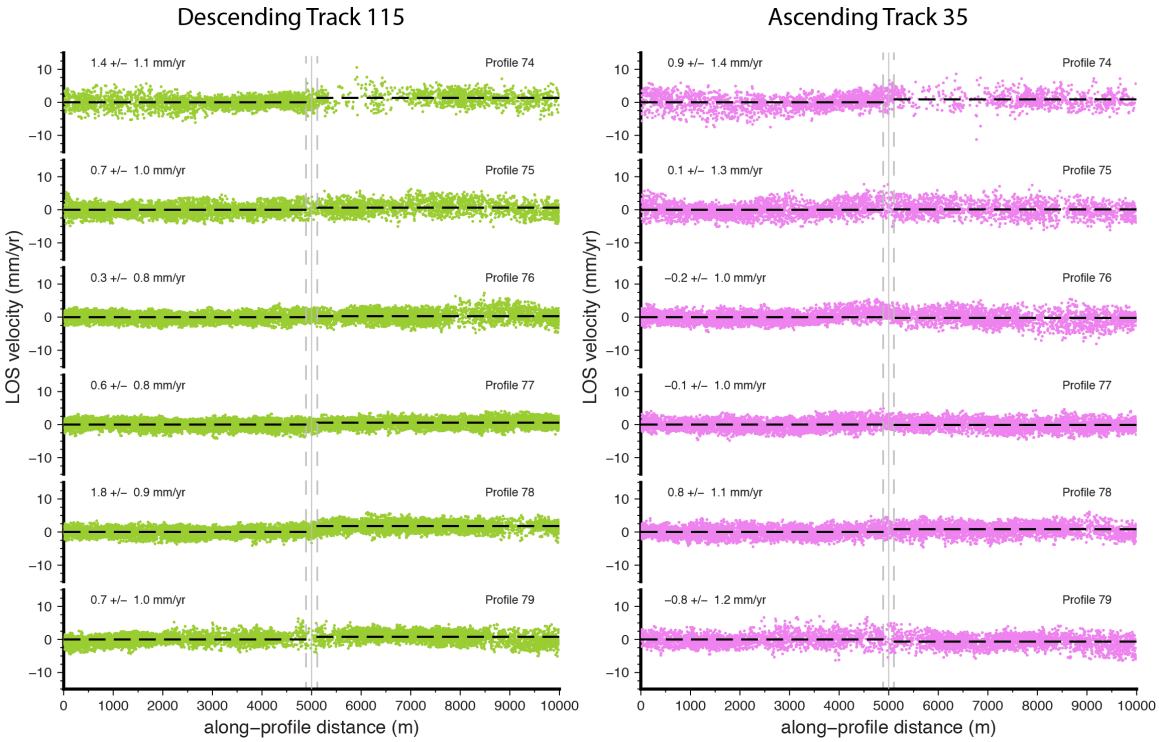

Figure 2.17: Detrended InSAR LOS velocity profiles from Sentinel-1 descending track 115 (left) and ascending track 35 (right) in the Santa Rosa, CA area. Procedure for detrending and estimating the offset are described in Figure 2.12 with errors presented as 2 standard deviation uncertainties. Solid gray line is the fault location and the dashed gray lines denotes the area not included in the offset estimation. Location of profiles are given in Figure 2.11.

2.5.2 Decomposing LOS Velocity Offsets Into Horizontal and Vertical Components

The InSAR velocity offset estimates for each viewing geometry (ascending and descending) are measured in the line-of-sight direction which is defined by the vector between the satellite and the ground target for each pixel. Combining the two independent measurements from the ascending and descending viewing geometries (Figure 2.18), we can estimate horizontal and vertical motion, if we assume that all horizontal motion is in a particular direction. To estimate the fault-parallel motion, we resolve the horizontal deformation into the fault strike direction with the assumption that most of the horizontal motion close to a fault is fault-parallel motion. We decompose the ascending and descending LOS velocity measurements into their vertical (z-axis) and horizontal (x- and y-axis) displacements through the following procedure.

The LOS velocity measurements are movements of the ground projected into the satellite's LOS direction. The full three-component velocity of the ground is given by:

$$\boldsymbol{u} = [u_x \quad u_y \quad u_z]$$

The unit pointing vector for ground deformation is the vector from the ground to the satellite. This is important to note as it is different from the range-change pointing vector which is the vector from the satellite to the ground. Knowing which pointing vector to reference impacts the pointing vectors sign convention used for decomposition into horizontal and vertical motions. Using the viewing geometry of each satellite with respect to the ground

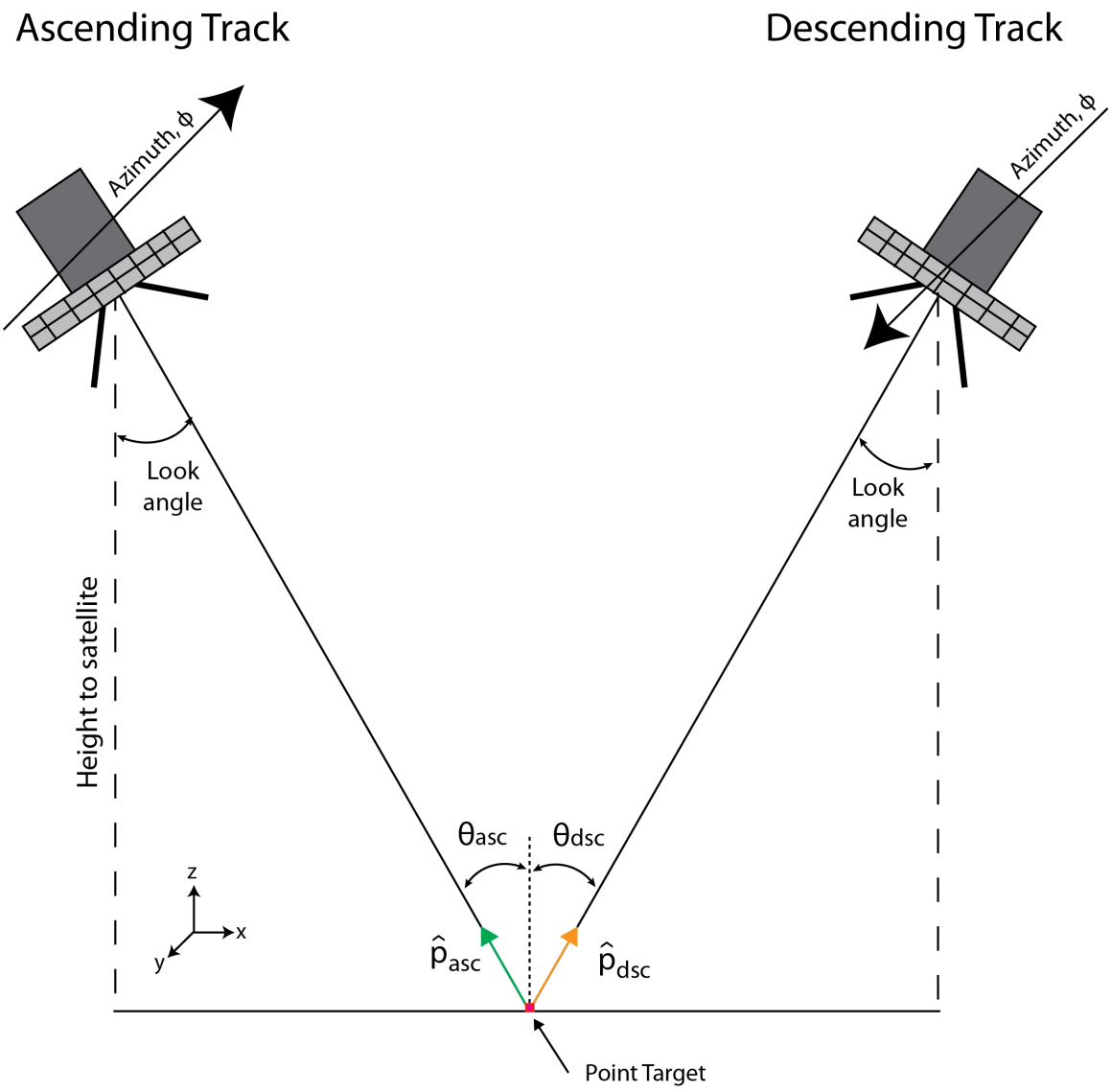

Figure 2.18: Viewing geometries of the ascending and descending tracks. The incidence angle is the angle that the radar ray makes with the vertical at the point target and is noted as θ_{asc} and θ_{dsc}, for ascending and descending tracks respectively. The unit pointing vectors (pointing from the ground target to the satellite) for each viewing geometry are noted as $\hat{p}$ where $\hat{p}_{asc}$ is green and $\hat{p}_{dsc}$ is orange. Note that the x-axis direction for $\hat{p}_{asc}$ will be in the negative x direction, opposite from the descending pointing vector.

point target (Figure 2.18), the pointing vectors in the LOS direction are expressed as:

$$\hat{\boldsymbol{p}}_{\boldsymbol{dsc}} = [\hat{p}_x \quad \hat{p}_y \quad \hat{p}_z] = [\cos\phi \sin\theta \quad -\sin\phi \sin\theta \quad \cos\theta]$$

$$\hat{\boldsymbol{p}}_{\boldsymbol{asc}} = [\hat{p}_x \quad \hat{p}_y \quad \hat{p}_z] = [\cos\phi \sin\theta \quad -\sin\phi \sin\theta \quad \cos\theta]$$

The satellite heading azimuth is ϕ and the local incidence angle at the ground point target is θ. The subscripts indicate whether it is for the ascending ("asc") or descending ("dsc") tracks. In the ISCE processing software, the satellite pointing azimuth is not measured from geographical North but instead it is measured 0° from East and increases counter-clockwise. Conversion to true azimuth is $\phi = -1 * \phi_{orig} + 90°$. (Both of these measurements can be found in the ISCE products in the file *los.rdr.geo*). With the two independent LOS velocity rates ($\dot{r}$) and two different viewing geometries, we can write two equations in terms of the pointing vectors ($\hat{p}$) and ground deformation, $\boldsymbol{u}$:

$$\dot{r}_{asc} = \hat{\boldsymbol{p}}_{\boldsymbol{asc}} \cdot \boldsymbol{u}$$

$$\dot{r}_{dsc} = \hat{\boldsymbol{p}}_{\boldsymbol{dsc}} \cdot \boldsymbol{u}$$

The measured LOS ground deformation rates can be decomposed into the horizontal (u_{horz}) and vertical (u_{vert}) components:

$$\dot{r}_{asc} = u_{horz}(\hat{\boldsymbol{p}}_{\boldsymbol{asc}} \cdot \boldsymbol{u}) + u_z \hat{p}_{vert,asc}$$

$$\dot{r}_{dsc} = u_{horz}(\hat{\boldsymbol{p}}_{\boldsymbol{dsc}} \cdot \boldsymbol{u}) + u_z \hat{p}_{vert,dsc}$$

The horizontal component is further defined by projecting the deformation into the average strike direction (σ) using the fault strike unit vector of $\hat{\boldsymbol{u}}_{horz} = [\sin\sigma \quad \cos\sigma]$.

Writing these equations as simultaneous equations in matrix form:

$$\mathbf{Am} = \dot{r} + \mathbf{e}$$

$$\begin{bmatrix} \hat{\boldsymbol{p}}_{\boldsymbol{asc}} \cdot \hat{\boldsymbol{u}}_{horz} & \hat{p}_{z,asc} \\ \hat{\boldsymbol{p}}_{\boldsymbol{dsc}} \cdot \hat{\boldsymbol{u}}_{horz} & \hat{p}_{z,dsc} \end{bmatrix} \begin{bmatrix} u_{horz} \\ u_z \end{bmatrix} = \begin{bmatrix} \dot{r}_{asc} \\ \dot{r}_{dsc} \end{bmatrix} + \begin{bmatrix} e_{asc} \\ e_{dsc} \end{bmatrix}$$

where $\boldsymbol{m}$ is the model ground deformation and ($\boldsymbol{e}$) are the errors defined as the standard deviation of the residuals to the best fitting line for each profile. We then solve for the best fitting model velocities ($\boldsymbol{m}$) given through the least squares inversion method given by:

$$\boldsymbol{m} = (\boldsymbol{A^T E^{-1} A})^{-1} \boldsymbol{A^T E^{-1} \dot{r}}$$

where E is the variance-covariance matrix with the ascending and descending errors ($\boldsymbol{e_{asc}}$ and $\boldsymbol{e_{dsc}}$)

$$\boldsymbol{E} = \begin{bmatrix} \boldsymbol{e}_{asc}^2 & 0 \\ 0 & \boldsymbol{e}_{dsc}^2 \end{bmatrix}$$

Tables 2.3-2.5 and Figure 2.19 show the along-strike variation in fault-parallel and vertical offset rates that are estimated from the LOS profile offsets by applying the decomposition method mention in Section 2.5.2. The along-strike LOS variation for the ascending and descending data are provided in Appendix 2.9. We provide 2σ uncertainties of these values. As mentioned before, the values denoted as gray boxes are profiles that showed little to no LOS values in the descending track, which indicates a low likelihood of creep along that fault segment. There are two sections along the Maacama fault and two sections along the Rodgers Creek fault where we estimate consistent values of fault-parallel creep motion which are more than 2σ above zero – we have high confidence in the occurrence of fault creep at these locations. Along the Maacama fault, a 40 km section spanning the

the Willits and Ukiah area has a range of creep rates of 1.7 to 7.0 mm/yr (Figure 2.19) with an average creep rate of $\sim$ 4.2 mm/yr in Willits and northern Ukiah which then decreases to 2 mm/yr in southern Ukiah (Profiles 25–30) (Figures 2.13 - 2.14). There is also a 30 km section of the Maacama fault, near Cloverdale that shows a larger range of fault-parallel creep rates from 1.3 to 11 mm/yr (Figure 2.19). Profile 39, has an estimated creep rate of $\sim$ 4 mm/yr which increases to the highest creep rates observed of $\sim$11 mm/yr at profile 45 and gradually decreases to $\sim$2 mm/yr at the end of the section at profile 50 (Figure 2.5.1).

Along the Rodgers Creek fault, in the Healdsburg and Santa Rosa areas we estimate lower fault-parallel creep rate values, from 0.6 to 2.5 mm/yr (Figures 2.16 and 2.19). The Healdsburg area has an average creep rate of 1.8 mm/yr (Profiles 65 to 70; 12 km section) and the Santa Rosa area has a variation where the northern section has very low rates of 0.7 mm/yr (profiles 74 to 76; 7.5 km section) which then steps up to 2.2 mm/yr at the southern most section (profiles 77 to 79; 7.5 km section). Overall, we can resolve fault creep along sections of the Maacama fault that have not been observed before, and we resolve creep on the Rodgers Creek fault as well.

2.6 Discussion

From our small baselines InSAR analysis of Sentinel-1 ascending and descending data we find that we can resolve fault creep along along the Maacama fault at locations not observed before and along the Rodgers Creek fault in locations where fault creep has been observed. The northern section of the Maacama fault has creep rates ranging between 1.7

Table 2.3: Creep rate estimates from profile offsets for the northern Maacama Fault

Profile	Distance (km)	Descending rate (mm/yr)	Ascending Rate (mm/yr)	Creep Rate (mm/yr)	Vertical Rate (mm/yr)
1	0.0	1.9 ± 1.7	1.6 ± 2.4	0.8 ± 0.1	2.1 ± 0.4
2	2.5	1.0 ± 2.1	-0.1 ± 2.7	2.6 ± 3.1	0.2 ± 0.9
3	5.0	1.2 ± 2.1	1.6 ± 3.1	-0.5 ± 4.4	1.8 ± 2.7
5	10.0	-0.8 ± 1.9	-2.3 ± 2.7	4.0 ± 0.7	-2.6 ± 0.1
6	12.5	2.2 ± 2.1	-1.2 ± 2.7	5.6 ± 1.8	-0.2 ± 0.8
8	17.5	1.8 ± 2.1	0.5 ± 3.1	2.1 ± 2.0	1.1 ± 2.5
9	20.0	3.3 ± 1.7	0.9 ± 2.7	4.4 ± 0.1	2.0 ± 0.2
13	30.0	-0.3 ± 1.6	-1.5 ± 2.3	1.5 ± 0.1	-1.3 ± 0.6
14	32.5	0.4 ± 1.3	-1.5 ± 1.8	3.3 ± 1.7	-1.2 ± 0.3
15	35.0	1.4 ± 1.4	-1.5 ± 1.8	4.8 ± 1.7	-0.7 ± 0.7
16	37.5	2.9 ± 1.6	0.6 ± 2.3	4.5 ± 1.3	1.6 ± 0.7
18	42.5	3.1 ± 1.5	-0.4 ± 1.9	5.2 ± 1.9	1.0 ± 0.5
19	45.0	2.2 ± 1.7	-3.1 ± 2.0	7.0 ± 0.7	-1.6 ± 0.1
20	47.5	0.9 ± 1.7	-2.8 ± 2.1	4.8 ± 1.5	-1.8 ± 0.3
21	50.0	1.0 ± 1.7	-0.4 ± 1.8	2.5 ± 2.2	0.1 ± 0.2
22	52.5	1.6 ± 1.6	0.8 ± 1.8	1.7 ± 1.1	1.3 ± 1.0
23	55.0	2.9 ± 1.7	-0.1 ± 2.0	5.5 ± 4.9	1.0 ± 0.3
24	57.5	1.2 ± 1.5	-1.8 ± 1.8	6.2 ± 2.9	-1.3 ± 0.5
25	60.0	1.2 ± 1.2	0.0 ± 1.5	2.3 ± 0.8	0.4 ± 0.5
26	62.5	1.0 ± 1.1	0.9 ± 1.4	0.4 ± 0.9	1.2 ± 2.3
27	65.0	0.2 ± 1.0	0.0 ± 1.1	0.4 ± 0.6	0.1 ± 3.6
28	67.5	0.8 ± 1.2	0.0 ± 1.4	2.0 ± 2.7	0.2 ± 0.6
29	70.0	0.4 ± 1.4	-0.7 ± 1.8	2.1 ± 1.4	-0.5 ± 0.5

Table 2.4: Creep rate estimates from profile offsets for the southern Maacama Fault

Profile	Distance (km)	Descending rate (mm/yr)	Ascending Rate (mm/yr)	Creep Rate (mm/yr)	Vertical Rate (mm/yr)
30	72.5	-1.1 ± 1.4	-1.1 ± 1.8	-0.2 ± 0.1	-1.3 ± 0.2
31	75.0	-2.0 ± 1.5	-1.2 ± 1.8	-1.5 ± 0.1	-1.8 ± 0.1
32	77.5	-0.6 ± 1.6	-3.2 ± 1.7	3.4 ± 0.3	-2.9 ± 0.5
33	80.0	-1 ± 1.5	-1.1 ± 1.8	0.0 ± 0.1	-1.3 ± 0.3
34	82.5	-0.5 ± 1.4	0.0 ± 1.6	-0.8 ± 0.8	-0.2 ± 0.3
35	85.0	-1.1 ± 1.4	-0.3 ± 1.6	-1.8 ± 1.5	-0.6 ± 1.4
36	87.5	-1.0 ± 1.4	-1.3 ± 1.7	1.1 ± 0.4	-1.7 ± 0.4
37	90.0	0.00 ± 1.5	-2.6 ± 1.8	7.1 ± 1.3	-2.7 ± 0.1
38	92.5	0.3 ± 1.5	0.0 ± 1.9	0.9 ± 2.4	0.1 ± 0.9
39	95.0	2.1 ± 1.4	0.3 ± 1.8	4.1 ± 0.1	1.0 ± 0.1
40	97.5	-1.9 ± 1.5	-3.6 ± 1.8	4.4 ± 2.0	-4.2 ± 1.1
41	100.0	3.3 ± 1.6	-4.7 ± 2.0	9.0 ± 0.9	-1.9 ± 0.2
42	102.5	2.4 ± 1.5	-2.8 ± 1.8	7.6 ± 0.6	-1.2 ± 0.1
43	105.0	0.4 ± 1.3	-4.6 ± 1.6	7.2 ± 1.5	-3.6 ± 0.4
44	107.5	1.6 ± 1.5	-3.9 ± 1.8	8.0 ± 0.5	-2.5 ± 0.1
45	110.0	5.2 ± 1.5	-2.3 ± 1.6	11.0 ± 2.4	0.5 ± 1.1
46	112.5	4.8 ± 1.3	-0.4 ± 1.5	6.9 ± 2.5	2.0 ± 0.3
47	115.0	4.0 ± 1.3	-0.3 ± 1.7	5.6 ± 1.3	1.7 ± 0.1
48	117.5	2.4 ± 1.3	-0.7 ± 1.6	3.5 ± 0.8	0.7 ± 0.2
49	120.0	2.0 ± 1.3	-0.5 ± 1.6	2.9 ± 0.6	0.7 ± 0.1
50	122.5	0.2 ± 1.3	-0.8 ± 1.6	1.3 ± 0.5	-0.5 ± 0.1
51	125.0	0.5 ± 1.4	-1.9 ± 1.6	3.0 ± 0.6	-1.2 ± 0.1
52	127.5	-1.0 ± 1.5	1.1 ± 1.9	-2.7 ± 2.3	0.3 ± 0.3
53	130.0	-3.1 ± 1.5	0.8 ± 1.8	-5.5 ± 0.3	-0.8 ± 0.1
54	132.5	-2.2 ± 1.4	0.6 ± 1.6	-3.4 ± 0.2	-0.6 ± 0.1
55	135.0	0.5 ± 1.4	-0.7 ± 1.6	1.9 ± 1.1	-0.4 ± 0.2
56	137.5	-0.9 ± 1.4	-1.5 ± 1.5	0.8 ± 0.5	-1.6 ± 0.7
58	142.5	1.1 ± 1.4	-2.1 ± 1.6	3.2 ± 0.9	-0.9 ± 0.3
59	145.0	0.0 ± 1.3	-0.4 ± 1.5	0.9 ± 0.4	-0.4 ± 0.5
60	147.5	-0.3 ± 1.3	-0.4 ± 1.4	0.0 ± 1.1	-0.4 ± 0.4

Table 2.5: Creep rate estimates from profile offsets for the Rodgers Creek Fault

Profile	Distance (km)	Descending rate (mm/yr)	Ascending Rate (mm/yr)	Creep Rate (mm/yr)	Vertical Rate (mm/yr)
61	0.0	1.9 ± 1.2	-0.5 ± 1.4	3.7 ± 1.7	0.4 ± 0.3
62	2.5	-0.1 ± 1.3	0.6 ± 1.5	-0.9 ± 0.7	0.4 ± 0.2
63	5.0	-0.3 ± 1.4	-0.4 ± 1.5	0.1 ± 0.5	-0.5 ± 0.5
64	7.5	-1.2 ± 1.3	1.0 ± 1.5	-2.6 ± 0.5	0.1 ± 0.1
65	10.0	0.3 ± 1.3	-0.4 ± 1.6	0.7 ± 0.3	-0.1 ± 0.1
66	12.5	0.9 ± 1.3	-0.9 ± 1.5	1.9 ± 0.5	-0.1 ± 0.2
67	15.0	-0.1 ± 1.1	-1.6 ± 1.3	2.1 ± 0.3	-1.3 ± 1.6
68	17.5	0.5 ± 1.0	-1.6 ± 1.1	2.3 ± 3.8	-1.0 ± 0.3
69	20.0	1.1 ± 1.3	-1.2 ± 1.6	2.5 ± 0.6	-0.3 ± 0.1
70	22.5	0.0 ± 1.3	-1.2 ± 1.5	1.4 ± 0.1	-0.9 ± 0.2
71	25.0	-0.6 ± 1.1	0.0 ± 1.3	-1.1 ± 0.3	-0.3 ± 1.1
72	27.5	1.0 ± 0.9	1.5 ± 1.1	-0.7 ± 0.3	1.7 ± 2.1
73	30.0	0.9 ± 1.0	2.9 ± 1.2	-4.2 ± 0.5	2.9 ± 0.9
74	32.5	1.4 ± 1.1	0.9 ± 1.4	0.6 ± 0.6	1.3 ± 0.4
75	35.0	0.7 ± 1.0	0.1 ± 1.3	0.7 ± 0.3	0.4 ± 0.9
76	37.5	0.3 ± 0.8	-0.2 ± 1.0	0.7 ± 2.8	0.0 ± 0.4
77	40.0	0.6 ± 0.8	-0.1 ± 1.0	2.0 ± 0.7	0.0 ± 0.2
78	42.5	1.8 ± 0.9	0.8 ± 1.1	2.2 ± 0.2	1.4 ± 0.5
79	45.0	0.7 ± 1.0	-0.8 ± 1.2	2.4 ± 0.5	-0.3 ± 0.1

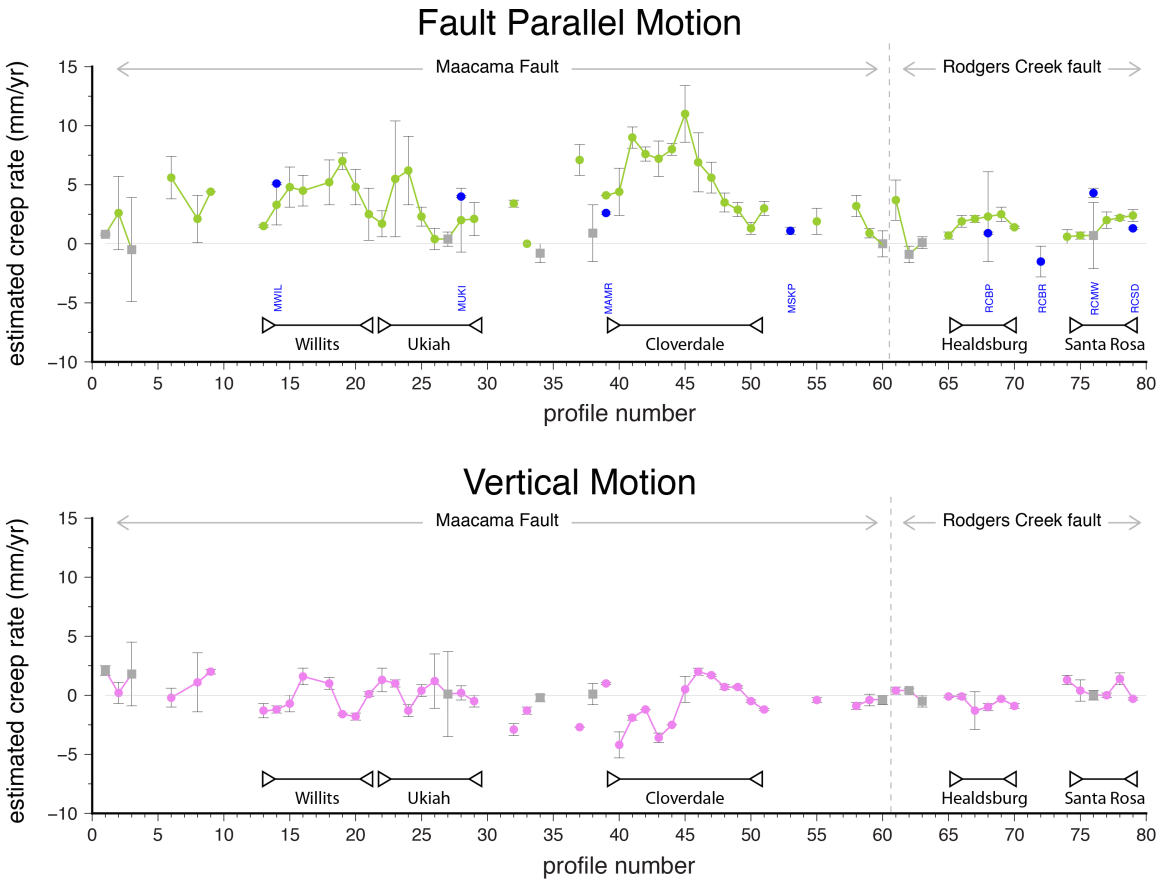

Figure 2.19: Distribution of fault-parallel (green dots) and vertical (pink dots) movement along the Maacama and Rodgers Creek faults. Gray squares indicate profiles that might not exhibit fault creep from LOS profile analysis. Blue circles are the alignment array total creep rate values from McFarland et al. (2018).

to 7.0 mm/yr , the southern section between 4.2 to 11 mm/yr, and the Rodgers Creek fault has creep rates ranging between of 0.7 to 2.4 mm/yr .

2.6.1 Comparison to Other Fault Creep Studies

There are several previous studies that estimate creep rates for both faults including GPS-based models (Murray et al., 2014), alignment arrays (Lienkaemper et al., 2014; McFarland et al., 2018), repeating earthquake data (Shakibay Senobari and Funning, 2019), and previous InSAR studies on the northern Rodgers Creek fault (Funning et al., 2007; Tong et al., 2013; Jin and Funning, 2017). The Tong et al. (2013) study spans both faults from 2006 to 2010 using the L-band ALOS SAR satellite, Funning et al. (2007) and Jin and Funning (2017) studies focus on the northern Rodgers creek faults spanning 1992 to 2001 using the ERS satellite, and 2003 to 2010 using the Envisat satellite, respectively. The compilation of sections where we are confident the fault is creeping from InSAR, along with locations of repeating earthquake families (Shakibay Senobari and Funning, 2019) and alignment arrays (McFarland et al., 2018) are all shown in Figure 2.20 to show the distribution of noted fault creep.

Maacama fault

The northern-most section of the Maacama fault, in Laytonville, we estimate fault-parallel creep at a four of the profiles ranging from 2 to 5 mm/yr (Figure 2.19). This is consistent with calculated creep rates from repeating earthquakes occurring at depths of $\sim$10 km at 5 mm/yr (Shakibay Senobari and Funning, 2019). Near Willits, we estimate

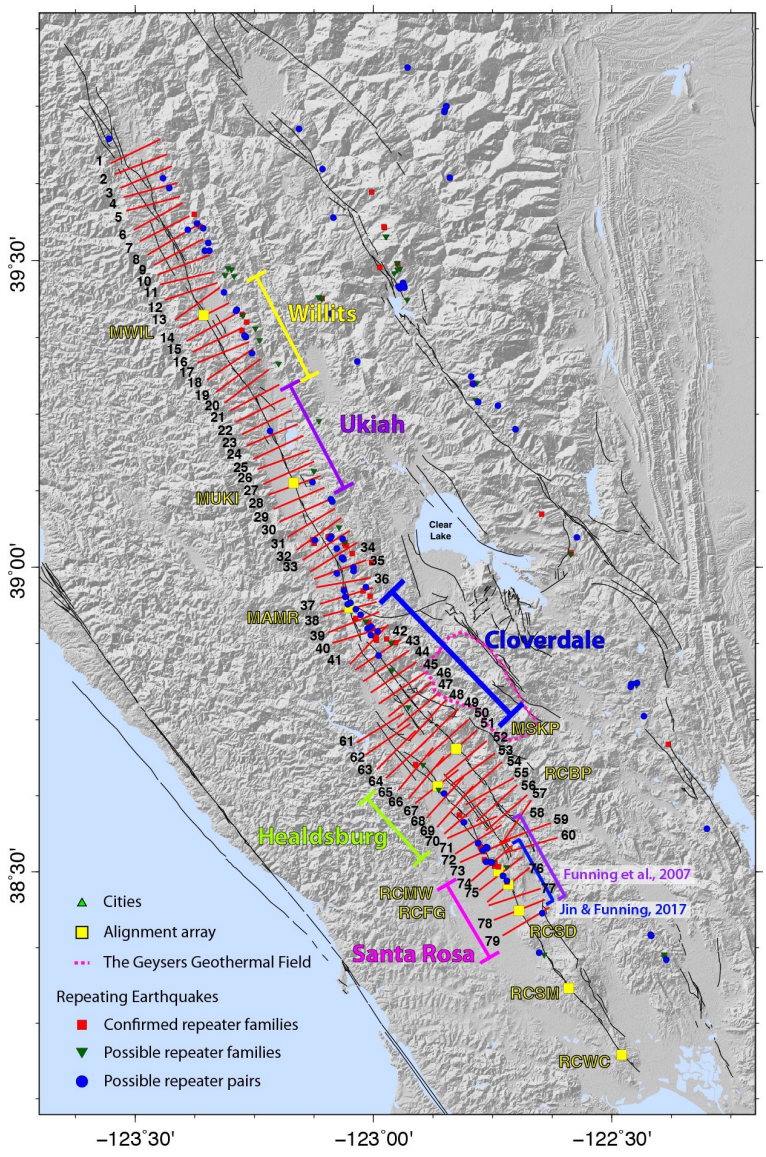

Figure 2.20: Compilation of creep rate observations along the Maacama and Rodgers Creek faults from alignment arrays (McFarland et al., 2018, yellow squares), Sentinel-1 InSAR data (sections highlighted with colored brackets), and repeating earthquake families (Shakibay Senobari and Funning, 2019, red squares, green triangles, blue circles). The types of repeating earthquake families plotted are noted in the legend where the red squares are confirmed repeating earthquake families with precise locations validated. The green triangles are possible repeating earthquake families with locations that are highly correlated (cross-correlation coefficients > 0.9). The blue circles are possible repeating earthquake pairs where their locations overlap but with only two events, years apart. The Geysers Geothermal Field is defined by the dashed pink outline south of Clear Lake.

creep rates of 1.7–7.0 mm/yr which are in agreement with the local alignment array (MWIL) rate measuring 5.1 ± 0.1 McFarland et al. (2018), located in profile 14. There are also field observations along the fault trace of offset building walls, sidewalks, railroad tracks, and en echelon cracks forming in the pavement through main sections of the city (Prentice (2006) and personal field work).

The Willits alignment array and now this InSAR study, have surface creep rate estimates lower than the estimated creep rates from the GPS-based model of Murray et al. (2014) which estimates ∼10 mm/yr along the Maacama fault. In addition to these measurements, there are also repeating earthquakes along this segment with a range of hypocentral depths of 1 to 10 km; Shakibay Senobari and Funning (2019) estimate a creep rate of ∼4 mm/yr from those events. Shakibay Senobari and Funning (2019) suggest the reason for the higher detected GPS creep rate is due to additional slip occurring on the East Willits fault, ∼5 km west of the Maacama fault trace (on which repeating events are also found) which biases the GPS estimate. If this is true, the alignment array measurements are at a lower rate than the GPS as they do not include the East Willits fault (McFarland et al., 2018). Our results also measure a lower rate because the profile is not long enough to measure estimates across the East Willits fault as profile spans only 5 km either side of the Maacama fault.

The Ukiah area (Profiles 22 to 30) is a 20 km section of the fault with very few repeating earthquake families detected by Shakibay Senobari and Funning (2019) but we do infer surface fault creep within this 'gap of repeating earthquakes' ranging between 0.4 to 6.2 mm/yr. This section has an average creep rate of ∼3 mm/yr, lower than the Willits area

at 4.2 mm/yr. Profile 28 contains the alignment array, MUKI, that measures a creep rate of 4.0 ± 0.1 mm/yr (McFarland et al., 2018); this is within the error of our estimated fault-parallel creep rate of 2.0 ± 2.7 mm/yr. Tong et al. (2013) also estimate a creep rate in this area of up to 3 mm/yr at the location of profile 26. In addition to these two measurements, I have observed an offset sidewalk on Beltrami Drive, located within profile 25 (personal field work, unpublished).

Along the central section of the Maacama fault, Shakibay Senobari and Funning (2019) detect a high number of repeating earthquakes between 2 to 8 km depths with creep rate estimates of ∼2 mm/yr. There are two profiles (32 and 37) that imply creep rates of ∼3 mm/yr and ∼7 mm/yr (respectively), but the surrounding profiles do not agree, thus we cannot confidently determine if there is surface creep along this central portion from our InSAR data set (i.e., profiles 31 to 38).

From Hopland to Cloverdale (defined as the Cloverdale area in Figure 2.20), we estimate creep rates ranging from 1.3–11 mm/yr. The highest creep rates of 7–11 mm/yr are estimated for profiles 41–46 (Figure 2.15, Table 2.4). Other studies estimating creep, previously mentioned (i.e., Lienkaemper, 1992; Tong et al., 2013; Murray et al., 2014; McFarland et al., 2018), do not infer fault creep along this section of the Maacama fault but do infer creep to the north and south. Near profiles 39 and 40 we measure a creep rate of ∼4 mm/yr and Tong et al. (2013) estimates a higher creep rate of ∼8 mm/yr. Tong et al. (2013) is most likely over-estimating the creep rate because they only use the descending data set and assume all LOS motion is in the fault-parallel direction. There is an alignment array (MAMR) to the north, in profile 38, that estimates a creep rate of 2.5 ± 0.6 mm/yr

and there are nearby repeating earthquakes consistent with creep rates of 2 to 3 mm/yr occurring at 1 to 7 km depths (McFarland et al., 2018; Shakibay Senobari and Funning, 2019). Our creep rate estimates fall within a similar range for profiles 37 - 39 (Figure 2.19). The highest creep rate along the Maacama fault is 11 ± 2.4 mm/yr, in profile 45. Tong et al. (2013) also measures a creep rate in profile 46 but at a lower rate of ∼5 mm/yr and Murray et al. (2014) estimates ∼5 mm/yr surface creep rate along this southern section of the Maacama fault as well. There are no repeating earthquakes within this vicinity. This area is adjacent to the Geysers Geothermal Field (dashed pink outline south of Clear Lake; Figure 2.20) which contributes to the large LOS signals present in the ascending and descending data (Figures 2.9 and 2.10) indicative of vertical motion due to subsidence. These high surface creep rates near the Geysers might suggest an influence of fluids within the fault zone. If there are fluids trapped within the fault zone, there could be a increase in pore fluid pressure resulting in a reduced normal stress that may potentially influence the fault to creep.

Rodgers Creek fault

We resolve fault-parallel creep rates of up to 2.4 mm/yr within the cities of Healdsburg and Santa Rosa along the Rodgers Creek faults. The alignment array in Healdsburg (RCBP) measures a creep rate 0.9 ± 0.1 mm/yr which is within the error of our measured creep rate of 2.3 ± 3.8 mm/yr (profile 68). Comparing the two alignment arrays in Santa Rosa, sites RCMW and RCSD, to our fault creep measurements, they do not fully agree. RCMW measures a higher creep rate of 4.3 ∼0.4 mm/yr than our estimate of 0.7 ±2.8 mm/yr (profile 75) and RCSD measures a lower creep rate of 1.3 ±0.1 mm/yr than

our 2.4 ±0.5 mm/yr creep rate (Profile 78). This difference in measurements could be due to the area the alignment array versus the InSAR study are sampling. The alignment arrays are measuring over a narrower zone across the fault of ∼90 m to ∼150 m, respectively (McFarland et al., 2018) and our InSAR study is measuring 10 km across the fault in which we do not take into the 100 m on either side of the fault. Our study is less sensitive to direct surface creep and instead is integrating over the top 2–3 km of the fault.

We now look at comparing our results to earlier InSAR studies along the Rodgers Creek fault at different time periods – from 1992 to 2001 using the ESA (European Space Agency) ERS satellites (Funning et al., 2007), and from 2003 to 2010 using the ESA Envisat satellite (Jin and Funning, 2017). Funning et al. (2007) only had the descending track data to estimate creep rates which means that all of the estimated LOS offset rate along a profile was assumed to be fault-parallel motion, and thus the estimated creep rate. This does not take into account any possible vertical motion along the fault. Jin and Funning (2017) used data from one ascending and one descending track to decompose the LOS values into fault-parallel and vertical motions. We used the same method to decompose our data set. Funning et al. (2007) uses a profile width of 5 km and Jin and Funning (2017) splits this width in half to have 2.5 km width profiles.

We estimate the relative location of each profile and plot all calculated fault-parallel estimates in Figure 2.21 for comparison. We focus on profiles where we are able to resolve fault-parallel creep (i.e profiles 65-70 and 74-79). The northern section, near Healdsburg, falls within error (2σ uncertainties) of both studies, including the alignment array. The southern section also has similar observations to Jin and Funning (2017) where

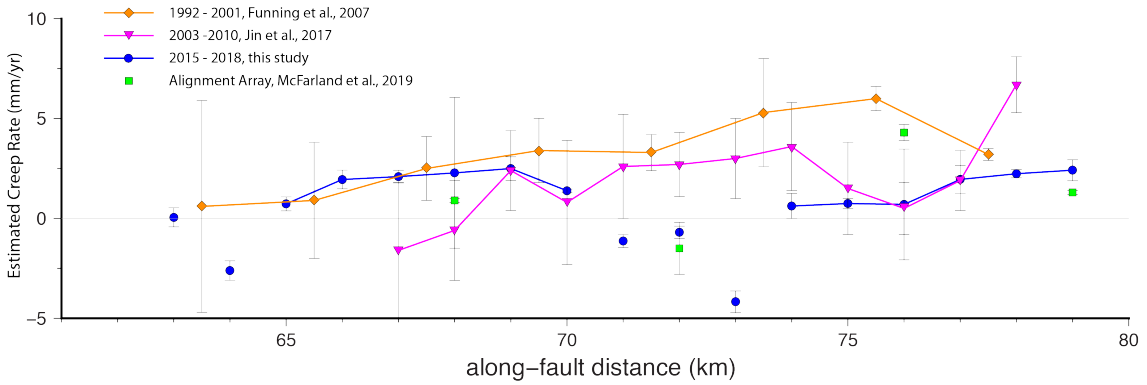

Figure 2.21: Comparison of fault creep studies along the northern Rodgers Creek fault. Two InSAR studies spanning two different decades, Funning et al. (2007) (orange diamonds) from 1992 to 2001 and Jin and Funning (2017) (pink triangles) from 2003 to 2010, and local alignment arrays (McFarland et al., 2018). Funning et al. (2007) inferred creep along the entire fault section using one descending track but the study by Jin and Funning (2017) shows that using only one viewing geometry is not enough to discern the variability of fault parallel versus vertical motion along the fault. Our data (blue circles) agrees with Jin and Funning (2017)'s lower creep rates in the Santa Rosa area (profiles 75 to 77), not including their last profile (profile 77) showing a higher creep rate but our data agrees with the alignment array values at the southern end of the fault. The creep rates in Healdsburg (Profiles 65 to 70) follow the trend of Funning et al. (2007) but are within error of the Jin and Funning (2017) and McFarland et al. (2018) estimates as well. Data points that are not fit with a line are profiles that do not have motion indicative of right-lateral fault creep in the LOS profile offsets for both ascending and descending data.

the values are much lower than the estimated creep rates from Funning et al. (2007). The estimated creep rates at the end of the fault, at profiles 78 and 79, do not agree with those of Jin and Funning (2017) and instead, are closer to the creep rate value from the alignment array, RCSD. Overall, most of our data set falls within error of the Jin and Funning (2017) values, and we similarly note a large difference in creep rates in Santa Rosa (near profiles 75-76) which could imply that the earlier data set (Funning et al., 2007) is overestimating the creep rate due to only using one viewing geometry and assuming all LOS profile offsets are attributed to horizontal motions.

2.6.2 Seismic Hazard Implications

This study has provided new evidence of fault creep spanning ∼54% of the Maacama fault (i.e., ∼ 93 km is observed to creep out of 170 km) and ∼40% of the Rodgers Creek fault (i.e., ∼ 28 km out of 70 km). This has implications for seismic hazard assessment as fault creep has the potential to reduce the rate of strain accumulation and/or reduce the size of the locked area that is capable of rupturing in a future earthquake, and could possibly delay the time in between large earthquakes. Dynamic rupture models have shown that creeping sections of faults can divert or ultimately stop an earthquake from propagating farther along a fault (Lozos, 2013; Lozos et al., 2015). In addition, identifying repeating earthquakes at depth along sections where surface creep is observed points towards the possibility of a smaller locked area that can rupture (Shakibay Senobari and Funning, 2019). This size reduction of possible locked areas can impact the length of time between large earthquakes, reduce the size of a future earthquake, and/or stop an earthquake from rupturing a large portion of the fault, thus reducing the seismic hazard posed by these faults. Our results would be useful for incorporation into future versions of the Uniform California Earthquake Rupture Forecast (UCERF), for estimating the seismic moment reduction over a fault surface due to fault creep. UCERF3 uses one InSAR study to estimate the creep rate values along the Maaacama and Rodgers Creek faults (i.e., Tong et al., 2013; Weldon et al., 2013) which, as previously mentioned, only uses one viewing geometry to estimate fault creep along both faults. The use of this study and others (i.e., Funning et al., 2007; Jin and Funning, 2017) would provide a more detailed picture of the variation of fault creep

along both the Maacama and Rodgers Creek faults for UCERF to use when estimated the reduction in seismic moment along both faults.

2.7 Conclusion

Our profile analysis of the Sentinel-1 ascending and descending data along the Maacama and Rodgers Creek faults from 2015 to 2018 shows evidence of fault creep on both faults. We divided the fault into 2.5 km segments where we estimate LOS velocity offsets along profiles spanning 5 km either side of the fault. These LOS velocity offsets were decomposed into their fault-parallel and vertical components, allowing us to identify sections of the fault that have a creep rate robustly above zero. Through this analysis we infer observe that at least 54% of the Maacama fault and 40% of the Rodgers Creek fault may be creeping at the surface.

Our estimated fault creep rates are similar to other, complimentary methods to measure fault creep – an elastic dislocation modeling of GPS data, alignment arrays, and other InSAR data sets spanning different time periods (e.g., Funning et al., 2007; Tong et al., 2013; Lienkaemper et al., 2014; Murray et al., 2014; Jin and Funning, 2017; McFarland et al., 2018). The alignment array rates and our measured creep rates are within similar ranges (Lienkaemper et al., 2014; McFarland et al., 2018). The InSAR data along the Maacama fault shows creep at locations that are also observed to be creeping in an earlier time period using a different InSAR data set and method (2006–2010) (Tong et al., 2013). The InSAR data along the Rodgers Creek fault adds to previous InSAR data (Funning et al., 2007; Jin and Funning, 2017) from two different time periods (i.e., 1992–2001 and 2003–2010) and

confirms that there is fault creep in the city of Healdsburg and Santa Rosa. Comparing these two previous studies with our data set shows that there is a need for using at least two viewing geometries (e.g., SAR satellite ascending and descending data) to distinguish between vertical and fault-parallel motions as the earlier study likely overestimates the creep rates due to using one viewing geometry and assuming all motion was fault-parallel.

Additional InSAR studies from other satellites along the Maacama fault would be useful to observe variations in creep, if any, as there are no other studies other than Tong et al. (2013) observing fault creep along the Maacama fault. For example, data is available from ERS-1 and -2 and Envisat for the time period of ∼1992 to ∼2012 and possibly Radarsat-2 from 2012 to 2015. The fault segment with the highest creep rates measured, next to the Geysers Geothermal field, should be further investigated to study the influence of normal stress and the large vertical motions with fault creep. This could be achieved through additional methods such as GPS, alignment arrays, as well as differential lidar and the airborne SAR method, UAVSAR (Uninhabited Aerial Vehicle Synthetic Aperture Radar), two methods with available data in this area. The Rodgers Creek fault has been observed to creep from InSAR observations starting in 1992 (i.e., 1992–2001, 2003–2010, and 2015–2018) with the largest gap between 2010–2015 which could possible be filled in with Radarsat-2, for example. There should also be an InSAR study extending to the southern Rodgers Creek fault and northern Maacama fault sections as these two areas are not covered in this study. This would be beneficial to have a full distribution of fault creep along both faults. For other complimentary methods such as GPS and alignment arrays,

the addition of new sites focused in the areas where we observe creep would be useful to corroborate our observations and to measure the creep rates in the area.

2.8 Appendix A: ISCE to StaMPS Processing

Once there is a stack of coregistered SLCS, we use StaMPS to perform interferometric processing. In order to use the output products from ISCE into StaMPS, the files need to be converted into a readable format with a new set of files. These steps to create these files are explained in this section and the StaMPS directory structure is shown in Figure 2.22.

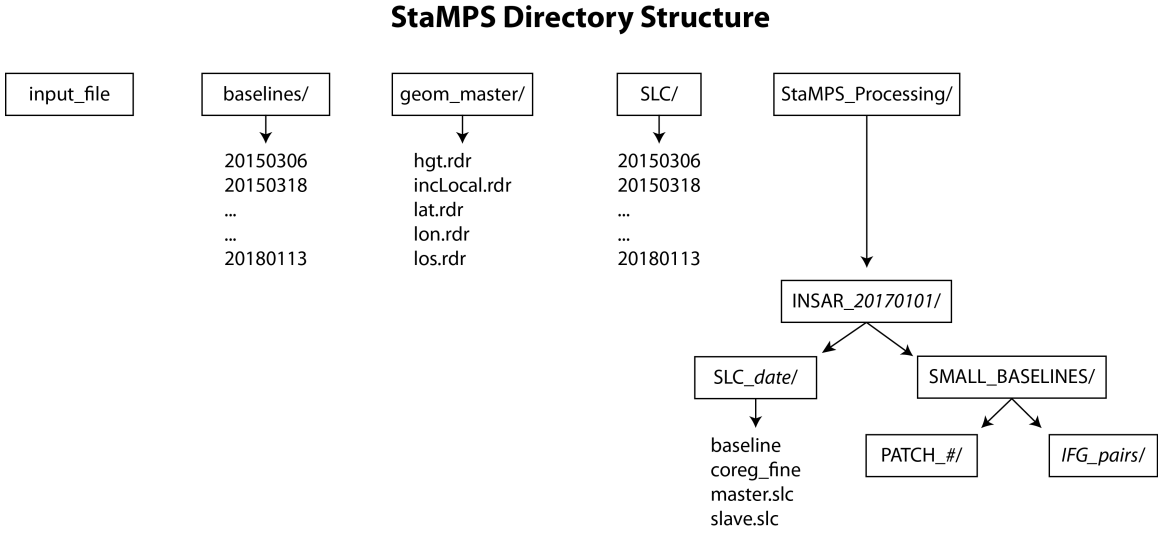

Figure 2.22: The working StaMPS directory structure showing the tree of main directories containing the SLCs baselines, SLCs, master gemoetry, and the main StaMPS processing directory and the main files contained within.

The main files that we need from ISCE that are put into the StaMPS working directory are three directories containing baseline information for each SLC (Figure 2.22, baselines/), the geometry of the master date chose (Figure 2.22, geom_master/), and the SLCs for each date (Figure 2.22, SLC/). In addition, an input file ('input_file') containing information about the co-registered SLCs is needed.

range_looks	40
aspect_ratio	4
azimuth_looks	10
lambda	0.056
slc_suffix	.full
geom_suffix	.full
source_data	slc_stack
slc_stack_path	/data3/north_bay_StaMPS_Ascending/SLC
slc_stack_master	20170119
slc_stack_geom_path	/data3/north_bay_StaMPS_Ascending/geom_master
slc_stack_baseline_path	/data3/north_bay_StaMPS_Ascending/baselines
overwrite	n

Figure 2.23: Sample input_file for creating the single master stack

Within the working directory executing the script *make_single_master_stack_isce* will make an INSAR_<master_date> folder with directories for each SLC date containing the SLCs and its associated files (Figure 2.22). Once this is completed, *mt_extract_info_isce* extracts information from the ISCE processing that will be used in the StaMPS processing. Examples of files include: wavelength and heading of satellite, the master acquisition date, the other image acquisition dates, the perpendicular baselines for each SLC, the SLC oversampling factor, and the length and width for all SLCs. In a series of MATLAB scripts, we load in information for each SLC (*ps_load_info*) and calculate (*sb_find*) the best possible network of interferograms using the requirements of having a maximum temporal baseline (Ddiff_max) of 1-year, a maximum perpendicular baseline (Bdiff_max) of 100 meters, and a minimum coherence (rho_min) of 0.35. These parameters were used as a longer temporal baseline can result in less coherence because more time has passed for the ground to change, and larger perpendicular baselines can cause different back-scattering characteristics over the entire study area, thus lower coherence over the study area. We plot all the possible interferograms to check that every date is connected to at least 2

other dates in the network (Figure 2.8). All possible combination of interferograms are listed in small_baselines.list. Once we have a network with the desired parameters, we execute *make_small_baselines_isce* which creates a subdirectory in the INSAR_<master_date> folder labeled SMALL_BASELINES and produces all small baseline interferograms within this folder (Figure 2.22).

For faster processing purposes, StaMPS grids the interferograms based on a number of patches in range and azimuth, specified. For our study, the ideal number of patches to divided each interferogram into was 105 patches in range and 20 in azimuth for a total of 2,100.

Processing all patches in the three swath frame would be computationally intensive and require months of processing. Since we are interested in surface creep, near the faults, we only process patches that are near the faults in question, ∼20 km across the faults (Figure 2.6). To do this, we modified the *mt_prep_isce* script to plot all patches, determine the patches along the fault, and output a final patch list for the Rodgers Creek and Maacama fault ('RCF.list'). The next step requires a patch file ('patch.list') that has all the patches to process, we swap this for our RCF.list. The final number of patches used in the descending frame is 213 and the ascending frame is 172.

The next step, *mt_extract_cands*, will extract the candidate pixels from each patch listed in the patch.list file and the final output is a folder for each patch in the patch.list file which contains all candidate pixels for that patch. Once this is done, StaMPS processing begins.

2.9 Appendix B: Along Fault LOS Offset Values

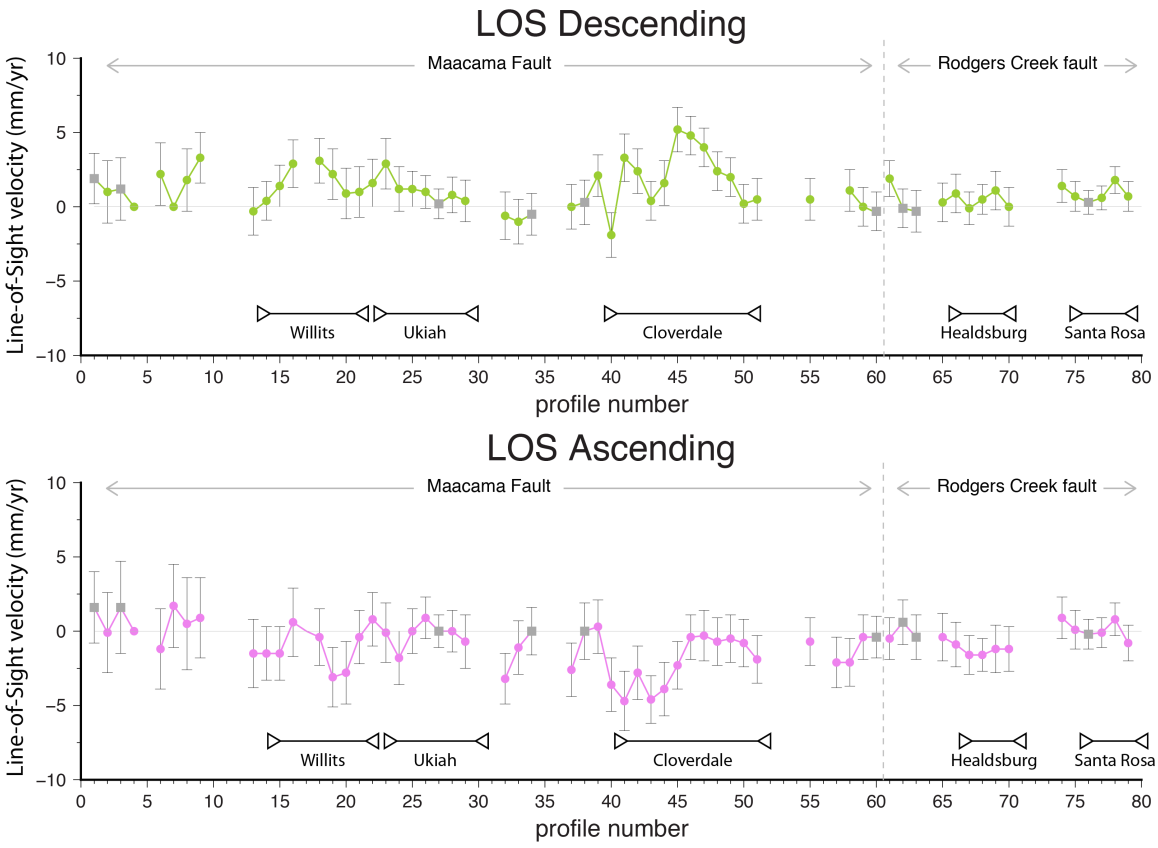

Figure 2.24: Line-of-Sight offsets for the descending (green, top) and ascending (pink, bottom) profiles along the fault. Gray squares indicate profiles that might not exhibit fault creep from LOS profile analysis. Blue circles are the alignment array total creep rate values from McFarland et al. (2018).

2.10 Appendix C: Profiles

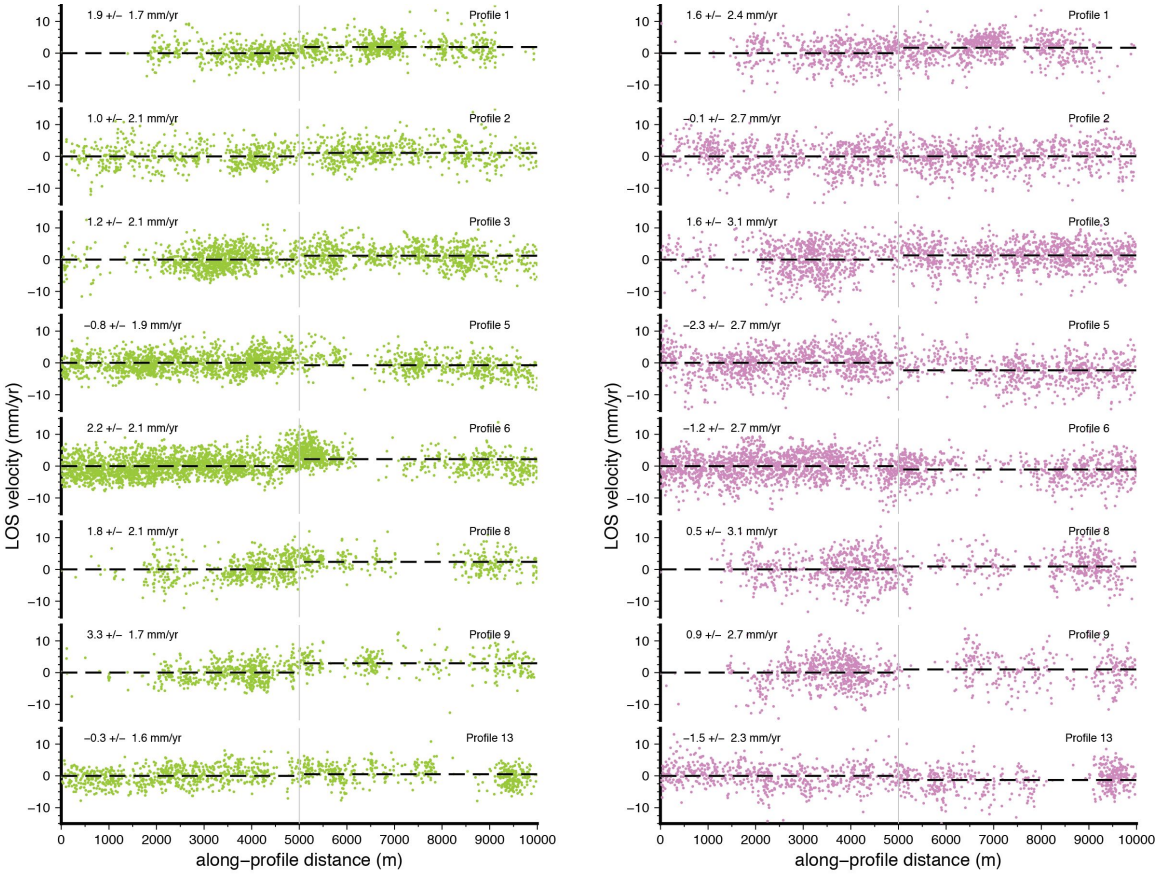

Figure 2.25: Profiles along the Maacama fault near the city of Laytonville. Profiles 1, 2, 3, 5, 6, 8, 9, 13.

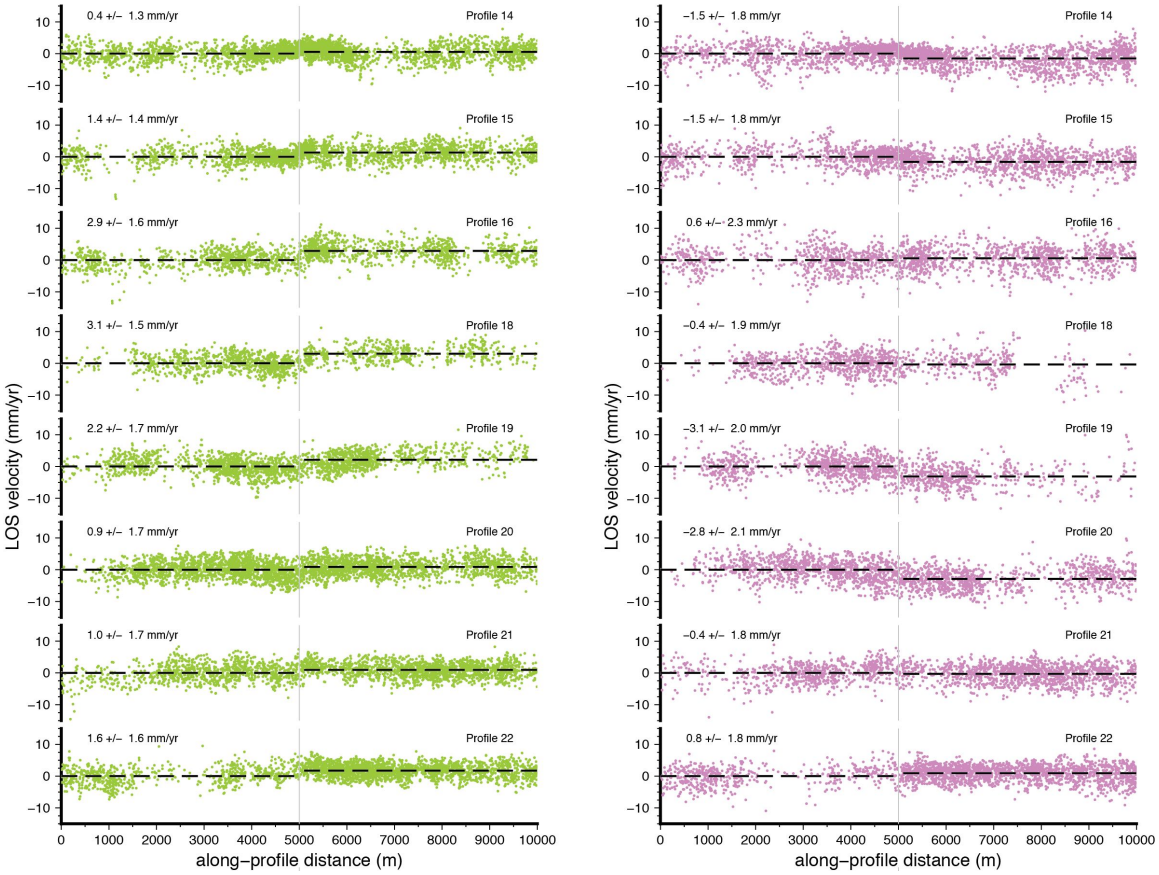

Figure 2.26: Profiles along the Maacama fault near the city of Willits. Profiles 14-16, 18-22.

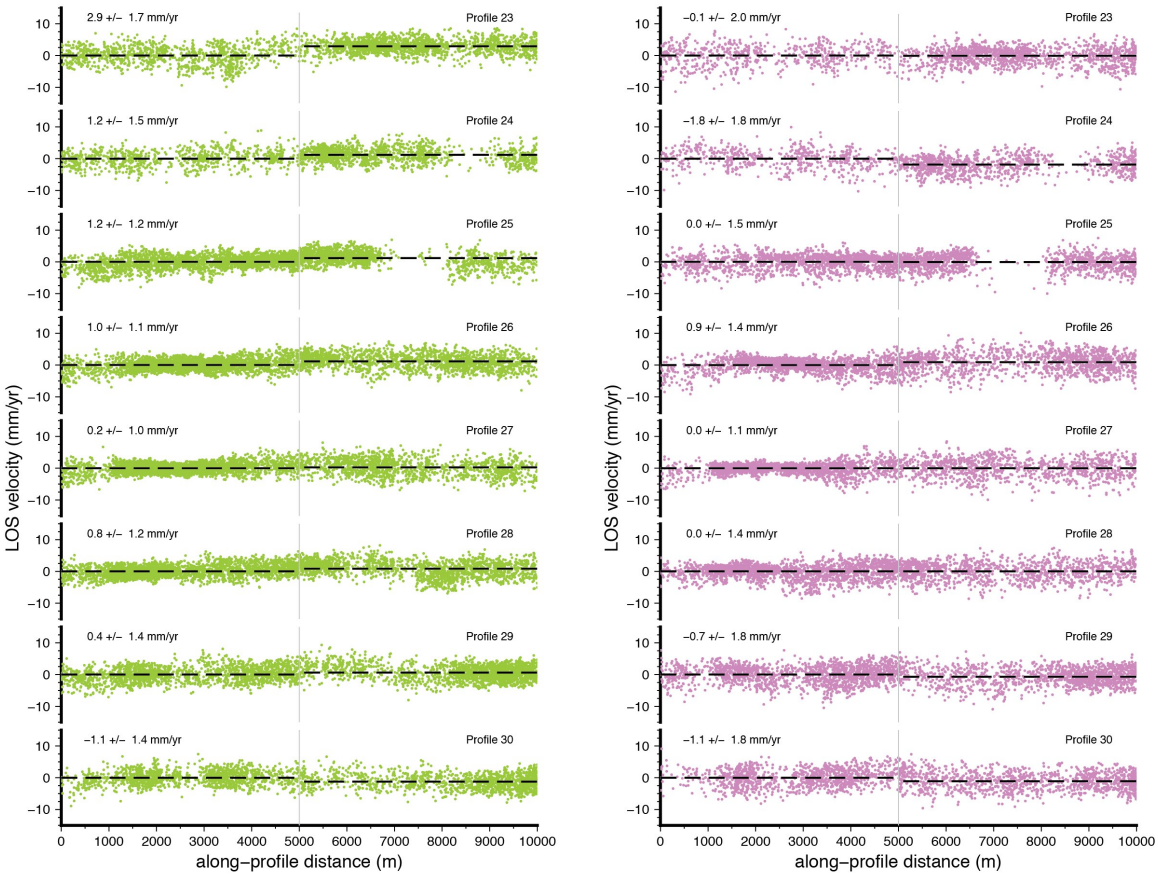

Figure 2.27: Profiles along the Maacama fault near the city of Ukiah. Profiles 23 - 30.

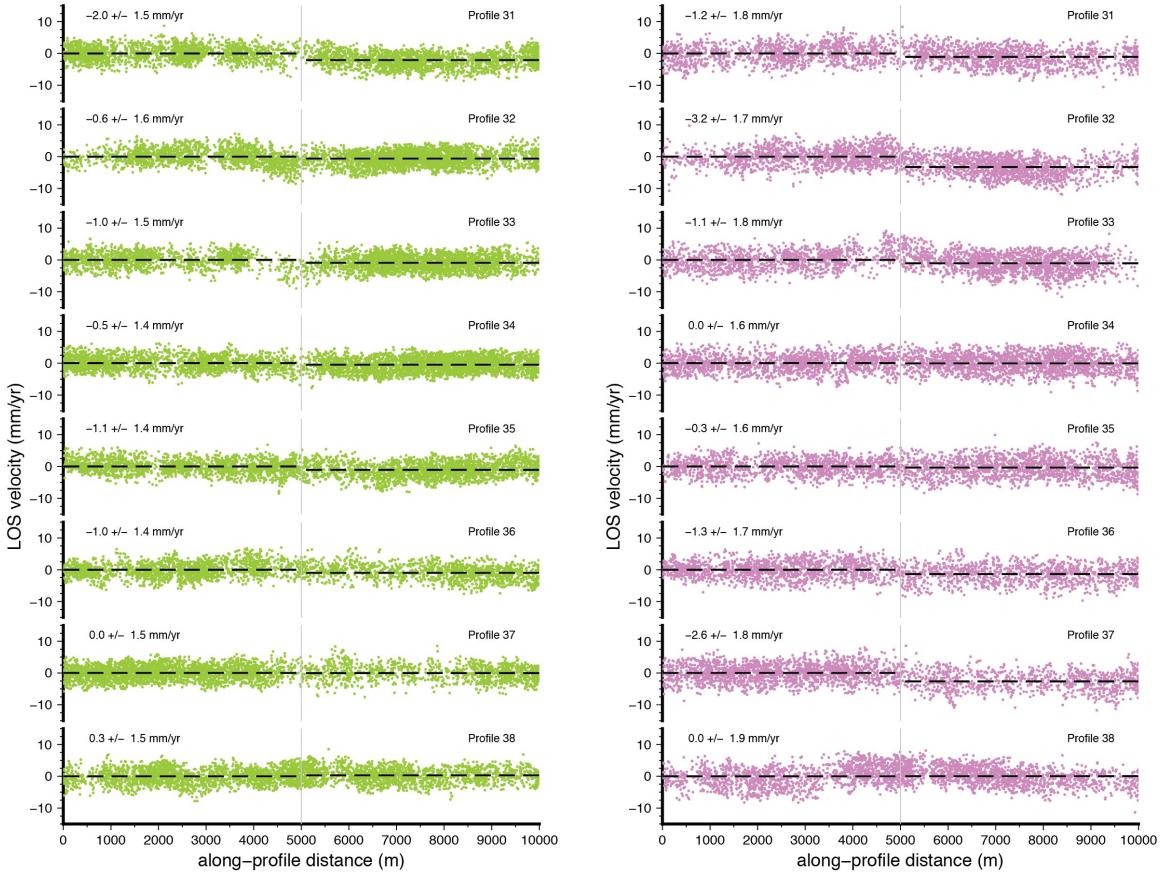

Figure 2.28: Profiles along the Maacama fault near the southern end of Ukiah. Profiles 31 - 38.

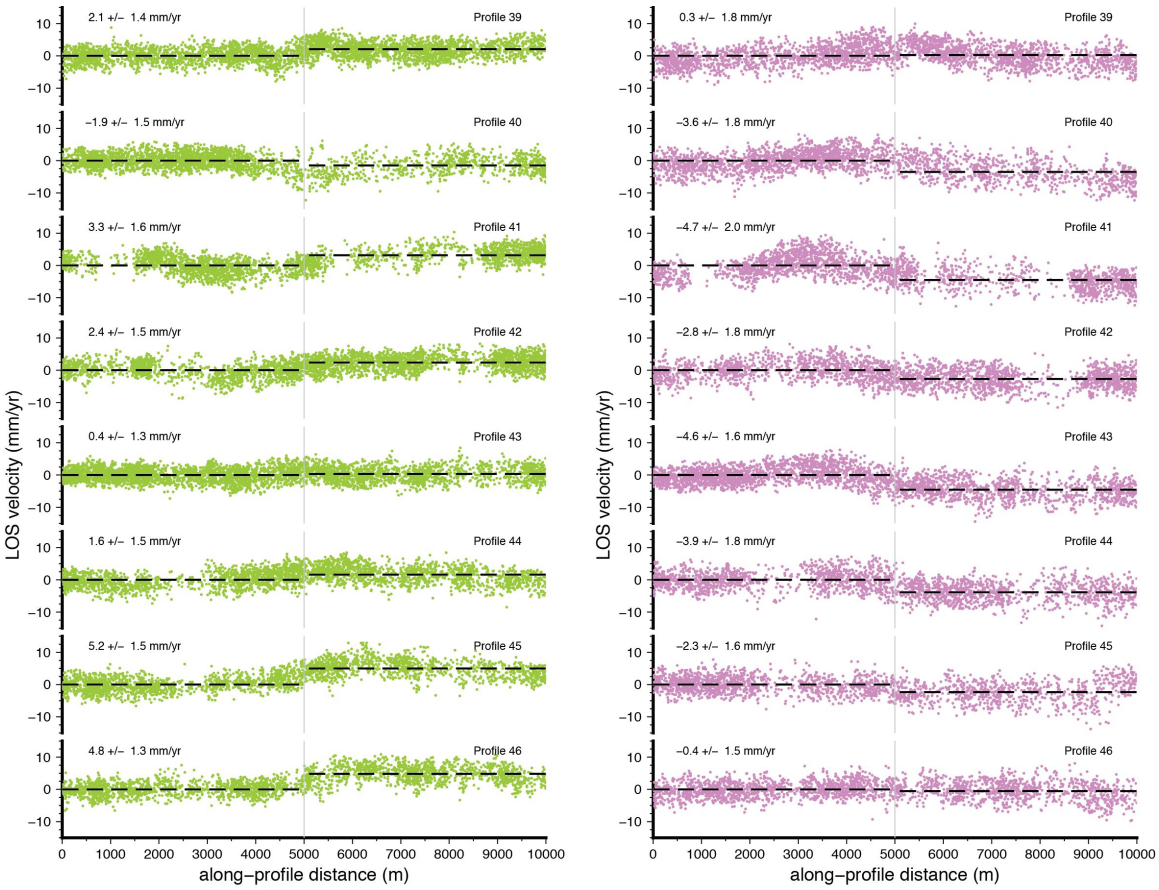

Figure 2.29: Profiles along the Maacama fault near the city of Cloverdale and to the west of the Geysers Geothermal Field. Profiles 39 - 46.

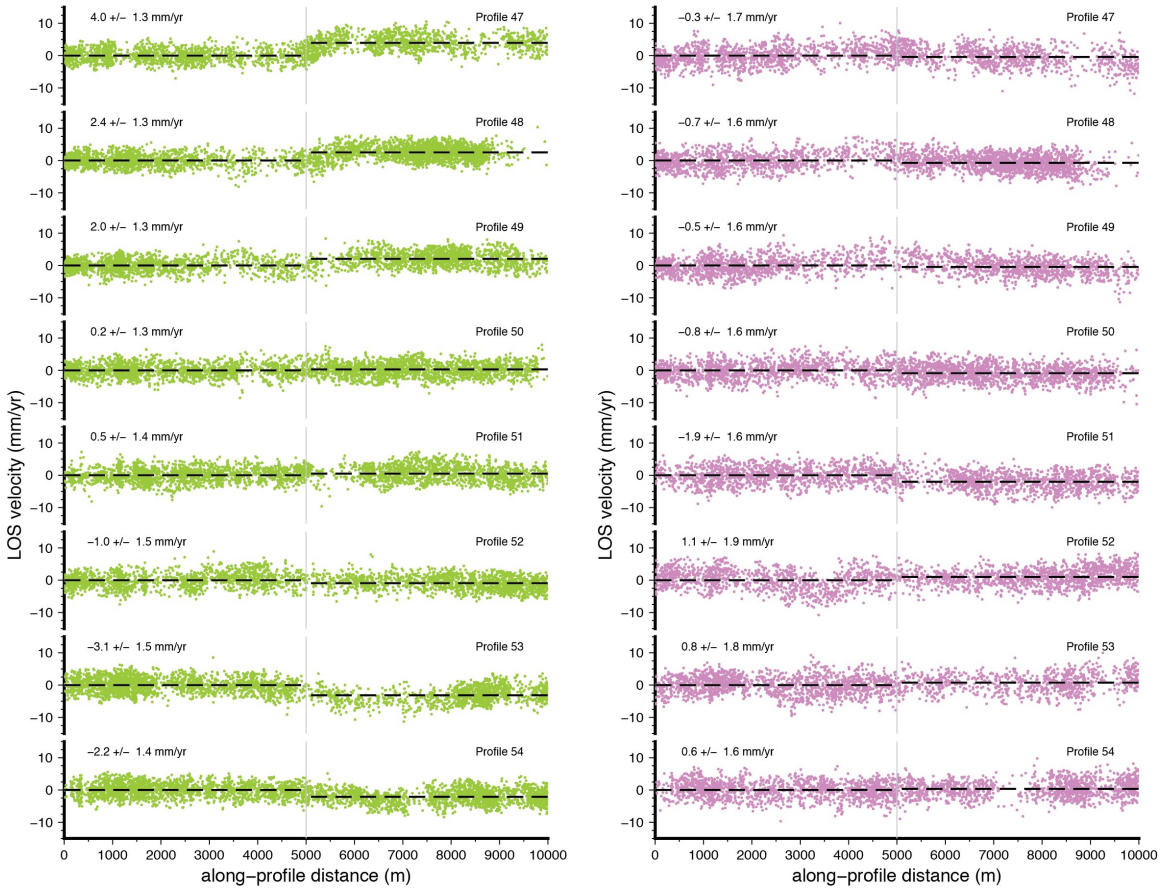

Figure 2.30: Profiles along the Maacama fault near the city of Cloverdale area and to the west of the Geysers Geothermal Field. Profiles 47 - 54.

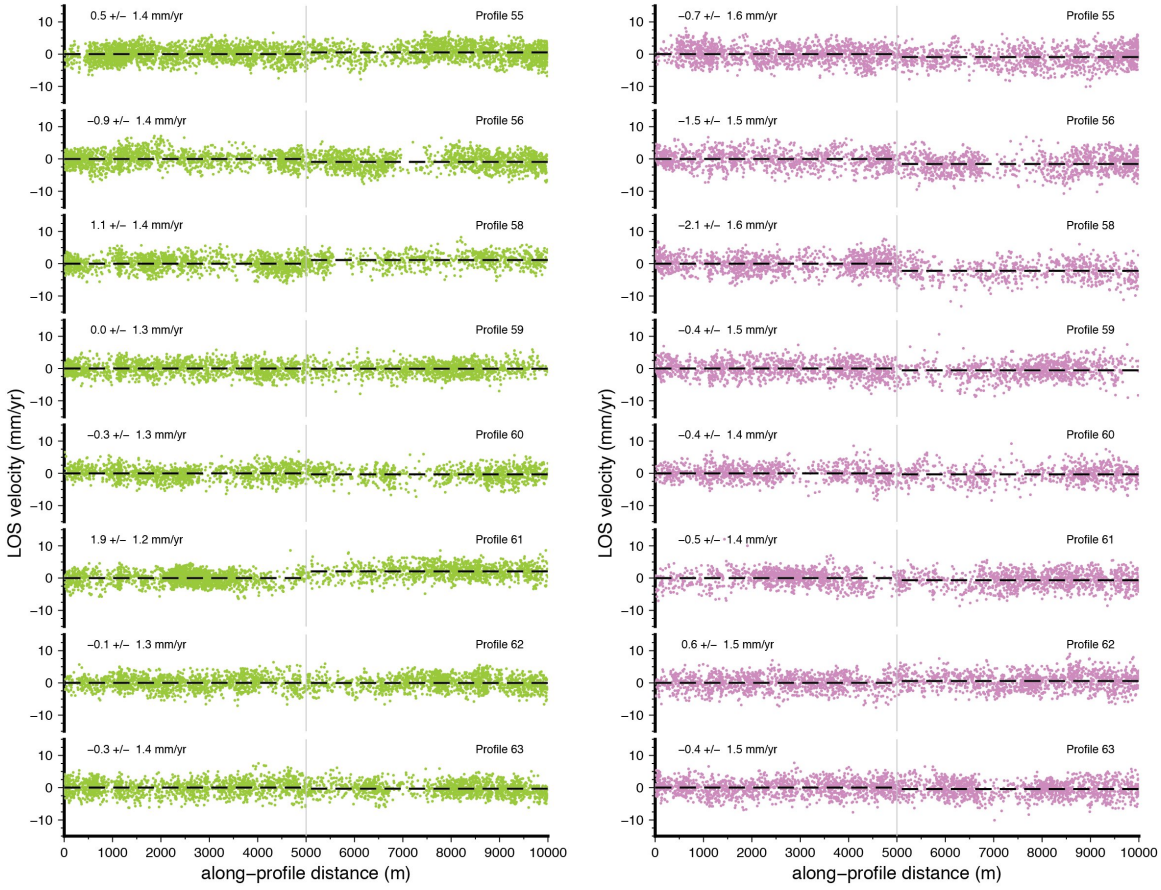

Figure 2.31: Profiles at the southern end of the Maacama Fault. Profiles 55 - 63.

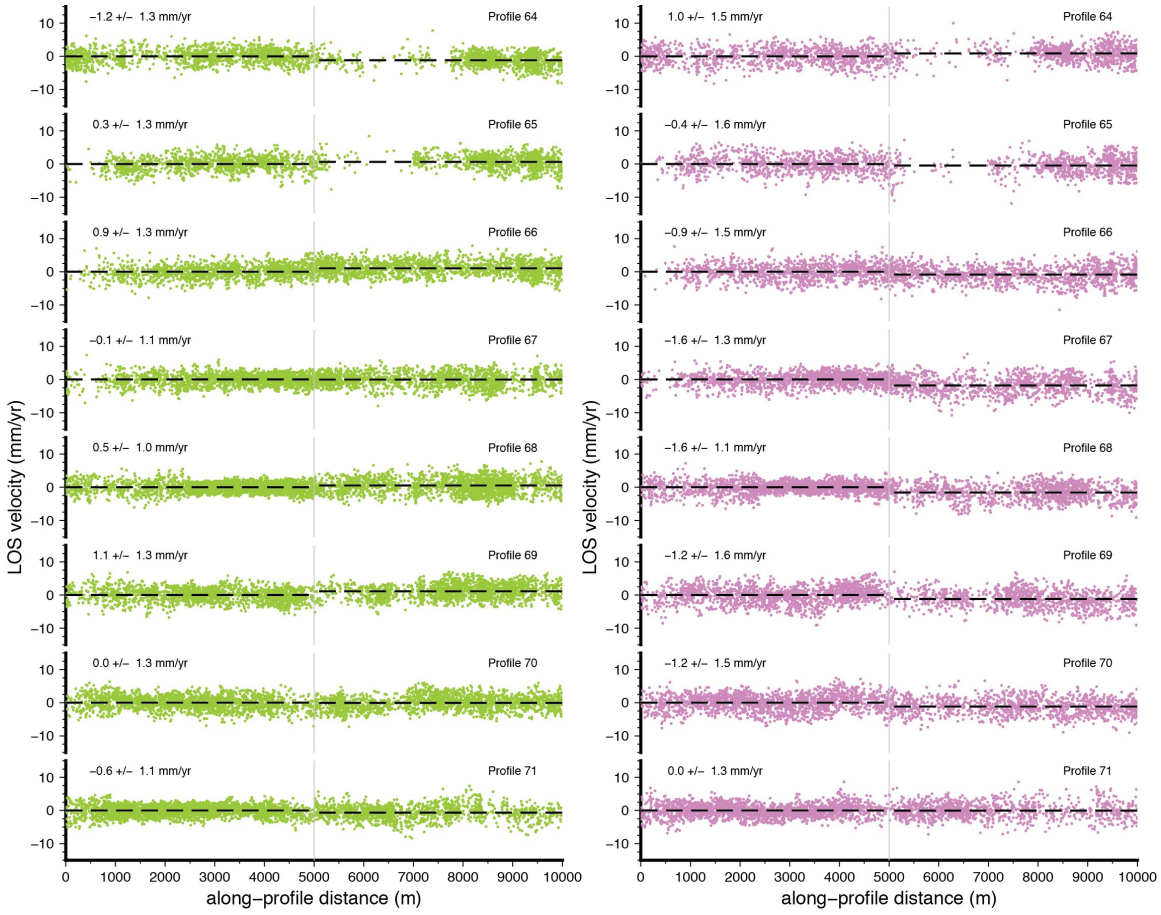

Figure 2.32: Profiles along the Rodgers Creek fault near the city of Healdsburg. Profiles 64-71.

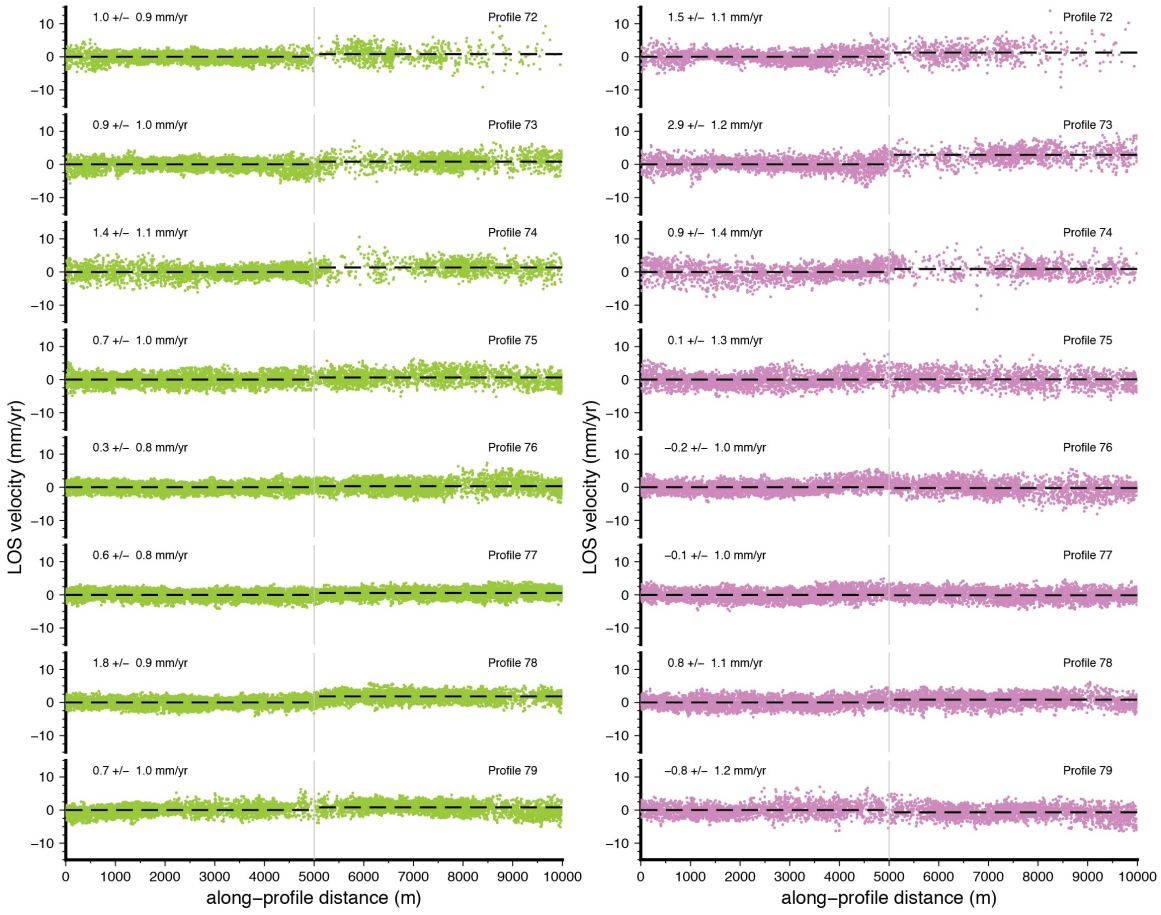

Figure 2.33: Profiles along the Rodgers Creek fault in the city of Santa Rosa. Profiles 72-79.

Chapter 3

Monitoring creep along the Hayward Fault using Structure from Motion

3.1 Introduction

The Hayward Fault, in the San Francisco Bay Area, has had twelve known earthquakes in the last ∼2000 years (Lienkaemper and Williams, 2007; Lienkaemper et al., 2010). The last known event was a M6.9 earthquake in 1868 with a mean slip of 1.9 ± 0.4 m (Yu and Segall, 1996) and an estimated rupture length of 45–60 km, approximately from Berkeley to Fremont (Lienkaemper and Galehouse, 1998). Since then, there have been no M6.5+ earthquakes on the Hayward fault and instead, due to fault creep (aseismic slip of the fault), the fault has accumulated strain at a slower rate compared to a locked fault. There are many studies documenting the creep rate along the entire fault length from near-field measurements using creepmeters and alignment arrays (e.g., Bilham et al., 2009; Lienkaemper et al., 2014; McFarland et al., 2018) to far-field measurements using remote sensing techniques such as GPS and InSAR (e.g., Schmidt et al., 2005; Bürgmann et al., 2000). The rate of fault creep varies along the fault from ∼ 2.6 mm/yr to ∼ 7.9 mm/yr; the highest creep rates being located at the southern end of the fault (Lienkaemper et al., 2014, Figure 3.1). For the cities that lie along the fault, fault creep can cause ongoing problems to man-made infrastructure such as fences, buildings, and sidewalks. Cities go through constant repairs of such infrastructure for the safety of the citizens, including realignment of curbs (e.g., Lin, 2016), and buildings built across the fault are deemed unsafe due to infrastructure flaws (e.g., Hayward's abandoned City Hall built in the 1930s (Stoffer, 2008) and the University of California, Berkeley's Memorial Stadium (Radbruch and Lennert, 1966; Doolin et al., 2005)). For scientists, monitoring offset features allows us to document the expression of fault creep at the surface in an urban setting. Here we monitor offset curbs thought to be

associated with fault creep to firstly, document how the urban environment accommodates fault creep and secondly, to define the main zone/width of deformation occurring along the creeping Hayward fault.

We monitor fault creep from offset man-made features within the city of Fremont, CA, which is located along the segment of the Hayward fault where the highest creep rates are observed (Schmidt et al., 2005). We monitor curb offsets as they are easily visible along streets where they become increasingly more noticeable over the years due to ongoing fault movement. This study will provide a location-specific measurement of fault creep that is being expressed in an urban setting.

There are 36 offset curb sites used for this study that were previously identified and monitored by Funning et al. (2010) from 2009 to 2011. Sites are shown in Figure 3.1 and the location and description for each site are listed in Tables 3.1-3.3. Funning et al. (2010) used a camera setup on a tripod 1 meter above the curb offset, aligned horizontal to the curb, centered on the offset, and leveled with the ground, in order to avoid problems of parallax. Two photos were taken; one with a compass, handheld GPS, and a tape measure and one without. Then, they manually measured the offset curb with a ruler.

In this study, we instead use the 'Structure from Motion' (SfM) photogrammetric technique to monitor 3D displacement of each curb from 2015 to 2018. SfM can render the 3D structure of an object from multiple overlapping, offset photographs taken around the object in question (Figure 3.3). SfM is not a new method but with the improvement in computing power and development of computationally efficient and user friendly software has made SfM more widespread and its application to geoscience useful and effective (Ull-

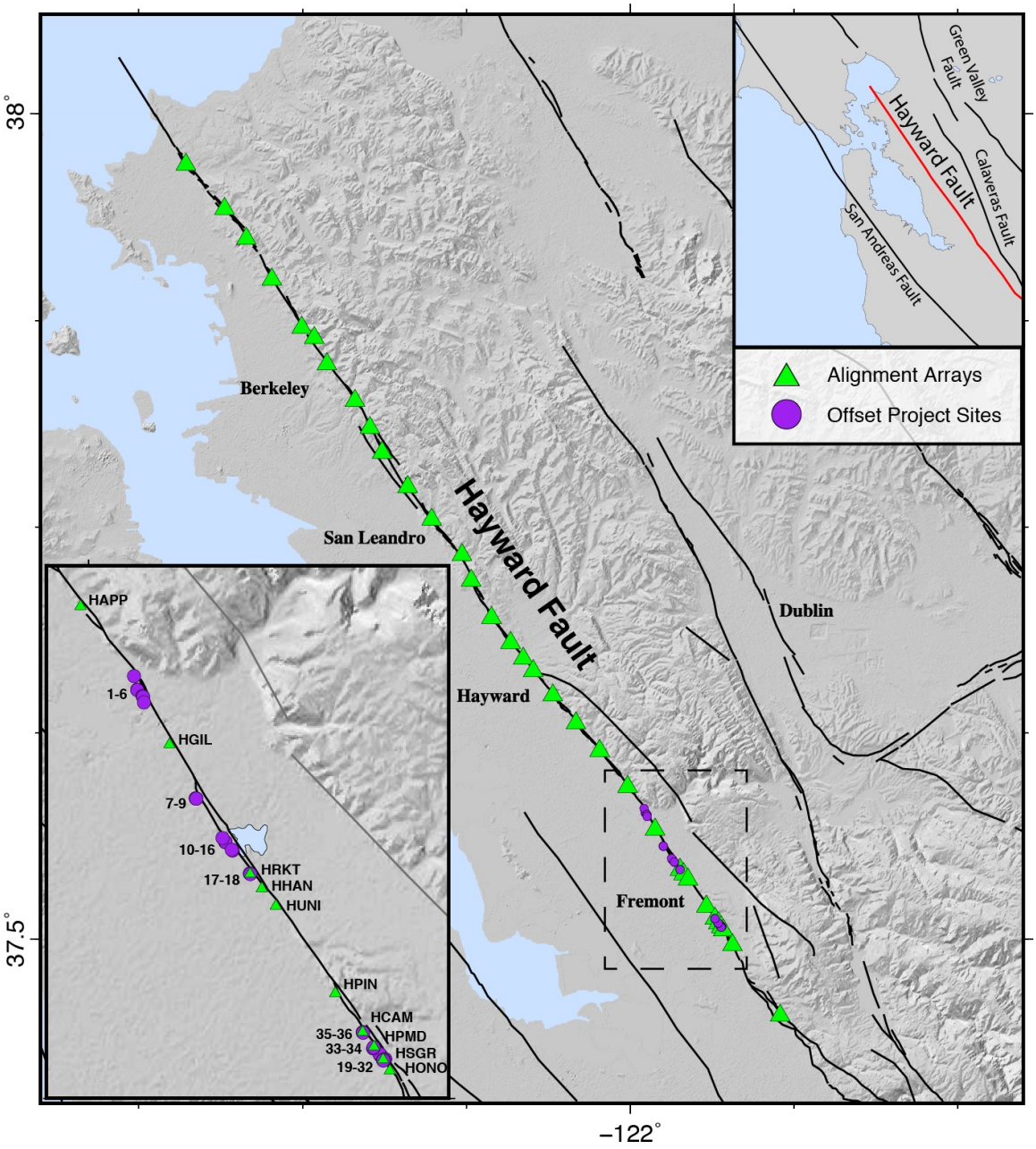

Figure 3.1: Map of the Hayward fault and the distribution of alignment arrays (green triangles) and the locations of monitored offset curbs in Fremont, CA (purple circle). Dashed box shows area of the offset curbs shown in bottom inset map. Top inset map: Main faults (Black line) in the San Francisco Bay Area, including the Hayward fault (red line). Bottom inset map: Zoomed in map show the offset curb locations, alignment arrays and the Hayward fault (black line) and the Mission and Chabot faults (gray lines).

Figure 3.2: (A) The original setup to photograph an offset curb in 2009–2010 (after Funning et al., 2010) in which the camera is centered, leveled, and positioned 1 meter above the curb. Two photographs were taken; (B) one with a tape measure for scale, a portable GPS, and a compass and (C) one with nothing.

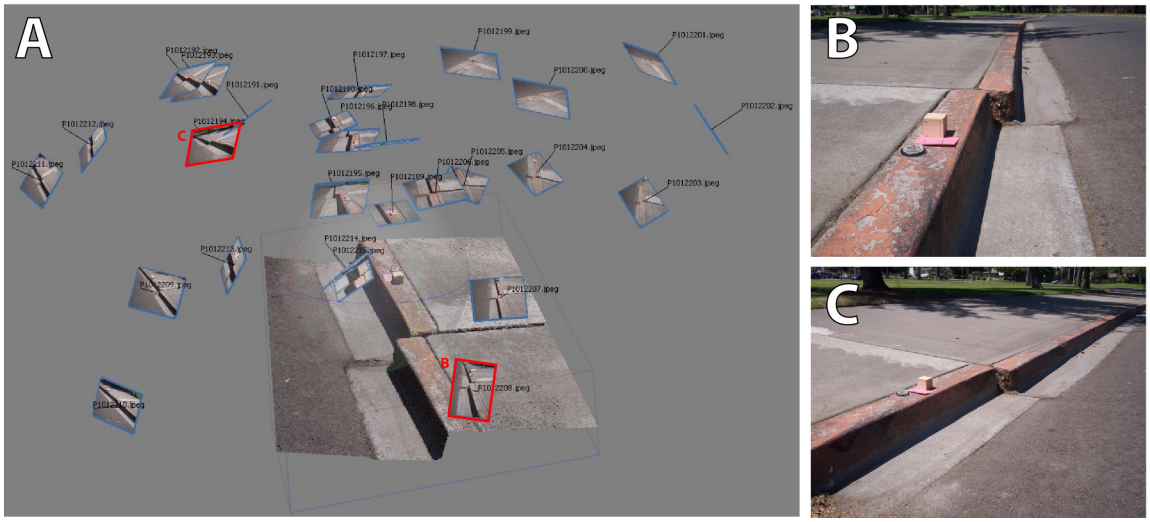

Figure 3.3: (A) Setup for the new method to monitor offset curbs using Structure from Motion. The only requirements are multiple photographs taken from a wide array of positions and vantage points. The pictures in the blue boxes around the 3D point cloud show the location and orientation of the camera for each specific photograph. The two pictures in the red boxes show the orientation of the two pictures in B and C.

man, 1979; Westoby et al., 2012). The benefit of using SfM is that it eliminates the need to carefully align and level the camera and allows for the observation of 3D deformation, not just 2D deformation. The main requirements are to have overlapping photographs around the offset curb that are captured from a wide array of positions, at multiple vantage points (Figure 3.3, right), and an object with a known vertical and horizontal length to calibrate the scale of each photograph.

A main use of SfM is for topographic differencing which allows for the quantifiable observation of active deformation/morphology changes and Iterative Closest Point (ICP) analysis that enables 3D displacement estimation. There have been many applications using SfM that include geological applications such as cliff (Warrick et al., 2016; Ružić et al., 2014) and river morphology (Javernick et al., 2014; Woodget et al., 2015), monitoring slow

moving landslides (Lucieer et al., 2014), volcanic activity (Carr et al., 2018; Ontiveros and Delgado-Granados, 2015), archaeological applications to measure the erosion of fossilized footprints (Zimmer et al., 2018), and active tectonics applications such as measuring fault zone topography (Johnson et al., 2014). Here we will apply the SfM approach to generate 3D point clouds/models from different years and then align them to estimate the 3D displacement of each offset curb, and ultimately estimate surface creep rates.

3.2 Methods

3.2.1 Construction of 3D Model: Workflow

Image Acquisition

Photographs of most curbs were taken every year from 2015 to 2018 (Figure 3.4) depending on the accessibility of the site (e.g., some sites were not photographed on some visits due to parked cars). A camera with a fixed focal length lens was used. Camera settings that are most ideal for SfM applications are a fast shutter speed as possible to minimize blur and a narrow aperture which allows for the entire photo to be in focus. Photos were taken during all weather conditions but the most ideal conditions are during overcast skies due to the lack of shadows (e.g., Figure 3.4). When photographing, we sweep the area within 2 to 3 meters of the offset clean of any debris. A note card with the site number, a compass, and an object for scale is positioned next to and photographed with the curb offset. The object used for scale developed over the years; from 2015 to 2017, a tape measure, compass, or broom was used for scale but defining a vertical scale with these objects was difficult, so for later visits a 5 cm cubic block was used instead, starting in 2018. Photos were taken within

Figure 3.4: Variations in curb photo setup and weather conditions. In 2015 and 2016 we used a tape measure, compass, and brush. In 2017 and 2018 we used a compass and 5 cm block. The overcast weather conditions in 2015 and 2018 show more defined details where as the sunny conditions in 2016 and 2017 which introduces unwanted shadows.

3 to 4 feet of the offset at high and low vantage points, all around the offset curb (Figure 3.3). The number of photos taken varied for each site ranged between 18 to 60 photos with an average of 32 photos per site. The acquired images were then aligned and a 3D point cloud model were produced using Agisoft PhotoScan Pro, a SfM multi-view stereo software.

Table 3.1: Description and locations of the northern sites 1 to 9.

Site	Lattitude	Longitude	Description
1	-121.9885	37.57675	Northern offset curb (out of 2) on Hillview Drive, that is part the 290 Hillview Drive driveway. Offset is where the '290' address is painted on the left/northern side of driveway.
2	-121.9885	37.57667	Southern offset curb (out of 2) on Hillview Drive, that part of the 320 Hillview Drive driveway. Offset is on the left/northern side of driveway, where there is a pipe hole on side of curb.
3	-121.9893	37.57927	Sidewalk paving on Niles Blvd. that is opposite to the driveway entrance to the Unity Church of Fremont.
4	-121.9873	37.57554	Northern offset curb on Bodily Ave. in front of 37166 Bodily Ave, on the right/eastern side of their path to front door. Note: usually car parked in front.
5	-121.9872	37.57539	Southern offset curb on Bodily Ave, on the property (fence) line between 37171 and 37189 Bodily Ave and across the street from site 4. The pavers are usually popping up or missing where as the surrounding pavers are not.
6	-121.987	37.57435	Offset underneath a cherry blossom tree and near the right/northern end of the red brick wall. Across the street from 448 D. Street
7	-121.9748	37.55635	Taken out due to BART parking being rebuilt and all curbs were taken out (none show offsets)
8	-121.9746	37.55629	Taken out due to BART parking being rebuilt and all curbs were taken out (none show offsets)
9	-121.9746	37.55626	Taken out due to BART parking being rebuilt and all curbs were taken out (none show offsets)

Table 3.2: Description and location of the central sites 10 to 18.

Site	Lattitude	Longitude	Description
10	-121.9678	37.54816	NorthEast offset (out of 4) on Sailway Drive, in between the Fremont Teen Center parking lot and the light post. This is a curb site.
11	-121.9678	37.54817	NorthWest offset (out of 4) on Sailway Drive, in between the Fremont Teen Center parking lot and the light post. This is a curb site where it has the letters 'GV-XX' spray painted on the left side of offset.
12	-121.9677	37.54809	Southeast offset (out of 4) on Sailway Drive, before the Fremont Teen Center parking lot. Sidewalk slab associated with the Earthquake Walk signage. This is a sidewalk site and is the largest of the 4 offsets.
13	-121.9677	37.54811	Southeast offset (out of 4) on Sailway Drive, before the Fremont Teen Center parking lot. Sidewalk slab associated with the "Earthquake Walk" signage. This is a sidewalk site.
14	-121.9684	37.54889	In the Fremont Teen Center parking lot, off Sailway Drive on the northern side of the roundabout (painted red). Near the pathway entrance into Fremont Park. - Crack (no precut) in curb is the offset.
15	-121.9661	37.54654	Southern offset (out of 2) at the parking lot entrance to the Fremont Senior Center where there are two associated curbs.
16	-121.9663	37.54668	Northern offset (out of 2) at the parking lot entrance to the Fremont Senior Center. Located in front of the Handicap parking.
17	-121.962	37.54222	Northern offset (out of 2) on Rockett Drive, near 3011 Rockett Drive.
18	-121.9619	37.54212	Southern offset (out of 2) on Rockett Drive, near 3004 Rockett Drive.

Table 3.3: Description and location of the southern sites 19 to 36.

Site	Lattitude	Longitude	Description
19	-121.931	37.50798	Northern offset (out of 2), across the street from 44951 Gardenia Way, next to the Arroyo Agua Caliente Park.
20	-121.9311	37.50794	Southern offset (out of 2), across the street from 44951 Gardenia Way, next to the Arroyo Agua Caliente Park.
21	-121.9312	37.5081	Near the junction of Ivy Way and Gardenia Way, just to the left of the third bush (counting from the left (when facing offset)/South. There is a slight crack near the inner corner of the left side of the curb.
22	-121.9312	37.50821	Eastern offset (out of 2) in front of 1912 Ivy Way. A large gap that extends across entire sidewalk, filled in with asphalt. It is to the east of the 5th bush, counting from the right (when facing offset)/West.
23	-121.9313	37.50823	Eastern offset (out of 2) in front of 1912 Ivy Way. A large gap that extends across entire sidewalk, filled in with asphalt. It is to the east of the 5th bush, counting from the right (when facing offset)/West.
24	-121.9313	37.50831	Western offset (out of 2) in front of 1903 Ivy Way, it has the largest gap that extends the entire sidewalk where it is filled in with asphalt.
25	-121.9314	37.50834	Eastern offset (out of 2) in front of 1903 Ivy Way, the next through going crack to the east of Site 24.
26	-121.93	37.50734	Eastern offset curb, in front of site 27, on north side of S. Grimmer Blvd. near the wooden electrical post.
27	-121.9301	37.50733	Offset pathway on S. Grimmer Blvd. near the wooden electrical post.
28	-121.9305	37.50714	Offset pathway on South side of S. Grimmer Blvd., southern side of pathway that is across the street from site 29.
29	-121.9305	37.50718	North-Western-most offset curb (out of 3) on S. Grimmer Blvd, right next to the painted arrow for the painted bicyclist on the pavement.
30	-121.9305	37.5072	North-Middle offset curb (out of 3) on S. Grimmer Blvd, ~1 m East of painted bicyclist on the pavement.
31	-121.9304	37.50722	North-Eastern-most offset curb (out of 3) on S. Grimmer Blvd, ~12 m West of light post and 8 m East of painted bicyclist on the pavement.
32	-121.9305	37.50709	Offset pathway on South side of S. Grimmer Blvd., northern side of pathway that is across the street from site 29.
33	-121.9329	37.50936	Southern offset curb at the junction of Parkmeadow Drive and Winding Lane, across the street from 44757 Parkmeadow Drive. The sidewalk shows large signs of uplift, in front of a tree.
34	-121.9328	37.50957	Northern offset, in between 44743 and 44757 Parkmeadow Drive. There is a spray painted arrow and '14' on the left side of the curb offset and the right side has the corner of the offset curb broken off. There is also, in red spray paint, 'GV-VI' on the curb.
35	-121.9353	37.51242	Northern curb, infront of 44389 Camelia Drive where the sidewalk is filled in the asphalt with words spray painted in white on the curb.
36	-121.9353	37.51231	Northwest curb in between 44398 and 44380 Parkmeadow Drive where the left side is a darker color than the right side of the offset.

Structure from Motion-Multi-view Stereo (SfM-MVS)

Structure from Motion is an image based modeling method which attempts to recover camera parameters, orientation, and the camera position (i.e., where the camera was when the photo was taken) from a set of 2D photos to infer the 3D scene structure from a set of differently oriented photos of an object (Ullman, 1979). The main difference between SfM and traditional photogrammetry is the ability of SfM to process overlapping photographs taken from random viewing angles and still create a 3D model whereas the latter needs lines of parallel, overlapping images (Fonstad et al., 2013). This ability to have different viewing angles is due to the Scale Invariant Feature Transformation (SIFT) (Lowe et al., 1999) which allows for the matching of features (i.e., distinctive areas of an image that are identifiable in more than one image) in images despite the change in camera orientation and distance from the object. SIFT is an automated image matching algorithm that can identify physical features in the images through the detection of image brightness and color gradients (Lowe et al., 1999). The use of the photographs brightness and color variations instead of pixel properties, used in traditional photogrammetry, allows for the use of images of mixed resolution. One requirement, however, is that each physical point on the 3D model/point cloud must be present in multiple photographs in order to be rendered.

There are three steps to SfM: (1) detecting the most prominent features in each image using SIFT, (2) matching these features between all images, and then (3) using the matched features to find the camera position and determine the camera parameters. This includes finding the positions of all camera locations, the orientations of all images, and calculating the 3D coordinates for each feature point, all simultaneously – this is called

a bundle adjustment (Bemis et al., 2014). This will create a sparse 3D point cloud of all feature points that represents the main structure of the object within a local, relative coordinate system. This point cloud is sparse because it is using only robust features that match between images. The multi-view stereo (MVS) method is used to densify the point cloud by searching over a grid of pixels to identify the best pixel matches between all images for each grid cell (Furukawa and Ponce, 2010). The output is a dense point cloud which can have two to three orders of magnitude more pixels than the sparse point cloud (e.g., 20,000 points to 9,000,000 points). The final product is in a relative coordinate system. Agisoft Photoscan can transform the 3D point cloud into an absolute coordinate system if ground point controls are provided such as from GPS locations, known locations of the camera for each image. For the purpose of our study, we used the height/length scale object (i.e., 5 cm wooden block) as ground control points to define a local x, y, z coordinate system. There are uncertainties in the model due to model warping at the edges of the model, a result of less photographs observing the 'far field'.

For our study we photograph ∼3 meters around, centered on the offset sidewalk but only measure distances ∼1 meter across the offset which helps account for any edge of model warps/defects.

3.2.2 Alignment of Point Clouds to Measure Curb Movement

Once two dense point clouds from two different dates are produced for a curb offset, we use the CloudCompare software to align two point clouds together and then estimate the displacement that occurred between the two acquisition dates.

3D Point Cloud Alignment

With the right-lateral displacement of each curb offset oriented on the right side of the model, we align the left side of the curb offset as the goal is to measure the displacement between the point clouds on the other side of the offset. There are two steps to aligning data from the same curb from two different dates; a manual rough alignment and fine alignment using the Iterative Closest Point (ICP) method (Chen and Medioni, 1992). The first step is the rough alignment of the left side of the curb offset where we manually pick points, called 'anchors', that are visually the same between each point cloud. We use both color and texture of the point clouds to make our picks. We choose at least 6 anchors in the horizontal plane and at least 2 points in the vertical plane. The distribution of anchors also needs to cover a wide enough area that the point cloud is aligned both close to and far from the offset. An example of a candidate anchor is the corner of a gravel clast within the cement of the sidewalk and/or curb (Figure 3.5). The rough alignment will translate and rotate one point cloud into the other to find the best fit to all anchors.

Once the two point clouds are roughly aligned, we cut out features in each point cloud that have the potential to be different from each acquisition. Examples of features to remove include plants, grout lines between cement blocks, the note card with the site number, and the reference scale. We also narrow the focus of the point cloud and cut out everything more than $\sim$2 meters from the offset on each side.

With the two point clouds roughly aligned, the second alignment step uses the Iterative Closest Point (ICP) algorithm to fine tune the matching of the two point clouds where the rough alignment is required. The ICP method is able to align two irregular point

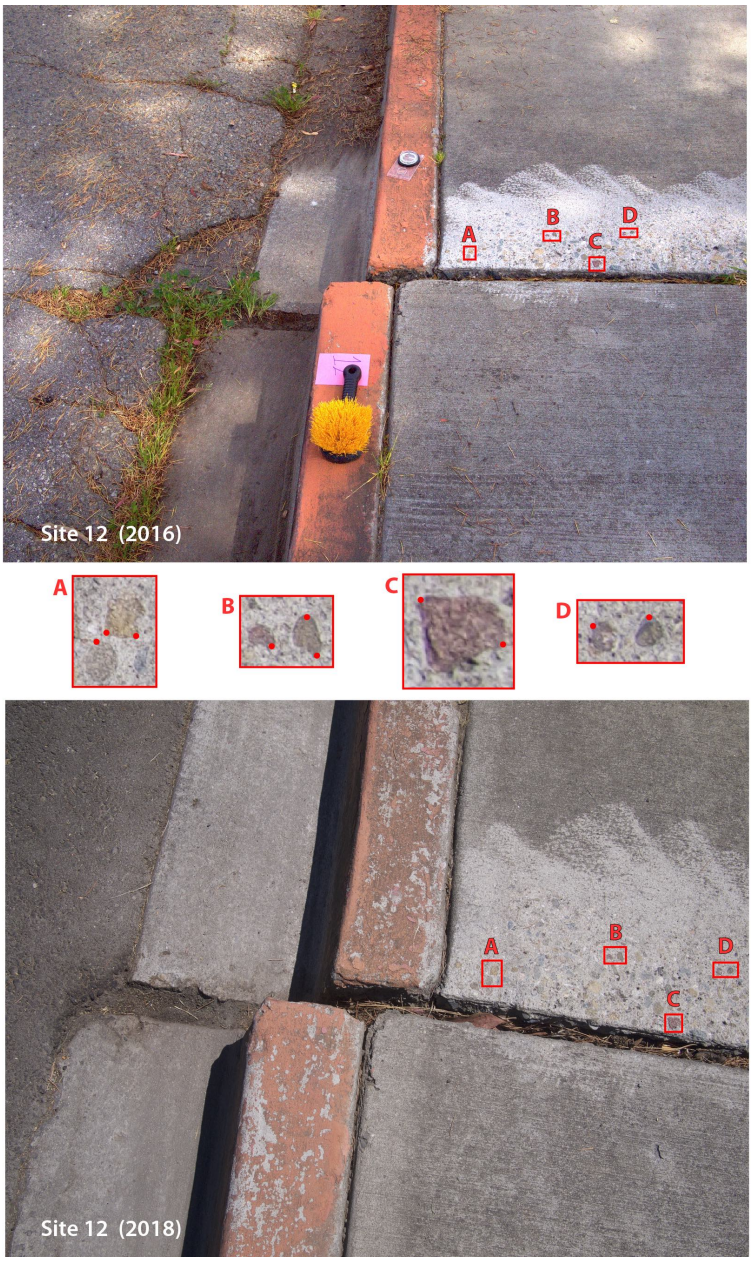

Figure 3.5: Example of anchors chosen for site 12 from 2016 and 2018 photos. Red boxes within photos show distinct gravel clasts within the cement in both dates. Zoomed in boxes A, B, C, D show points (red dots) chosen as the anchors between the two point clouds used to manually align the point clouds.

clouds by minimizing the distance between two point pair distances with an iterative rigid body transformation consisting of a translation and rotation. This process repeats, trying to minimize the mean square error between all paired points until a a local minimum is met (Nissen et al., 2012).

In order to use the ICP method to align only one side of the offset, we first separate the left and right side of the offset, then apply the ICP method to finely align the left side only. Cloud Compare gives the rigid body transformation matrix used to finely align the left side which we then apply to the right side of the offset. The final product is two point clouds in which the left side of the curb is fully aligned and overlapping. If there was any movement between the two dates of acquisition, the two point clouds on the right side will not be overlapping and the different position of the point clouds can be measured. This difference in the two point clouds is the displacement of the curb over the time interval which we interpret as the local offset due to fault creep for the curb.

Measurement of Curb Displacement

The differences between the two point clouds are measured within CloudCompare which decomposes the results into three orthogonal directions: curb vertical, curb parallel, and curb perpendicular directions (Figure 3.6). An example of the difference between two point clouds for each direction of movement is shown in Figure 3.7 for site 4 spanning 2017 to 2018. For each curb direction, we plot a histogram showing the range of spatial differences between the two point clouds, shown on the right of each color bar in Figure 3.7. The highest peak corresponds to the largest difference between the 3D models and the width of the peak defines the measurement uncertainty. A normal/Gaussian distribution curve is fit

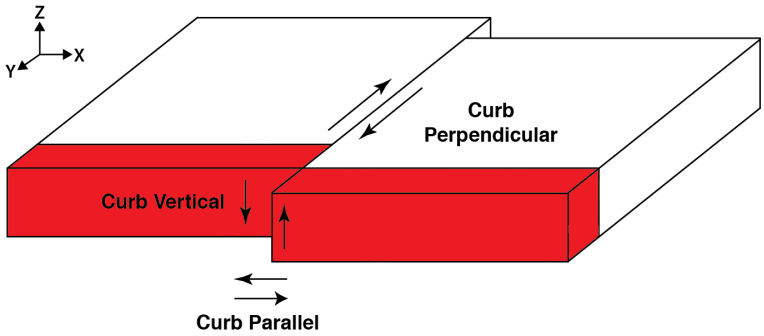

Figure 3.6: Directions of curb movement where curb curb-parallel movement is the defined x-direction, curb-perpendicular movement is the y-direction, and curb-vertical movement is the z-direction. Directions of x-, y-, z-axis arrows are in the positive direction.

to each peak value to obtain the mean and standard deviation of curb displacement in each direction (Table 3.5). This curb offset displacement is then divided by the time interval to obtain a curb offset rate (Table 3.6). The time interval is calculated by the number of days in between each acquisition date (mentioned in Results), taking into account that 2016 was a leap year and the value, in years, is shown in Table 3.5.

3.3 Results

We acquired photographs from 2015 to 2018 (in MM/DD/YYYY format: 12/20/2015, 02/26/2016, 01/26/2017, and 07/27/2018). Not all sites were photographed every year due to road access, safety, or weather conditions. Sites 7, 8, and 9 were not photographed at all due to offset curbs being demolished in 2015. A 3D point cloud was generated for every time each site was photographed and the point cloud densities are listed in Appendix 3.6. For each site, we measured the displacements from the longest time interval possible, up to three years. Other reasons for not using a specific year varied for each site such as; bad 3D

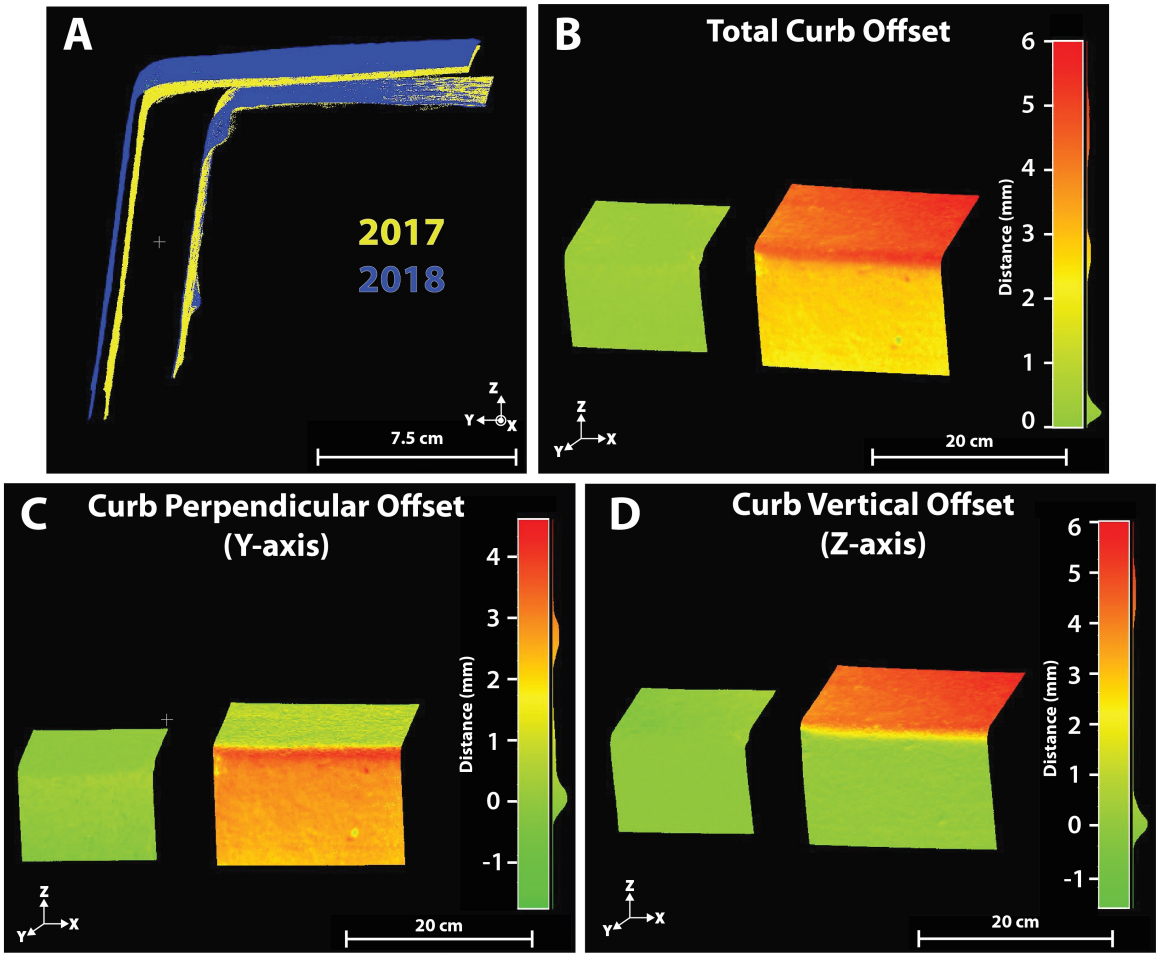

Figure 3.7: 3D model distance difference for site 4, spanning 2017 to 2018, showing the aligned point clouds (A) and that the 2018 point cloud (blue) moved up and out compared to the 2017 point cloud (yellow). For the total curb offset in all directions (B) – the left side (green) did not move (i.e., 0 mm) and the right side moved in the y- and z-directions. The total curb offset is decomposed into the curb-vertical (z-axis) movement (C) and curb-perpendicular (y-axis) movement (D). The curb-perpendicular movement (C) shows the right side moved a positive distance of ∼2.5 mm (red/orange), the curb-vertical (D) movement shows the right side moved a positive distance, upward, a total of ∼4.5 mm (red). Refer to Figure 3.6 for axes definitions.

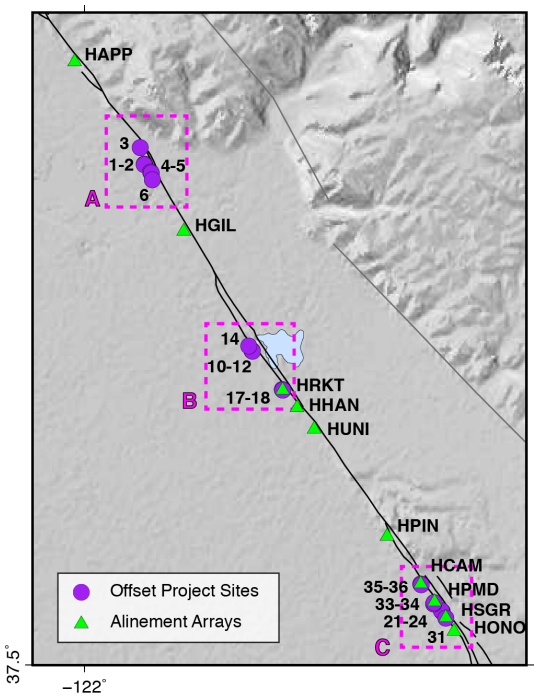

Figure 3.8: Map of sites that were measured. Pink dashed boxes denotes the zoomed in area for Figure 3.10.

point cloud renderings due to a small number of photos or not enough overlapping photos, too bright or too dark conditions, wrong curbs photographed, or only one year of photos were taken. Specific explanations for the years used are noted in Table 3.4. In total, 21 sites were measured spanning the three main areas originally monitored in Fremont (northern, center, and southern sections) and shown in an updated map (Figure 3.8). The mean offset displacements for each direction of curb movement and the number of years between each set of acquired photos are is shown in Table 3.5 and Figure 3.15. The curb offset rates for each site in each direction of curb movement are shown in 3.6 and Figure 3.9.

Table 3.4: Description of all sites, when a site was photographed, the dates used to measure displacement, and descriptions of why specific dates were not used.

Site	Dates Photographed	Year Pairs	Notes
1	2016, 2017, 2018	2016-2018	
2	2016, 2017, 2018	2016-2018	
3	2016, 2017, 2018	2016-2018	
4	2016, 2017, 2018	2017-2018	2016: Car parked in front
5	2016, 2017, 2018	2016-2018	
6	2016, 2017, 2018	2016-2018	
7 - 9		-	BART site - no photos taken
10	2016, 2017, 2018	2017-2018	2016: overgrown grass that left very little distinguishable features. 2017: overgrown grass where we could not find many distinguishable features, textures, or colors.
11	2016, 2017, 2018	2016-2018	
12	2016, 2017, 2018	2016-2018	
13	2016, 2017, 2018	-	2016: not a good rendering of vertical side of sidewalk. 2017: not have enough pixels to find distinguishable features.
14	2016, 2017, 2018	2016-2018	
15	2016, 2017, 2018	-	2018: Curb painted. For all dates, there are not enough contrasting features.
16	2016, 2017, 2018	-	2016 & 2018: generated point clouds do not have enough distinguishable features.
17	2016, 2017, 2018	2016-2018	
18	2016, 2017, 2018	2016-2018	
19	2015, 2016, 2018	-	Two different offsets were taken
20	2015, 2016	-	Two different offsets were taken
21	2015, 2016	2015-2018	
22	2015, 2016, 2018	2016-2018	2015: wrong offset photo taken
23	2015, 2016, 2018	2015-2018	
24	2015, 2016, 2018	2016-2018	2015: wrong offset photo taken
25	2016	-	Photos only taken in 2016
26	2016	-	Photos only taken in 2016
27	2016	-	Photos only taken in 2016
28	2016	-	Photos only taken in 2016
29	2015, 2016	-	Two different offsets were taken
30	2016	-	Photos only taken in 2016
31	2015, 2016	2015-2016	
32	2016	-	Photos only taken in 2016
33	2015, 2016, 2017, 2018	2015-2018	
34	2015, 2016, 2017, 2018	2016-2018	2015: Not enough photos
35	2016, 2017, 2018	2017-2018	2016: Car parked in front
36	2016, 2017, 2018	2016-2018	

Table 3.5: Offset displacements in the curb-parallel, curb-vertical, and curb-perpendicular directions. The sites are in order of location from the northern-most to the southern-most site (Figure 3.10).

Sites	Years Differenced	Number of Years	Curb Perpendicular (mm)		Curb Vertical (mm)		Curb Parallel (mm)	
			Mean Displacement	Standard Deviation	Mean Displacement	Standard Deviation	Mean Displacement	Standard Deviation
3	2016-2018	2.42	0.0	0.3	2.6	0.5	0.1	0.3
2	2016-2018	2.42	0.1	0.2	2.2	0.5	0.0	0.2
1	2016-2018	2.42	4.1	0.5	4.6	0.9	0.2	0.5
4	2017-2018	1.50	4.9	0.3	2.2	0.3	0.0	0.4
5	2016-2018	2.42	2.0	0.2	2.0	0.2	0.0	0.2
6	2016-2018	2.42	0.8	0.3	0.5	0.2	0.0	0.2
14	2016-2018	2.42	0.9	0.6	0.9	0.5	0.0	0.3
11	2016-2018	2.42	0.4	0.5	3.1	0.5	0.0	0.3
10	2017-2018	1.50	0.6	0.9	5.8	0.3	0.0	0.3
12	2016-2018	2.42	7.8	0.7	1.5	0.2	0.0	0.4
17	2016-2018	2.42	5.2	1.0	6.9	0.9	0.1	0.6
18	2016-2018	2.42	2.8	1.7	2.8	1.5	0.0	0.6
35	2017-2018	1.50	3.2	0.3	0.5	0.6	0.2	0.4
36	2016-2018	2.42	3.1	1.3	2.2	0.9	0.0	0.5
34	2016-2018	2.42	1.1	0.2	0.2	0.3	0.0	0.2
33	2015-2018	2.60	4.9	1.3	1.6	0.8	0.0	0.5
24	2016-2018	2.42	7.0	1.2	0.3	0.6	0.0	0.4
23	2015-2018	2.60	0.1	0.6	0.1	0.3	0.0	0.2
22	2016-2018	2.42	3.4	0.9	3.5	1.3	0.0	0.5
21	2015-2018	2.60	3.6	0.6	5.7	0.5	0.0	0.4

Table 3.6: Offset rates in the curb-parallel, curb-vertical, and curb-perpendicular directions and the total offset rate projected into the fault parallel direction. The number of years between dates are referenced in Table 3.5. The sites are in order of location from the northern-most to the southern-most site (Figure 3.10).

Sites	Years Differenced	Curb Perpendicular (mm/yr)		Curb Vertical (mm/yr)		Curb Parallel (mm/yr)		Total Rate Projected in Fault Direction	Uncertainty
		Offset Rate	Error	Offset Rate	Error	Offset Rate	Error		
3	2016-2018	0.0	0.1	1.1	0.2	0.0	0.1	1.6	0.4
2	2016-2018	0.0	0.1	0.9	0.2	0.0	0.1	1.7	0.5
1	2016-2018	1.7	0.2	1.9	0.4	0.1	0.2	5.0	1.0
4	2017-2018	3.3	0.2	1.5	0.2	0.0	0.2	4.3	0.4
5	2016-2018	0.8	0.1	0.8	0.1	0.0	0.1	1.4	0.2
6	2016-2018	0.3	0.1	0.2	0.1	0.0	0.1	0.6	0.3
14	2016-2018	0.4	0.2	0.4	0.2	0.0	0.1	0.7	0.5
11	2016-2018	0.1	0.2	1.3	0.2	0.0	0.1	1.4	0.3
10	2017-2018	0.4	0.6	3.9	0.2	0.0	0.2	4.2	0.7
12	2016-2018	3.2	0.3	0.6	0.1	0.0	0.2	3.6	0.4
17	2016-2018	2.1	0.4	2.8	0.4	0.0	0.2	3.6	0.6
18	2016-2018	1.1	0.7	1.1	0.6	0.0	0.2	1.6	1.0
35	2017-2018	2.2	0.2	0.4	0.4	0.1	0.2	2.2	0.5
36	2016-2018	1.3	0.5	0.9	0.4	0.0	0.2	1.6	0.7
34	2016-2018	0.5	0.1	0.1	0.1	0.0	0.1	0.5	0.2
33	2015-2018	1.9	0.5	0.6	0.3	0.0	0.2	2.0	0.6
24	2016-2018	2.9	0.5	0.1	0.2	0.0	0.1	4.4	0.9
23	2015-2018	0.0	0.2	0.0	0.1	0.0	0.1	0.1	0.5
22	2016-2018	1.4	0.4	1.5	0.5	0.0	0.2	3.7	1.2
21	2015-2018	1.4	0.2	2.2	0.2	0.0	0.2	4.5	0.6

3.3.1 Curb Offset Rates

The distribution of curb movement varies from curb to curb with the majority of displacement observed in the curb-perpendicular and curb-vertical directions, and minimal movement observed in the curb-parallel direction (Figure 3.9 and Table 3.6). For a right-lateral sense of motion (i.e., the right side of the offset curb moves to the right with respect to the left side), the curb-perpendicular values will be positive y-values. For right-side up motion, the curb-vertical values will be positive in the z-direction and for opening (i.e., curbs moving apart), the curb-parallel values will be in the positive x-direction (Figure 3.6). The small amount of movement in the curb parallel direction is due to not having enough points within the cloud to difference in the curb parallel direction (i.e., there is no physical curb plane to difference in the curb parallel direction, unlike in the curb vertical or curb perpendicular directions). The uncertainties plotted in Figure 3.9 are calculated from the 1 standard deviation displacement measurement divided by the time interval for each offset curb.

Eight of the curbs show the largest displacement in the curb-perpendicular direction (e.g., sites 4, 12, 35, 36, 34, 33). Five of the sites show most of the movement in the curb-vertical direction (e.g., sites 3, 2, 11, and 10). Seven curb sites show approximately equal amounts of movement in both directions (e.g., sites 1, 17, 18, 22). Site 10, in particular, shows a large curb-vertical displacement of -3.85 $\pm$ 0.22 mm/yr with respect to the left side of the curb being aligned. This movement is not interpreted as downward movement but rather upward movement of the left-side curb, which can be seen from field photos (Figure 3.11).

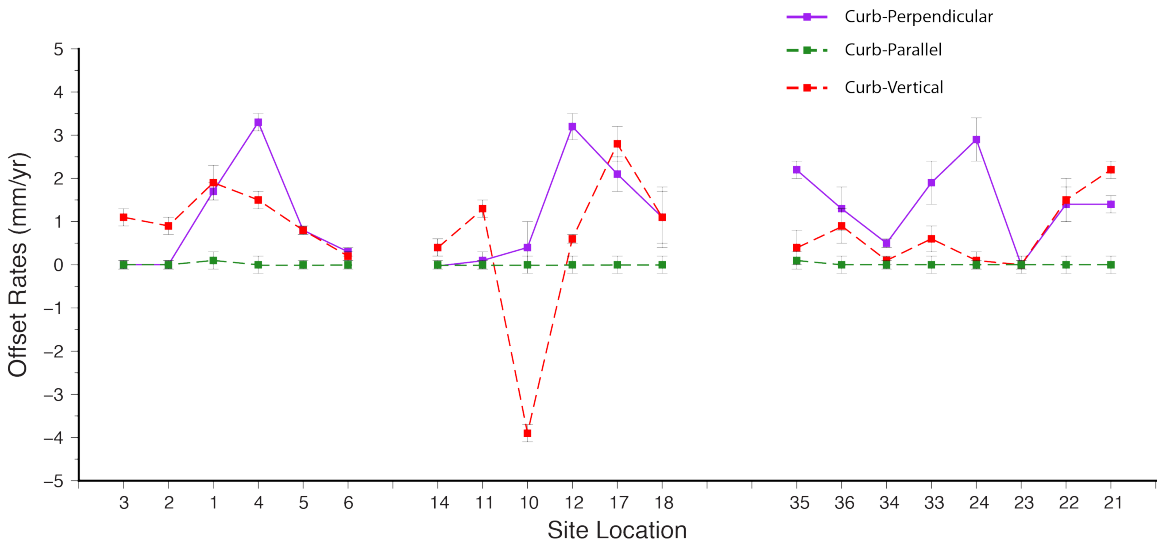

Figure 3.9: Offset rates for each site in the curb-perpendicular (purple), curb-vertical (red), and curb-parallel (green) directions. The rates are with respect to the align left side of the offset curb. The uncertainties are calculated from the 1 standard deviation displacement measurement, divided by the time interval for each offset curb.

The curb-perpendicular and curb-vertical rates are spatially plotted along the fault trace in Figure 3.10 to understand the spatial movement of each curb. In Figure 3.9, the curb-perpendicular values from Figure 3.9 are projected into the local fault strike directions. Sites 1-2, 10-11, and 21-23 are on the same side of the road and are summed to show the total movement accommodated by offsets on that side of the road (Figure 3.10). Sites 4 and 33 have trees growing in close proximity and which could influence the movement of the curb and are not considered in the curb interpretations (Figure 3.12A, B, D).

From our comparisons of the curb perpendicular velocities (i.e., red arrows) at sites across the road from one another, we can identify some areas that show compression and others that show extension. Sites 17–18 and 35–36 both show compression, with the northernmost curb exhibiting more curb-perpendicular movement than the southernmost curb. In addition to the curb perpendicular results, both sites are located at the bases of

hills. Although sites 4–5 are not considered in our interpretation, field photos at site 5 show compression which is observed from tiles buckling between the offset curb site and the pathway (Figure 3.12C). Sites 11–12 and 21–24 both show extension in which the northernmost curb has less curb-perpendicular movement than the southernmost curb. This is corroborated by field photos from 2009 that show pronounced en echelon cracks in the pavement that look to be small depressions in the roads (Figure 3.13).

The curb-perpendicular rates are projected into the fault-parallel direction to resolve the amount of fault movement per year necessary to produce these total offset rates (Table 3.6). The projected values range from ∼0.5 mm/yr to ∼4.5 mm/yr – showing wider variation than the rates estimated from the nearest alignment array to the curb site (Figure 3.14). One reason for this difference could be the width of the fault zone being sampled. An alignment array measures the creep rate over a ∼ 120 m aperture, whereas each offset curb is capturing displacements within a zone less than 3 m wide.

3.3.2 Curb Displacement Variations in Time

The number of years between displacement measurements varies due to reasons mentioned in Table 3.4. The majority of the measurements are from the 2–year interval, 2016–2018, and the 1-year interval, 2017–2018. Three measurements span 2015–2018 and two span 2016–2017. Overall, there is one main trend that can be connected through the sites for 2016–2018, but there are not enough measured sites for the other time intervals to connect them. Three of the 2017–2018 sites and one of the 2015-2016 sites fall within the

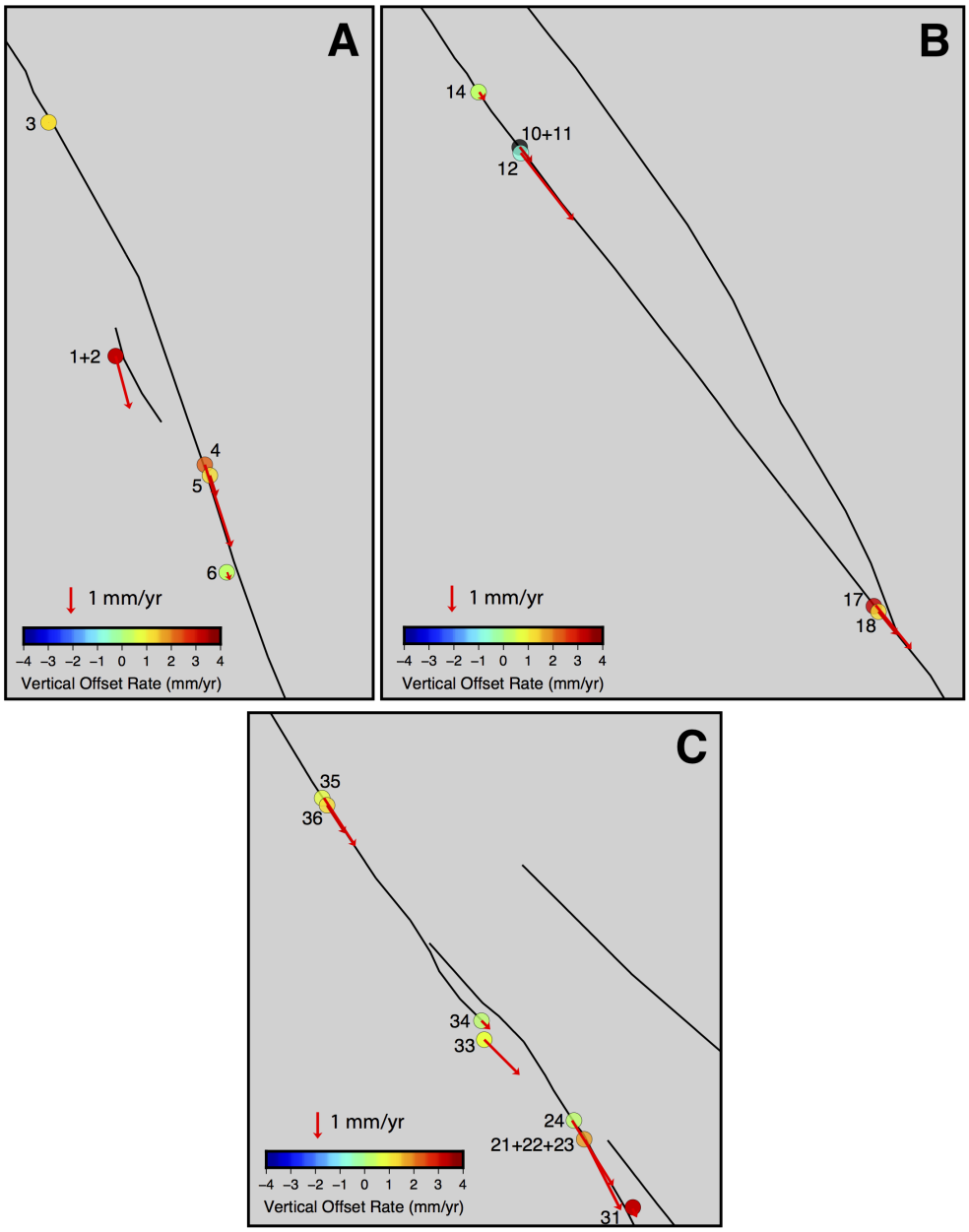

Figure 3.10: Mapped fault trace (Lienkaemper, 2009), curb-perpendicular values projected into the local fault strike direction (red arrows), and curb-vertical (colored circles) offset rates each offset curb. A, B, and C are noted as insets in Figure 3.8 as the northern, middle, and southern sections of sites. Sites that are on the same side of the road are summed together (i.e., sites 1–2, sites 10–11, sites 21–23.

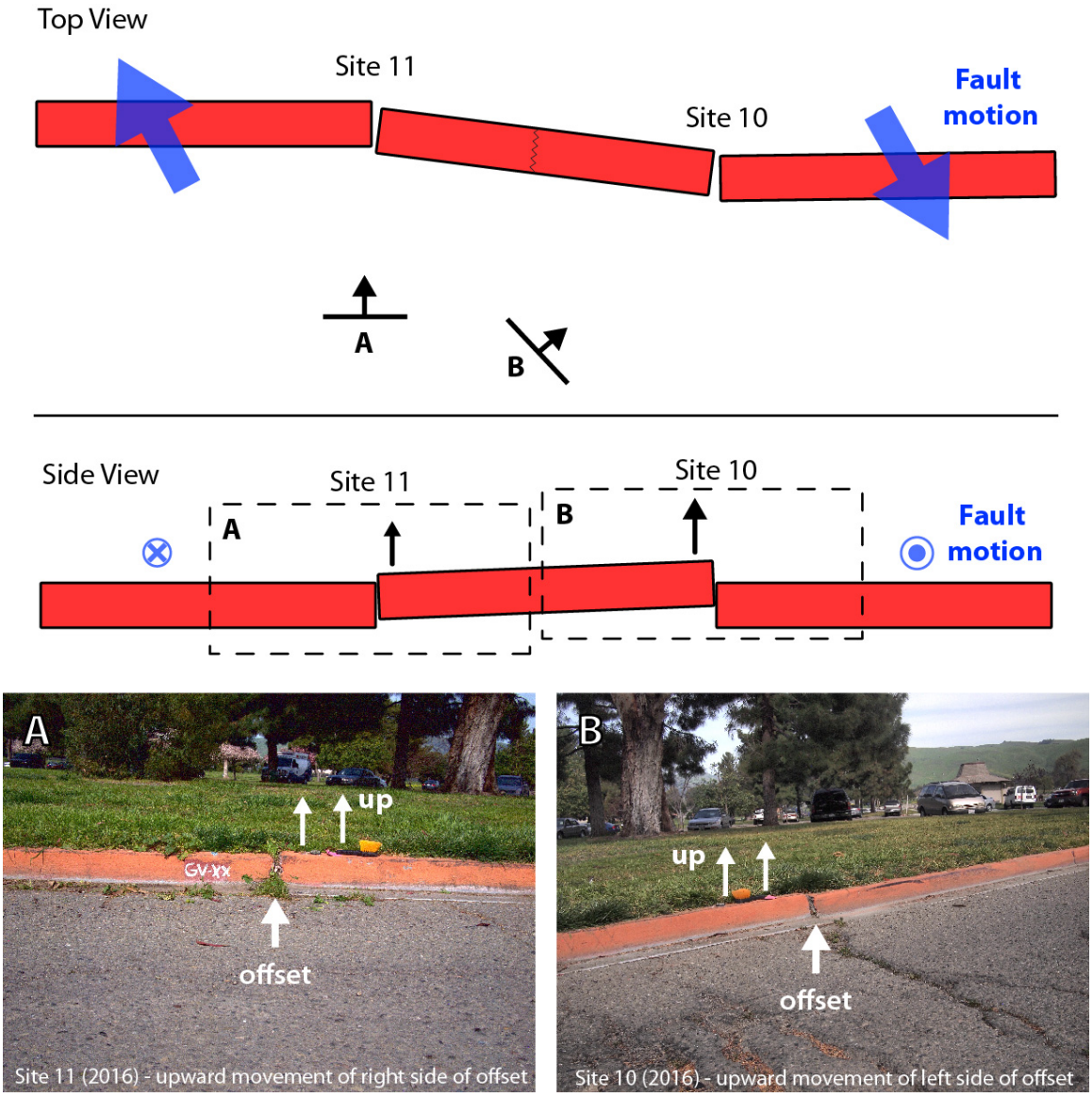

Figure 3.11: Upward motion of curb in between sites 10 and 11. Top view and side view schematics showing how the two curbs are being offset by the fault motion, the camera vantage point of where photos A and B were taken (line with perpendicular arrow) in top view, and the area of the photos in side view (dashed boxes).

Figure 3.12: Field photos of sites 4, 5, and 33 which show nearby trees that can influence curb movement (A and D), parked cars that obstruct the view of taking photos from different vantage points (A). Also observations of offset pathways adjacent to the offset curb (B), and broken, popped up tiles in between a pathway and offset curb (C).

Figure 3.13: Field photos of en echelon cracks at sites 10–13 and 21–23. Both sites have been repaved since these photos were taken.

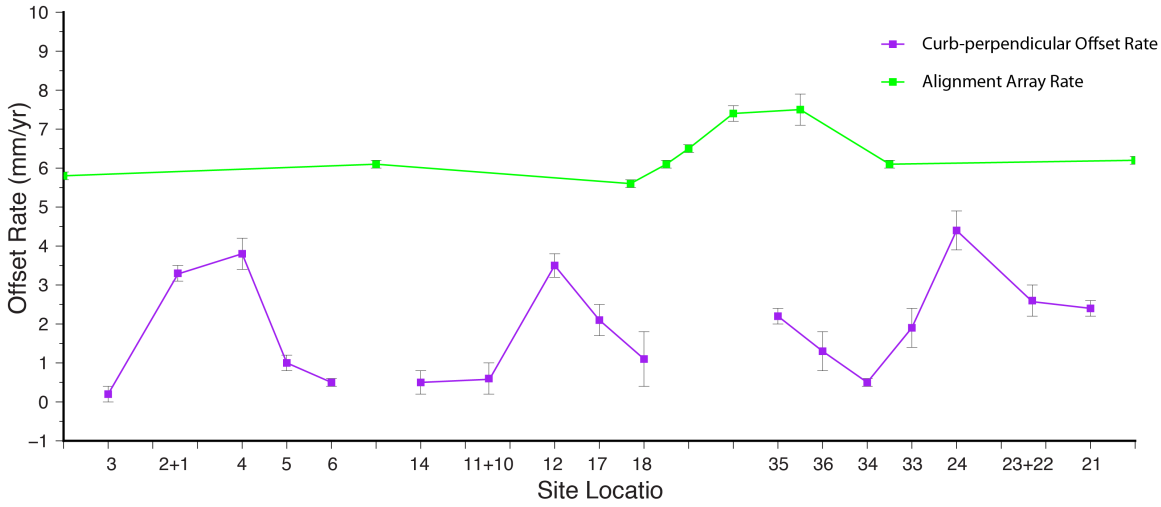

Figure 3.14: Curb-perpendicular offset rates projected into the fault direction (purple) and alignment array rates (green) where the curb offset rates are all less than the alignment array rates. Sites that are on the same side of the road are summed together.

2016–2018 trend line which implies that the total offsets per year may be varying (e.g., one year there is more displacement than the following year).

One exception is site 23 which shows little to no total curb offset in our study period, but comparing our results to photos taken in 2009, movement at this specific site may be occurring in the curb-parallel direction (see Section 3.3.3 and Figure 3.18).

There are four sites (sites 1, 12, 17, and 18) that have more than one displacement measurement over different time intervals (i.e., 2016–2017, 2017–2018, and 2016–2018) (Figure 3.16). Site 1 has three measurements of displacement in which the total displacement is equivalent to an average rate of ∼3 mm/yr with right-lateral sense of motion (i.e., positive y-axis). Separating the total offset into curb-perpendicular and curb-vertical directions show the curb primarily moves in a different direction each year. In 2016-2017, there was 0.0 ± 0.3 mm displacement in the curb-perpendicular direction and 2.4 ± 0.7 mm in the

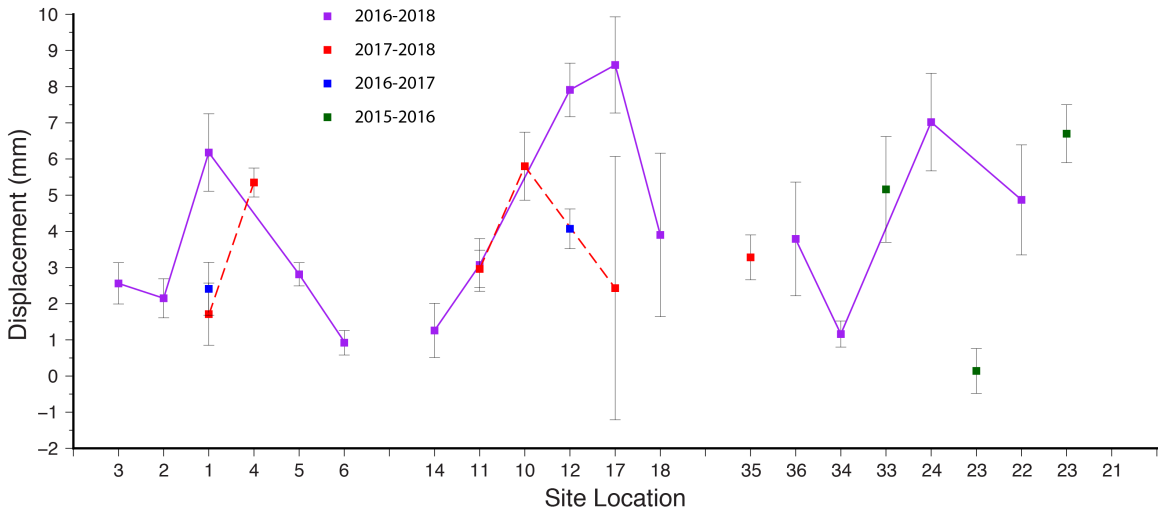

Figure 3.15: Comparisons of total displacements for each time interval measured (2016–2018, 2017–2018, 2016–2017, 2015–2018). Site 23 does not show much movement which is in part due to being one of two offset curbs on the same site of the road (site 22).

curb-vertical direction whereas in 2017-2018, there was 1.8 ± 0.3 mm displacement in the curb-perpendicular direction and 0.4 ± 0.8 mm/yr in the curb-vertical direction.

Site 10 has two measurements for 2017–2018 and 2016–2018 which are within error of one another, which show majority of the displacement in the two-year interval (2016–2018) occurred in 2017–2018. Site 12 has measurements for 2016–2017 and 2016–2018; the total displacement for 2016–2018 is ∼8 mm. Separating these into the curb-perpendicular and vertical displacements shows that the amount of displacement is variable for each year, similar to site 1.

Site 17 has two measurements: 2017–2018 and 2016–2018 showing variability in displacement throughout each year. The displacement between these two time intervals suggest that the 2016–2017 time interval, not measured due to lack of distinguishable features, must have had a larger displacement than 2017–2018.

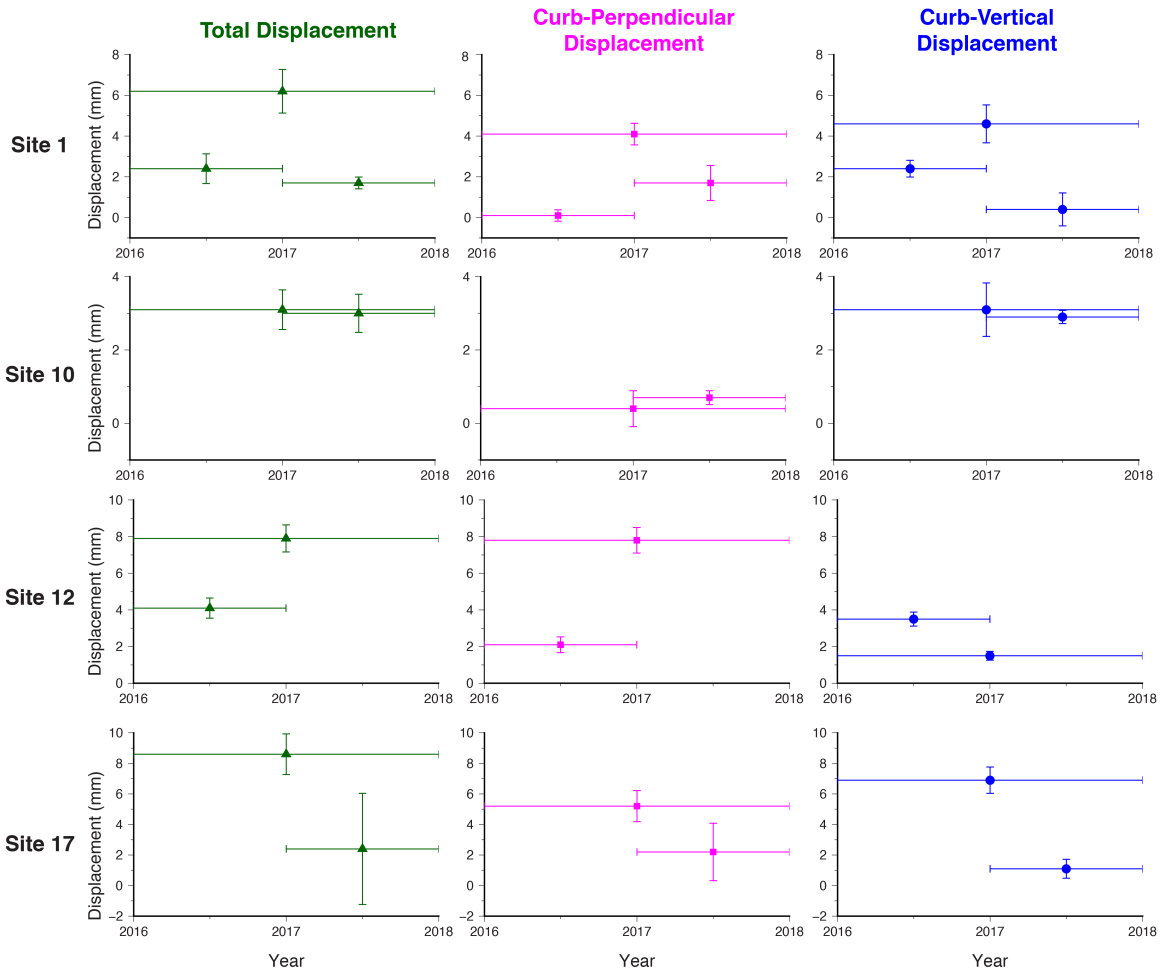

Figure 3.16: Total offset curb displacement (green), curb-perpendicular displacement(pink), curb-vertical (blue) displacement for sites 1, 12, 17, and 18 showing the variability in movement in each direction. X-axis shows the location of data point that is halfway between the interval of time interval. The width of the bar denotes the span of time this measurement covers. For example, data point for site one at 2017.5 spans the time interval of 2017 to 2018.

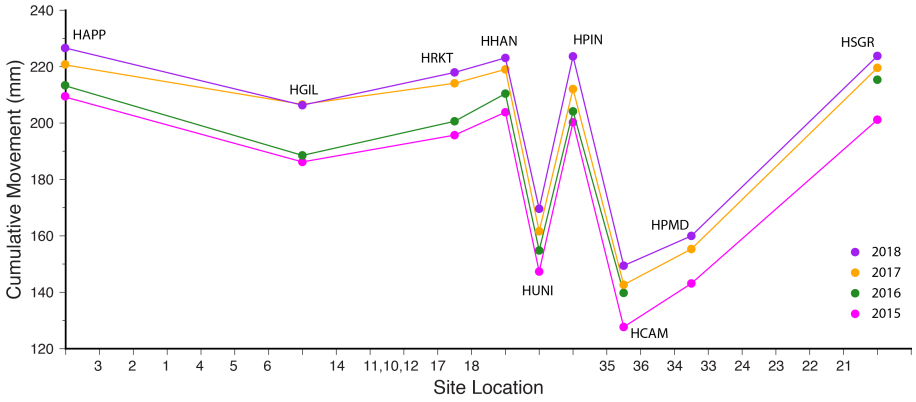

Figure 3.17: Variations in yearly alignment array cumulative displacement measurements in Fremont, CA (Lienkaemper et al., 2014). The amount of displacement between each year at any given site is not consistent suggesting that some years the fault moves more than others.

The displacement measurements suggest that the amount of curb-perpendicular offset each year is variable and may not be consistent. This is also seen in alignment array creep rate measurements where from year to year, there is variability in the cumulative displacement. Figure 3.17 shows all the alignment array displacements along the fault are consistent at each site but the amount displaced in one year can differ. For example, site HRKT from 2015 to 2016 measures a small displacement of $\sim$4 mm then from 2016 to 2017 the displacement is larger at $\sim$14 mm, where then from 2017 to 2018, there is small displacement of $\sim$4 mm again. This shows that there can be variability in the amount of movement between different years which might apply to our variable total site movement between dates (Figure 3.15).

3.3.3 Using Orthophotos

Photographs of the curbs were taken previously by Funning et al. (2010) in 2009 and 2010 using a camera mounted on a tripod and leveled (method mentioned in introduction). We compare 3D point clouds to these 2009/2010 photos by taking an orthophoto (i.e., geometrically corrected photo with a uniform scale through out) view of the 3D point clouds that are centered on the curb and leveled to the ground. We orient the point cloud into the alignment of the 2009/2010 photos to get a longer time span of displacement. We scaled both photos to the same size, overlaid the images, aligned the left side of the offset, and measured the offset on right side. Not all 2009/2010 photos are aligned completely perpendicular to the curb or leveled to the ground. To account for this, we rotated the 3D point cloud into the same viewing angle manually. The average uncertainty of manually rotating the point cloud into the same position every time (attempted same measurement thee times) is $\pm$ 4.5 mm.

Displacements of the offset curbs can be visually seen between the 2009 and 2018 photos in the curb perpendicular as well as in the curb parallel direction, which is not well resolved using the 3D point cloud differencing. This comparison allows for the determination of of motion in the curb parallel direction which indicates opening of the curb segments (Figure 3.18). Comparing the displacement rates of the 3D point clouds to the 9.5 year displacement rates, they have a similar trends in the middle and southern sections. In the northern section, sites 1 and 4 do not follow the 2016–2018 trend which might point towards the influence of tree growth at site 4 and thus are not plotted in Figure 3.19.

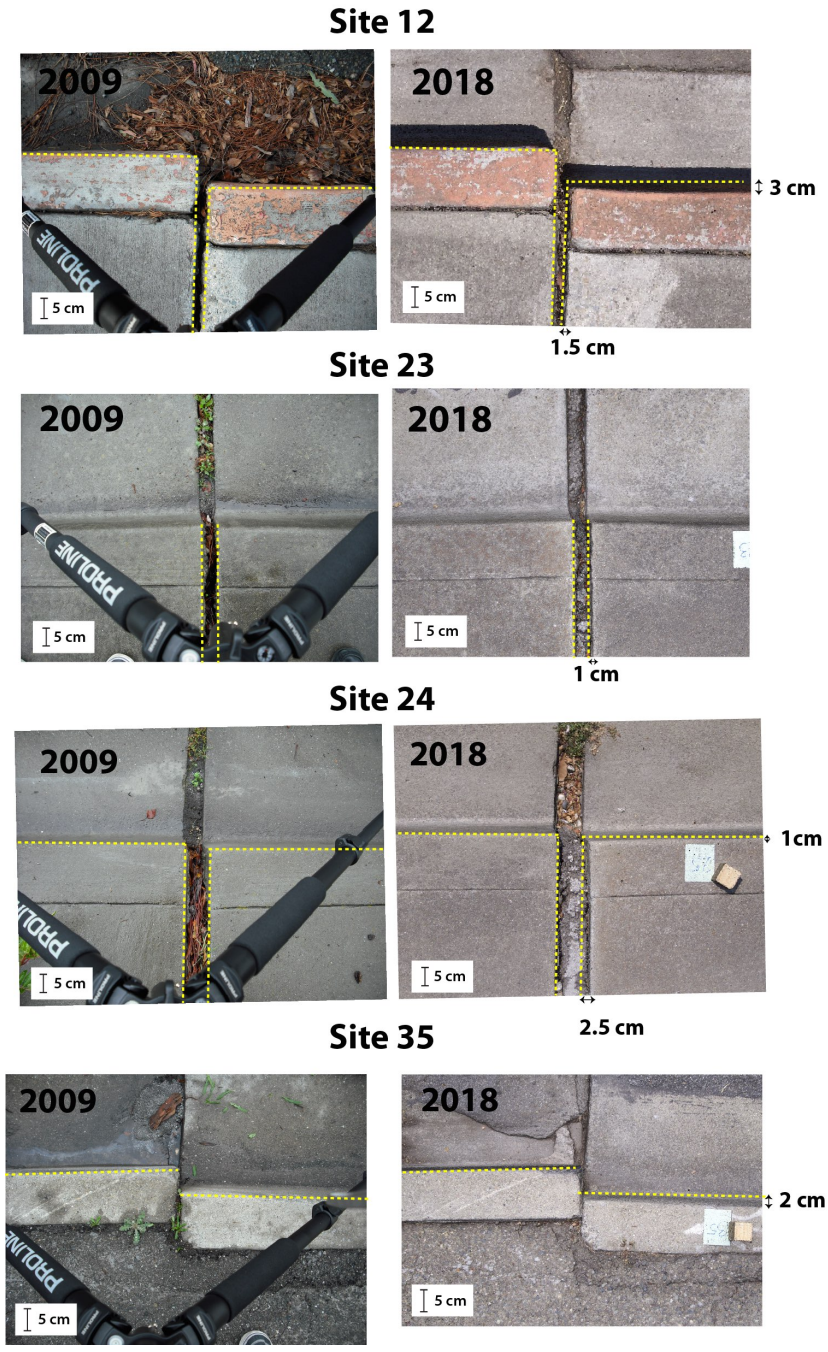

Figure 3.18: Comparing 2009 photos to 2018 photos that show visual differences in the curb perpendicular offset (i.e., sites 12, 24, 35) and in the curb parallel opening (i.e., sites 12, 23, 24). The yellow dashed lines align with the 2009 photos which are overlain on top of the 2018 photos and the difference is shown on the margins.

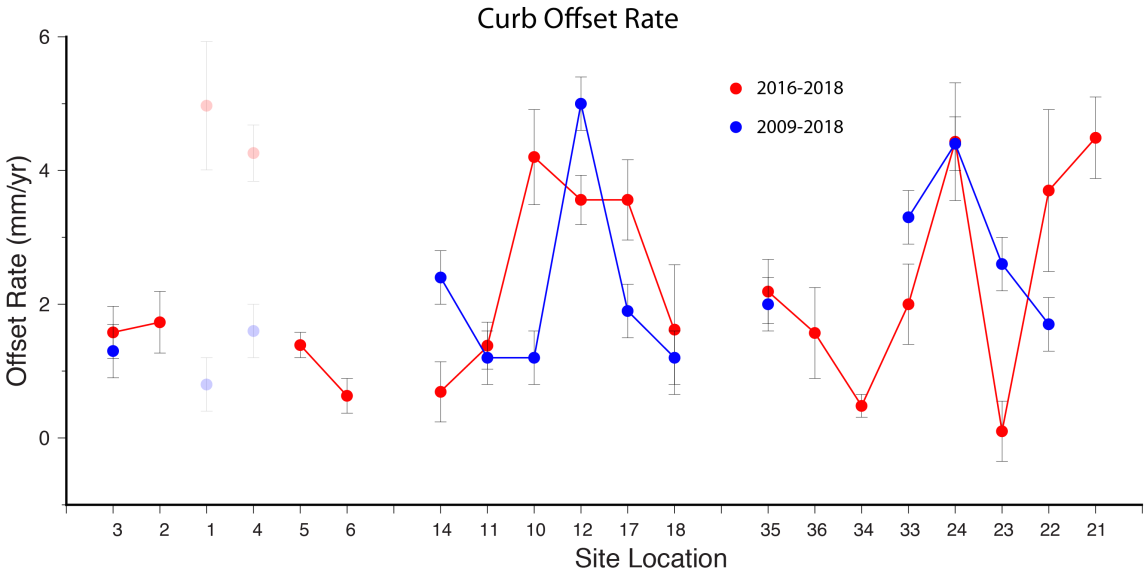

Figure 3.19: Calculated creep rates in mm/yr for the 2009–2018 years. Gaps in data are from sites where no quantifiable measurement was made.

3.3.4 Curb Interpretations

In cases where the curbs along the same road are all accommodating the local movement of the fault together, looking at sets of curbs on the same road can give insight into how the fault movement is deforming the road surface. This shows the variability in how the surface deforms each road, the possible weak points in the road surfaces, and the localization of fault deformation, which can help us to determine how much off-fault deformation there is at each site. There are four places where offset curbs along the same road can be used to make such interpretations. All interpretations are based upon offset estimates from using CloudCompare and field photos.

At sites 10 to 13, on Sailway Drive (Figure 3.20), the fault is mapped in between sites 11 and 10 and sites 12 and 13 which show en echelon cracks across the road (Figure 3.13). Sites 10 and 11 show a rotation and upward motion of the curb segment in between

the two sites (Figure 3.11). More upward motion is shown at site 10 which is noted in the offset rates measured as −3.85 mm/yr (Table 3.6 and Figure 3.9) due to aligning the left side of the curb. The rotation can be seen in field photos (Figure 3.11); the curb does not have the same strike as the rest of the curbs along the road. The curb at site 11 shows a rotation inward of the two curbs, whereas site 10 is showing a rotation outward which leads to the conclusion that the curb in between is rotating clockwise and being pushed up (Figure 3.21 3.21). The rotation of both sites also contributes to the low curb-perpendicular displacement measured (Figure 3.10B and 3.9). A more accurate measurement of the curb perpendicular displacement would be the two curbs on either side of the rotating curb segment. There is also a crack forming in the middle of this curb, which creates a point of weakness that could potentially start to be offset in the future. Sites 12 and 13 are being pulled apart uniformly along the length of the sidewalk, site 12 showing a larger gap than site 13. These two sites are also showing upward motion of the sidewalk segment in between the two sites where it is easily seen in field photos as the sidewalk has been shaved down to be level (Figure 3.21). There are no observations of the sidewalk being rotated which is possibly due to buttressing from the slabs of the adjacent sidewalk. In contrast, sites 10 and 11 are flanked on their northern side by grass and soil, and the curb width of ∼5 inches provides little resistance to rotation.

Sites 17 and 18, on Rockett Drive, show variability in how the curbs are accommodating fault motion (Figure 3.22). At site 17, there is a curb offset with multiple offset cracks in the curb on either side of the main offset. In contrast, the site 18 curb does not have cracks and instead shows a clockwise rotation of the right side of curb, similar to

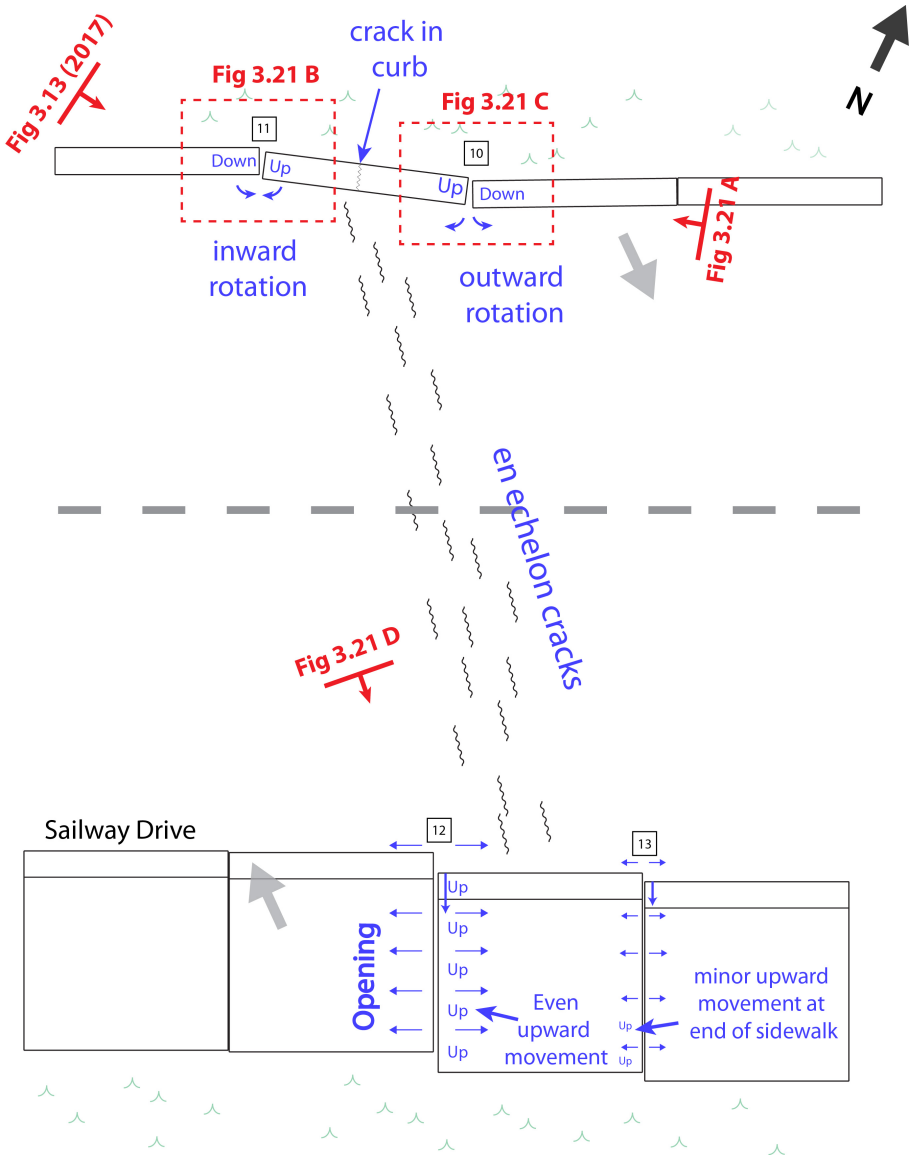

Figure 3.20: Interpretation of offset curbs, sites 10–13, on Sailway Drive. Blue notations are interpretations from field photos and SfM measurements. Red notations show the location and vantage points of photographs in Figures 3.13 and 3.21. Large gray arrows indicate the fault motion (right-lateral).

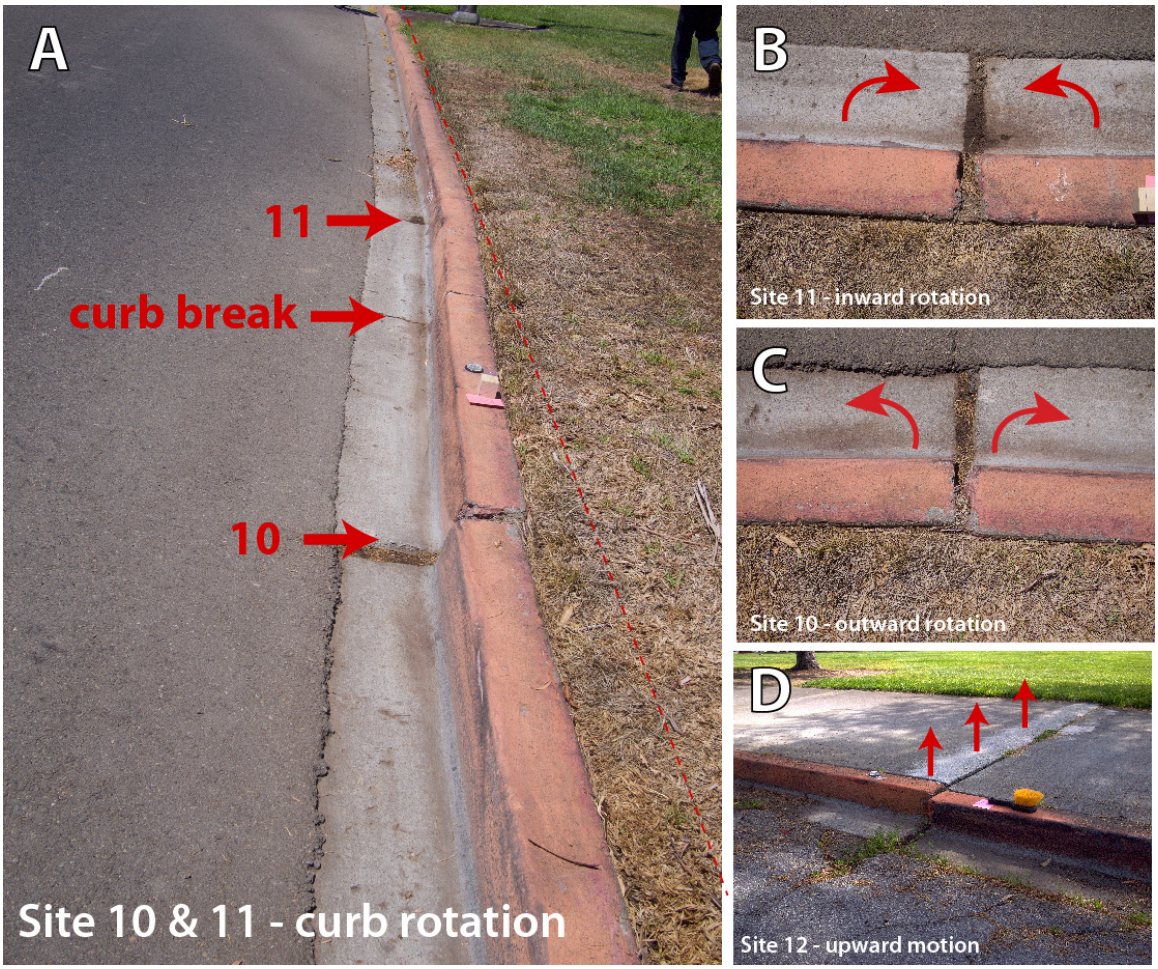

Figure 3.21: Sites 10 and 11 showing the rotation of the curb segment in between the two sites. Dashed red line in A shows the strike trajectory of the curbs before site 11 where the curbs deviate from this line after starting at site 11. Due to the fault movement, site 11 is rotating inward (B), and site 10 is rotating outward (C). Site 12 (D), across the street from sites 10 and 11, has upward motion of the left side and shows signs of having been shaved down to reduce trip hazard.

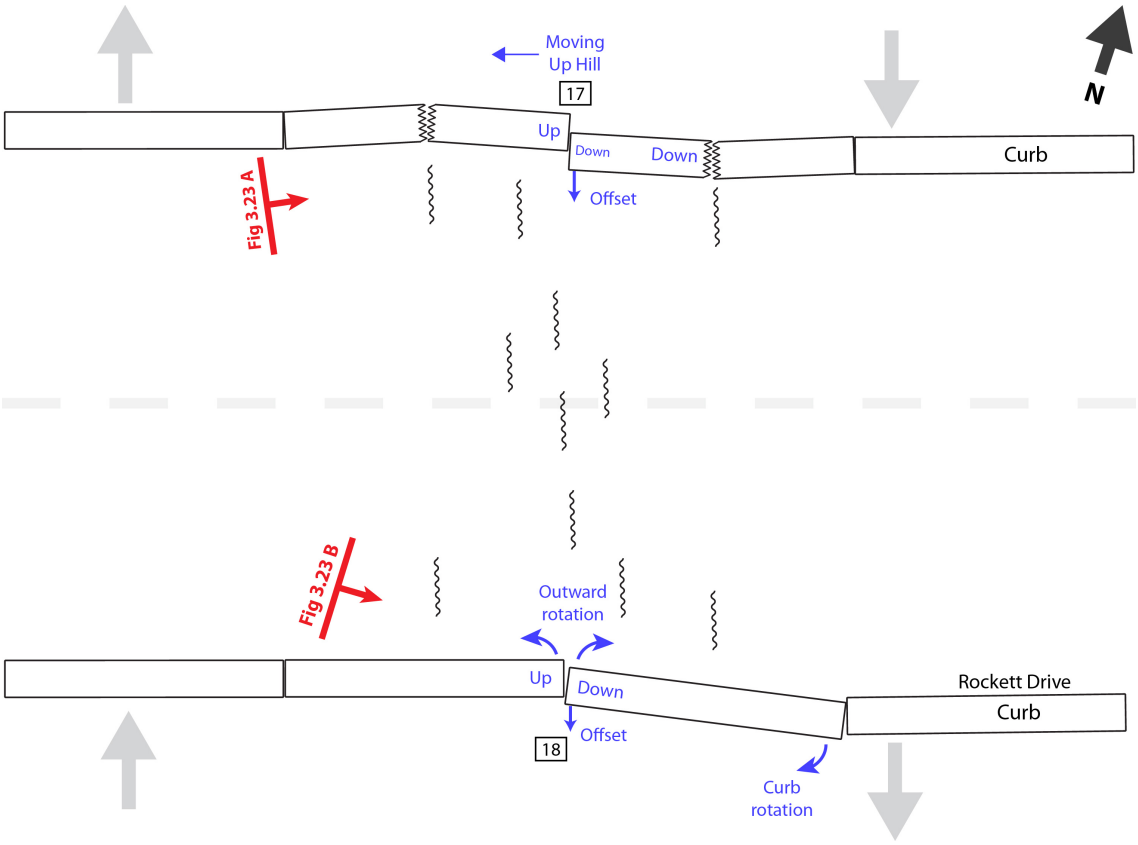

Figure 3.22: Interpretation of offset curbs, sites 17 and 18, on Rockett Drive. Blue notations are interpretations from field photos and SfM measurements. Red notations show the location and vantage points of photo graphs in Figure 3.23. Blue notations are interpretations from field photos and SfM measurements. Large gray arrows indicate the fault motion (right-lateral).

the curb in between sites 10 and 11 (Figure 3.23). Also, similar to site 11, site 18 is also showing an outward rotation between the two curbs, consistent with clockwise movement of the curb. There are minor en echelon cracks in the pavement where there are two thin cracks leading from the cracked curbs near site 17 to the toward curbs across the road near site 18. These could lead to future cracked curbs on either side of site 18, similar to the

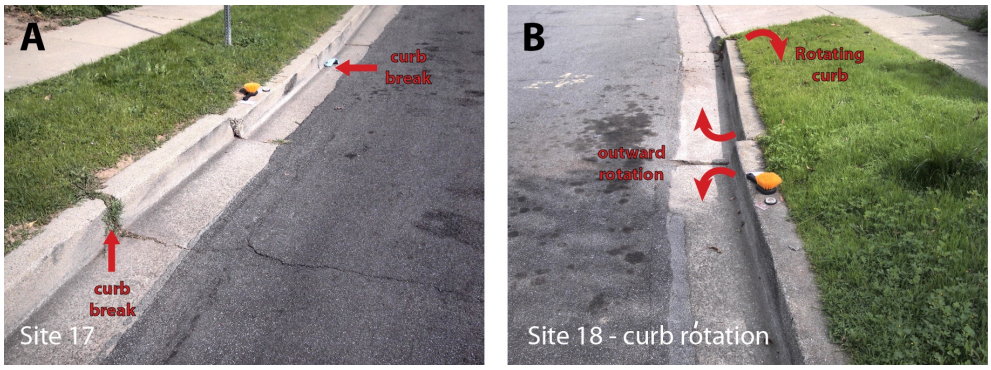

Figure 3.23: Site 17 (A) showing breaks in the curb. Site 18 (B) showing the slab rotating.

cracks near site 17. Both sites are showing upward motion of the left side curb which is consistent with the hill to the west of the offset curbs.

Sites 35 and 36, on Camellia Drive, shows two offset curbs (Figure 3.24). The left side of site 35 and the right side of site 36 are moving up relative to the other sides. For site 35, the pathway portion of the sidewalk (not including the curb) is filled in with asphalt which is showing cracks localized on the left side of the offset curb. There are cracks in the road but there are no clear field photos to determine if they are en echelon cracks or not. Site 36 is also being pulled apart at the offset which tapers off as you move down the length of the sidewalk.

Sites 21 to 25, on Ivy and Gardenia Way, are along a section of the fault that is showing local extension due to a left bend in the fault (Figure 3.10) which can be seen in the complexity of the sidewalk sites (Figure 3.25). In 2009, there were well developed en echelon cracks along the fault trace on both roads (Figure 3.13) which have since been paved over at least twice. The cracks were not seen in 2015 and the streets were repaved between the 2016 and 2018 photo acquisitions. Starting from the North on Ivy Way, sites 24

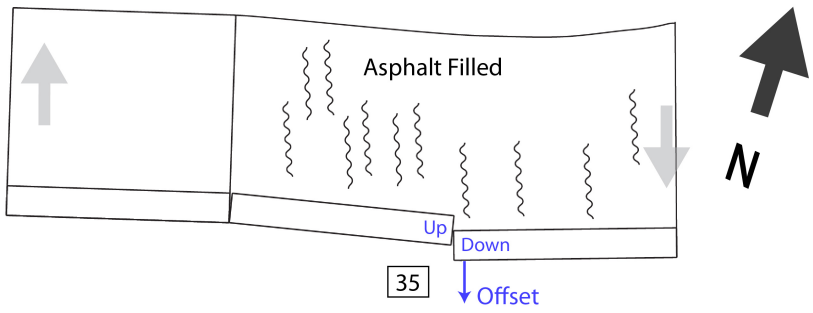

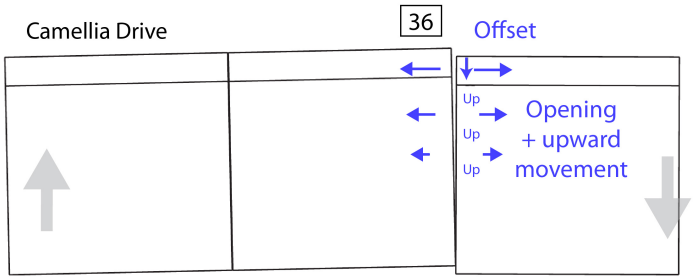

Figure 3.24: Interpretation of offset curbs, sites 35 and 36, on Camellia Drive. Blue notations are interpretations from field photos and SfM measurements. Red notations show the location and vantage points of photo graphs in Figure 3.13. Large gray arrows indicate the fault motion (right-lateral).

and 25 show extension, where there are large gaps in between each offset. Due to the gaps not being uniform along the length of the sidewalk, it looks to be rotating clockwise, in the direction of the fault. Extension is also shown across the street at site 23 – there is a large gap indicating the majority of its movement is in the curb parallel direction and not in the curb perpendicular or curb vertical directions. Site 22 has a portion of upward motion and opening that increases along the length of the sidewalk. Moving across to Gardenia Way at site 21, the northern side of the sidewalk is moving up and being offset as en echelon cracks start right at this offset and moves across the street to two other sites (sites 19 and 20, not shown in figure due to no second set of photos refer to Table 3.4).

3.4 Discussion

The curb offset rates at each site vary along the fault, from 0.7 mm/yr to 4.9 mm/yr, and consistently show rates lower than the alignment array measured creep rates of 5.2–6.1 mm/yr. This may be due to fault deformation occurring over a wider area than the <3 meters that each offset curb is sampling and the alignment arrays sample the fault at a larger aperture of ∼120 meters (McFarland et al., 2018). The offset curbs are the direct effect of the creeping fault at the surface in which the rest of the fault deformation occurs over a larger zone that varies along strike but can be as wide as ∼20 meters (Lienkaemper, 1992). Deformation that occurs within the fault zone, not being expressed through offset curbs, we consider as off-fault deformation and we calculate as the difference (as a percentage) between the alignment array measurement and the total offset rate projected into the fault direction (Figure 3.26). There are nine curb sites that show >50% of the

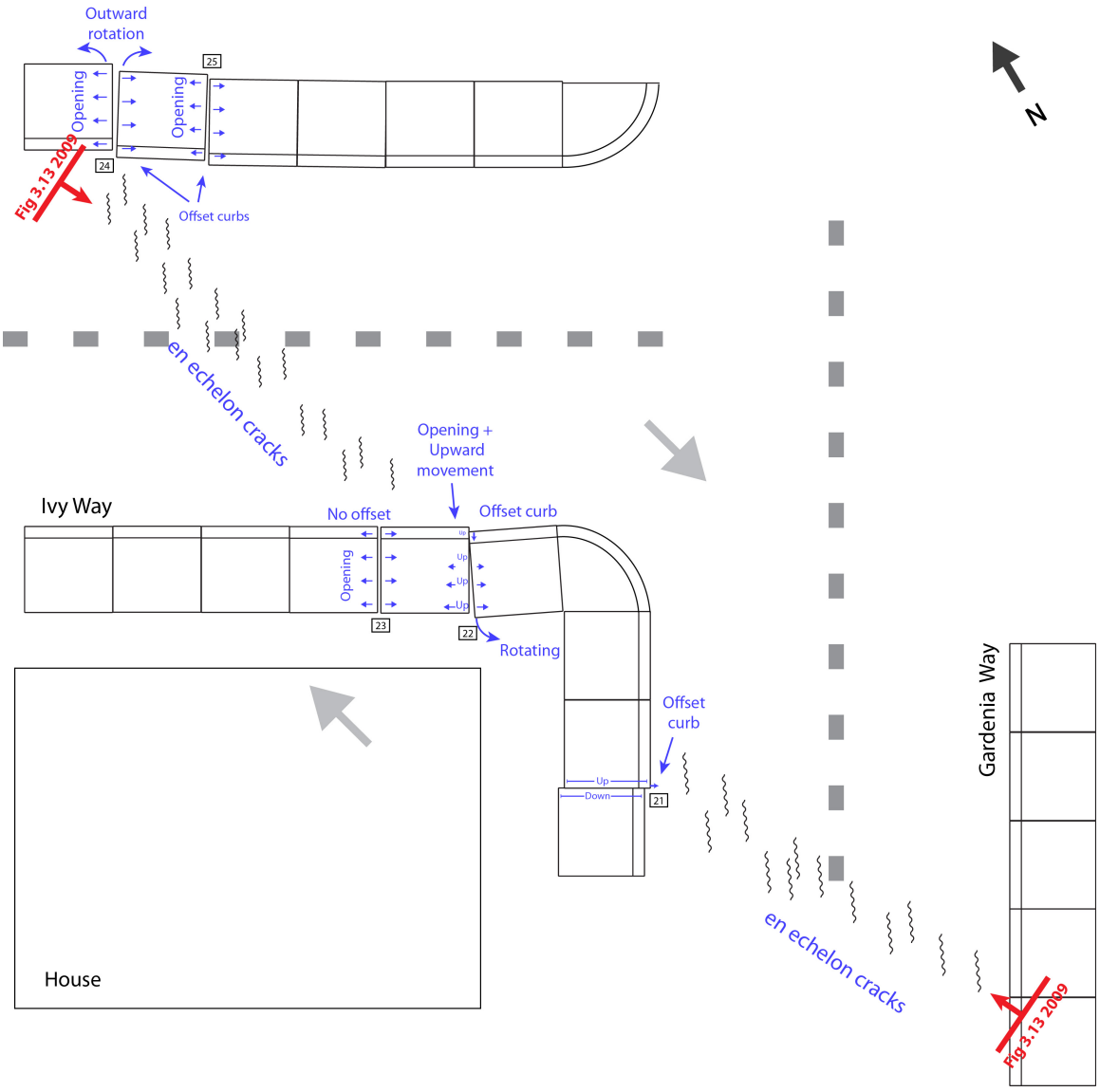

Figure 3.25: Interpretation of offset curbs, sites 21 to 25, on Ivy and Gardenia Way (all shown in blue). Site 11 is showing inward rotation of the curb, sit 10 is showing outward rotation of the curb where the curb between these two sites is moving up. There are en echelon cracks in the pavement leading from sites 11 and 10 to sites 12 and 13. Site 12 and 13 are both showing opening and the sidewalk segment in between the two sites is also showing upward motion). The red lines with a perpendicular arrows denotes the vantage point of the photos shown in Figures 3.13. The large gray arrows indicate the fault motion (right-lateral).

deformation is off-fault deformation, six sites that show <50% is off-fault deformation, and one site with little to no off-fault deformation. The site with no off-fault deformation are due to two combined curbs on the same side of the road, implying the need to monitor multiple offset curbs adjacent to one another rather than treating each as an individual. Monitoring multiple curb sites on the same side of the road could help in determining the width of where the main fault deformation occurs. Similarly, there was a creepmeter installed (site cfw) and operational from 1992 to 2009 near the alignment array HUNI (Figure 3.1; Bilham et al., 2009). During this time period the creepmeter measured 6.6 mm/yr and the closest alignment array measured a similar rate of 6.4 ± 0.1 mm/yr. The difference in area sampled is 30 m vs ∼120 m, respectively which shows the concentration the fault creep is being expressed within a smaller area and the amount of off-fault deformation occurs over a smaller area than the alignment arrays. Some factors to take into account are the sensitivity of our method in the curb-parallel direction and the orientation of the curb with respect to the fault. The curb-parallel direction is difficult to measure due to lacking planar features in this direction that we can use to measure a displacement. We observed there is motion in this direction from comparing 2009 photos with 2018 photos; the latter show a larger opening than the former, suggesting that we are under estimating the full offset rate on the curbs (Figure 3.19). Also, the orientation of the curb with respect to the fault plays a large role on what type of displacement occurs on the curb because if the curb is parallel to the fault strike there will be no observable offset.

Observing curb offset sites along the same road, where the fault cuts through both sides of the road, can give insight into the distribution of deformation and the width of the

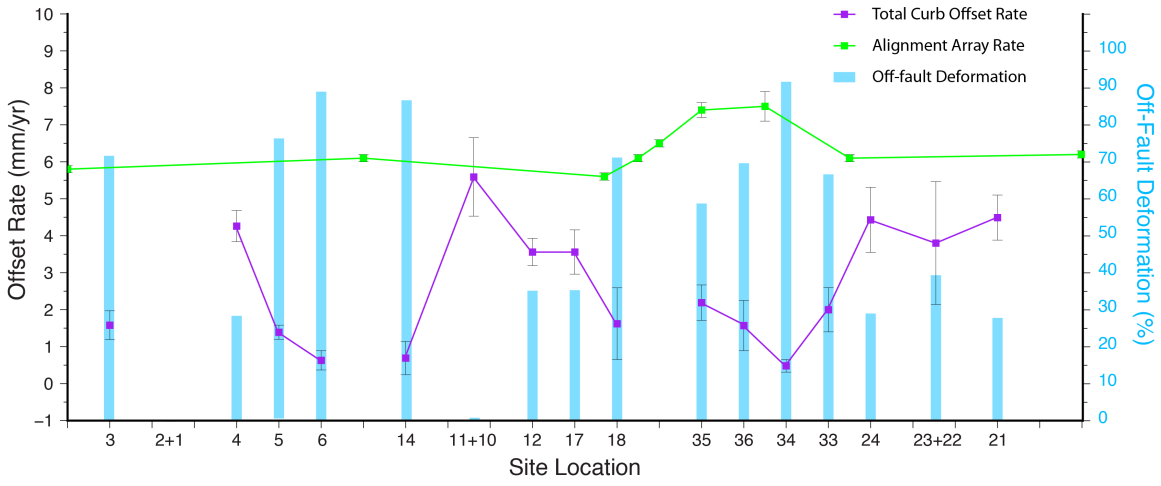

Figure 3.26: Estimating the percent amount of off-fault deformation (pink bars) that is not being expressed at the curb offset and instead is occurring in the surrounding area. Off-fault deformation is calculated from the difference in the total curb offset rate projected into the fault direction (purple) and the closest alignment array creep rate (green). Sites located the same side of the road are summed together (i.e., 2 and 1, 10 and 11, and 22 and 23.

active fault zone. This level of observations can be useful in understanding how the fault drives deformation in a developed, urban landscape and give insight to cities on the type of road conditions to expect, the integrity of infrastructure through time, and how they could prepare for it.

3.4.1 Lessons Learned

Over the past three years, we have learned from various obstacles/issues with data acquisition, processing, and differencing of photos which we list here:

Painted curbs: Finding features that are the same in each photo becomes difficult with a painted curb (e.g., fire lanes, disabled parking) because they are frequently repainted and there are usually no recognizable features from one year to the next (e.g., Figure 3.27). When there are no conserved features between the painted curbs, it becomes difficult to

Figure 3.27: Site 15 showing the curb getting painted between the 2016 and 2018 photos.

measure displacements. In addition to having no similar features due to the paint, the thickness of the paint over time can become a source of error when trying to measure mm–scale differences in the sidewalks with larger time intervals (Zimmer et al., 2018).

Cleaning curbs: Trash and debris can be swept away using a brush but overgrown vegetation can get in the way of observing features in the sidewalk (e.g., Figure 3.28). Gardening tools should be used to cut the grass to expose as many features in the sidewalk as possible.

If there is grass/vegetation all around the curbs in two different years, it can cover up some of the curb that is present (example: site 10 or 11 with grass) reducing the available features that can be matched between point clouds.

Scale: A horizontal and vertical scale are needed to determine the dimensions of the photo. We implemented a wooden cube in 2017 with known dimensions for this purpose (e.g., Figure 3.29).

Figure 3.28: Site 18 showing 2017 photo having overgrown grass and having shadows due to sunny conditions versus the 2018 photo showing no grass and overcast conditions.

Figure 3.29: Wooden block with 5 cm sides that was implemented in 2018 (Site 13).

Figure 3.30: Site 4 in 2017 showing black permanent marker markings on the vertical and horizontal planes of the curb.

Permanent reference markers: In 2017, we tried using black cement markers to draw points on the ground that we hoped to use the following year but the marks faded by 2018 (e.g., Figure 3.30). The use of physical reference markers, at least 4 distributed close and far from the offset on the horizontal and vertical planes, would allow for a fast alignment of the yearly photos without the need of finding features within the cement. A few suggestions would be to glue a small square token to the ground, hammer an anchor pin into the cement, or score the cement.

Weather: Overcast conditions are the best weather conditions to take photos in as there are no bright areas to reflect light into the camera and there are no dark shadows (e.g., Figure 3.28). Both bright photos and dark shadows are not ideal as finding features can be obscured. If it is a bright and sunny day, we recommend bringing a form of shade, such as an umbrella or canopy.

3.5 Conclusions and Future Work

Yearly observations of offset curbs through simple photographs allows for measuring the displacement of the curbs through the use of Structure from Motion. Measurements show that the curb displacements are not uniform year-after-year, in the curb-perpendicular vs. curb-vertical vs. curb-parallel directions, thus measuring curb movement is beneficial to understanding how the urban infrastructure is accommodating fault creep. We calculated the rate of movement along the offset curbs that, over time, will start to effect the integrity of the roads and possibly house foundations that lie on top of the creeping fault trace.

Measuring all offset curbs along the same road and documenting other forms of off-fault deformation (e.g., en echelon cracks) can help determine the width of active deformation, within the area sampled by alignment arrays. We have already seen, from a smaller aperture creepmeter array that the active deformation zone is concentrated in a much smaller area than what is sampled from the larger aperture alignment arrays. Measuring offset curbs along the roads can help better determine this width of deformation which can in turn help the city from an engineering standpoint in identifying what materials are better suited for areas that will experience more deformation over time.

Our methodology could be improved in two different ways. First, an update in how the photos are taken by installing permanent ground markers into the pavement to have specific anchors that do not vary from model to model. These permanent markers will provide better accuracy in measuring curb-parallel displacements as the markers will be the same anchors to align all point clouds to thereafter. Second, taking photographs along a larger length of each offset can help account for/measure the main area being deformed

by the fault. An improvement for this could be to use a flow flying drone along the street length which can help help quantify the localization of fault deformation occurring near the fault trace versus within the larger zone of deformation measured by alignment arrays.

Additional work in finding other offset curbs in the area and specifically photographing the roads in between offset curbs where en echelon cracks are expected to form would also be beneficial to document over time. It is also expected that roads along the fault trace are being repaired more often than roads elsewhere. Obtaining city records that document when and where roads and curbs have been repaired over the last decade would help to determine the rate at which the urban roads show significant signs of fault creep. This information would be useful for the city to help maintain roads and to keep infrastructure safe for the community as this slow movement of the fault can slowly degrade the structural integrity of infrastructures on the active fault trace (e.g., Hayward's abandoned City Hall and the UC Berkeley's Memorial Stadium)

3.6 Appendix A: Point Cloud Density

Sites	12/20/15			2/26/16			1/26/17			7/27/18		
	Photos*	Tie Points[a]	Dense Cloud Points	Photos*	Tie Points[a]	Dense Cloud Points	Photos*	Tie Points[a]	Dense Cloud Points	Photos*	Tie Points[a]	Dense Cloud Points
1				37/40	36,298	35,985,512	34/35	30,715	25,351,156	36/36	24,727	37,679,211
2				39/42	32,063	35,968,932	29/29	24,588	27,369,585	31/31	31,807	49,664,686
3				18/23	12,926	16,784,800	32/33	15,751	26,241,641	31/32	27,416	41,221,695
4				18/18	16,326	6,280,903	36/36	30,237	24,642,206	31/31	31,410	16,646,336
5				35/43	20,765	27,004,918	38/38	27,627	28,668,625	36/36	32,727	42,165,644
6				57/62	58,804	44,004,813	25/25	21,928	29,568,515	16/16	17,858	28,983,932
10				29/31	20,538	24,480,432	25/25	19,602	15,448,128	28/28	26,597	27,990,103
11				29/31	19,037	23,307,339	26/26	24,951	18,755,929	32/32	30,309	33,530,946
12				38/39	30,623	46,147,639	26/26	21,637	30,750,297	27/27	22,509	37,131,830
13				27/31	20,067	34,576,261	23/23	15,630	26,353,079	30/31	28,197	36,804,473
14				32/39	33,981	33,465,885	28/28	17,303	28,816,274	22/24	17,545	32,782,308
15				28/34	23,217	29,885,130	32/32	27,006	15,557,487	26/30	21,566	29,758,462
16				31/35	23,664	31,510,777	26/26	29,414	20,634,076	25/25	26,262	26,210,921
17				13/28	6,349	12,288,386	31/31	26,809	18,096,946	34/34	35,438	38,001,758
18				33/38	21,798	29,016,230	32/32	23,416	15,777,127	30/30	33,269	39,198,469
21	23/27	20,288	26,905,696	50/52	41,526	38,239,426				41/41	39,536	49,057,803
22				34/37	33,737	34,915,111				23/23	25,607	37,801,743
23	22/26	26,147	34,068,723	25/30	18,175	31,890,769				36/36	31,853	43,345,499
24	22/26	12,742	30,647,433	36/36	30,155	42,368,721				34/34	39,924	50,605,652
30	Wouldn't align, not enough photos	-	-	34/36	30,075	30,773,157						
31	29/36	26,590	32,351,916	42/42	22,810	34,150,763						
33	32/35	36,192	47,754,363	33/38	25,381	29,775,921	23/23	20,819	22,633,866	38/38	30,610	47,564,133
34	Not enough photos (4 photos)	-	-	39/39	22,320	28,488,193	27/27	28,489	26,050,903	45/45	44,778	48,658,799
35				Car parked infront	-	-	37/39	47,583	28,700,645	46/46	44,595	46,556,139
36				32/32	22,324	30,201,977	25/27	26,247	26,078,389	37/37	43,556	45,490,982

Figure 3.31: Point cloud density for each 3D model generated from Agisoft Photoscan. *: The photos values shows the number of photos align out of the total number of photos taken. a: The tie points the number of matches between the SIFT points detected on two or more different images.

Chapter 4

Influence of metasomatic alteration on the frictional properties of serpentinite-bearing gouge from a creeping segment of the Bartlett Springs Fault, northern California

4.1 Abstract

There is a ∼1.5 m-wide surface exposure of the core of the Bartlett Springs fault, near Lake Pillsbury, along a segment of the fault known to be creeping at 3.4 ± 0.9 mm/yr (McFarland et al., 2018). This provided an opportunity to collect fault gouge samples from a known creeping fault, for the first time in northern California. The fault gouge collected contains sheared antigorite serpentinite, interlayered with metasomatic alteration layers/zones consisting of talc, tremolite, and chlorite. This mineral assemblage is interpreted to have been tectonically entrained in the fault from depths near the base of the seismogenic layer where it rose buoyantly to the surface within the fault zone (Moore et al., 2018). The bulk chemistry of the gouge and the mode of transportation is similar to samples from the creeping segment of the San Andreas fault at SAFOD (San Andreas Fault Observatory at Depth). Antigorite has been shown to promote fault creep when sheared between crustal rocks at hydrothermal conditions (Moore and Lockner, 2013). What is unknown is, if the antigorite completely converted into the alteration mineral assemblage talc + tremolite + chlorite, which potentially could be the case at depth, the fault still exhibit fault creep?

We conducted a series of mixing-law experiments on synthetic gouge mixtures to determine (1) the frictional strength of each mineral and (2) which synthetic gouge mixtures can support fault creep. Focusing on the secondary mineral assemblage components—talc, tremolite, and chlorite—found in the Lake Pillsbury fault gouge, we prepared the synthetic fault gouges by mixing varying proportions of these minerals and measured their frictional properties using a triaxial apparatus under hydrothermal conditions representing 9-10 km depths. For the frictional strengths of the gouges, tremolite is shown to be the strongest

mineral (coefficient of friction, $\mu \sim 0.55$), talc is the weakest ($\mu \sim 0.12$), and chlorite is an intermediate strength ($\mu \sim 0.30$). In the synthetic mixtures, talc is more effective than chlorite in weakening any of the tremolite-bearing gouges. For the velocity dependence of the gouges, talc and chlorite are velocity strengthening (promoting stable slip) and tremolite is velocity weakening (promoting stick-slip behavior). In the synthetic mixtures, talc promotes stable slip in tremolite-bearing mixtures containing >50% talc, whereas chlorite does not promote stable slip in any of the tremolite-bearing mixtures. This suggests that talc, in the case of no serpentine left within the fault zone, is the main factor promoting fault creep at depth within the fault zone. The talc would need to be concentrated into layers within the sheared gouge matrix to promote creep in thoroughly altered antigorite serpentinite at depth.

4.2 Introduction

4.2.1 Overview of the Bartlett Springs Fault at Lake Pillsbury

The Bartlett Springs fault is the easternmost branch of the San Andreas fault system in northern California, with the San Andreas Fault and the Maacama-Rodgers Creek fault to the West (Figure 5.1, inset). It accommodates the lowest geodetic slip rates among the three main active fault strands at ~7.5 mm/yr (Murray et al., 2014). Lake Pillsbury is located at an extensional stepover along the Bartlett Springs fault (Ohlin et al., 2010; McLaughlin et al., 2018). Surface creep is identified along specific segments of this fault from alignment arrays (Lienkaemper et al., 2014) and campaign GPS data (Murray et al., 2014). Both data sets observe the highest creep rates just north of Lake Pillsbury;

the alignment array (BSLP; 102 m aperture) shows a fault creep rate of 3.4 ± 0.9 mm/yr (Lienkaemper et al., 2014; McFarland et al., 2018) and the GPS pair (WOTI-ISLE; 932 m aperture) exhibits 7.0 ± 0.7 mm/yr (Murray et al., 2014). The Franciscan Central Belt geologic unit, north of Lake Pillsbury is offset as well as a serpeninite magnetic anomaly to the south which measures a ∼7.4–8 km offset due to right-lateral displacement for the Lake Pillsbury region (Ohlin et al., 2010; Langenheim et al., 2007).

About 1 km north of Lake Pillsbury, a stream-cut terrace has a ∼1.5 meter-wide surface exposure of the serpentinite-bearing fault gouge. The blue-grey colored fault gouge is a noticeable stark contrast to the surrounding orange-yellow colored sedimentary wall rocks (Figure 5.2). This allows us to collect fault gouge from a fault known to be creeping at the surface. The fault gouge is a heterogeneous mixture containing four main rock types: the high-temperature serpentine mineral, antigorite and layers of the metasomatic mineral assemblage talc-chlorite-tremolite. The gouge varies between lighter and darker-colored zones within the fine-grained matrix (Figure 4.3). The lighter-colored gouge is mainly antigorite serpentinite, with minor amounts of the low-temperature chrysotile and lizardite serpentinite minerals within the sheared matrix. The darker-colored gouge consists of porphyroclasts of the minerals talc, chlorite, and/or tremolite in a sheared matrix of the same minerals. The tremolite-rich porphyroclast is the largest grain in outcrop and in thin section, the chlorite-rich porphyroclast nearly as large as the tremolite-rich, and talc is the smallest. Talc and chlorite make up the gouge matrix with talc grains arranged in bands parallel to the foliation suggesting that they were smeared out by shearing. Chlorite is smeared out in a similar way. This mineral assemblage most likely formed due to

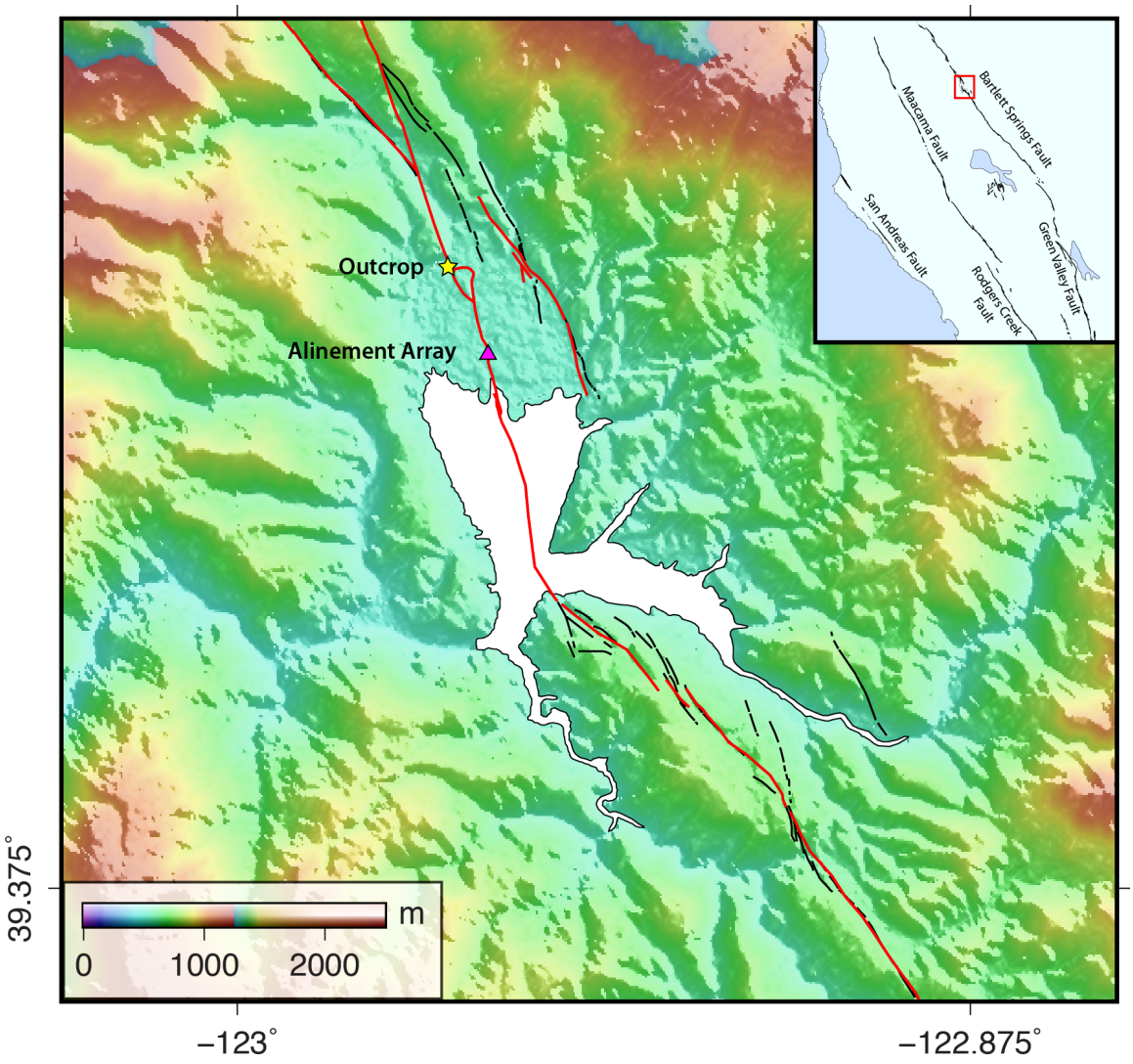

Figure 4.1: Geologic map of Lake Pillsbury region of northern Coast Ranges of California. Red line: recently active trace of the Bartlett Springs fault (Lienkaemper, 2010). Yellow star: location of outcrop in Figure 5.2 & 4.3. Pink triangle: alignment array, BSLP and location of en echelon cracks in pavement.

hydrothermal metamorphism between ultramafic gouge and felsic crustal rocks at depth (Moore et al., 2018). The gouge matrix, concentrated in the darker portions, shows minor low-temperature alteration to the Mg-rich smectite clay, saponite, which is found at depth

along the creeping section of SAFOD and is shown to promote stable slip (Moore et al., 2018).

Figure 4.2: A 1.5 m wide serpentinite-bearing outcrop of the Bartlett Springs fault at Lake Pillsbury (greyish coloring) cutting fluvial fan deposits on either side of the fault (orange-yellow coloring). (Credit: James Lienkaemper, 2009)

Figure 4.3: Close-up of the fault gouge showing the heterogeneous fine-grained matrix; darker colored gouge is the talc-chlorite-tremolite assemblage (example: inset B), lighter colored gouge is the antigorite serpentinite (example: inset B).

This Bartlett Springs fault and gouge samples from the creeping section of the San Andreas Fault the SAFOD (San Andreas Fault Observatory at Depth; SAFOD) are both tapping into a similar deep serpentinite body which rose buoyantly up the fault zone and to the surface (Moore et al., 2018). At both locations, the emplacement of this serpentinite-rich gouge between quartzofeldspathic crustal rocks has been shown to be weakening the gouge and promoting velocity-strengthening behavior (Moore and Lockner, 2013). The Bartlett Springs fault at Lake Pillsbury is thought to cut into this deeply buried serpentinite source that is now rising to the surface and being subjected to shearing in the fault zone (Moore et al., 2018).

When comparing the two mineral assemblages bulk chemistry, the talc-chlorite-tremolite mineral assemblage found at Lake Pillsbury is considered the higher-temperature equivalent of the Mg-rich smectite clays from SAFOD (Moore et al., 2018). The SAFOD fault gouge is shown to promote fault creep at shallow depths along the fault (Moore and Rymer, 2007b), but it is not known if this higher-temperature assemblage is able to promote fault creep near the base of the seismogenic zone. Here we conduct a series of mixing-law experiments focused on understanding the frictional properties of this alteration mineral assemblage — talc-chlorite-tremolite — found at Lake Pillsbury along the Bartlett Springs fault. We create synthetic gouge mixtures in order to understand the frictional strength of each mineral as well as which synthetic gouge mixtures can support fault creep at depth.

4.3 Experiments

We conducted a series of mixing-law experiments on the alteration mineral assemblage, talc + tremolite + chlorite (i.e., various mixtures of each mineral by mass), to determine the frictional strength of each mineral and to investigate what amounts of each mineral is needed to promote stable slip within the fault. We performed experiments on each end member gouge and four sets of synthetic gouge mixtures: chlorite-tremolite, talc-tremolite, talc-chlorite, and talc-chlorite-tremolite. In total, 17 different synthetic gouges were made and tested.

4.3.1 Synthetic Gouge Mixtures

Synthetic gouge mixtures were prepared using varying proportions by weight of each mineral (chlorite, tremolite, and talc). The chlorite and tremolite minerals used are ground-up portions of porphyroclasts collected from the Bartlett Springs fault gouge. The talc clasts from the fault gouge were too small to collect, thus the talc used is from stock samples used in previous studies (e.g., Moore and Lockner, 2008). This talc is a pure mineral separate that is representative of a monomineralic talc zone. X-ray diffraction patterns show that the talc is a pure sample, the chlorite has small amounts of titanite ± apatite impurities, and the tremolite contains small amounts of chlorite (Moore et al., 2018). The titanite and apatite are likely to have little effect on the friction of weak phyllosilicates. All mineral end-member samples were ground and passed through a 90 μm sieve on have all grain sizes smaller than the 90 μm sieve openings. All end-member samples were oven-dried at 120° C in a vacuum oven before preparing the mixtures to remove any adsorbed water.

Table 4.1: Summary of experiments performed with (a-b) values at corresponding velocity step and the coefficient of friction at 2 mm axial displacement used for Figure 4.8.

Gouge Sample	**Velocity Step (μm/s)**	**μ at 2 mm**	**(a-b)**	**Error ($\pm$)**
100% Tremolite	0.1 - 0.01	0.557	-0.0064	0.0017
	0.01 - 0.1		-0.0034	0.0018
	0.1 - 1		-0.0023	0.0005
100% Chlorite	0.1 - 0.01	0.302	0.0070	0.0010
	0.01 - 0.1		0.0012	0.0010
	0.1 - 1		0.0020	0.0003
	1 - 0.1		0.0044	0.0002
	0.1 - 3		0.0044	0.0001
100% Talc	0.1 - 0.01	0.127	0.0016	0.0009
	0.01 - 0.1		0.0019	0.0008
	0.1 - 1		0.0027	0.0003
	1 - 0.1		0.0017	0.0003
15% Chlorite, 85% Tremolite	0.1 - 0.01	0.4960	-0.0087	0.0015
	0.01 - 0.1		-0.0021	0.0014
25% Chlorite, 75% Tremolite	0.1 - 0.01	0.462	-0.0039	0.0021
	0.01 - 0.1		-0.0037	0.0012
	0.1 - 1		-0.0026	0.0009
50% Chlorite, 50% Tremolite	0.1 - 0.01	0.413	-0.0018	0.0011
	0.01 - 0.1		-0.0031	0.0011

Table 4.1 continued from previous page

Gouge Sample	Velocity Step (μm/s)	μ at 2 mm	(a-b)	Error ($\pm$)
	0.1 - 1		-0.0027	0.0002
75% Chlorite, 25% Tremolite	0.1 - 0.01	0.362	-0.0012	0.0012
	0.01 - 0.1		-0.0034	0.0002
	0.1 - 1		-0.0011	0.0011
	1 - 0.1		-0.0018	-0.0001
10% Talc, 90% Tremolite	0.1 - 0.01	0.398	-0.0082	0.0020
	0.01 - 0.1		-0.0023	0.0021
	0.1 - 1		0.0015	0.0003
25% Talc, 75% Chlorite	0.1 - 0.01	0.1980	-0.0013	0.0009
	0.01 - 0.1		-0.0004	0.0012
	0.1 - 1		0.0045	0.0002
50% Talc, 50% Tremolite	0.1 - 0.01	0.2040	-0.0003	0.0010
	0.01 - 0.1		-0.0001	0.0012
	0.1 - 1		0.0042	0.0004
75% Talc, 25% Tremolite	0.1 - 0.01	0.1480	0.0011	0.0009
	0.01 - 0.1		0.0014	0.0006
	0.1 - 1		0.0037	0.0006
	1 - 0.1		0.0041	0.0002
25% Talc, 75% Chlorite	0.1 - 0.01	0.1980	-0.0013	0.0009
	0.01 - 0.1		-0.0004	0.0012

Table 4.1 continued from previous page

Gouge Sample	Velocity Step (μm/s)	μ at 2 mm	(a-b)	Error ($\pm$)
	0.1 - 1		0.0045	0.0002
50% Talc, 50% Chlorite	0.1 - 0.01	0.1590	-0.0003	0.0009
	0.01 - 0.1		0.0003	0.0008
	0.1 - 1		0.0032	0.0004
75% Talc, 25% Chlorite	0.1 - 0.01	0.1290	0.0008	0.0006
	0.01 - 0.1		0.0015	0.0007
	0.1 - 1		0.0042	0.0002
	1 - 0.1		0.0041	0.0001
	0.1 - 3		0.0056	0.0001
12.5% Talc, 12.5% Chlorite, 75% Tremolite	0.1 - 0.01	0.3650	-0.0025	0.0016
	0.01 - 0.1		-0.0006	0.0011
	0.1 - 1		0.0045	0.0002
25% Talc, 25% Chlorite, 50% Tremolite	0.1 - 0.01	0.257	-0.0041	0.0011
	0.01 - 0.1		-0.0022	0.0011
	0.1 - 1		0.0038	0.0005
37.5% Talc, 37.5% Chlorite, 25% Tremolite	0.1 - 0.01	0.202	-0.0036	0.0009
	0.01 - 0.1		-0.0006	0.0009
	0.1 - 1		0.0025	0.0000

4.3.2 Experimental Procedure

All experiments were conducted in a triaxial apparatus under hydrothermal conditions (temperature of 290° C, pressure 230 MPa, and pore pressure 90 MPa) - assuming a 30° C/km geothermal gradient. These conditions represent 9–10 km burial depths where this greenschist facies alteration mineral assemblage (Ernst and McLaughlin, 2012) would have been stable. We prepared two cylindrical driving blocks (19.1 mm in diameter and 41 mm in length) that contained saw cut inclined at 30°to the cylinder axis (Figure 5.3). The driving blocks are composed of Westerly granite and the saw cut faces ground with 120-grit SiC. A 1 mm-thick layer of synthetic gouge was sandwiched between the two halves of the driving blocks (Figure 5.3). The synthetic gouge was prepared as a thick paste with deionized water, smeared onto the saw cut of the lower driving block, and the upper driving block was placed over the gouge layer. The upper driving block contains a borehole for pore-fluid entry; a short steel tube is inserted into the borehole to minimize the extrusion of gouge into the borehole during the experiment. The prepared sample—driving blocks with the layer of synthetic gouge—was then inserted into an annealed copper jacket to keep the assembly in place. A furnace is then placed around the jacketed assembly; the space between the furnace and sample is loosely packed with boron nitride—a good thermal insulator and poor electrical conductor. A Teflon shim is placed between the end plug and steel piston to allow for lateral shear.

Corrections were made for the cooper jacket and the seal friction (i.e., the seal between the machine and piston). Although the strength of the cooper jacket decreases with increasing temperature, a correction is still made for the strength of the jacket (Moore

and Lockner, 2008), which is removed from the total shear stress after the experiment. A correction for the seal friction is necessary because the shear resistance of the seal is a function of confining pressure which will change throughout the experiment. The seal friction value is measured before there is contact with the sample and the load cell reading is adjusted. Corrections made for the copper jacket include a correction for the frictional velocity dependence of shear strength at 290° C and 140 MPa, which is -0.0007. There is also a correction for velocity dependence of seal friction, measured at the beginning of each experiment before sample contact and, on average, is 0.0035.

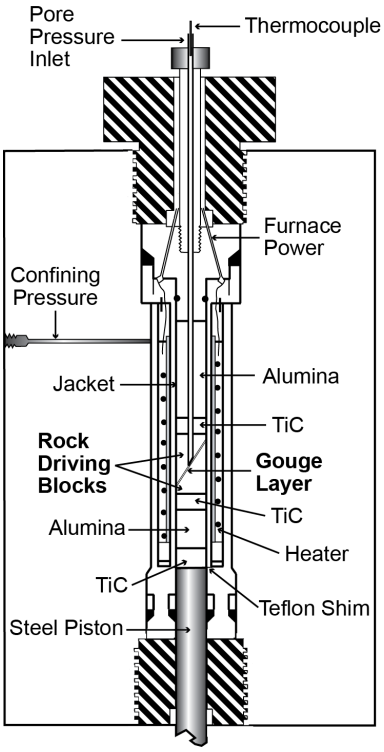

Figure 4.4: Experimental apparatus setup. Modified from Moore and Lockner (2013).

Once the full assembly is in the traxial machine, confining pressure was first applied, followed by pore pressure—using deionized water for the pore fluid. Argon gas was used as the confining pressure medium. The pore fluid pressure was 90 MPa and the effective normal stress was therefore 140 MPa for a 230 MPa applied normal stress. The temperature was then raised to 290° C and monitored by a thermocouple inserted in the pore pressure inlet. During the experiment, the effective normal stress was held constant and maintained through computer-controlled adjustments to the confining pressure. A steel piston at the bottom of the apparatus pushed up against the base of the sample column which resulted in shearing within the layer of gouge. The axial displacement rates changed in steps that varied between 0.01 μm/s and 3.0 μm/s. A reference velocity of 0.1 μm/s was used for every other step (i.e., step 1, 3, and 5) to account for any displacement dependent changes in frictional resistance (reference velocity is shown in Figure 4.5).

4.4 Results

The first set of experiments conducted were on the end-member gouge of each mineral; talc, chlorite, and tremolite (Figure 4.5). The other 4 sets of experiments conducted were on synthetic gouges with combinations of these three minerals (Figure 4.6). In five of the experiments, there was a abrupt decrease in μ within a velocity step (e.g., in the 50% Chlorite, 50% Tremolite experiment at 1.75 mm) which could be attributed to a furnace malfunction where there was a quick temperature change that recovered. For three of these experiments, the strength recovered to the value before the temperature changed. For two experiments, the strength did not recover and instead decreased and came to a new, lower

steady state μ value (i.e., 25% Talc, 25% Chlorite, 50% Tremolite, and 75% Talc, 25% Chlorite). This lower μ value, after the temperature change, was used for all calculations.

4.4.1 Strength of Gouge Mixtures

End-Member Gouges:

The tremolite gouge is the strongest of the three (Figure 4.5), with μ ∼0.55; talc is the weakest with μ ∼0.12, and chlorite is intermediate with μ ∼0.30.

Synthetic Mixtures:

Both talc and chlorite weaken tremolite bearing gouges but talc is more effective (Figure 4.6). Talc contributes to weakening all mixed gouges that include it. In the talc-chlorite mixed gouge, having 25% of talc weakens chlorite from a μ of ∼0.3 to below 0.2—a 58% decrease in strength (Figure 4.6C). In the talc-tremolite mixed gouge, having just 25% of talc will weaken the gouge, from a μ of ∼0.55 to less than ∼0.3—a 60% decrease in strength (Figure 4.6B). Chlorite also weakens tremolite-bearing gouge but not as significantly as talc. Comparing the chlorite-tremolite and talc-tremolite gouges (Figure 4.6A & 4.6B), 50% of talc lowers μ by ∼83% (∼0.55 to ∼0.20) whereas 50% of chlorite lowers μ by ∼62% (∼0.55 to ∼0.40). All percentage values reference the minimum μ of each gouge mixture:

$$1 - \frac{\mu_{decrease} - \mu_{min}}{\mu_{max} - \mu_{min}}$$

μ_{max} is the maximum μ in the gouge mixture and $\mu_{decrease}$ is the new, decreased μ from μ_{max}.

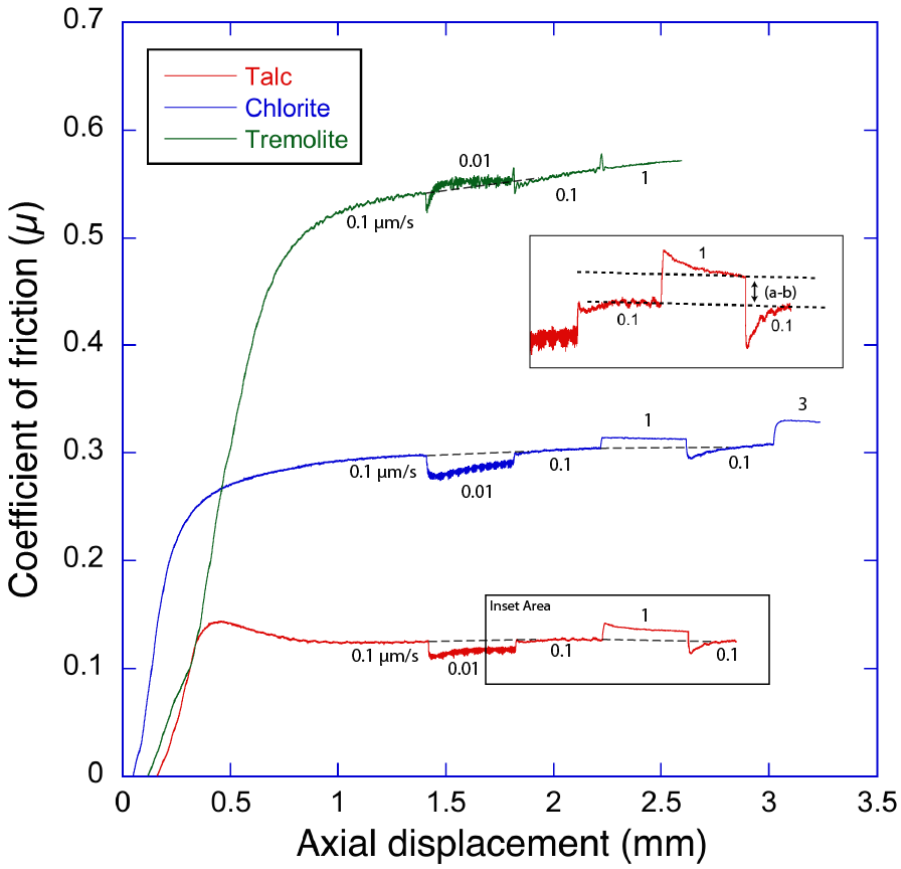

Figure 4.5: Frictional strengths of the end-member samples talc, chlorite, and tremolite. All experiments were run at 290° C, 90 MPa pore fluid pressure and 230 MPa normal stress (140 MPa effective normal stress) to simulate conditions at ∼9 km depth. Axial velocities varied from 0.01 μm/s to 3 μm/s and are noted along the curves. Inset: a zoomed in section of the frictional response of talc to changes in velocity between 1.75 and 3 mm axial displacement shows how the change in friction, (a-b), is determined.

All experiments reached the end of the 0.1 μm/s displacement interval at 2.2 mm axial displacement (Figure 4.6). The strengths of all the mixtures at that displacement were measured and plotted in a 2-phase diagram (Figure 4.7) with respect to the increasing mineral content of the weaker mineral in the mixture. In the case of the ternary mixture, the 'weaker mineral' is the 50:50 mixture of talc and chlorite. The tremolite-chlorite binary mixture (Figure 4.7, black trend line) shows a linear trend with a higher rate of decrease at

$\leq 25\%$ chlorite initially, which changes to a slower rate for gouges with $\geq 25\%$ chlorite. All mixtures containing talc (Figure 4.7, green, blue, red trend lines), have a significantly greater decrease in strength at low concentrations of talc, compared to the tremolite-chlorite gouge. Overall, chlorite is not as effective as talc in weakening tremolite-bearing gouge (Figure 4.7, blue and green trend lines).

4.4.2 Velocity Dependence of Gouge Mixtures

To measure $(a - b)$ at each velocity step, we fit a best-fit line through the data points, before and after the velocity step, for each velocity step (Figure 4.5, inset). The noise in the experiment is due to the cycling of the furnace controller, most notably seen in the slow step (0.01 μm/s), this fluctuation in temperature is $\leq 1°$. Values of $(a - b)$ for all experiments are listed in Table 4.1. The term 'velocity neutral' is used to describe the few experiments where the change in μ is $\sim$0.

For the end-member gouges, talc and chlorite are velocity strengthening and tremolite is velocity weakening (Figure, 4.5, Table 4.1). In the mixed gouges, talc promotes velocity strengthening behavior in some of the tremolite-bearing gouges whereas chlorite does not influence the tremolite-bearing gouges at all (Table 4.1). Binary mixtures containing $\geq$50% talc all have $\mu \leq 0.2$, and are all velocity strengthening with the exception of 50% tremolite and 50% talc which shows a 'mixed behavior' of either velocity strengthening or weakening at different velocity step (Table 4.1).

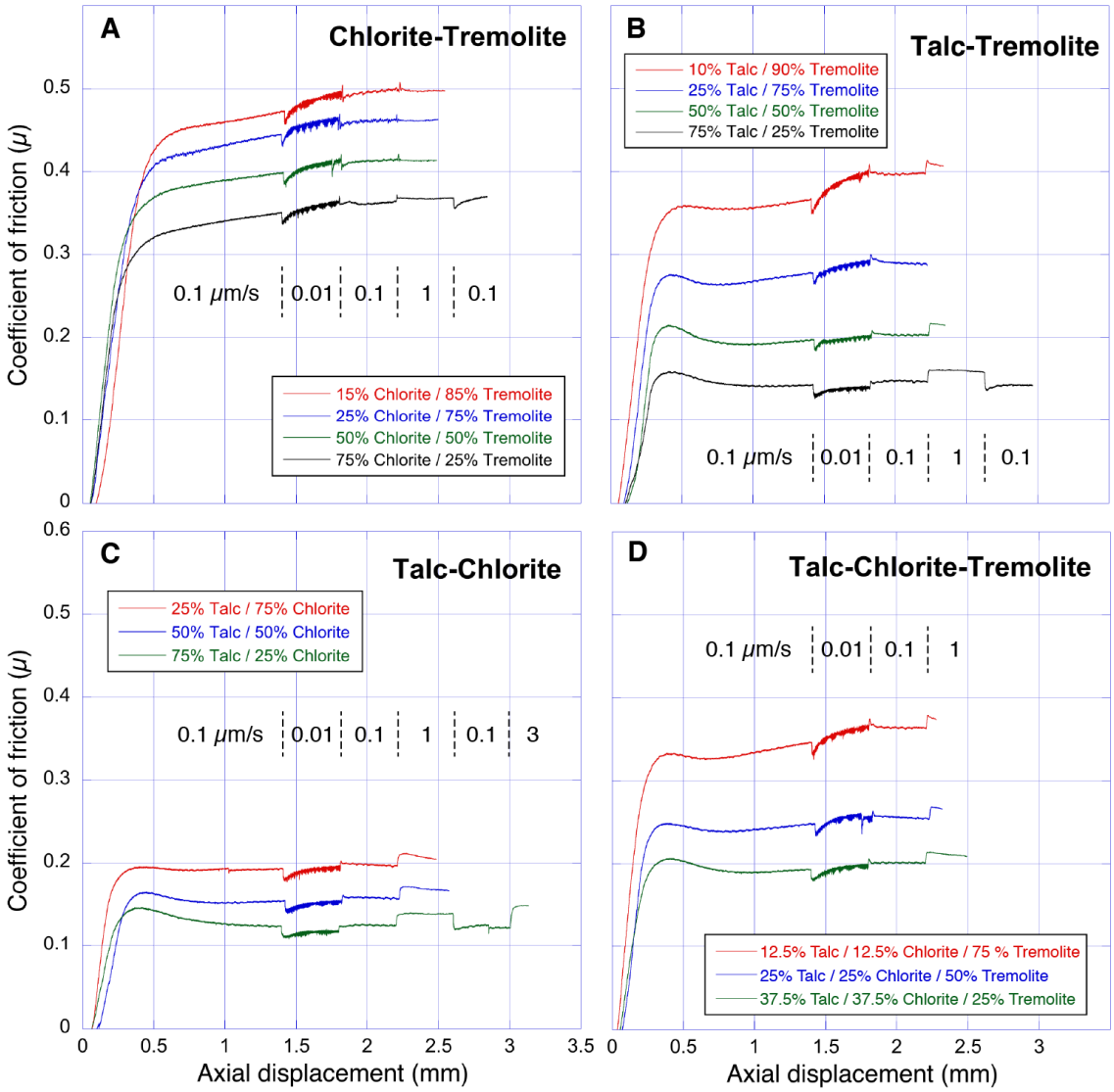

Figure 4.6: Frictional strength experiments on mixtures of talc, chlorite, and tremolite. All experiments were run at 290° C, 90 MPa pore fluid pressure and 230 MPa normal stress (140 MPa effective normal stress) to simulate conditions at ∼9 km depth. Axial velocities varied from 0.01 μm/s to 3 μm/s. The axial sliding velocities are noted on each figure.

4.5 Discussion

4.5.1 End-member Gouge

There are many published friction experimental studies on talc, a few on chlorite, and there are no friction data, to our knowledge, on tremolite. Talc at 290° C has a

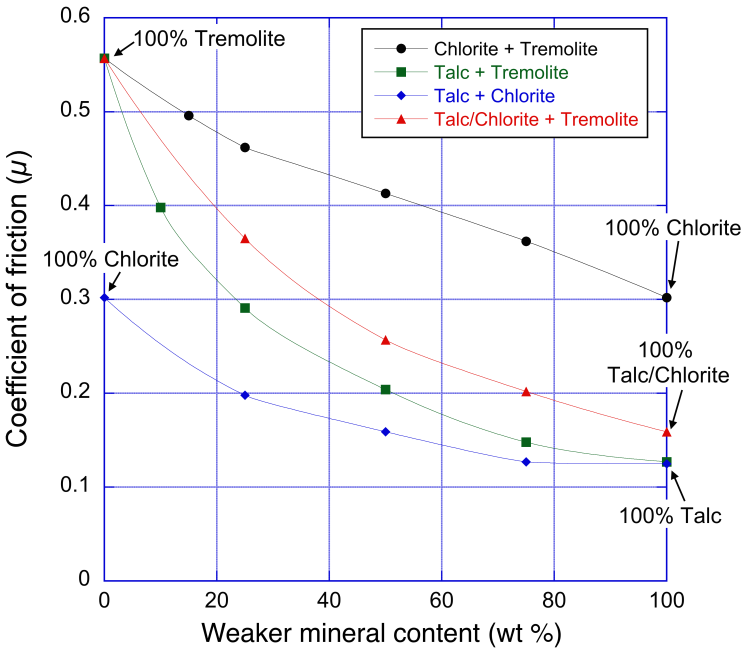

Figure 4.7: Evolution of the coefficient of friction (μ) for different binary mixtures (weight percent). Values of μ were measured at 2.2 mm axial displacement.

low frictional strength and promotes stable sliding/velocity strengthening behavior which agrees with previously published friction data showing talc is velocity strengthening for the temperature range from 25° C to 400° C (Moore and Lockner, 2008).

Chlorite is velocity strengthening at a range of temperatures from 25° C to 300° C, consistent with our results (Moore and Lockner, 2015). The chlorite collected from Lake Pillsbury also has a similar composition to previously collected chlorite gouge which is shown to be weak ($\mu < 0.36$) (Moore and Lockner, 2015).

4.5.2 Synthetic Gouge Mixtures

Mixtures

The talc-tremolite trend (Figure 4.7, green trend line) shows a significant decrease of μ with increasing weight percent content of talc. This has similarities to other studies looking at binary mixtures of a strong mineral with a very weak mineral such as the study of Moore and Lockner (2011) on quartz-talc and the study of Tembe et al. (2010) on quartz-montmorillonite. Both studies are similar to the three-regime soil mechanics model of Lupini et al. (1981) which describes three distinct regimes in bentonite-quartz experiments with increasing bentonite-clay content. In the first regime, the bentonite clay concentration is low, the clays fit into the pore spaces in between the framework of quartz grains, and μ is close to that of quartz. In the second regime, the clay concentration is high enough so that they clay can form a connected network of weak minerals, thus the strength decreases significantly as more clay is introduced. In the third regime, there is an oversaturation of clay content and the clays are all connected, each grain of quartz is no longer in contact with another, and the friction is close to that of bentonite. These mixtures will initially have a moderate reduction in frictional strength (within the first $\sim$ 25%) followed by a more significant decrease in μ (between 25% to 75%), followed by a moderate decrease to the end-member value. Although the talc-tremolite gouge does have a significant decrease in strength with increasing talc content, the trend does not show this first regime of Lupini et al. (1981). The talc-tremolite trend instead follows a trend similar to the talc-serpentine trends in Moore and Lockner (2011), showing a rapid drop in frictional strength up to 75% of talc which tapers off to the end-member value of talc. This is due to both talc and

chlorite, just like talc and serpentinite in Moore and Lockner (2011), are platy minerals with no equant (i.e round) grains creating pore space for the phyllosilicate minerals to fill in. The equal parts talc-chlorite-tremolite mixture and the chlorite-talc mixture both do not show the first-regime either (Figure 4.7, blue and red trend lines).

The chlorite-tremolite (Figure 4.7, black trend line) mixtures follow a near linear decrease at two different rates, different from the talc-bearing mixtures. The chlorite-tremolite mixture initially has a significant decrease in friction strength from 0% to 25% chlorite content and then, at higher percentages of chlorite has a moderate decrease in strength to the end-member value of chlorite. This is similar to other studies looking at an intermediate strength mineral like chlorite (such as illite, kaolinite, muscovite) mixed with a strong mineral such as tremolite. Such studies includes the illite-quartz trend from Tembe et al. (2010), kaolinite-quartz from Crawford et al. (2008), and muscovite-quartz from Lupini et al. (1981) which while being conducted under differing conditions, all still show a 2-regime, decreasing slope to the fitted curve with increasing clay content between all the mixtures. When compared to the Tembe et al. (2010) mixture using a strong mineral with equal proportions of an intermediate and weak mineral (quartz, illite, and montmorillonite, respectively), the Tembe et al. (2010) mixture still fit within the three-regime model of (Lupini et al., 1981), whereas our data does not show these three distinct regimes. Instead, our data follows a significant decrease similar to that of the talc-tremolite trend line but at slightly higher values (Figure 4.7).

Talc is the main mineral that is most effective at weakening and promoting stable slip for all of our tremolite-bearing gouges. The talc-bearing gouges do not follow the 3-

regime trend of Lupini et al. (1981) and instead show a significant decrease in strength at all talc concentrations suggesting that even small amounts of talc have a significant effect on the gouge strength. This is further seen in the chlorite-tremolite gouge which does not show this large decrease in strength that is seen for the talc-bearing gouges. For talc to promote fault creep in thoroughly altered serpentinite at depths of ∼9 km, it will need to be concentrated in layers within the sheared gouge matrix such as regime two of Lupini et al. (1981), as the talc needs to be interconnected .

Ternary Diagram

The experimental results are summarized in a ternary compositional plot (Figure 4.8), showing the value of μ at 2.2 mm displacement and the combined velocity data of each synthetic mixture (Table 4.1). The color of the circle corresponds to whether the synthetic mixture exhibited stable slip (velocity strengthening; red dots), unstable slip (velocity weakening; blue dots), or a mixed sliding behavior (green dots).

We plot contour lines of constant μ (Figure 4.8, dashed lines) to map out the variation of the coefficient of friction throughout the diagram, based on the fitted curves in Figure 4.7. Overall, the contour lines are approximately straight except near the tremolite corner. Talc has a large influence on lowering the strength for all mixtures at all concentrations.

The distribution of mixtures that exhibit velocity strengthening behaviors (stable slip; red dots) versus velocity weakening behaviors (unstable slip; blue dots) occur on different sides of the ternary diagram. The velocity strengthening behavior is focused on the chlorite-talc mixtures and talc-tremolite mixtures with $\geq$ 75% talc. The velocity weaken-

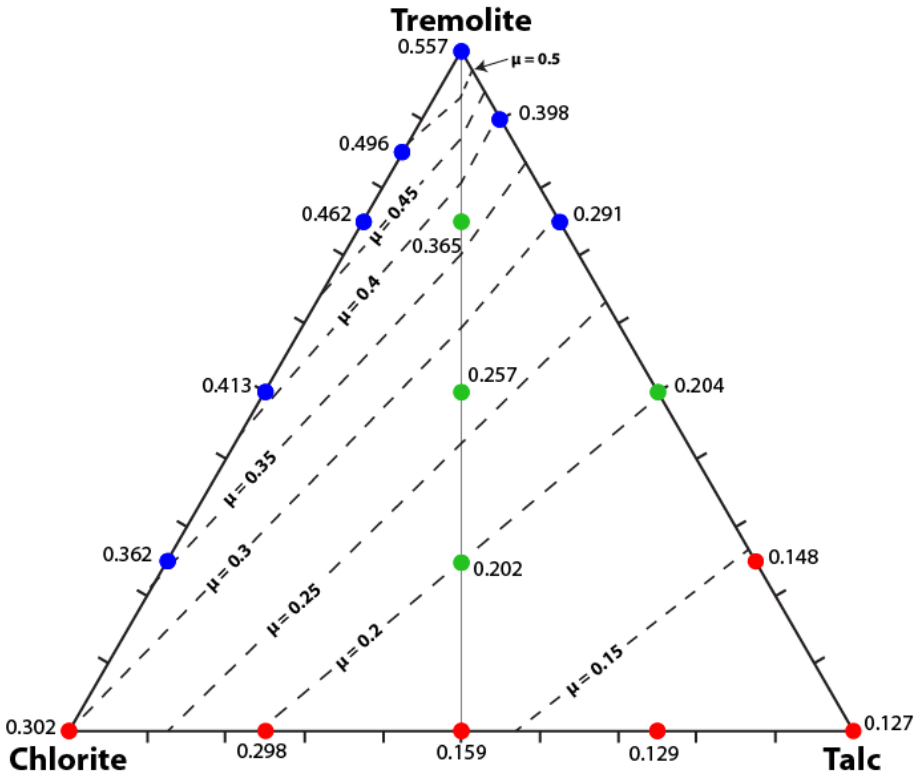

Figure 4.8: The ternary diagram (right) showing all talc-chlorite-tremolite synthetic mixtures used at 290° C, represented as dots. Each dot is associated with the coefficient of friction value for each mixture (Figure 4.7 and Table 4.1). The contour lines (dashed lines) were constructed using values from Figure 4.7. The colors of the dots represent whether each composition promoted stable slip (i.e., velocity strengthening; red) or unstable slip (i.e., velocity weakening; blue) at all velocity steps, or mixed sliding behavior (green). Mixed sliding behavior means the gouge exhibited different behaviors at different velocity steps.

ing behavior is focused on all chlorite-tremolite mixtures and talc-tremolite mixtures with $\leq$25% talc. All ternary mixtures and the 50:50 talc-tremolite mixture have mixed behavior which means the gouges exhibited velocity strengthening, weakening, or neutral behaviors at different velocity steps (Table 4.1). The two main minerals driving whether the synthetic gouge is velocity strengthening or velocity weakening are talc and tremolite. Chlorite is velocity strengthening but can easily be influenced to be velocity weakening with minor amounts of tremolite. Thus, if the fault is creeping there must be a higher amount of talc

within the fault zone that is concentrated into a connected network of layers/veins within the gouge.

4.5.3 Implications for Fault Creep

Moore et al. (2018) determined the talc, chlorite, tremolite mineral assemblage represents hydrothermal metamorphism (metasomatism) that occurred at depth (temperature ≥ 250 ° C) due to the contact between ultramafic and siliceous rocks. This mineral assemblage is common in hydrothermally metamorphosed oceanic rocks over a range of temperatures and is found in other tectonic environments such as at oceanic detachment faults, oceanic fracture zones, and found in orogenic belts (Boschi et al., 2006). From the textures of the rock types collected at Lake Pillsbury, it is most likely that this metasomatism at the Bartlett Springs fault was a static process where the resultant product was later incorporated into the Bartlett Springs fault, and then subjected to shearing (Moore et al., 2018).

These sets of experiments provide insight into what type of fault behavior would be expected if the antigorite serpentinite within the fault were to be fully converted into the talc + chlorite + tremolite mineral assemblage at depth. If a high (>50 %) amount of talc is present within the fault zone, fault creep will most likely occur. If there is a higher portion of tremolite than talc within the fault zone, fault creep can still occur if the talc is concentrated into layers/veins within the gouge. Chlorite can promote fault creep if concentrated into layers or if mixed with the talc but will not promote fault creep if mixed with the tremolite, although it will weaken the strength of the tremolite. If there is higher amounts of tremolite than talc, and the talc is not able to form into layers within the gouge,

the fault will most likely not exhibit fault creep. In a realistic setting, there is a combination of this mineral assemblage and the antigorite serpentinite within the fault zone where there should be higher proportions of the antigorite, talc, and/or chlorite than the tremolite in order for fault creep to occur.

SAFOD provided the first evidence of a direct connection between serpentinite and Mg-rich phyllosilicates in promoting fault creep (e.g., Moore and Rymer, 2007b). The Bartlett Springs fault gouge is the higher temperature, deeper source equivalent to the SAFOD gouge (Moore et al., 2018). There are other serpentinite outcrops along other known creeping faults in northern California (Schroeder, 2010), including the Maacama and Rodgers Creek faults. These faults could also be tapping into a similar ophiolite source at depth as that suggested for the Bartlett Springs Fault (Moore et al., 2018) and could also explain the observations of fault creep along these faults. Finding this connection at other localities in northern California and identifying their relationship between their mineralogy and frictional behavior should be investigated further.

Chapter 5

Strength of ultramafic-rich gouge from the Bartlett Springs Fault, California compared to SAFOD gouges: Implications for fault creep

5.1 Introduction

Fault creep, or aseismic fault slip, has been identified along many faults in California from studies on a regional scale (i.e., using InSAR Funning et al., 2007; Jin and Funning, 2017) to local scales (e.g., using GPS Murray et al., 2014), alignment arrays (Langenheim et al., 2007; Lienkaemper et al., 2014), creepmeters, and offset man-made structures). Such studies have allowed for a more detailed map of where faults are creeping versus where they are locked, which has implications for the seismic hazard of these regions. A creeping fault releases a portion of the accumulated elastic strain along it, thus having the potential to reduce the overall magnitude of a future earthquake. Identifying the extent of creep along the fault trace allows us to understand not only where faults are creeping but why — what mineralogical and frictional properties of the fault material are promoting a fault to creep and what geological factors are important / distinctive to faults that creep.

One large study connecting fault creep to a geological and/or mineralogical control was the San Andreas Fault Observatory at Depth (SAFOD) drilling project. SAFOD collected fault zone material from a known creeping section of the San Andreas fault where repeating earthquakes were occurring at about 2.7 km depth (Zoback et al., 2010). Two actively creeping strands of the San Andreas fault were identified in a 200 m wide damage zone — the Central Deforming Zone (CDZ) and Southwest Deforming Zone (SDZ) — based on the deformation of steel casings in the borehole (Zoback et al., 2010). The SDZ and CDZ consist of a Mg-rich clay matrix with porphyroclasts of serpentinite and other sedimentary rock types through out the matrix where the serpentinite is not seen anywhere else in the borehole (Moore and Rymer, 2012; Moore, 2014). At Nelson Creek, about 2 km

north of SAFOD, there is a ∼3 m wide outcrop of serpentinite abutting the San Andreas fault containing Mg-rich clay gouge. This gouge is texturally and mineralogicaly similar to the CDZ and SDZ gouge where the serpentinite gouge has been subjected to fluid-assisted and shearing-enhanced reaction with the quartzofeldspathic wall rocks to form the Mg-rich clays in the boreholes at ∼3 km depth (Moore and Rymer, 2012). Serpentinite has also been observed in other parts of the creeping section of the San Andreas fault (e.g., Allen (1968); Irwin and Barnes (1975); Moore and Rymer (2012); Bradbury et al. (2015)) and have been associated with fault creep (e.g., Moore and Lockner (2013); Reinen (2000)).

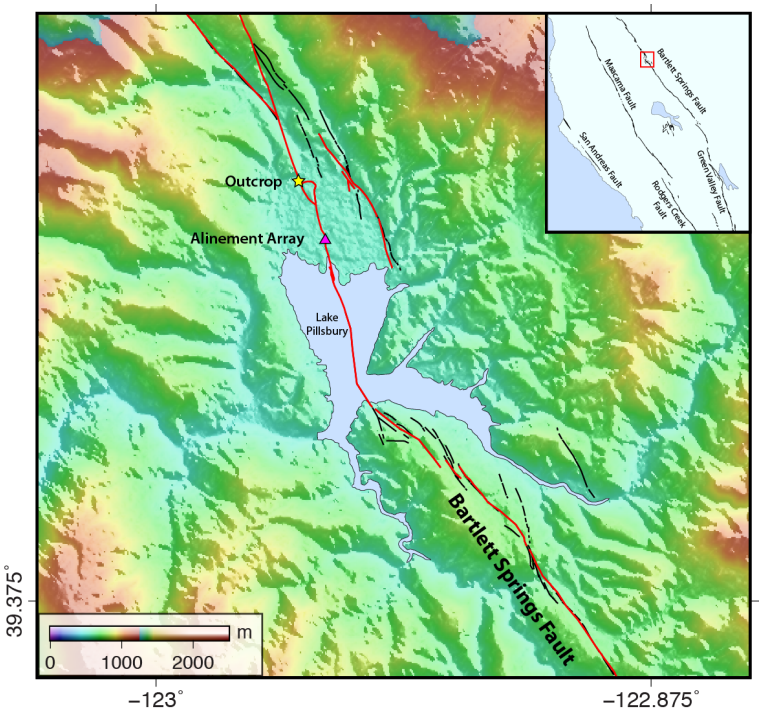

Figure 5.1: Map of Lake Pillsbury region on the Bartlett Springs Fault showing the recently active fault traces (red lines; (Lienkaemper, 2010)) and the locations of the outcrop (yellow star; Figure 5.2) and the alinement array measuring 3.4 ± 0.1 mm/yr of surface creep (pink triangle; (Lienkaemper et al., 2014)).

Additional studies on other faults are needed to find connections between mineralogical and frictional properties that can promote fault creep. A good candidate for comparison to SAFOD is a surface exposure of the Bartlett Springs fault core near Lake Pillsbury, where fault creep has been observed (Figure 5.2). A segment of this fault, in northern California, is known to be stably slipping at the surface and at depth (Lienkaemper et al., 2014) where the highest surface creep rate is located near Lake Pillsbury (McFarland et al., 2018; Murray et al., 2014)(Figure 5.1). The ∼1.5 m-wide fault exposure consists of a serpentinite-bearing fault gouge that is sandwiched between Late Pleistocene sedimentary wall rocks (Moore et al., 2018) (Figure 5.2). The fault gouge consists of the serpentine mineral antigorite and the metasomatic alteration minerals chlorite, tremolite-actinolite, and talc in a matrix of the same materials (Moore et al., 2018). Moore et al. (2018) concluded that the Bartlett Springs mineral assemblage is the higher-temperature (≥250° C) equivalent of SAFOD assemblage at CDZ and SDZ. From Chapter 4 on synthetic binary and ternary mixtures of talc, tremolite, and chlorite we have found that talc is most effective in weakening and promoting velocity strengthening behavior whereas tremolite promotes the opposite (i.e., strengthening and velocity weakening behavior). If all the antigorite serpentinite were altered to the metasomatic mineral assemblage talc + chlorite + tremolite, in order for fault creep to occur on the Bartlett Springs fault at ∼9 km depth, there needs to be concentrated talc and chlorite layers within the fault gouge where shearing is taking place. Now that we know the frictional properties and velocity dependence of each mineral in the fault gouge, we now investigate the frictional properties of the natural Bartlett

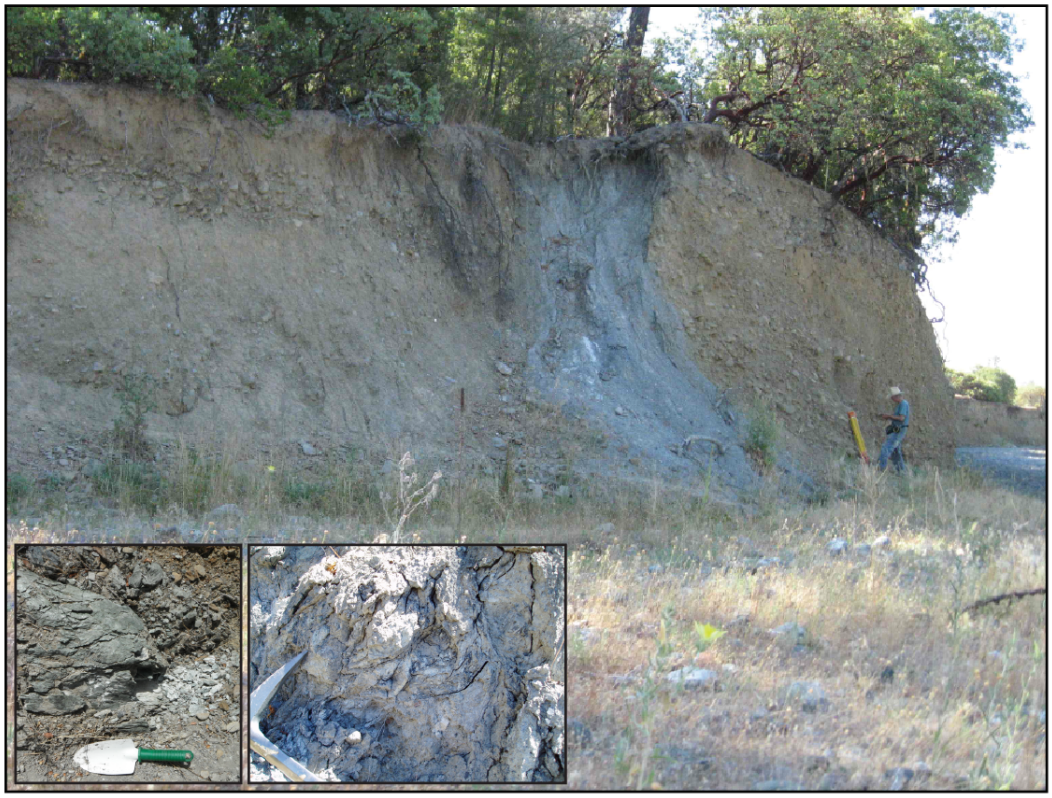

Figure 5.2: Outcrop of the Bartlett Springs fault at Lake Pillsbury (greyish coloring) embedded in the fluvial fan deposits on either side of the fault (orange-yellow coloring) (Credit: James Lienkaemper, 2009). Inset: (left) Largest tremolite clast in outcrop. (right) Heterogeneous gouge showing a mixed, fine-grained matrix of dark and light colored gouge.

Springs fault gouge at temperatures similar to the CDZ and SDZ SAFOD samples (Moore et al., 2016) to determine whether or not they are similar at both locations.

5.2 Experiments

5.2.1 Natural Fault Gouge-matrix Samples

The compositions of four gouge-matrix samples were obtained through whole-rock X-ray fluorescence techniques (Tables 5.1). The samples are briefly described below; for more detailed sample descriptions see Moore et al. (2018).

There are four gouge-matrix samples (Table 5.1). LP15-1f is an antigorite serpentinite-rich gouge matrix, with minor chromian-spinel and magnetite impurities, and no low-temperature alteration minerals (i.e., lizardite and chrysotile). LP16-5 is a chlorite-rich matrix containing clasts of serpentine. D3b-2 contains all minerals found within the fault zone (i.e., talc, chlorite, tremolite, serpentinite, quartz, ±titanite) including low temperature alterations of swelling clay components (i.e., saponite). LP15-c is a chlorite- and talc-rich matrix with porphyroclasts of varying minerals (e.g., serpentinite, tremolite, quartz) and also has a low temperature alteration swelling clay component. Clasts $\geq$ 2 mm in diameter were removed from latter two samples (D3b-2 and LP15-1c). The larger and more rounded serpentinite clasts were removed from LP15-1f. All samples were then ground and passed through a 90-μm sieve.

Each sample was tested at temperatures similar to the temperature at the depth of the SAFOD core (100–110° C) and at temperatures where the antigorite serpentinite and metasomatic mineral assemblage talc, tremolite-actinolite, and chlorite is stable and would have initially crystallized in the gouge (>250–300° C). Refer to Table 5.2 for experiment specific temperature and pressure conditions.

Table 5.1: Major and minor element compositions of Bartlett Springs fault gouge samples, obtained by X-Ray Fluorescence (XRF) techniques. For the full chemical analysis of each sample refer to Appendix A. *Total Fe expressed as FeO.

Gouge sample	**LP15-1f**	**LP16-5**	**D3b-2**	**LP15-1c**
Sample description	Antigorite serpentinite matrix	Chlorite, serpentinite, and talc-rich matrix	Mixture of all fault material matrix	Chlorite, talc, and metasedimentary clasts-rich matrix
SiO_2	40.39	44.42	45.14	45.69
TiO_2	0.01	0.38	0.45	0.51
Al_2O_3	0.53	7.28	8.8	7.32
Cr_2O_3	0.32	0.2	0.19	0.26
FeO*	7.64	6.85	7.38	7.79
NiO	0.28	0.19	0.16	0.18
MnO	0.1	0.1	0.12	0.15
MgO	37.2	24.71	22.2	22.67
CaO	0.75	1.1	2.41	3.61
Na_2O	0	0.35	0.43	0.3
K_2O	0	0.6	0.52	0.15
P_2O_5	0.01	0.09	0.1	0.09
Sum	87.23	86.27	87.92	88.72
LOI %	12.54	13.51	11.57	10.82

Table 5.2: Description of fault gouge-matrix samples tested at varying conditions.

Gouge Sample	Rock Type	Temp (°C)	Driving block	Jacket	Pore Pressure (MPa)	Confining Pressure (MPa)	Effective Normal Stress (MPa)
LP15-1F	Antigorite gouge	25	Granite	Pb	20	50	30
		290	Granite	Cu	90	230	140
		290	Serpentinite	Cu	90	230	140
LP16-5	Chlorite-rich gouge	110	Granite	Pb	30	76.5	46.5
		290	Granite	Cu	90	230	140
D3B-2	Fully mixed gouge	110	Granite	Pb	30	76.5	46.5
		290	Granite	Cu	90	230	140
LP15-1C	Chlorite- & talc-rich gouge	110	Granite	Pb	30	76.5	46.5

5.2.2 Experimental Procedure

All experiments were conducted under varying conditions and listed in Table 5.2 (i.e., pore pressure, confining pressure, effective normal stress, and driving blocks and jackets used). We use a triaxial apparatus (Figure 5.3) with a prepared cylindrical driving block (19.1 mm in diameter and 41 mm in length) with a saw cut inclined at 30°. The driving block is composed of either Westerly granite or antigorite serpentinite and the saw cut faces were ground with a 120-grit SiC. A 1 mm-thick layer of the gouge is sandwiched between the two halves of the driving block. The gouge is mixed with deionized water and smeared as a thick paste onto the saw-cut surface of the lower driving block; the upper driving block is then placed over the gouge layer. The upper driving block contains a borehole for pore-fluid entry; a short steel tube is inserted into the borehole to reduce the extrusion of gouge into the borehole during the experiment. The prepared sample—driving blocks with the layer of

gouge—is then inserted into a jacket to keep the assembly in place. Lead jackets were used for the experiments at $\leq$110° C, and copper jackets for experiments at 290° C. The shear resistance of the jacket is removed from the total shear stress after the experiment. Details on the lead jacket corrections are discussed in Moore and Lockner (2011) and the annealed copper jacket corrections are in Moore and Lockner (2008). A furnace is then placed around the jacketed assembly; the space in between the furnace and sample is loosely packed with boron nitride—a good thermal insulator and poor electrical conductor.

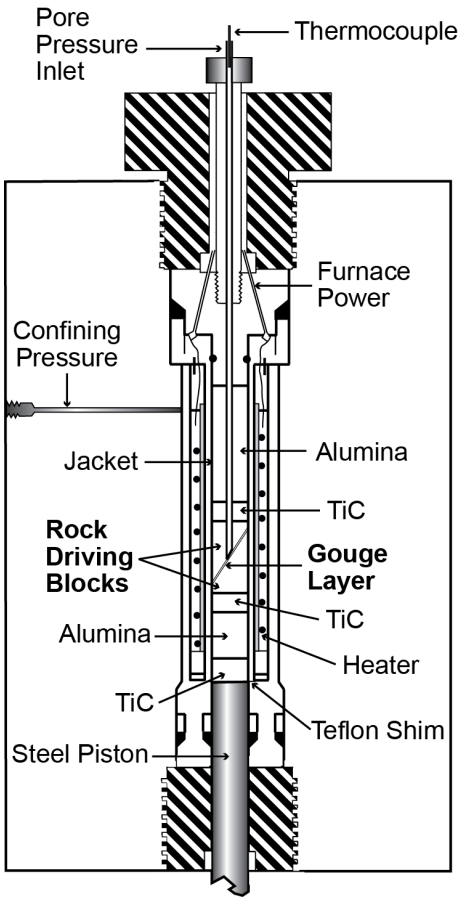

Figure 5.3: Experimental apparatus setup. Modified from Moore and Lockner (2013).

Once the full assembly is in the traxial machine, confining pressure is first applied, followed by pore pressure—using deionized water for the pore fluid. The normal stress is held constant and maintained through computer-controlled adjustments to the confining pressure. The temperature is then raised and monitored by a thermocouple inserted in the pore pressure inlet. The pore fluid pressure, effective normal stress, normal stress, and temperatures are noted in Table 5.2. During the experiment, a steel piston at the bottom of the apparatus pushed up against the base of the sample column which resulted in shearing within the layer of gouge. The axial displacement rates changed in steps that varied between 0.01 μm/s and 3.0 μm/s. A Teflon shim, between the end plug and steel piston was greased to allow for lateral slip during shear. Corrections for seal friction were accounted for using the procedure of Moore and Lockner (2008).

5.3 Results

5.3.1 Serpentinite

We ran three experiments in total (Table 5.3) on the serpentinite gouge (LP15-1F): a 25° C temperature experiment using granite driving blocks, a 290° C temperature experiment using granite driving blocks (Figure 5.4A), and an additional 290° C temperature experiment using serpentinite driving blocks (Figure 5.4B).

At the 25° C temperature conditions, the strength of the gouge did not vary significantly with changes in shearing rates, with μ ranging between 0.35 to 0.40 (Figure 5.4A). The reference velocity of 0.1 μm/s had a coefficient of friction (μ) at $\sim$0.4 through

Table 5.3: Velocity dependence of serpentinite samples.

Gouge Sample	Velocity Step	(a-b)	Error (±)
LP15-1f 25°C	0.1 - 0.01	0.0005	0.0003
	0.01 - 0.1	0.0019	0.0006
	0.1 - 1	-0.0023	0.0003
	1 - 0.1	-0.0052	0.0003
	0.1 - 3	-0.0004	0.0002
LP15-1f 290°C Granite	0.1 - 1	0.0070	0.0005
LP15-1f 290°C Serpentinite	0.1 - 0.01	0.0055	0.0009
	0.01 - 0.1	0.0078	0.0009
	0.1 - 1	0.0056	0.0005
	1 - 0.1	0.0026	0.0003

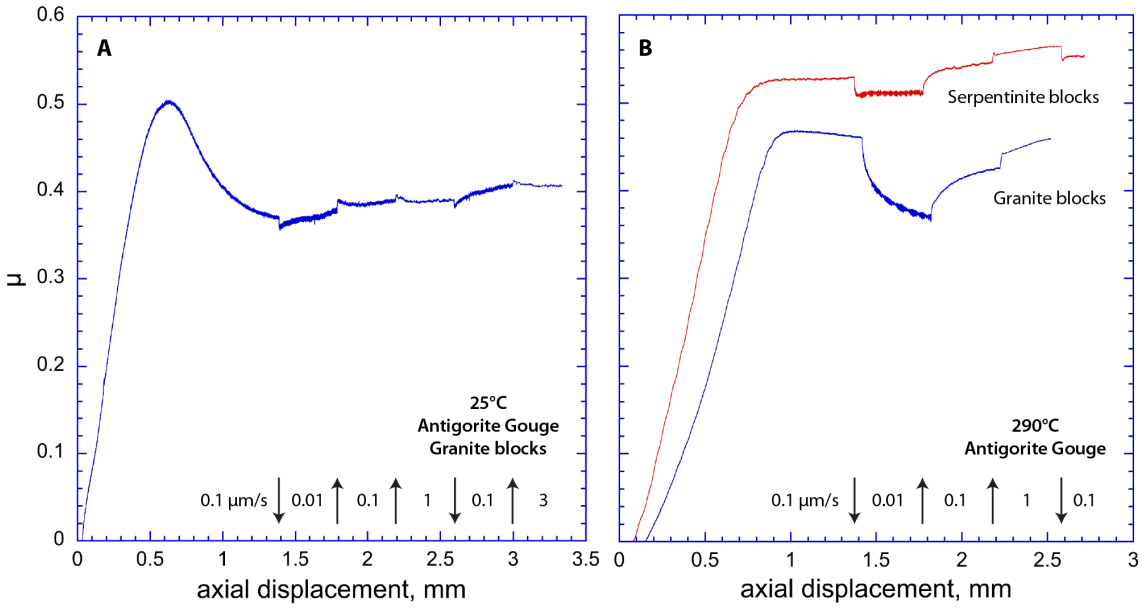

Figure 5.4: Antigorite serpenitnite gouge strengths at 25° C (Figure A) and 290° C (Figure B) temperatures. There were two experiments run at 290°C temperatures which either used two serpentinite driving blocks or granite driving blocks. Arrows indicate if the velocity step was an increase (up arrow) or decrease (down arrow) in velocity.

Table 5.4: Velocity dependence of natural samples.

Gouge Sample	Velocity Step	(a-b)	Error (±)
LP16-5 110˚C	0.1 - 0.01	0.0017	0.0013
	0.01 - 0.1	0.0025	0.0009
	0.1 - 1	0.0028	0.0007
	1 - 0.1	0.0038	0.0003
	0.1 - 3	0.0051	0.0002
	3 - 0.1	0.0029	0.0003
D3b-2 110˚C	0.1 - 0.01	0.0025	0.0004
	0.01 - 0.1	0.0043	0.0019
	0.1 - 1	0.0060	0.0000
	1 - 0.1	0.0057	0.0006
	0.1 - 3	0.0073	0.0004
	3 - 0.1	0.0064	0.0004
LP15-1c 110˚C	0.1 - 0.01	0.0040	0.0015
	0.01 - 0.1	0.0053	0.0023
	0.1 - 1	0.0073	0.0005
	1 - 0.1	0.0069	0.0007
	0.1 - 3	0.0075	0.0006
	3 - 0.1	0.0074	0.0007
LP16-5 290˚C	0.1 - 0.01	0.0001	0.0011
	0.01 - 0.1	0.0014	0.0006
	0.1 - 1	0.0037	0.0004
	1 - 0.1	0.0033	0.0004
	0.1 - 3	0.0095	0.0003
D3b-2 290˚C	0.1 - 0.01	0.0009	0.0011
	0.01 - 0.1	0.0016	0.0013
	0.1 - 1	0.0052	0.0002
	1 - 0.1	0.0039	0.0002

all velocity step changes. The gouge has a mixed sliding behavior characterized by velocity-strengthening behavior at the lowest velocity step and velocity weakening at higher velocities (Figure 5.5).

At the 290° C temperature condition, the gouge is velocity strengthening (Figure 5.5) but the strength of the gouge varies more significantly, ranging between ∼0.47 to ∼0.36 (Figure 5.4). There is a significant decrease in strength (μ range: 0.46 to 0.36) during the slowest shearing rate of 0.01 μm/s. This is influenced by a chemical reaction that is weakening the gouge, which most prominent in the slowest rate. The following velocity step increase (0.01 to 0.1 μm/s) shows a recovery ($\Delta\mu$ ∼0.05) from the weakening in the previous, slowest interval, where the strength trend initially has a steep slope but then changes to a more gradual trend by the end of the interval. After the last velocity step change, this interval (1 μm/s) shows the same gradual trend from the end of the previous step. All (a-b) values are higher than the corresponding 25° C and the serpentinite gouge sheared between granite driving blocks exhibits the highest value at the velocity step range of -0.5 (Figure 5.5).

In the two experiments using granite driving blocks versus serpentinite driving blocks, the granite driving blocks significantly weaken the gouge strength when compared to the reference strength of the gouge in the serpentinite driving blocks at increased temperatures. In the serpentinite driving blocks, the gouge exhibits velocity strengthening behavior where μ ranged between 0.5 to 0.55 with no change in strength during the slowest velocity step. In this ultramafic chemical system (i.e., serpentinite gouge within serpentinite driving blocks), the serpentinite gouge gets stronger when heated. When shearing

the gouge between granite driving blocks, as described above, the gouge weakens during the slowest velocity step due to a chemical reaction between the serpenitite gouge and the granite driving blocks. This chemical reaction has also been seen in shearing serpenitnite gouge between ultramafic driving blocks versus granite driving blocks (Moore and Rymer, 2007a; Moore and Lockner, 2013).

When comparing the velocity dependence of shearing strength (i.e., a-b values) between the 25° C and 290° C values, all negative step changes (i.e., a decrease in velocity as indicated by the arrows in Figure 5.4) exhibit a lower (a-b) value than there corresponding positive step change (Figure 5.5). The change in (a-b) between the positive and negative step for the same velocity step show a similar decrease in (a-b) value. For example, at the -0.5 velocity step change, the change in (a-b) between the positive and negative step for the 25° C and 290° C, respectively, are the same at 0.0028.

5.3.2 Fault Gouge Matrix

There are three gouge matrix samples – LP15-C, LP16-5, D3B-2 – that were tested at 110° C and last two were also tested at 290° C (Table 5.4). At 110° C, all three gouges have a low frictional strength with $\mu < 0.21$. The chlorite-talc rich matrix (LP15-C) and the fully mixed matrix (D3B-2) samples have values of μ that overlap through almost all of the velocity steps. The chlorite rich (LP16-5) matrix sample has the lowest μ of all of them ranging between 0.14-0.17. All of the gouges are velocity strengthening where the (a-b)

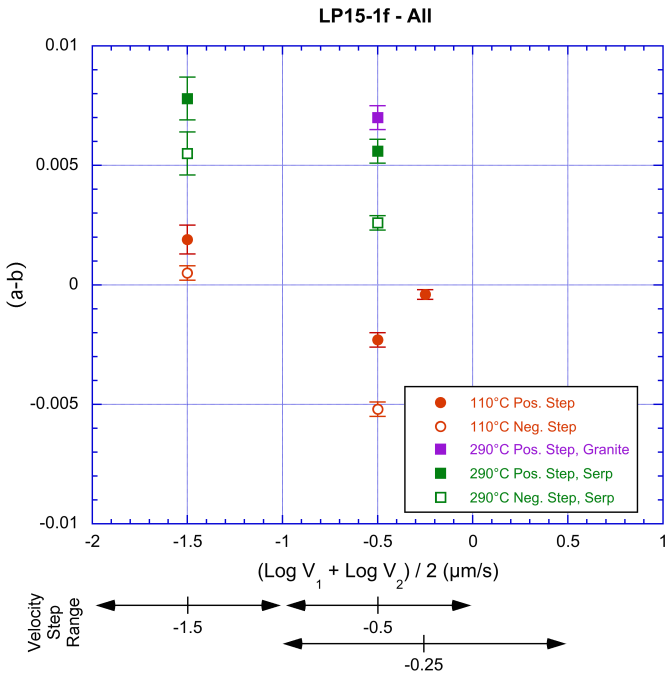

Figure 5.5: Summary of velocity data, (a-b), versus log$V$, for LP15-1f. Data are plotted at the midpoints of the velocity steps, $[(\log V_2 + \log V_1)/2]$, where V_1 is the initial velocity and V_2 the velocity following the step. The velocity range of a given step is shown at the bottom of the figure. The red symbols are represent the 110° C experiments, the purple symbols represent the 290° C experiments using granite driving blocks and the green symbols represent the 290° C experiments using serpentinite driving blocks. The solid symbols denote a positive velocity step and the open symbols denote a negative velocity step.

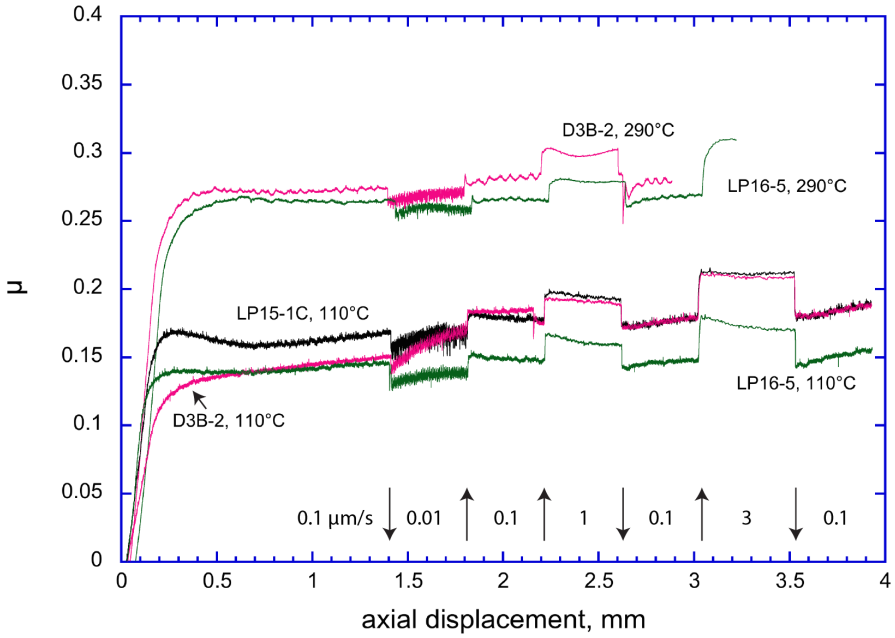

Figure 5.6: Frictional strengths of the fault gouge-matrix samples. Arrows indicate if the velocity step was an increase (up arrow) or decrease (down arrow) in velocity.

value for the negative step changes are all lower than the equivalent positive step changes with the exception of the 1 μm/s to 0.1 μm/s step for LP16-5 (Figure 5.7).

Two of the gouges were tested at higher temperatures (290° C) to see how the gouges would behave at greater depths. LP16-5 was chosen because the sample does not show any swelling clay components in the X-ray diffraction patterns. D3B-2 was tested as a comparison to LP16-5 because it contains a saponite-bearing, swelling clay component. The strengths of both gouge samples increased with temperature where LP16-5 has a slightly lower μ for the same velocity steps as D3B-2 (Figure 5.6). A single straight line can connect all of the reference velocity (0.1 μm/s) steps. All of the samples exhibited velocity-strengthening behavior except for range of (a-b) values at the 0.1 μm/s to 0.01 μm/s for LP16-5 and D3b-2 includes some velocity weakening values (Figure 5.7). Most of the (a-

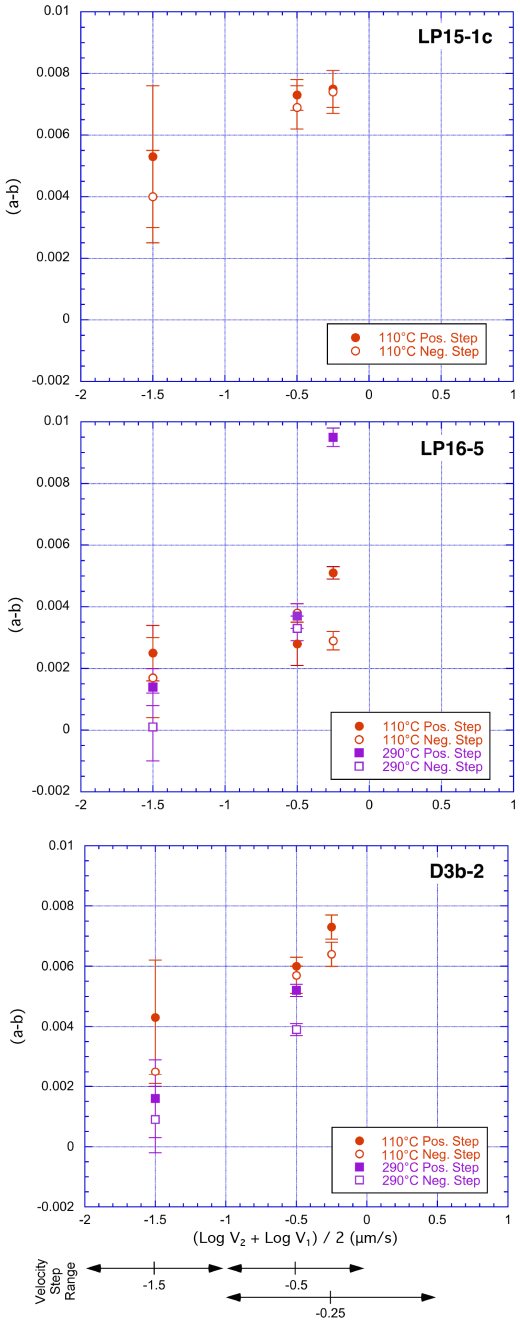

Figure 5.7: Summary of velocity data, (a-b), versus log$V$, for LP15-1c, LP16-5, and D3b-2. Data are plotted at the midpoints of the velocity steps, $[(\log V_2 + \log V_1)/2]$, where V_1 is the initial velocity and V_2 the velocity following the step. The velocity range of a given step is shown at the bottom of the figure. The red symbols are represent the 110° C experiments and the purple symbols represent the 290° C experiments. The solid symbols denote a positive velocity step and the open symbols denote a negative velocity step.

b) values for the negative step changes are lower than the positive step changes with the exception of the same step for LP16-5 as seen at the lower temperature, it is flipped.

Comparing the velocity dependence of shearing strength, (a-b) values, for each gouge at the two temperatures, D3b-2 shows a decrease in (a-b) for all steps with increasing temperature whereas LP16-5 shows a mixed behavior (Figure 5.7). LP16-5 exhibits velocity strengthening behavior for all steps except for the 290° C negative velocity step from 0.1 to 0.01 m/s where the range in values transitions into velocity weakening behavior. The (a-b) values change as the $\Delta LogV$ step decreases (i.e., $\Delta LogV$ step for 0.1 $\mu m/s$ to 0.01 $\mu m/s$ is larger than 0.1 $\mu m/s$ to 3 $\mu m/s$). At the -1.5 velocity range, the 110° C is stronger than the 290° C gouges which becomes similar at the -0.5 velocity range and then reverses at -0.25 where the 290° C is stronger than the 110° C.

5.3.3 Comparison to SAFOD

Fault mineral assemblage previously collected from SAFOD (Moore et al., 2016), at CDZ and SDZ, has been found to be the lower temperature equivalent of the Bartlett Springs Fault gouges samples (Moore et al., 2018). At the lower temperature of 110° C (BSF) and 100° C (SAFOD), the μ values for each fault gouges are similar to SAFOD (Moore et al., 2016) and are all velocity strengthening (Figure 5.7-5.8, Table 5.4). LP16–5, has the lowest range of μ (0.12–0.18) for the Bartlett Springs fault and fall within the range of the SDZ and CDZ μ values of 0.13–0.17 and 0.12–0.16, respectively. The CDZ gouge has the lowest μ values for all samples.

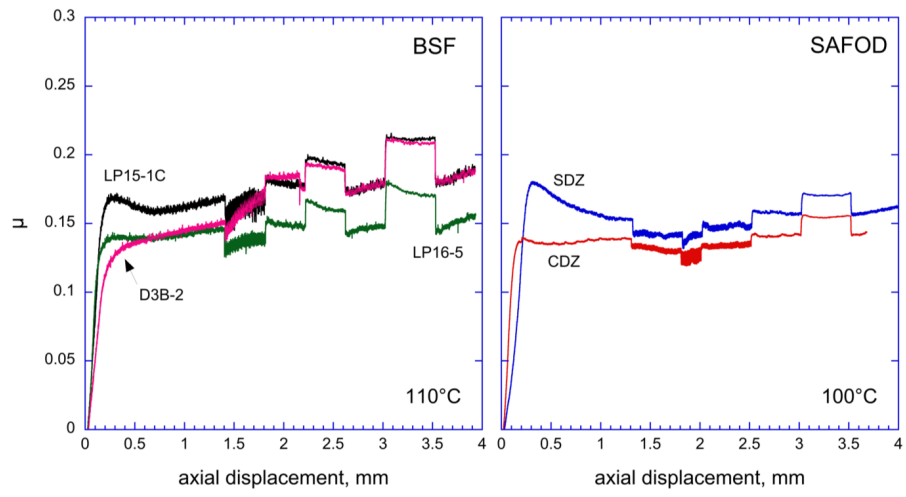

Figure 5.8: Low temperature, frictional strength comparison of SAFOD at 100° C (Moore et al., 2016) and BSF gouge-matrix at 110° C samples. Arrows indicate if the velocity step was an increase (up arrow) or decrease (down arrow) in velocity.

At the higher temperature of 290° C (BSF) and 250° C (SAFOD), the BSF gouge increases with temperature whereas the SAFOD gouges do not (Figure 5.9). The CDZ and SDZ μ ranges from 0.09 to 0.19 where the CDZ μ decreases slightly from the 100° C values (0.09–0.15) and the SDZ stays the same (0.14–0.19). The two gouges tested from the Bartlett Springs fault gouge (D3b-2 and LP16-5), both have an increase in μ by $\sim$0.1. D3B-2 is slightly stronger than LP16-5 at 290° C where at 110° C their strengths were overlapping (Figure 5.8). Although the Bartlett Springs fault gouges strengths increased with temperature, it is velocity strengthening at all velocity steps (Figure 5.7, Table 5.4), which is the same for the SAFOD gouges (Moore et al., 2016).

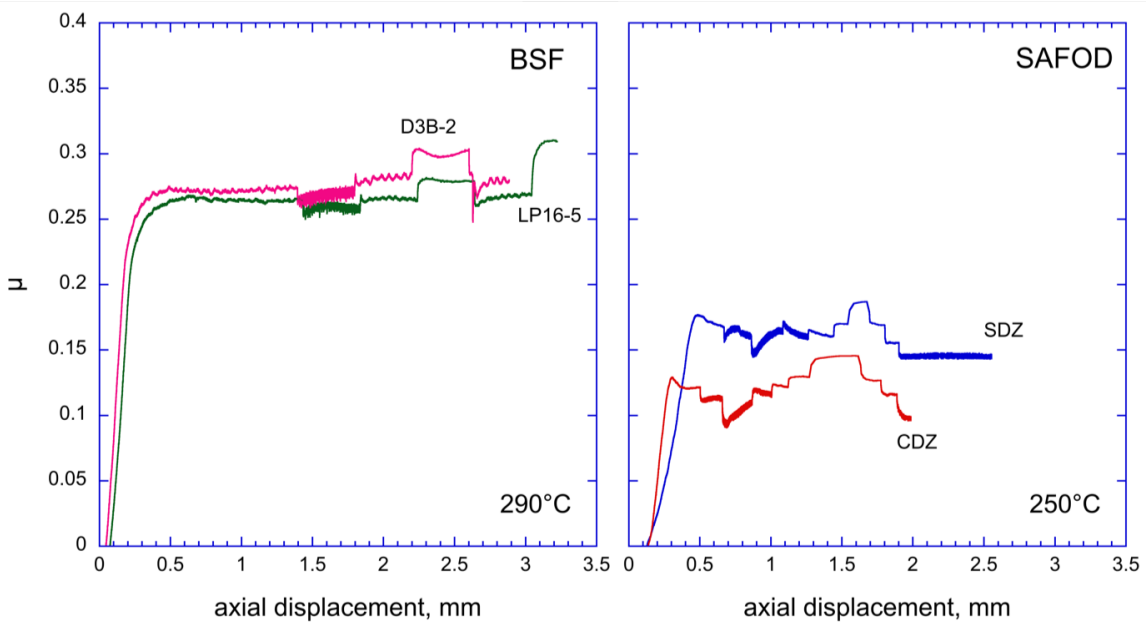

Figure 5.9: High temperature frictional strength comparison of SAFOD at 250° C (Moore et al., 2016) and BSF gouge-matrix at 290° C samples

5.4 Discussion

Serpentinite gouge being sheared between quartzofeldspathic crustal rocks will weaken and promote stable slip at depth which is seen through the experiments at high temperatures (Moore and Lockner, 2013). This chemical weakening behavior, not seen at the lower temperature of 25° C, points to the contrasting composition and temperature as driving factors for weakening the fault gouge. Since all the gouge samples tested show velocity strengthening behavior at low and high temperatures, this indicates that the fault has the potential to be stably slipping throughout the seismogenic zone, up to 9 km depths.

The Bartlett Springs Fault gouge consists of the higher-temperature talc + chlorite + tremolite-actinolite mineral assemblage that is equivalent to the lower-temperature Mg-smectite clays found at SAFOD (Moore et al., 2018). The BSF minerals are most likely

forming at temperatures $\geq 250^{\circ}$ C where the antigorite serpentinite is also stable, and this is most likely where the serpentinite is being incorporated into the fault. At 110° C, the coefficient of friction of the BSF gouges are $\sim$0.15 to 0.20 which falls within the same range as the gouge samples tested at similar temperatures from SAFOD. Both gouges also promote stable slip at all velocity steps tested. The samples still remain velocity strengthening at the higher temperature and pressure conditions, of 290° C and 140 MPa effective normal stress, which correspond to $\sim$ 9 km depth. Thus the Mg-phyllosilicate mineral assemblage at the BSF and the Mg-rich clays at SAFOD are both able to promote stable slip indicating the possibility of fault creep at the surface and at depths to $\sim$9 km where repeating earthquakes have been identified at depth ranges from 1 to 15 km (Shakibay Senobari and Funning, 2019).

5.5 Conclusion

The serpentinite-bearing fault gouge along the Bartlett Springs Fault near Lake Pillsbury is similar in composition to SAFOD, where the low temperature Mg-rich assemblage from SAFOD is equivalent to the Bartlett Springs Fault gouge implying both faults are tapping into a serpentinite source at depth but where the tectonic environments are different (Moore et al., 2018). The frictional behaviors of the BSF and SAFOD fault gouges from both creeping faults are similar, where the Bartlett Springs fault gouge promotes stable slip at low and high temperatures indicating the possibility of fault creep at the shallow and deeper depths of up to $\sim$9 km, which is where repeating earthquakes have been identified. Over time, the serpentinite-bearing gouge being incorporated into the fault zone will

gradually lead to more weakening of the fault with increasing time and displacement. Since the greatest weakening and velocity strengthening properties are due to the alteration of the mineral assemblage to Mg-rich phyllosilicate minerals, this suggests that the present-day shearing along the Bartlett Springs Fault is concentrated in the mixed-gouge matrix materials. Collecting fault gouge from other creeping faults will continue to help understand the mechanisms that are driving fault creep along the San Andreas Fault system.

Chapter 6

Conclusions

In three different projects, we observed fault creep on different length scales to better constrain the distribution of surface creep, estimate how much movement is concentrated on a mapped fault trace versus within a fault zone width, and determine what minerals and gouges are associated with fault creep due to low frictional strength and velocity strengthening behavior. We show that using information from these independent but complimentary techniques as well as others (i.e., alignment arrays, GPS, creepmeters, repeating earthquake families), we have gain a better picture/understanding of the distribution of fault creep along the Maacama, Rodgers Creek faults, the main zone of deformation on the Hayward fault, and the influence of specific minerals to fault creep on the Bartlett Springs fault.

6.1 Main findings

In the first project (Chapter 2), we used InSAR to delimit the extent of fault creep along the Maacama and Rodgers Creek faults to add to previous observations (e.g., McFarland et al. (2018); Lienkaemper et al. (2014); Bilham et al. (2009); Murray et al. (2014); Tong et al. (2013); Funning et al. (2007); Jin and Funning (2017). We use Sentinel-1 data spanning 2015 to 2018 from two different viewing geometries (i.e., ascending and descending tracks) and use the SBAS method which is more effective in a less developed region such as the North Bay. We focus on any LOS velocities changes across the fault by dividing the fault length into 2.5 km sections, project all data within each area onto a profile, detrend the profile and measure the change in LOS velocity as you cross the fault, if any. We sample the data within 5 km on either side of the fault which is sensitive to creep in the upper few kilometers of the fault.

Previous studies on both faults have observed fault creep at specific locations from alignment arrays (McFarland et al., 2018), an InSAR study on the Maacama fault (Tong et al., 2013), and inferred from a GPS-based model (Murray et al., 2014). The northern Rodgers Creek fault has additional InSAR studies from two different decades (Funning et al., 2007; Jin and Funning, 2017). Our results show surface creep along majority of both faults, in locations where creep has not been observed before. Along the Maacama fault we show that more than half of the fault is creeping at the surface. In addition, combining the InSAR observations with repeating earthquake locations from Shakibay Senobari and Funning (2019) suggest that near the city of Willits, the Maacama fault is creeping at the surface and at 10 km depth, south of Ukiah there are fewer repeating earthquakes but a

clear indication of surface creep. North of Cloverdale, there is a high number of repeating earthquakes occurring throughout the seismogenic zone, up to ∼7 km depths in an area where we do not resolve creep but to the south of Cloverdale, near the Geysers Geothermal field we resolve fault creep at rates up to 11 mm/yr, not seen before. Along the northern Rodgers Creek fault, we resolve fault creep at locations observed by previous studies in the previous decade (Funning et al., 2007; Jin and Funning, 2017), at similar rates. It is necessary to use two viewing geometries to decompose the LOS velocities into the fault-parallel and vertical components in order to not over estimate the amount of fault creep along the fault. Future work would include decomposing each ascending and descending data set track to look at the spatial distribution of fault-parallel and vertical motions along the fault. Additional mapping of the local geology and small aquifers in the region can help potentially explain creep rate highs and lows in the data set by exploring associations between creep rate and lithology.

In the second project (Chapter 3), we use Structure from Motion to construct 3D models of offset sidewalks to monitor how fault creep is being expressed within an urban city along the Hayward fault. We acquired photos from 2015 to 2018 from 36 sites, taken from an array of vantage points around the offset sidewalk which were then converted into 3D point cloud models. The models from each site were then compared between different years by aligning the left side of the offset using the Iterative Closest Point matching method and measuring the change in offset on the right side. We conclude that this increasing offset is due to fault creep based on the mapped fault trace and other signs of creep (e.g., en echelon cracks in the pavement, other offset curbs next to and across the road). Our

results show that each offset sidewalk accommodates fault movement in different ways, for example, through multiple offset curbs within a distributed shear zone over ∼3 meters wide, or expressing movement through curb-vertical movement one year and curb-perpendicular movement the next. On average we are sampling less than 40% of the overall creep rate measured from nearby alignment arrays (McFarland et al., 2018) suggesting that fault deformation occurs within a larger area than one offset curb but smaller than an alignment array. In monitoring offset sidewalks, we are not measuring the full fault zone width that an alignment array is measuring but instead are measuring the main zone of deformation due to fault creep. Future work would be to install permanent markers and to monitor a larger area than just each offset curb. A suggestion is to use a low flying drone to photograph the entire road length surrounding each offset curb to measure deformation within the immediate area. This would allow for a better definition of off-fault deformation and help quantify the main zone of deformation.

In the third project (Chapters 4 and 5), we analyze fault gouge collected from the Bartlett Springs fault at a location known to be creeping. The gouge consists of antigorite serpentinite and the metasomatic mineral assemblage talc-chlorite-tremolite, considered to be the higher-temperature equivalents of Mg-rich smectite clays from the San Andreas Fault Observatory at Depth (SAFOD) (i.e., both gouges have the same bulk chemistry Moore et al., 2018) which are shown to promote shallow fault creep. We conducted two sets of experiments, the first experiment being a series of mixing-law experiments (i.e., different proportions of minerals in each synthetic gouge), at temperatures similar to where this mineral assemblage would have formed, focused on understanding their frictional properties.

We created synthetic gouge mixtures to investigate the strength of each mineral and what proportions of each are needed to support fault creep at depth. The second experiment was to investigate the frictional properties of the natural fault gouge at temperatures similar to the SAFOD samples to compare whether they are similar at both locations.

Our mixing-law experiments show that there is a possibility for fault creep to occur if the antigorite serpentinite gouge is fully converted into the talc-chlorite-tremolite mineral assemblage at depth. Both chlorite and talc can promote fault creep, whereas tremolite does not support fault creep. Talc is the main mineral component needed to promote creep; at least 50% talc is needed. Thus, in order for a fault to creep, the talc needs to be connected in concentrated layers within the fault zone. The talc and chlorite are most likely promoting fault creep within concentrated layers in the fault zone. If there are higher amounts of tremolite where talc cannot form into layers within the gouge, the fault will most likely not creep. Our natural gouge results show that the Bartlett Springs fault gouge and the San Andreas Fault Observatory at Depth (SAFOD) have similar frictional behaviors – the Bartlett Springs fault gouge promotes stable slip at both high and low temperatures suggesting that fault creep can occur at shallow depths and at depths of ∼9 km on the Bartlett Springs fault. This is further corroborated by the occurrence of repeating earthquakes, and therefore likely creep, at ∼10 km depth (Shakibay Senobari and Funning, 2019). At both locations, the fault is tapping into a deep serpentinite source at depth, and over time this serpentinite-bearing gouge is slowly incorporated more into the fault zone as it rises buoyantly to the surface, there will be more weakening of the fault resulting in more fault creep occurring along the Bartlett Springs fault. It is most likely

that the present-day shearing along the Bartlett Springs fault is occurring within a gouge matrix containing the talc-chlorite-tremolite mineral assemblage with concentrated layers with higher percentages of talc (>50%). Future work would include collecting fault gouge and running frictional experiments on samples from other creeping faults in California to develop a profile/definition for the mineralogical and frictional properties of creeping faults associated with the San Andreas fault system.

In summary, these projects explored complementary approaches aimed at understanding different aspects of fault creep; the extent of fault creep along the Maacama and Rodgers Creek faults, the frictional properties associated with a creeping fault and what depths the fault is expected to creep, and the expression of fault creep manifesting within an urban environment. Compiling additional studies focused on fault creep, for example geologic studies, other geodetic studies, seismology, and friction experiments we can build a better, overall picture of the distribution of fault creep at the surface and at depth, the geological conditions and mineralogy necessary for a fault to creep.

Bibliography

Allen, C. R. (1968). The tectonic environments of seismically active and inactive areas along the San Andreas fault system. *Stanford University Publications. Geological Sciences 11*, 70–80.

Ambraseys, N. N. (1970). Some characteristic features of the anatolian fault zone. *Tectonophysics 9*(2-3), 143–165.

Bekaert, D., A. Hooper, and T. Wright (2015). Reassessing the 2006 guerrero slow-slip event, mexico: Implications for large earthquakes in the guerrero gap. *Journal of Geophysical Research: Solid Earth 120*(2), 1357–1375.

Bekaert, D., R. Walters, T. Wright, A. Hooper, and D. Parker (2015). Statistical comparison of insar tropospheric correction techniques. *Remote Sensing of Environment 170*, 40–47.

Bemis, S. P., S. Micklethwaite, D. Turner, M. R. James, S. Akciz, S. T. Thiele, and H. A. Bangash (2014). Ground-based and uav-based photogrammetry: A multi-scale, high-resolution mapping tool for structural geology and paleoseismology. *Journal of Structural Geology 69*, 163–178.

Berardino, P., F. Gianfranco, R. Lanari, and E. Sansosti (2002). A new algorithm for monitoring localized deformation phenomena based on small baseline differential SAR interferograms. *IEEE International Geoscience and Remote Sensing Symposium 2*(11), 2375–2383.

Bilham, R., N. Suszek, and S. Pinkney (2004). California creepmeters. *Seismological Research Letters 75*(4), 481.

Bilham, R., N. Suszek, and S. Pinkney (2009). California Creepmeters. *Seismological Research Letters 75*(4), 481–492.

Boschi, C., G. L. Früh-green, and J. Escartín (2006). Occurrence and significance of serpentine-hosted, talc- and amphibole-rich fault rock in modern oceanic setting and ophiolite complexes: an overview. *Ofioliti 31*(2), 129–140.

Bradbury, K. K., C. R. Davis, J. W. Shervais, S. U. Janecke, and J. P. Evans (2015). Composition, alteration, and texture of fault-related rocks from safod core and surface outcrop analogs: Evidence for deformation processes and fluid-rock interactions. *Pure and Applied Geophysics 172*(5), 1053–1078.

Budding, K. E., D. P. Schwartz, and D. H. Oppenheimer (1991). Slip rate, earthquake recurrence, and seismogenic potential of the rodgers creek fault zone, northern california: Initial results. *Geophysical Research Letters 18*(3), 447–450.

Bürgmann, R., P. A. Rosen, and E. J. Fielding (2000). Synthetic aperture radar interferometry to measure earths surface topography and its deformation. *Annual review of earth and planetary sciences 28*(1), 169–209.

Bürgmann, R., D. A. Schmidt, R. M. Nadeau, M. A. D'Alessio, E. J. Fielding, D. Manaker, T. V. McEvilly, and M. H. Murray (2000). Earthquake Potential Along the Northern Hayward Fault, California. *Science 289*(August), 1178–1183.

Carr, B. B., A. B. Clarke, J. R. Arrowsmith, L. Vanderkluysen, and B. E. Dhanu (2018). The emplacement of the active lava flow at sinabung volcano, sumatra, indonesia, documented by structure-from-motion photogrammetry. *Journal of Volcanology and Geothermal Research*.

Cetin, E., Z. Cakir, M. Meghraoui, S. Ergintav, and A. M. Akoglu (2014). Extent and distribution of aseismic slip on the ismetpaşa segment of the north anatolian fault (turkey) from persistent scatterer insar. *Geochemistry, Geophysics, Geosystems 15*(7), 2883–2894.

Chaussard, E., R. Bürgmann, H. Fattahi, C. Johnson, R. Nadeau, T. Taira, and I. Johanson (2015). Interseismic coupling and refined earthquake potential on the hayward-calaveras fault zone. *Journal of Geophysical Research: Solid Earth 120*(12), 8570–8590.

Chen, Y. and G. Medioni (1992). Object modelling by registration of multiple range images. *Image and vision computing 10*(3), 145–155.

Chéry, J. (2008). Geodetic strain across the San Andreas fault reflects elastic plate thickness variations (rather than fault slip rate). *Earth and Planetary Science Letters 269*(3-4), 351–364.

Crawford, B., D. Faulkner, and E. Rutter (2008). Strength, porosity, and permeability development during hydrostatic and shear loading of synthetic quartz-clay fault gouge. *Journal of Geophysical Research: Solid Earth 113*(B3).

d'Alessio, M., I. Johanson, R. Bürgmann, D. Schmidt, and M. Murray (2005). Slicing up the san francisco bay area: Block kinematics and fault slip rates from gps-derived surface velocities. *Journal of Geophysical Research: Solid Earth 110*(B6).

De Zan, F. and A. M. Guarnieri (2006). Topsar: Terrain observation by progressive scans. *IEEE Transactions on Geoscience and Remote Sensing 44*(9), 2352–2360.

Dieterich, J. H. (1978). Time-dependent friction and the mechanics of stick-slip. In *Rock Friction and Earthquake Prediction*, pp. 790–806. Springer.

Doolin, D. M., D. L. Wells, and P. L. Williams (2005). Assessment of fault-creep deformation at memorial stadium, university of california, berkeley, california. *Environmental & Engineering Geoscience 11*(2), 125–139.

Ernst, W. and R. J. McLaughlin (2012). Mineral parageneses, regional architecture, and tectonic evolution of franciscan metagraywackes, cape mendocino-garberville-covelo 30× 60 quadrangles, northwest california. *Tectonics 31*(1).

Field, E. H., G. P. Biasi, P. Bird, T. E. Dawson, K. R. Felzer, D. D. Jackson, K. M. Johnson, T. H. Jordan, C. Madden, A. J. Michael, et al. (2015). Long-term time-dependent probabilities for the third uniform california earthquake rupture forecast (ucerf3). *Bulletin of the Seismological Society of America 105*(2A), 511–543.

Fonstad, M. A., J. T. Dietrich, B. C. Courville, J. L. Jensen, and P. E. Carbonneau (2013). Topographic structure from motion: a new development in photogrammetric measurement. *Earth Surface Processes and Landforms 38*(4), 421–430.

Freymueller, J. T., M. H. Murray, P. Segall, and D. Castillo (1999). Kinematics of the Pacific-North America plate boundary zone, northern California. *J. Geophys. Res. 104*(B4), 7419–7441.

Funning, G. J., J. R. Blueford, K. York, and G. McAlpine (2010). 'Citizen Creepmeters': involving high school students in monitoring of fault movements using inexpensive equipment.

Funning, G. J., R. Bürgmann, A. Ferretti, F. Novali, and A. Fumagalli (2007). Creep on the Rodgers Creek fault, northern San Francisco Bay area from a 10 year PS-InSAR dataset. *Geophysical Research Letters 34*(L19306), 3–7.

Funning, G. J., B. Parsons, T. J. Wright, J. A. Jackson, and E. J. Fielding (2005). Surface displacements and source parameters of the 2003 Bam (Iran) earthquake from Envisat advanced synthetic aperture radar imagery. *Journal of Geophysical Research B: Solid Earth 110*(B09406), 1–23.

Furukawa, Y. and J. Ponce (2010). Accurate, dense, and robust multiview stereopsis. *IEEE transactions on pattern analysis and machine intelligence 32*(8), 1362–1376.

Galehouse, J. S. and J. J. Lienkaemper (2003). Inferences drawn from two decades of alinement array measurements of creep on faults in the San Francisco Bay Region. *Bulletin of the Seismological Society of America 93*(6), 2415–2433.

Harris, R. A. (2017). Large earthquakes and creeping faults. *Reviews of Geophysics 55*(1), 169–198.

Harsh, P. W., E. H. Pampeyan, and J. M. Coakley (1978). Slip on the Willits fault (abstract). *Earthquake notes 49*, 22.

Hecker, S., D. Pantosti, D. P. Schwartz, J. C. Hamilton, L. M. Reidy, and T. J. Powers (2005). The most recent large earthquake on the rodgers creek fault, san francisco bay area. *Bulletin of the Seismological Society of America 95*(3), 844–860.

Hooper, A. (2008). A multi-temporal InSAR method incorporating both persistent scatterer and small baseline approaches. *Geophysical Research Letters 35*(16), 1–5.

Hooper, A., D. Bekaert, K. Spaans, and M. Arıkan (2012). Recent advances in sar interferometry time series analysis for measuring crustal deformation. *Tectonophysics 514*, 1–13.

Hooper, A., P. Segall, and H. Zebker (2007). Persistent scatterer interferometric synthetic aperture radar for crustal deformation analysis, with application to Volcan Alcedo, Galapagos. *Journal of Geophysical Research: Solid Earth 112*(7), 1–21.

Hooper, A., K. Spaans, D. Bekaert, M. C. Cuenca, M. Arıkan, and A. Oyen (2010). Stamps/mti manual. *Delft Institute of Earth Observation and Space Systems Delft University of Technology, Kluyverweg 1*, 2629.

Irwin, W. P. and I. Barnes (1975). Effect of geologic structure and metamorphic fluids on seismic behavior of the san andreas fault system in central and northern california. *Geology 3*(12), 713–716.

Javernick, L., J. Brasington, and B. Caruso (2014). Modeling the topography of shallow braided rivers using Structure-from-Motion photogrammetry. *Geomorphology 213*, 166–182.

Jin, L. and G. J. Funning (2017). Testing the inference of creep on the northern rodgers creek fault, california, using ascending and descending persistent scatterer insar data. *Journal of Geophysical Research: Solid Earth 122*(3), 2373–2389.

Johnson, K., E. Nissen, S. Saripalli, J. R. Arrowsmith, P. McGarey, K. Scharer, P. Williams, and K. Blisniuk (2014). Rapid mapping of ultrafine fault zone topography with structure from motion. *Geosphere 10*(5), 969–986.

Jolivet, R., R. Grandin, C. Lasserre, M.-P. Doin, and G. Peltzer (2011). Systematic insar tropospheric phase delay corrections from global meteorological reanalysis data. *Geophysical Research Letters 38*(17).

Jolivet, R., C. Lasserre, M.-P. Doin, S. Guillaso, G. Peltzer, R. Dailu, J. Sun, Z.-K. Shen, and X. Xu (2012). Shallow creep on the haiyuan fault (gansu, china) revealed by sar interferometry. *Journal of Geophysical Research: Solid Earth 117*(B6).

Langenheim, V. E., R. C. Jachens, R. L. Morin, and C. A. McCabe (2007). Preliminary gravity and magnetic data of the lake pillsbury region, northern coast ranges, california. Technical report, Geological Survey (US).

Lee, J.-C., J. Angelier, H.-T. Chu, J.-C. Hu, F.-S. Jeng, and R.-J. Rau (2003). Active fault creep variations at chihshang, taiwan, revealed by creep meter monitoring, 1998–2001. *Journal of Geophysical Research: Solid Earth 108*(B11).

Li, Z., E. Fielding, P. Cross, and R. Preusker (2009). Advanced insar atmospheric correction: Meris/modis combination and stacked water vapour models. *International Journal of Remote Sensing 30*(13), 3343–3363.

Li, Z., E. J. Fielding, P. Cross, and J.-P. Muller (2006). Interferometric synthetic aperture radar atmospheric correction: Gps topography-dependent turbulence model. *Journal of Geophysical Research: Solid Earth 111*(B2).

Li, Z., J.-P. Muller, P. Cross, and E. J. Fielding (2005). Interferometric synthetic aperture radar (insar) atmospheric correction: Gps, moderate resolution imaging spectroradiometer (modis), and insar integration. *Journal of Geophysical Research: Solid Earth 110*(B3).

Lienkaemper, J. (2009). Digital database of recently active traces along the hayward fault, california: Us geological survey data series ds-177, 20 p.

Lienkaemper, J. J. (1992). Map of recently active traces of the hayward fault, alameda and contra costa counties, california.

Lienkaemper, J. J. (2010). Recently active traces of the bartlett springs fault, california: A digital database. *US Geological Survey Data Series 541*(7).

Lienkaemper, J. J. and J. S. Galehouse (1998). New evidence doubles the seismic potential of the hayward fault. *Seismological Research Letters 69*(6), 519–523.

Lienkaemper, J. J., F. S. Mcfarland, R. W. Simpson, and S. J. Caskey (2014). Using Surface Creep Rate to Infer Fraction Locked for Sections of the San Andreas Fault System in Northern California from Alignment Array and GPS Data SE. *Bulletin of the Seismological Society of America 104*(6), 3094–3114.

Lienkaemper, J. J. and P. L. Williams (2007). A record of large earthquakes on the southern hayward fault for the past 1800 years. *Bulletin of the Seismological Society of America 97*(6), 1803–1819.

Lienkaemper, J. J., P. L. Williams, and T. P. Guilderson (2010). Evidence for a twelfth large earthquake on the southern hayward fault in the past 1900 years. *Bulletin of the Seismological Society of America 100*(5A), 2024–2034.

Lin, R.-g. (2016, jul). The Holy Grail' for earthquake scientists has been accidentally destroyed.

Lindsey, E. O. and Y. Fialko (2013). Geodetic slip rates in the southern San Andreas Fault system: Effects of elastic heterogeneity and fault geometry. *Journal of Geophysical Research: Solid Earth 118*(2).

Liu, S., R. Hanssen, and Á. Mika (2009). On the value of high-resolution weather models for atmospheric mitigation in sar interferometry. In *2009 IEEE International Geoscience and Remote Sensing Symposium*, Volume 2, pp. II–749. IEEE.

Lowe, D. G. et al. (1999). Object recognition from local scale-invariant features. In *iccv*, Volume 99, pp. 1150–1157.

Lozos, J. (2013). *Dynamic Rupture and Ground Motion Modeling on Realistically Complex Strike-Slip Faults*. Ph. D. thesis, University of California, Riverside.

Lozos, J., R. A. Harris, J. R. Murray, and J. J. Lienkaemper (2015). Dynamic rupture models of earthquakes on the Bartlett Springs Fault, Northern California. *Geophysical Research Letters 42*(063802), 4343–4349.

Lucieer, A., S. M. de Jong, and D. Turner (2014). Mapping landslide displacements using Structure from Motion (SfM) and image correlation of multi-temporal UAV photography. *Progress in Physical Geography: Earth and Environment 38*(1), 97–116.

Lupini, J., A. Skinner, and P. Vaughan (1981). The drained residual strength of cohesive soils. *Geotechnique 31*(2), 181–213.

Massonnet, D. and K. L. Feigl (1998). Radar interferometry and its application to changes in the earth's surface. *Reviews of geophysics 36*(4), 441–500.

McFarland, F. S., J. J. Lienkaemper, and J. S. Caskey (2018). Data from Theodolite Measurements of Creep Rates on San Francisco Bay Region Faults, California (version 1.1, March 2018). Technical report, U.S. Geological Survey data release.

McLaughlin, R. J., B. Hitchcock, and Z. CS Valin (2018). Framework geologic map and structure sections along the bartlett springs fault zone and adjacent area from round valley to wilbur springs, northern coast ranges, california.

McLaughlin, R. J., A. M. Sarna-Wojcicki, D. L. Wagner, R. J. Fleck, V. E. Langenheim, R. C. Jachens, K. Clahan, and J. R. Allen (2012). Evolution of the rodgers creek–maacama right-lateral fault system and associated basins east of the northward-migrating mendocino triple junction, northern california. *Geosphere 8*(2), 342–373.

Moore, D. and D. Lockner (2015). Correlation of chlorite frictional strength with composition. In *AGU Fall Meeting Abstracts*.

Moore, D. E. (2014). Comparative mineral chemistry and textures of safod fault gouge and damage-zone rocks. *Journal of Structural Geology 68*, 82–96.

Moore, D. E. and D. A. Lockner (2008). Talc friction in the temperature range 25-400C: Relevance for Fault-Zone Weakening. *Tectonophysics 449*(1-4), 120–132.

Moore, D. E. and D. A. Lockner (2011). Frictional strengths of talc-serpentine and talc-quartz mixtures. *Journal of Geophysical Research: Solid Earth 116*(1), 1–17.

Moore, D. E. and D. A. Lockner (2013). Chemical controls on fault behavior: Weakening of serpentinite sheared against quartz-bearing rocks and its significance for fault creep in the San Andreas system. *Journal of Geophysical Research: Solid Earth 118*(5), 2558–2570.

Moore, D. E., D. A. Lockner, and S. Hickman (2016). Hydrothermal frictional strengths of rock and mineral samples relevant to the creeping section of the San Andreas Fault. *Journal of Structural Geology 89*, 153–167.

Moore, D. E., R. J. McLaughlin, and J. J. Lienkaemper (2018). SerpentiniteRich Gouge in a Creeping Segment of the Bartlett Springs Fault, Northern California: Comparison With SAFOD and Implications for Seismic Hazard. *Tectonics*, 2018TC005307.

Moore, D. E. and M. J. Rymer (2007a). Talc-bearing serpentinite and the creeping section of the san andreas fault. *Nature 448*(7155), 795.

Moore, D. E. and M. J. Rymer (2007b, aug). Talc-bearing serpentinite and the creeping section of the San Andreas fault. *Nature 448*(7155), 795–797.

Moore, D. E. and M. J. Rymer (2012). Correlation of clayey gouge in a surface exposure of serpentinite in the San Andreas Fault with gouge from the San Andreas Fault Observatory at Depth (SAFOD). *Journal of Structural Geology 38*, 51–60.

Murray, J. R., S. E. Minson, and J. Svarc (2014). Slip rates and spatially variable creep on faults of the northern San Andreas system inferred through Bayesian inversion of Global Positioning System data. *Journal of Geophysical Research : Solid Earth 119*, 6023–6047.

Nissen, E., A. K. Krishnan, J. R. Arrowsmith, and S. Saripalli (2012). Three-dimensional surface displacements and rotations from differencing pre-and post-earthquake lidar point clouds. *Geophysical Research Letters 39*(16).

Ohlin, H. N., R. J. Mclaughlin, B. C. Moring, and T. L. Sawyer (2010). Geologic map of the Bartlett Springs Fault Zone in the Vicinity of Lake Pillsbury and Adjacent Areas of Mendocino , Lake , and Glenn Counties , California By. (November), 94025.

Ontiveros, G. and H. Delgado-Granados (2015). Application of structure from motion (sfm) to volcano monitoring at popocatépetl (méxico). In *EGU General Assembly Conference Abstracts*, Volume 17.

Parsons, T., R. Sliter, E. L. Geist, R. C. Jachens, B. E. Jaffe, A. Foxgrover, P. E. Hart, and J. McCarthy (2003). Structure and mechanics of the Hayward-Rodgers Creek Fault step-over, San Francisco Bay, California. *Bulletin of the Seismological Society of America 93*(5), 2187–2200.

Prentice, C. S. (2006). *1906 San Francisco Earthquake Centennial Field Guides: Field Trips Associated with the 100th Anniversary Conference, 18-23 April 2006, San Francisco, California*, Volume 7. Geological Society of America.

Prentice, C. S., M. C. Larsen, H. M. Kelsey, and J. Zachariasen (2014). Late holocene slip rate and ages of prehistoric earthquakes along the maacama fault near willits, mendocino county, northern california. *Bulletin of the Seismological Society of America 104*(6), 2966–2984.

Radbruch, D. H. and B. J. Lennert (1966). Damage to culvert under memorial stadium, university of california, berkeley, caused by slippage in the hayward fault zone. *Bulletin of the Seismological Society of America 56*(2), 295–304.

Reinen, L. A. (2000). Seismic and aseismic slip indicators in serpentinite gouge. *Geology 28*(2), 135–138.

Rosen, P. A., E. M. Gurrola, G. Franco Sacco, and H. A. Zebker (2012). The InSAR Scientific Computing Environment. *Proceedings of the 9th European Conference on Synthetic Aperture Radar*, 730–733.

Ruina, A. (1983). Slip instability and state variable friction laws. *Journal of Geophysical Research: Solid Earth 88*(B12), 10359–10370.

Ružić, I., I. Marović, Č. Benac, and S. Ilić (2014). Coastal cliff geometry derived from structure-from-motion photogrammetry at stara baška, krk island, croatia. *Geo-marine letters 34*(6), 555–565.

Schmidt, D. A. and R. Bürgmann (2003). Time-dependent land uplift and subsidence in the Santa Clara valley, California, from a large interferometric synthetic aperture radar data set. *Journal of Geophysical Research: Solid Earth 108*(B9), 2416.

Schmidt, D. A., R. Bürgmann, R. M. Nadeau, and M. D'Alessio (2005). Distribution of aseismic slip rate on the Hayward fault inferred from seismic and geodetic data. *Journal of Geophysical Research B: Solid Earth 110*(8), 1–15.

Schroeder, R. D. (2010). *Kinematic evolution of the Maacama Fault Zone, Northern California Coast Ranges*. Ph. D. thesis, University of Calgary (Canada.

Schwartz, D., D. Pantosti, S. Hecker, K. Okumura, K. E. Budding, T. Powers, G. Borchardt, S. Hirschfeld, J. Lienkaemper, P. McClellan, et al. (1992). Late holocene behavior and seismogenic potential of the rodgers creek fault zone, sonoma county, california. In *Proceedings of the second conference on earthquake hazards in the eastern San Francisco Bay Area: California Department of Conservation, Division of Mines and Geology Special Publication*, Volume 113, pp. 393–398.

Shakibay Senobari, N. and G. J. Funning (2019). Widespread Fault Creep in the Northern San Francisco Bay Area Revealed by Multistation Cluster Detection of Repeating Earthquakes. *Geophysical Research Letters*, 6425–6434.

Simons, M. and P. Rosen (2007). Interferometric synthetic aperture radar geodesy.

Simpson, R., J. Lienkaemper, and J. Galehouse (2001). Variations in creep rate along the hayward fault, california, interpreted as changes in depth of creep. *Geophysical Research Letters 28*(11), 2269–2272.

Steinbrugge, K. and E. Zacher (1960). Creep on the san andreas fault: fault creep and property damage: Seismological society of america bulletin, v. 50.

Steinbrugge, K. V., W. K. Cloud, and N. H. Scott (1970). *The Santa Rosa, California, Earthquakes of October 1, 1969*, Volume 4. US Coast and Geodetic Survey.

Stoffer, P. W. (2008). Where's the Hayward Fault? A Green Guide to the Fault. *Geological Survey Open-File Report 2008-1135*, 1 – 96.

Tembe, S., D. A. Lockner, and T. F. Wong (2010). Effect of clay content and mineralogy on frictional sliding behavior of simulated gouges: Binary and ternary mixtures of quartz, illite, and montmorillonite. *Journal of Geophysical Research: Solid Earth 115*(3), 1–22.

Thomas, M. Y., J.-P. Avouac, J. Champenois, J.-C. Lee, and L.-C. Kuo (2014). Spatiotemporal evolution of seismic and aseismic slip on the longitudinal valley fault, taiwan. *Journal of Geophysical Research: Solid Earth 119*(6), 5114–5139.

Tong, X., D. T. Sandwell, and B. Smith-Konter (2013). High-resolution interseismic velocity data along the San Andreas Fault from GPS and InSAR. *Journal of Geophysical Research: Solid Earth 118*(1), 369–389.

Ullman, S. (1979). The interpretation of structure from motion. *Proceedings of the Royal Society of London. Series B. Biological Sciences 203*(1153), 405–426.

Warrick, J. A., A. C. Ritchie, G. Adelman, K. Adelman, and P. W. Limber (2016). New techniques to measure cliff change from historical oblique aerial photographs and structure-from-motion photogrammetry. *Journal of Coastal Research 33*(1), 39–55.

Watt, J., D. Ponce, T. Parsons, and P. Hart (2016). Missing link between the hayward and rodgers creek faults. *Science advances 2*(10), e1601441.

Wei, M., Y. Kaneko, Y. Liu, and J. J. McGuire (2013). Episodic fault creep events in California controlled by shallow frictional heterogeneity. *Nature Geoscience 6*(7), 566–570.

Weldon, R. J., D. A. Schmidt, L. J. Austin, E. M. Weldon, and T. E. Dawson (2013). Appendix d: Compilation of creep rate data for california faults and calculation of moment reduction due to creep. *US Geol. Surv. Open-File Rept. 2013-1165-D*.

Westoby, M. J., J. Brasington, N. F. Glasser, M. J. Hambrey, and J. Reynolds (2012). structure-from-motionphotogrammetry: A low-cost, effective tool for geoscience applications. *Geomorphology 179*, 300–314.

Wisely, B. A., D. A. Schmidt, and R. J. Weldon II (2008). Appendix p: Compilation of surface creep on california faults and comparison of wgcep 2007 deformation model to pacific-north american plate motion. *The Uniform California Earthquake Rupture Forecast, Version 2 (UCERF 2)*, 43.

Wong, I. G. (1991). Contemporary seismicity, active faulting and seismic hazards of the coast ranges between san francisco bay and healdsburg, california. *Journal of Geophysical Research: Solid Earth 96*(B12), 19891–19904.

Woodget, A. S., P. E. Carbonneau, F. Visser, and I. P. Maddock (2015). Quantifying submerged fluvial topography using hyperspatial resolution UAS imagery and structure from motion photogrammetry. *Earth Surface Processes and Landforms 40*(1), 47–64.

Yu, C., Z. Li, and N. T. Penna (2018). Interferometric synthetic aperture radar atmospheric correction using a gps-based iterative tropospheric decomposition model. *Remote Sensing of Environment 204*, 109–121.

Yu, C., Z. Li, N. T. Penna, and P. Crippa (2018). Generic atmospheric correction model for interferometric synthetic aperture radar observations. *Journal of Geophysical Research: Solid Earth 123*(10), 9202–9222.

Yu, C., N. T. Penna, and Z. Li (2017). Generation of real-time mode high-resolution water vapor fields from gps observations. *Journal of Geophysical Research: Atmospheres 122*(3), 2008–2025.

Yu, E. and P. Segall (1996). Slip in the 1868 hayward earthquake from the analysis of historical triangulation data. *Journal of Geophysical Research: Solid Earth 101*(B7), 16101–16118.

Zimmer, B., C. Liutkus-Pierce, S. T. Marshall, K. G. Hatala, A. Metallo, and V. Rossi (2018). Using differential structure-from-motion photogrammetry to quantify erosion at the engare sero footprint site, tanzania. *Quaternary Science Reviews 198*, 226–241.

Zoback, M., S. Hickman, and W. Ellsworth (2010). Scientific drilling into the san andreas fault zone. *Eos, Transactions American Geophysical Union 91*(22), 197–199.